MEASUREMENT OF THE W BOSON MASS

WITH THE DØ DETECTOR

USING THE ELECTRON E_T SPECTRUM

Ian Malcolm Adam

Submitted in partial fulfillment of the

requirements for the degree

of Doctor of Philosophy

in the Graduate School of Arts and Sciences

COLUMBIA UNIVERSITY

1997

ABSTRACT

MEASUREMENT OF THE W BOSON MASS

WITH THE DØ DETECTOR

USING THE ELECTRON E_T SPECTRUM

Ian Malcolm Adam

The W boson mass is extracted from a sample of $W \rightarrow e\nu$ and $Z \rightarrow ee$ events measured with the DØ detector at the Fermilab Tevatron Collider. The measurement is based on a fit to the E_T spectrum of the electron from the $W \rightarrow e\nu$ decay, a previously unexplored technique. The electron E_T fit is competitive with the standard transverse mass fit for the current data. It could potentially provide better accuracy than the standard fit in the high luminosity regimes of future Tevatron experiments.

Contents

List of Figures

ACKNOWLEDGEMENTS

First I would like to thank my adviser Mike Tuts, who has provided me with help of every kind and been generally a good guy in spite of being a New Yorker.

I owe a great deal to many teachers over the years. From Trinidad Mrs. Lord, Mr. Rowan, Mrs. Paddy and Father Arthur Lai Fook stand out, while from undergraduate years I'm particularly indebted to Professors Robert Gunning, Dan Marlow, Stew Smith and Elliot Lieb. Joan and Jan Guida were my first guides and bosses at D0 and taught me much about the calorimeter and the experiment in general. Lynn Bagby patiently taught me how to solder and helped me with electronics.

I have been fortunate enough to have had the opportunity to work closely with Uli Heintz and Eric Flattum on the Run 1b W mass. I owe a great deal from Uli in particular. Much of what I've learned of high energy physics, computing and analysis originates in his careful and patient help and advice.

Many others have also contributed a great deal both directly and indirectly, to the W mass analysis, particularly Ashutosh Kotwal. Much was also learned from the Run 1a analysis, led by Jon Sculli, Qiang Zhu, Marcel Demarteau and Kathy Streets. Many others were involved, including Chip Brock, Norman Graf, Srini Rajagopalan, Peter Nemethy and Allen Mincer.

I have learned a great deal from several outstanding senior scientists on DØ. I would especially like to mention Paul Grannis, Michael Rijssenbeek, Serban Protopescu and Mark Strovink. Hugh Montgomery has been singled out for special mention because of his occasional generosity with pitchers at the UC.

Also many friends made life interesting here at Fermilab – well, maybe "interesting" is too strong a word. I've enjoyed many an evening at the Users Center with Eric, Rich and Nancy and all the others, and valued the hospitality of Greg and Olga, Meena and Uli, and Jamal and Christine. Father Tom at Ss. Peter and Paul Church in Naperville has been a loyal friend. The gentlemen of the victorious soccer team Prerna are a glorious company whose names are written in burning gold in the arches of the firmament. The people of Java and Juice have provided many hours of fine conversation, espresso and hummus, especially Fran, Bill, Jen, Craig, Shelly, Amy, Marnie, Kate, Julie and Elizabeth, not to mention Terry, my successor. Life at Columbia was made interesting by Andrew, Alex and Sarah.

I would like to thank all my family, Mom and Dad, Jenny, Judy and Claire. Finally I would like to thank Kirsten, who has lightened my step and lifted my shoulders.

To my mother and father

and to Kirsten

Chapter 1

Introduction

In section 1.1 a general picture of particle physics is presented in a rather non–technical way for the lay reader. More details are available in references [4] and [5]. Section 1.2 introduces the electroweak sector of the Standard Model at an elementary but more technical level. Much of this material is derived from lecture notes taken during a graduate course by A. Mueller at Columbia University in 1991. References [6] and [7] provide a similar discussion in greater depth. In section 1.3 I discuss the motivation for performing a measurement of the W mass and explain what a "direct" W mass measurement means. The plan for the present experiment is then outlined in section 1.4. I explain why only $W \rightarrow e\nu$ decays are used, and the choice of kinematic variables used for the mass fit. Finally in section 1.5 other

W mass measurements from past, present and future are summarized.

1.1 Overview of Particle Physics

Modern particle physics concerns itself with the structure of matter at its most fundamental level. The study of matter is central to our understanding of reality as a whole. In fact, in the history of Western philosophy up to the end of the medieval period, the study of matter was considered to be one of the most important tasks of the philosopher.

The advances in science and technology which are among the most dramatic features of the 20^{th} century are in large part due to the trend towards the understanding of matter in terms of microscopic physics — the mechanisms which govern physical processes at smaller and smaller length scales. The fields of chemistry and biology are based on the theory that ordinary matter is composed of molecules, and molecules in turn composed of atoms. The length scales involved in atomic and molecular processes are of the order of Angstroms, where one Angstrom is $1\text{Å} = 10^{-10}m$. On the practical level, the atomic–molecular theory has provided us with an unprecedented ability to manipulate matter to serve our needs. On the intellectual level, it has given us a profound understanding of material phenomena.

Such diverse facts as the colors of the sky, the electrical conductivity of metals, why water flows and how DNA works are ultimately explained by microscopic physics. One could go on forever enumerating the host of phenomena illuminated by the theory of atoms and molecules, ranging from everyday experience to abstruse chemical and biological processes.

Detailed investigation of the structure of atoms and molecules revealed the need for even deeper structure. For example, the periodic table of the elements leads naturally to the postulate that atoms are made up of smaller, "sub–atomic" constituents. These turned out to be protons, neutrons and electrons. The scattering experiments of Rutherford and Marsden showed that the atom is composed of a compact, positively charged nucleus and a cloud of negative charge from electrons. The nucleus is made up of protons and neutrons. To be electrically neutral, the atom must have equal numbers of positively charged protons and negatively charged electrons. This number defines an element and is called the atomic number. Elements with the same number of protons and electrons but different numbers of neutrons are called isotopes. The neutron was observed by Chadwick in 1932.

The theory of atoms as composed of electrons plus a compact nucleus of protons and neutrons was necessary in order to explain the scattering experiments, the periodic table and the existence of isotopes. However, the theory raised new problems. One such problem was the compactness of the nucleus. Nuclear sizes are of the order of one fermi, where $1\,fm = 10^{-15}m$. Confining several positive charges into such a small region results in a very strong repulsive electrostatic force. If any nuclei are to be stable then the protons must be bound together by a force powerful enough to overcome this repulsion. This force was called the strong force.

A different kind of problem was raised by the simple observation that matter is stable. In classical electrodynamics it is impossible to construct stable matter out of a system of positive and negative charges with electromagnetic interactions. The stability of matter requires the introduction of quantum mechanics. Quantum mechanics was in fact required to explain many experimental observations, such as black–body radiation and the transitions of the hydrogen atom. Thus the investigation of matter at the length scales of atoms forced us to rework our entire system of mechanics, and to make the transition from a classical picture to a quantum picture. Any modern theory of particle physics must combine quantum mechanical principles and the special theory of relativity. Such a theory is called a quantum field theory (QFT). In a QFT every particle can be characterized by a set of quantum numbers, such as electrical charge or the analogous charges for the other interactions. One of the startling predictions of quantum field theory was that to every particle there should be a corresponding "antiparticle," which is a particle which has the same mass as the original but with all other quantum numbers opposite. This prediction was confirmed for the electron when the antiparticle to the electron, called the positron, was discovered by Anderson in 1932.

The observation of radioactivity added another piece to the puzzle. In particular, radioactive β decay, discovered in 1930, occurs when certain unstable atoms emit an electron and increase in atomic number by one. The momentum spectra observed for the electron implies that there is an unobserved particle produced, or else momentum would not be conserved. These atomic decays are explained by the subatomic neutron decay process $n \to p + e + \bar{\nu}_e$. This process can be explained by neither electromagnetic nor strong interactions, and so requires a new type of process called weak interactions.

Thus by the mid–1930's the overall picture was emerging that the description of particle physics needed to be a quantum field theory incorporating electromagnetic, strong and weak interactions.

In an effort to explain the strong interaction, the existence of a particle called the pion, denoted by the symbol π was postulated in 1934 by Yukawa. Anderson and Neddermeyer searched for this particle in cosmic rays, but found instead a different particle called the muon, μ. The muon is a particle with the same quantum numbers as the electron, but with a larger mass. Eventually the pion was found in cosmic ray experiments at Rome and Bristol in 1946–1947, but where the muon fit into the whole picture was not clear. The situation became chaotic as more and more particles were found in bubble chamber experiments. These particles were called "hadrons," meaning heavy, and were divided into lighter "mesons" and heavier "baryons." The increasing number of hadrons suggested substructure, analogous to the atomic substructure suggested by the periodic table of atoms. In 1960–1964 the static quark model was laid out by Gell-Mann and Zweig. This model proposed that the hadrons were made out of three more fundamental constituents called "quarks," of three types denoted up, down and strange (u,d and s.) Mesons are composed of a quark–antiquark pair and baryons out of three quarks. By enumerating all possible combinations this model accounted for all the hadrons then observed and predicted the existence of a new particle, the Ω^-. A major success of the static quark model was the observation of the Ω^- in 1964. In the late 1960's scattering of electrons off protons at the End Station A experiments at SLAC demonstrated the existence of substructure in the proton, in a manner very similar to the way the scattering experiments of Rutherford and Marsden proved the existence of substructure in the atom. The constituents of the proton observed in these experiments were called "partons," and are identified today as quarks.

The quarks must be bound together inside the proton by a specific interaction. The quanta of this interaction are called gluons. The strong force between protons and neutrons inside the nucleus is today believed to be a manifestation of the more fundamental interactions between quarks and gluons. Quarks have electrical charges which are multiples of 1/3 of the fundamental unit of charge, while gluons are electrically neutral. Quarks and gluons must also carry a charge, analogous to electrical charge, by which they interact strongly. This charge is called "color," and has no relation to ordinary optical color. There are three basic colors called red, green and blue, which are unrelated to the colors red, green and blue visible to the human eye. They are simply arbitrary labels. The rule that baryons are made from 3 quarks and the multiple of 1/3 fractional charges are related to the fact that there are three colors. The interactions between quarks and gluons governed by color are described by a theory called quantum chromodynamics, or QCD. Processes based on QCD are called strong interactions.

Since the static quark model was proposed, three more quarks have been discovered, the charm (c) quark in 1974, the bottom (b) quark in 1977 and the top (t) quark in 1995 [8, 9]. The quark model then predicts many more mesons and baryons. The study of these new hadrons is an ongoing project in modern particle physics experiments.

All the hadrons which have been observed in experiments up to the present day can be accounted for as combinations of the fundamental quarks. However, this leaves several particles out of the pattern, namely the electron, the muon and the neutrino produced in β decay. These particles were called "leptons" meaning light. More leptons have been added to the list since the mid–1930's. The pion decays to a muon and a neutrino. Steinberger et. al. showed that the neutrino produced in this decay is a distinct particle from that produced in β decay, so that the electron and muon each have a distinct partner neutrino, the ν_e and ν_μ respectively. In 1975 the τ lepton was discovered, and is believed to have its own partner neutrino, the ν_τ. The ν_τ has not been directly observed. The DONUT experiment currently in operation at Fermilab has as its goal the direct observation of ν_τ events.

All the fundamental matter particles currently known can be grouped into two sets, the quarks and the leptons. These particles are arranged into 3 similar groups called "generations." The first generation consists of the up and down quarks, the electron and the electron neutrino. This generation accounts for essentially all ordinary matter. The second and third generations follow a pattern like the first, but at higher masses, except for the massless neutrinos. The particles of the three generations are listed in table 1.1.

In the Standard Model there are also particles which mediate interactions be-

Particle type	Generation 1	Generation 2	Generation 3
quarks	up (u)	charm (c)	top (t)
	down (d)	strange (c)	bottom (b)
leptons	electron (e)	muon (μ)	tau (τ)
neutrinos	ν_e	ν_μ	ν_τ

Table 1.1: Particles of the three generations of the Standard Model.

tween the matter particles. These are called gauge bosons. A boson is a particle whose intrinsic angular momentum, or spin, is an integer, while fermions are particles whose spin is half–integral. The particles mediating interactions are called "gauge bosons" because in the Standard Model interactions are described by "gauge symmetries," an example of which is described in the next section. The gauge bosons in the Standard Model are the photon, well known since Einstein's work on the photoelectric effect in the early 1900's, the electrically charged W^+ and W^- bosons, which mediate radioactive β decay, the Z^0 which is a neutral partner to the W and is closely related to the photon, and finally the gluons which bind quarks together. Table 1.2 lists the gauge bosons of the Standard Model. The prediction of the existence of the W and Z by gauge theory was dramatically con-

Gauge Boson	Interaction type	Mass
Z	neutral weak currents	91.19 GeV
γ	electromagnetism	massless
W^+,W^-	charged weak currents	80.4 GeV
g	strong	massless

Table 1.2: Gauge bosons of the Standard Model.

firmed when W and Z events were observed by the UA1 and UA2 experiments at the CERN collider in the early 1980's. Since then scientists have made a concerted effort to study the properties of these massive particles. This thesis is a part of that ongoing effort.

1.2 W and Z bosons in the Standard Model

The W and Z bosons in the Standard Model are the quanta of local gauge fields. We will outline the model for the case of the first lepton generation, then generalize to the quarks and additional generations at the end. The starting point in the construction is the standard Lagrangian density for a free fermion field

$$\mathcal{L} = \tilde{\varphi} i \gamma^{\mu} \partial_{\mu} \varphi \tag{1.1}$$

The model must contain an interaction which links each lepton to its partner neutrino. Experimentally, no right handed neutrinos are observed so we choose to write the electron and neutrino fields as a left handed doublet and a right handed singlet

$$R_e = (e_R) \tag{1.2}$$
$$L_e = \begin{pmatrix} \nu_e \\ e_L \end{pmatrix} \tag{1.3}$$

where the left and right handed components of a field φ are defined by

$$\varphi_L = \frac{1+\gamma_5}{2}\varphi \tag{1.4}$$
$$\varphi_R = \frac{1-\gamma_5}{2}\varphi \tag{1.5}$$

Two quantum numbers are postulated, $SU(2)$ weak isospin T and $U(1)$ weak hypercharge Y. The doublet is assigned weak isospin $T = 1/2$ and the singlet $T = 0$. The upper component of the doublet has third component of weak isospin $T_3 = 1/2$ and the lower component has $T_3 = -1/2$. The electrical charge Q is related to the weak charges by $Q = T_3 + Y/2$. The free lagrangian for massless leptons can be written

$$\mathcal{L} = \tilde{L}_e i\gamma^\mu \partial_\mu L_e + \tilde{R}_e i\gamma^\mu \partial_\mu R_e \tag{1.6}$$

The free Lagrangian has three global gauge symmetries corresponding to coordinate transformations in the spaces describing the internal degrees of freedom. These are $U(1)_L$ on the L fields, $U(1)_R$ on the R field, and $SU(2)$ on the L fields. In order to force the left and right handed electrons to have the same mass we must restrict the $U(1)_L \times U(1)_R$ to the $U(1)_Y$ subgroup, so that the possible gauge transformations on the fields are

$$\left.\begin{aligned} L_e &\to e^{-i\alpha} L_e \\ R_e &\to e^{-2i\alpha} R_e \end{aligned}\right\} U(1)_Y \text{ transformation} \tag{1.7}$$

The factor 2 in the R_e exponent is from the assignment $Y = -2$ for the singlet. The $SU(2)$ group acts non–trivially only on the doublet

$$L_e \to e^{i\vec{\alpha}\cdot\vec{\tau}/2} L_e \tag{1.8}$$

These global gauge symmetries lead to conserved charges via Noether's theorem. Asking the gauge symmetries to hold locally corresponds to allowing the coefficients α to be functions of space–time. To maintain invariance of the Lagrangian then requires the introduction of gauge fields and the replacement of derivatives by gauge–covariant derivatives. For example, to gauge the $U(1)$ symmetry a vector field B_μ is introduced and the Lagrangian is modified to

$$\mathcal{L} = \tilde{L}_e i\gamma^\mu D_\mu L_e + \tilde{R}_e i\gamma^\mu D_\mu R_e + \frac{1}{4} F_{\mu\nu} F^{\mu\nu} \tag{1.9}$$

where the covariant derivative is given by $D_\mu = \partial_\mu - i\frac{g'}{2}YB_\mu$ and the field strength tensor $F_{\mu\nu}$ is given by

$$F_{\mu\nu} = \partial_\mu B_\nu - \partial_\nu B_\mu \tag{1.10}$$

The Lagrangian is then invariant under

$$\left.\begin{array}{l} L_e \rightarrow e^{-i\alpha(x)}L_e \\ \\ R_e \rightarrow e^{-2i\alpha(x)}R_e \\ \\ B_\mu \rightarrow B_\mu + \frac{2}{g'}\partial_\mu\alpha(x) \end{array}\right\} \text{local } U(1)_Y \text{ transformation} \tag{1.11}$$

Similarly, to gauge the $SU(2)_T$ symmetry we introduce fields W_μ^a, $a = 1, 2, 3$, and an $SU(2)$–valued field $\mathbf{W}_\mu = W_\mu^a \cdot \tau^a/2$. The field strength tensor for this field is

$$F_{\mu\nu}^a = \partial_\mu W_\nu^a - \partial_\nu W_\mu^a + ig\varepsilon^{abc}W_\mu^b W_\nu^c \tag{1.12}$$

The covariant derivative becomes $D_\mu = \partial_\mu - i\frac{g'}{2}YB_\mu + ig\mathbf{W}_\mu$ and the Lagrangian becomes

$$\mathcal{L} = \tilde{L}_e i\gamma^\mu D_\mu L_e + \tilde{R}_e i\gamma^\mu D_\mu R_e + \frac{1}{4}F_{\mu\nu}F^{\mu\nu} + \frac{1}{4}\mathbf{F}_{\mu\nu}\mathbf{F}^{\mu\nu} \tag{1.13}$$

This Lagrangian describes massless leptons interacting with four massless gauge fields. In the minimal version of the Standard Model the lepton and gauge boson masses are finite as a result of the Higgs mechanism. We introduce a doublet of complex scalar Higgs fields with $T = 1/2$ and $Y = 1$.

$$\phi = \begin{pmatrix} \phi^+ \\ \phi^0 \end{pmatrix} \tag{1.14}$$

and additional terms in the Lagrangian

$$\mathcal{L}_H = (D_\mu\phi)^\dagger(D_\mu\phi) + \mu^2\phi^\dagger\phi - \lambda(\phi^\dagger\phi)^2 \tag{1.15}$$

This is the usual self–interacting scalar field form of the Lagrangian. Higher powers of the field ϕ would spoil renormalizability. The couplings between the Higgs fields and the gauge bosons are determined by the covariant derivative term. The couplings of the Higgs to the leptons are given by

$$\mathcal{L}_{HL} = -G_l(\tilde{L}_l\phi R_l + \tilde{R}_l\phi^\dagger L_l) \tag{1.16}$$

Gauge invariance requires the Higgs–lepton coupling terms to have this form. For each term, gauge invariance implies that $\sum Y = 0$ and $\sum T = 0$, and the only ways to build terms with a product of two lepton factors and one Higgs factor which satisfy these constraints are the two terms shown in $\mathcal{L}_{HL}$. Having constructed the Lagrangian with the required symmetry properties, the quantum theory is obtained by determining the classical ground state and allowing for excitations above that state. Because of the signs of the terms in $\phi^\dagger\phi$ and $(\phi^\dagger\phi)^2$, the classical minimum of the potential is not at $\phi = \phi^\dagger = 0$. Instead the minimum occurs at

$$|\phi^\dagger \phi| = \frac{\mu^2}{2\lambda} = \frac{v}{\sqrt{2}} \tag{1.17}$$

In the quantum picture this means that the vacuum expectation value of the Higgs field is non–zero. This phenomenon is called spontaneous symmetry breaking. The Lagrangian exhibits a symmetry, but quantization must start from a ground state. The ground state may not have the full symmetry of the Lagrangian. The effective behavior of the system is determined by fluctuations of the field configuration around the ground state configuration. Hence, if the ground state does not have the full symmetry of the Lagrangian, the observable physical system will have a broken symmetry, i.e., the full symmetry of the Lagrangian will not be manifest. To ensure that electric charge is a good quantum number, we choose to put the non–zero expectation value of the Higgs field entirely into the neutral ϕ^0 field, so that we have

$$\langle 0|\phi^+|0\rangle = 0 \tag{1.18}$$

$$\langle 0|\phi^+|0\rangle = \frac{v}{\sqrt{2}} \tag{1.19}$$

It is always possible, via a gauge transformation, to write the doublet in a form where the charged field is identically zero. We can write the Higgs field doublet as

$$\phi = \begin{pmatrix} 0 \\ v + \eta(x) \end{pmatrix} \tag{1.20}$$

where the ground state configuration of the η field is $\eta(x) = 0$. The masses of the leptons and gauge bosons now follow by identifying the quadratic terms in the broken Lagrangian. For the electron the relevant terms are

$$\tilde{L}_e i\gamma^\mu \partial_\mu L_e + \tilde{R}_e i\gamma^\mu \partial_\mu R_e - \frac{G_e v}{\sqrt{2}}(\tilde{e}_L e_R + \tilde{e}_R e_L) \tag{1.21}$$

$$= \tilde{e}(i\gamma^\mu \partial_\mu - \frac{G_e v}{\sqrt{2}})e + \tilde{\nu}_{eL}(i\gamma^\mu \partial_\mu)\nu_{eL} \tag{1.22}$$

so that the left and right handed electrons have the same mass and the neutrino is massless. For the Higgs, the quadratic terms are

$$\frac{1}{2}\partial_\mu \eta \partial^\mu \eta + \frac{\mu^2}{2}(v+\eta)^2 + \frac{\lambda}{4}(v+\eta)^4 \tag{1.23}$$

$$= \frac{1}{2}(\partial\eta)^2 - \mu^2\eta^2 + \dots \tag{1.24}$$

so that the Higgs mass is $M_H = \sqrt{2}\mu = v\sqrt{2\lambda}$. For the gauge bosons, the mass terms are

$$\frac{1}{8}\left|(g\bar{\tau}\cdot\bar{W}_\mu + g' B_\mu)\begin{pmatrix} \phi^+ \\ \phi^0 \end{pmatrix}\right|^2 = \tag{1.25}$$

$$\frac{v^2}{8}\left[g^2(W^1_\mu - iW^2_\mu)(W^1\mu + iW^2\mu) + (g'B_\mu - gW^3_\mu)(g'B\mu - gW^3\mu)\right] \tag{1.26}$$

We define linear combinations of the W_μ^i and B_μ fields which are mass eigenstates

$$W_\mu = \frac{1}{\sqrt{2}}(W_\mu^1 - iW_\mu^2) \tag{1.27}$$

$$W_\mu^\dagger = \frac{1}{\sqrt{2}}(W_\mu^1 + iW_\mu^2) \tag{1.28}$$

$$Z_\mu = -\frac{g'}{\sqrt{g^2 + g'^2}}B_\mu + \frac{g}{\sqrt{g^2 + g'^2}}W_\mu^3 \tag{1.29}$$

$$A_\mu = \frac{g}{\sqrt{g^2 + g'^2}}B_\mu + \frac{g'}{\sqrt{g^2 + g'^2}}W_\mu^3 \tag{1.30}$$

To simplify notation we introduce an angle θ_W such that

$$\sin\theta_W = \frac{g'}{\sqrt{g^2 + g'^2}} \tag{1.31}$$

$$\cos\theta_W = \frac{g}{\sqrt{g^2 + g'^2}} \tag{1.32}$$

Then the quadratic terms for the W, Z and A fields are

$$\frac{g^2v^2}{4}W_\mu^\dagger W_\mu + \frac{g^2v^2}{8\cos^2\theta_W}Z_\mu Z^\mu \tag{1.33}$$

There are no terms quadratic in the A field so it remains massless after symmetry breaking, and is identified with the photon field of ordinary electromagnetism. The masses of the W and Z are then given by $M_W = gv/2$ and $M_Z = gv/(2\cos\theta_W)$.

For other lepton generations the construction is exactly analogous to that for the electron generation. Each generation has an independent coupling to the Higgs.

For the quarks, the construction is very similar except that the mass eigenstates of the quarks do not coincide with the weak interaction eigenstates. The quarks are organized into generations on the basis of mass. In weak interactions the fact that the weak eigenstates are not the same as the mass eigenstates is manifested by mixing between the generations. By convention the mixing assigned entirely to the $T = -1/2$ quarks. The transformation from the mass eigenstate basis to the weak eigenstate basis can be described by a unitary transformation implemented in the CKM matrix, named after Cabibbo, Kobayashi and Maskawa. The amplitude for a vertex $Wq_1\bar{q}_2$ is proportional to the CKM matrix element $V_{q_1q_2}$.

$$\begin{pmatrix} d' \\ s' \\ b' \end{pmatrix} = \begin{pmatrix} V_{ud} & V_{cd} & V_{td} \\ V_{us} & V_{cs} & V_{ts} \\ V_{ub} & V_{cb} & V_{tb} \end{pmatrix} \begin{pmatrix} d \\ s \\ b \end{pmatrix} \tag{1.34}$$

The preceding discussion outlines the basic mechanism by which the weak gauge fields acquire mass via the Higgs mechanism. To actually calculate the masses quantitatively requires inclusion of higher–order effects. The dominant higher order diagrams contributing to the W propagator are shown in figures 1.1 and 1.2.

The contribution of the top quark loop is given by

$$\Delta M_W \propto M_t^2 - M_b^2 \tag{1.35}$$

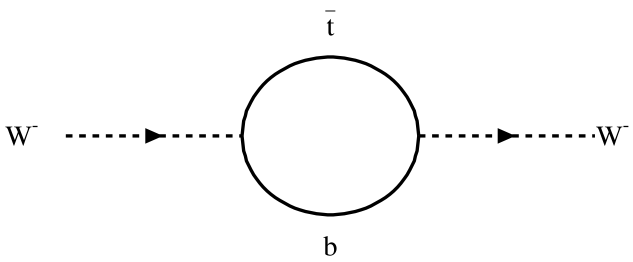

Figure 1.1: Top quark loop diagram contributing to the W propagator.

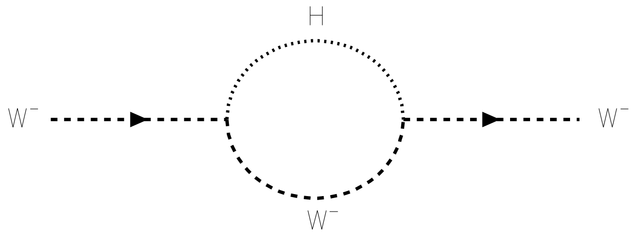

Figure 1.2: Higgs loop diagram contributing to the W propagator.

and that of the Higgs loop is given by

$$\Delta M_W \propto \log M_H \tag{1.36}$$

These contributions are often called radiative corrections, because they correspond to virtual radiation and reabsorption processes. The Higgs loop diagram, for example, can be interpreted as a process in which the W radiates and reabsorbs a Higgs boson.

1.3 Motivation for a precise direct M_W measurement

The Standard Model predicts values for the W and Z boson masses, which are related to the top quark and Higgs boson masses. These predicted masses can be compared to experiment. The Z boson mass has been measured with extreme precision, with a total uncertainty of a few MeV [63]. This level of precision is possible because the Z appears as a resonance in the total e^+e^- cross section as a function of center of mass energy ($\sqrt{s}$). High energy e^+e^- colliders such as LEP and SLC running at center of mass energies around the Z mass need only measure the total cross section as a function of $\sqrt{s}$. No explicit reconstruction and fit to the Z decay products observed in the detector is necessary. The W boson and the t quark masses have been measured much less precisely, since there is presently no e^+e^- collider with sufficient energy to produce W^+W^- or $t\bar{t}$ pairs. The LEP II collider, which began running in mid–1996 has the necessary energy (more than 161 GeV or so) to produce W^+W^- pairs, but the world will have to wait a long time for the 300–400 GeV collider which will be necessary to produce $t\bar{t}$ pairs. In practice the precise Z mass measurement serves as a normalization point, and the W and top quark masses are compared to theoretical predictions.

As discussed in the previous section, in the Standard Model the W propagator is modified by small quantum corrections, which can be calculated from loop diagrams involving the Higgs boson and the top quark. Therefore, sufficiently precise measurements of M_W and M_t together constrain the Higgs mass, M_H in the Standard Model. Previous, present and future M_W measurements are discussed in section 1.5. The top quark was directly observed for the first time by the DØ and CDF collaborations in the Run 1 Tevatron data. Its mass has been measured by both collaborations. Since the present top samples are statistically limited, the M_t measurements have large errors of 7–10 GeV. Future measurements of M_t in the Tevatron Run II are expected to achieve errors of about 3 GeV on M_t. The measurements of M_W and M_t attainable in the Tevatron Run II era should give interesting information about the Standard Model Higgs boson if it exists.

Alternatively, if the Higgs boson were to be found and its mass measured, then the comparison between the measured M_H and the calculated value from the pair (M_W, M_t) would provide an incisive test of the Standard Model. Searches for the Higgs boson are planned at the proposed CMS and ATLAS experiments at the LHC and at the upgraded DØ and CDF experiments at Fermilab. If these searches are successful then it should be possible to perform this test within the next decade.

Many physicists believe that the Standard Model is incomplete. Therefore a great deal of work is devoted to exploring possible scenarios which go beyond the Standard Model. The W mass is sensitive to corrections from several types of high mass objects which occur in hypothesized new physics models. Since M_W depends on $M_t^2 - M_b^2$, models which include extra quark generations will in general predict higher values for M_W than the Standard Model value, unless the new generations are degenerate in mass, i.e., unless the mass of the charge 2/3, u–type quark approximately equals the mass of the charge $-1/3$, d–type quark. The trend in the three observed generations is that the mass split between the u–type and d–type increases as the mass of either increases. The notion of a higher mass, degenerate quark doublet is therefore counter–intuitive. Nevertheless theorists continue to speculate on the possible existence of such extra degenerate quark doublets. In the Standard Model, the Higgs mechanism for spontaneous symmetry breaking is based on a single Higgs doublet field. The model predicts a single observable Higgs boson after symmetry breaking. Some extensions to the Standard Model begin with more than one Higgs doublet and predict the existence of several Higgs bosons. In these models, the additional Higgs bosons modify to the W mass, typically with corrections quadratic in the Higgs mass. In general, any model which postulates new particles which can couple to the W will predict a W mass different from the Standard Model prediction. The correspondence between the prediction and the directly measured value therefore provides a constraint on model building. An example of a Standard Model extension is the Minimal Supersymmetric Standard Model, or MSSM. Figure 1.3 shows the MSSM corrections to M_W for an ensemble of possible supersymmetric models [13].

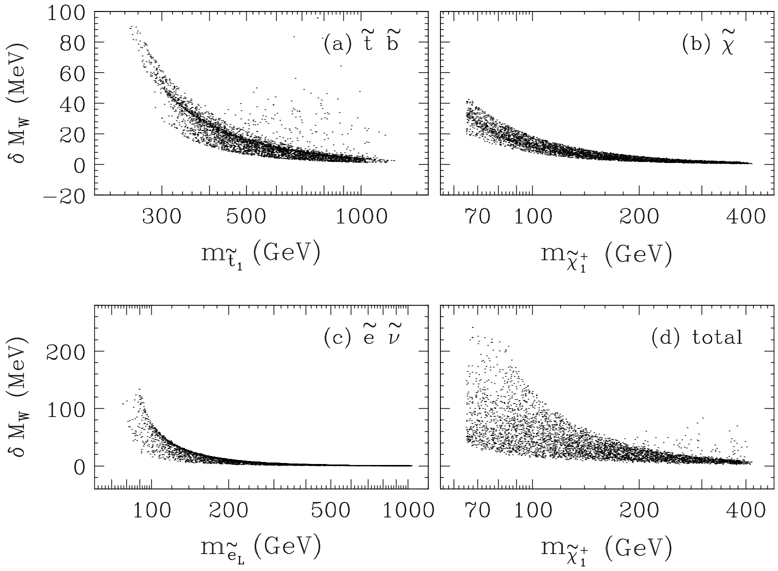

Figure 1.3: MSSM corrections to the W mass. (Figure from Damien Pierce.)

The W mass is closely related to the weak mixing angle. At leading order in the Standard Model they are related by

$$\sin^2 \theta_W = 1 - \frac{M_W^2}{M_Z^2} \tag{1.37}$$

where M_W and M_Z are the W and Z masses, and by

$$1 - 4\sin^2\theta_W = \frac{g_V^l}{g_A^l} \tag{1.38}$$

where g_V^l and g_A^l are the vector and axial vector couplings in the $Z^0 l^+ l^-$ vertex. Physical processes are not leading order, however. When higher order corrections are included, the meanings of $\sin^2\theta_W$ in these two equations is different. In the scheme proposed by Sirlin [10] the value defined by the physical W/Z mass ratio is called the on–shell value, $\sin^2\theta_W^{on-shell}$ or $\sin^2\theta_W^{Sirlin}$ while that defined by the relative couplings of the Z to left and right handed leptons is called $\sin^2\theta_{eff}^{lept}$.

In using a measured W mass to constrain new physics, it is important to bear in mind that such comparisons are only valid for measurements of the W propagator. Direct measurements, based on reconstructed decays of W bosons, probe the W propagator. Other processes which contain a W propagator include muon decay and charged current neutrino deep inelastic scattering. Measurements of $\sin^2\theta_{eff}^{lept}$ are different from direct W mass measurements, because they probe couplings rather than masses. An obvious example of this are the measurements of $\sin^2\theta_{eff}^{lept}$ from the forward–backward asymmetry A_{FB} and left–right asymmetry A_{LR} of Z decays at LEP and SLC [63]. In the Standard Model these asymmetries arise because of the asymmetry in the Z couplings to left and right handed fermions.

For example, for the electron the coupling terms in the Lagrangian are

$$\mathcal{L} = ... - \frac{g}{2\cos\theta_W}[2\sin^2\theta_W \tilde{e}_R \gamma_\mu e_R + (2\sin^2\theta_W - 1)\tilde{e}_L \gamma_\mu e_L] Z^\mu \qquad (1.39)$$

In the Z production and decay processes observed at LEP and SLC the W propagator does not appear anywhere. There are only Z bosons coupling differently to left and right handed leptons. Therefore such measurements cannot possibly probe the W propagator.

While in the Standard Model it is possible to precisely relate masses to couplings, once one allows for the possibility of new physics such relations must be recomputed for each new model considered. Typically, both the W mass and $\sin^2\theta_{eff}^{lept}$ are affected by particles such as supersymmetric partners or the Higgs boson, but with different sensitivities.

1.4 Plan for this Experiment

This thesis describes a direct measurement of the W boson mass using the 1992–1995 data collected by the DØ detector at the Fermilab Tevatron collider. The Tevatron provides DØ with $p\bar{p}$ collisions at $\sqrt{s} = 1800\,\mathrm{GeV}$. Fermilab has just completed a long running period from 1992 to 1995, called Run 1. Run 1 is subdivided into two shorter periods, Run 1a from 1992 to 1993 and Run 1b from

1993 to 1995. The $p\bar{p}$ collisions at the Tevatron are energetic enough to produce W and Z bosons. Approximately 1 out of every 50000 collisions is a W event. The subset of these events in which the W decays to an electron and a neutrino will be used to extract the W mass.

1.4.1 Choice of $W\rightarrow e\nu$ decays

While the W decays in several different modes, the mass will be measured using only the mode in which the W decays to an electron and antineutrino, or a positron and a neutrino. DØ has no central magnetic field and so does not distinguish between e^- and e^+ final states, so I will generically refer to e^- and e^+ as electrons, and to ν and $\bar{\nu}$ as neutrinos.

The reasons for using only the electron decays of the W for the mass measurement are as follows. W bosons decay in the modes $W^+\rightarrow e^+\nu$, $W^+\rightarrow \mu^+\nu$, $W^+\rightarrow \tau^+\nu$, $W^+\rightarrow u\bar{d}$, $W^+\rightarrow c\bar{s}$ and their charge conjugates and CKM variants. The decay $W^+\rightarrow t\bar{b}$ is kinematically forbidden since the top quark mass is greater than the W mass. The relative probability that a W will decay in any particular mode is called the branching fraction or branching ratio of that decay mode. The branching ratio for decays $W^+\rightarrow e^+\nu$ or the charge conjugate $W^-\rightarrow e^-\bar{\nu}$ is $(10.8 \pm 0.4)\%$. I will use the notation $W\rightarrow e\nu$ to refer to both the charge conjugate modes $W^+ \rightarrow e^+\nu$ and $W^- \rightarrow e^-\bar{\nu}$, and similarly for the other decay modes. Decays to muons are not used in the W mass measurement because the DØ muon acceptance and momentum resolution are poor. When the W decays via the $W \rightarrow u\bar{d}$ and $W \rightarrow c\bar{s}$ channels, the two final state quarks are manifested as jets of hadrons. Measuring the energy of a hadron jet is a difficult proposition experimentally. Jet energy resolutions are typically much worse than electron energy resolutions. Also, the jet energy measurement is subject to systematic biases which are difficult to estimate because they depend on details of parton fragmentation and hadronization. The detector response to hadrons is also more complex and difficult to calculate than the response for electrons. Hadronic final states are therefore relatively poorly measured. In addition, events in which a W decays to two jets are indistinguishable from events in which two jets are produced from QCD processes. These QCD events are called dijets and overwhelm the W decay event sample. It is therefore next to impossible to isolate a sample of W decays to hadrons, and certainly impossible to determine an accurate W mass that way. The $W^+ \rightarrow \tau^+\nu$ decay is identifiable, but τ leptons decay to hadrons or to states with neutrinos, and so they are difficult to trigger on and to measure.

Hence, although the branching ratios to other final states are appreciable, only the electron decays are used in the mass measurement at DØ.

1.4.2 Choosing variables to fit the W mass

Neutrinos almost never interact in the detector. Therefore, the neutrino from the $W \to e\nu$ decay is not detected. Instead, its presence is inferred from a large transverse momentum imbalance, called missing transverse energy ($\not\!\!E_T$). The neutrino in the final state of the $W \to e\nu$ decay precludes the possibility of reconstructing the invariant mass of the W. This makes the measurement tricky, requiring a fit to some other kinematic distribution which depends on the mass, such as the electron energy, missing transverse energy ($\not\!\!E_T$), electron transverse energy (E_T), or the "transverse mass," denoted M_T. The standard method of performing direct W mass measurements at hadronic colliders has been the transverse mass fit. This method is attractive because it is minimally sensitive to the W transverse momentum distribution. However, it is experimentally unattractive because it requires a measurement of the total hadronic recoil system which balances the transverse momentum of the W.

In this measurement, the W mass is determined from the electron E_T spectrum rather than the M_T spectrum. From the experimental point of view, this measurement is attractive because it gives much less importance to understanding the detector response to hadrons. From a theoretical standpoint, it suffers from a relatively strong dependence on the W production model. However, we will show that much of this uncertainty can be removed by studying Z decays. The p_T distributions of W and Z events should be very similar. Therefore, though it is difficult to calculate the p_T of the W from first principles, it is possible to use the observed distribution for the Z to constrain the model for the W events.

In the near future, the Tevatron will be upgraded by the addition of the Main Injector and other accelerator improvements. These improvements will allow the Tevatron to run at much higher luminosities than were possible during Run 1. It will then be possible to collect samples of W and Z bosons up to a factor of 20 larger than are currently available. The operation of the upgraded Tevatron is scheduled to begin in 1999, and is called Run II. An important consideration in the present analysis is to learn how to carry out the W mass measurement when very large samples are available. The strategy in such a case must be to minimize systematic errors. In the high luminosity Run II environment the missing transverse energy measurement is expected to degrade substantially, while the electron measurement will not degrade as much. These factors provide a strong motivation to attempt to understand the W mass measurement from the electron.

1.5 Previous and future M_W measurements

Until recently, real W bosons have been artificially produced only at hadron colliders, namely the $Sp\bar{p}S$ at CERN and the Tevatron at Fermilab. In 1996, the LEP II collider began to produce W pairs in e^+e^- collisions at $\sqrt{s}$ just greater than 180 GeV. The CERN $Sp\bar{p}S$ collider, decommissioned since 1989, operated at $\sqrt{s} =$ 540 or 630 GeV. The UA1 and UA2 experiments discovered the W and Z bosons and measured M_W. The original UA1 and UA2 measurements are no longer included in world averages, however, the later measurement from the upgraded UA2 experiment is still used.

Table 1.3 shows the results of previously published measurements of M_W. Early measurements with errors greater than 1 GeV are excluded, because the errors are so large that they do not contribute significantly to a combined mass result, and because they have much larger systematic errors than the more modern measurements. The UA2 experiment actually measured the ratio M_W/M_Z; the value quoted here is that ratio multiplied by the Z mass from LEP.

Table 1.4 shows the unpublished results from the DØ Run 1b W mass analyses, including the result of this thesis, the expected errors from the CDF Run 1b analyses, which were not yet complete at the time this thesis was written, and the anticipated errors from future experiments. For the Run II and TeV33 experiments

Experiment	W decay mode	M_W(GeV)	Total error (GeV)
CDF 88–89	electrons	79.84	-
	muons	79.78	-
	combined e, μ	79.91	0.39
UA2 92	electrons	80.49	0.49
CDF 92–93	electrons	80.49	0.23
	muons	80.31	0.24
	combined e, μ	80.41	0.18
D0 92–93	electrons	80.35	0.27

Table 1.3: Previous direct W mass measurements.

these numbers are essentially educated guesses.

The most precise measurement in the next few years is expected to come from the LEP II experiments. The LEP II collider at CERN will run at center of mass energies above the W pair production threshold. Four detectors (L3, ALEPH, OPAL and DELPHI) will attempt to measure the W mass using several methods. The first method is to measure of the total cross section at a single center of mass energy just above threshold. Assuming the Standard Model, one can calculate the the cross section vs. the W mass. This method will not ultimately be useful since it depends on the assumption that the $WW\gamma$ and WWZ vertex couplings are given by the Standard Model values. These couplings are relatively poorly constrained experimentally. A second method is to map out the W pair production threshold curve by scanning the beam energy across the threshold. This method would be model–independent, but would require long periods of running at each energy to obtain sufficiently small statistical errors, since the pair production process is non–resonant. The third method is to attempt to reconstruct the W mass from the decay products, including the hadronic decays. This would provide a direct measurement, but requires careful control of experimental systematics. However, the four independent detectors will have independent systematic effects and so the results will cross check one another. LEP II expects to be able to measure the W

Experiment	Decay mode	Anticipated error on M_W (MeV)
DØ 1b M_T fit	e	120
DØ 1b E_T fit	e	140
CDF 1b M_T fit	e and μ	100
LEP II, 4 experiments	all channels	40
Tevatron Run II	e and μ	50
TeV 33	e and μ	30

Table 1.4: Present and future W mass measurements.

mass to a precision of 40 MeV by combining the results from the four experiments. It remains to be seen whether the Tevatron experiments will be able to surpass those results in Run II.

Chapter 2

Experimental Apparatus

This chapter provides an overview of the subsystems of the Tevatron accelerator and the DØ detector relevant to this analysis. This material is included for completeness only. It has been described elsewhere several times before.

2.1 Accelerator systems

The accelerator subsystems necessary for colliding beam operations at $\sqrt{s} = 1800\,\mathrm{GeV}$ are well described in reference [16]. Information about the accelerator complex is also available in [17]. Figure 2.1 shows an overview of the accelerator complex and detector locations.

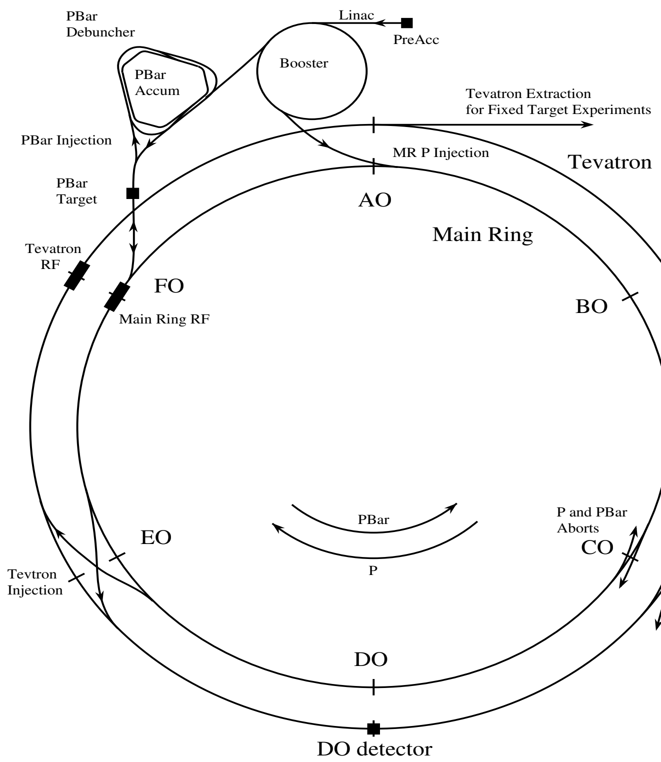

Figure 2.1: Overview of the Fermilab accelerator complex.

2.1.1 Preaccelerator, LINAC and Booster

The starting point for $p\bar{p}$ collisions is production of H^- ions from a magnetron source. The source produces a 50 mA beam of H^- ions at 18 keV. These ions are accelerated to 750 keV by a commercial Cockcroft–Walton accelerator. The ions from the Cockcroft–Walton are fed to the LINAC (LINear ACcelerator) by a transport line which includes focussing magnets and an RF cavity which bunches the H^- beam to match the LINAC frequency. The first stage of the LINAC is a 79 m long Alvarez drift tube device consisting of five resonant RF cavities. It accelerates particles to 116 MeV. It is followed by a more efficient side–coupled section which is based on seven 805 MHz klystrons operating at 10 MW. Quadrupole magnets between the cavities provide transverse focussing of the beam. The LINAC system accelerates H^- ions supplied by the preaccelerator to 400 MeV during Run 1b operations. This was upgraded from 200 MeV during Run 1a. The 400 MeV H^- ions from the LINAC are subjected to a charge–exchange process in which they are passed through a carbon stripping foil and some are converted to H^+ ions, or protons. The protons are injected into the Booster synchrotron and accelerated to 8 GeV.

2.1.2 Tevatron and Main Ring

The Tevatron is a unique scientific instrument, providing the CDF and DØ detectors with the world's highest energy $p\bar{p}$ collisions. The Tevatron itself is a synchrotron with a diameter of approximately 2 kilometers. The bending for the proton and antiproton beams is accomplished using 774 superconducting dipole magnets, liquid helium cooled to $4.6K$. Focussing is performed by a system of 216 superconducting quadrupoles as well as correction magnets.

In normal Tevatron operations there are 6 bunches of $\approx 150 \times 10^9$ protons and 6 bunches of $\approx 50 \times 10^9$ antiprotons counter–rotating in the beampipe. They are injected at 150 GeV from the Main Ring and accelerated to 900 GeV by a system of 53 MHz radio frequency (RF) cavities. The magnets are ramped synchronously so that the protons and antiprotons maintain their orbits at the Tevatron radius. Each RF bucket is $18.8\,ns$ and the bunch spacing is 186 or 187 buckets so that the beam crossing time is $3.5\,\mu s$. There are two luminous regions where the beams are allowed to collide, at the CDF and DØ detector locations. Electrostatic separators prevent the beams from colliding elsewhere. The luminous region at DØ has longitudinal size $\approx$ 25 cm and transverse size $\approx$ 40 microns. The crossing angle is zero.

The Main Ring is located in the same tunnel as the Tevatron. It is used as a 150 GeV injector for protons and antiprotons for the Tevatron. It also provides the 120 GeV proton beam used to initiate antiproton production.

2.2 The DØ detector

The DØ detector has been described in several publications and theses. Reference [18] is considered to be the definitive documentation of the DØ detector, however, reference [19] is more complete. The information in this section is mainly from these two documents.

The order more or less follows the path of particles produced in collisions. Detector pseudorapidity values, denoted $|\eta_{DET}|$, are calculated with respect to the nominal vertex, $z = 0$. Pseudorapidity is defined in appendix A.

2.2.1 Beampipe

The $p\bar{p}$ interactions take place along the beam axis, around which the whole detector is approximately centered. The beampipe is necessary to maintain the vacuum required for Tevatron operations. The beampipe geometry is locally cylindrical with an inner radius of about 3 inches. For most of the Tevatron circumference the beampipe is made of stainless steel. However, in order to reduce the amount of material which the particles must pass through before reaching the detector, the section of the pipe round the nominal interaction point is replaced by a beryllium section. Beryllium was chosen for its high tensile strength. The beryllium section is thin, yet strong enough to sustain the vacuum.

2.2.2 Vertex Drift Chamber (VTX)

Located immediately after the beampipe is the vertex drift chamber (VTX). It is used primarily to determine the position of the beam spot on a run–by–run basis in the xy view. The beam spot xy position varies only slightly from run to run, and negligibly within a run. Hence this measurement amounts to a determination of the event-by-event xy vertex position.

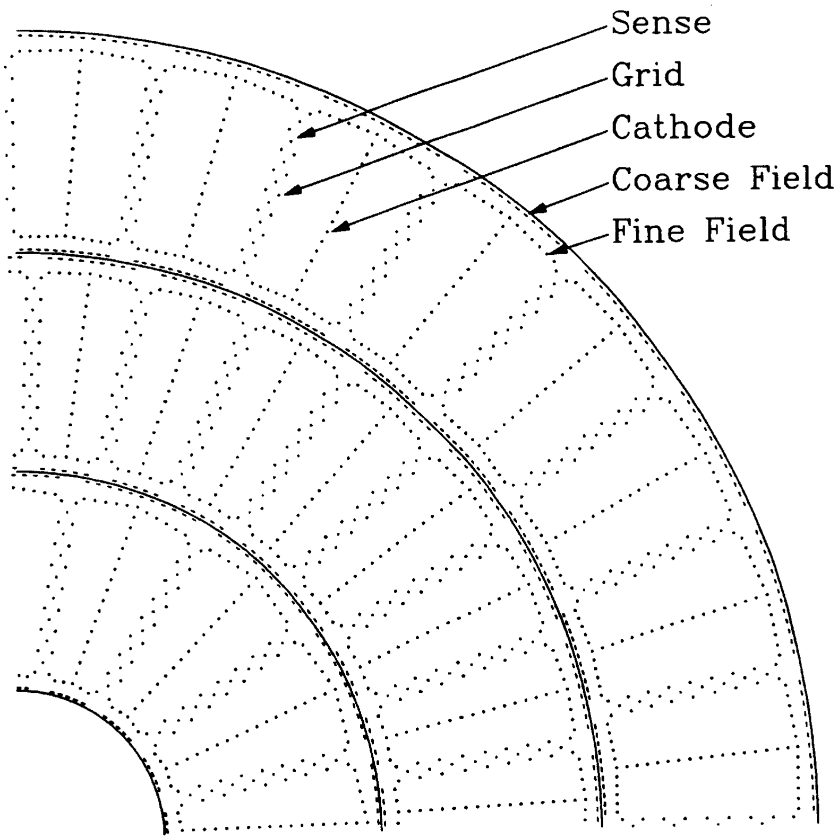

Figure 2.2: A quadrant of the VTX chamber, showing wire placement. The horizontal direction corresponds to $\phi = 0$.

The VTX covers the region $|\eta_{DET}| < 1.2$. Its geometry is that of an annular cylinder with axis of symmetry aligned along the beam axis, with inner radius

3.7 cm and outer radius 16.2 cm. An end view of one quadrant of the VTX is shown in figure 2.2.

It is divided in the radial direction into three layers. The inner, middle and outer layers are called layers 1,2 and 3. Each layer is divided in azimuth into sectors. Layer 1 is divided into 16 sectors and layers 2 and 3 into 32 sectors each. In each sector there are 8 sense wires aligned parallel to the beam axis, separated radially by 4.57 mm and staggered by ± 100 microns in the azimuthal direction relative to the cell centerline, to help resolve the left-right ambiguity. The sense wires are maintained at a potential of $+2.5$ kV and read out at both ends. Each wire measures a track point in the xy view via a drift time and in the rz view via charge division from the double sided readout. The maximum drift distances in the three layers are 1.37 cm, 1.14 cm and 1.60 cm. The drift velocity is approximately $7.3\,\mu m/ns$ for the nominal field of 1 kV/cm. In measuring electrons, the xy drift time measurement is precise enough to allow track matching in ϕ , however, because of the high hit multiplicity, the intrinsically poor resolution of the charge division technique and the small lever arm available, the VTX rz measurement has not proved useful.

The active layers extend to different z. Layer 1 occupies the region $|z| < 48.3$ cm and 3.73 cm $< r <$ 6.93 cm, where the radial boundaries quoted are those of the inner and outer sense wires. Layer 2 occupies $|z| < 53.3$ cm and $8.40 \text{ cm} < r < 11.60$ cm. Layer 3 covers $|z| < 58.4$ cm and $13.00 \text{ cm} < r < 16.23$ cm. These scales determine the geometric acceptance of the VTX.

The three layers of the VTX are mechanically independent. The inner radius of each layer is a carbon fiber tube which carries G–10 bulkheads which support the wires for that layer. In addition to the sense wires, there are 9 guard wires on each side of the sense wires in each sector and planes of cathode wires halfway between sense wire planes. These, along with aluminium traces on the carbon tubes determine the electrostatic configuration of the device. The sense wires carry a tension of 80 g and all other wires carry 360 g. The sense wires are made of 25 micron thick NiCoTin and the others of 152 micron thick aluminium with gold plating. The drift gas is 95% CO_2 – 5% ethane with a small amount of H_2O ($\approx$ 5%) to minimize radiation damage. The entire device is enclosed in a fourth carbon fiber tube.

2.2.3 Transition Radiation Detector (TRD)

Outside the VTX chamber is the transition radiation detector (TRD), a device intended to provide enhanced electron identification capability in the central region ($|\eta_{DET}| < 1.0$). The principle of the TRD is that charged particles crossing the boundary between two media with different dielectric constants radiate photons with probability inversely proportional to the particle mass. Thus electrons, with mass 0.511 MeV, radiate much more than any charged hadron, the lightest of which is the pion with mass 139.6 MeV. Therefore by measuring the transition radiation one can distinguish between electrons and charged hadrons.

The TRD is divided into three radial layers, each of which has a radiator section and a drift chamber to detect the transition radiation. Each radiator section is a stack of 393 layers of 18 micron thick polypropylene foil, separated by gaps of mean thickness 150 microns filled with dry nitrogen. The drift chamber gas is Xenon. Figure 2.3 shows a diagram of the TRD.

2.2.4 Central Drift Chamber (CDC)

The central drift chamber (CDC) is located outside the TRD and is one of the most important tools in identifying electrons and measuring their trajectories. The vertex z position for a given event is determined from the ensemble of all CDC tracks in that event. This vertex is used to compute $\not{E}_T$ and the hadronic recoil vector in W and Z events. The vertex defines "roads" used to associate tracks to electrons. The CDC track associated with an electron provides one of the points used to define the electron angle in the rz view. All electron candidates used in

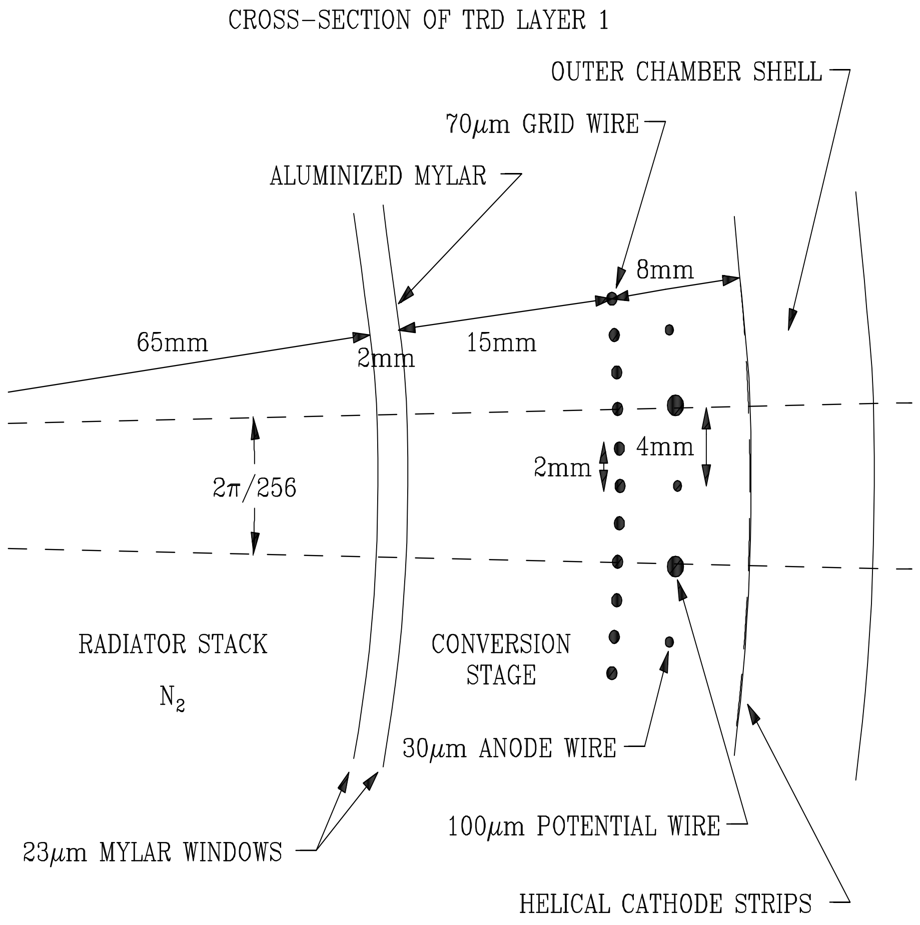

Figure 2.3: Diagram of the transition radiation detector.

this analysis are required to have a matched CDC track. The ionization measured for the track in the CDC can be used as an electron identification criterion.

The CDC geometry, like the VTX, is that of an annular cylinder with axis of symmetry aligned along the beam axis, with inner radius 49.5 cm and outer radius 74.5 cm. The CDC is divided in the radial direction into four layers which all extend between $\pm$ 135 cm in z. They are numbered 1 to 4 in increasing radius. Each layer is divided in azimuth ϕ into 32 sectors. Each sector contains 7 sense wires and 2 delay lines, which run parallel to the beam axis. Sectors in alternate layers are offset by 1/2 a cell in ϕ. The radial plane at $\phi = 0$ coincides with one of the 32 sense wire and delay line planes in layers 2 and 4. The radial plane at $\phi = 2\pi/64$ coincides with one of the sense wire and delay line planes in layers 1 and 3. Figure 2.4 shows a diagram of three sectors of the CDC.

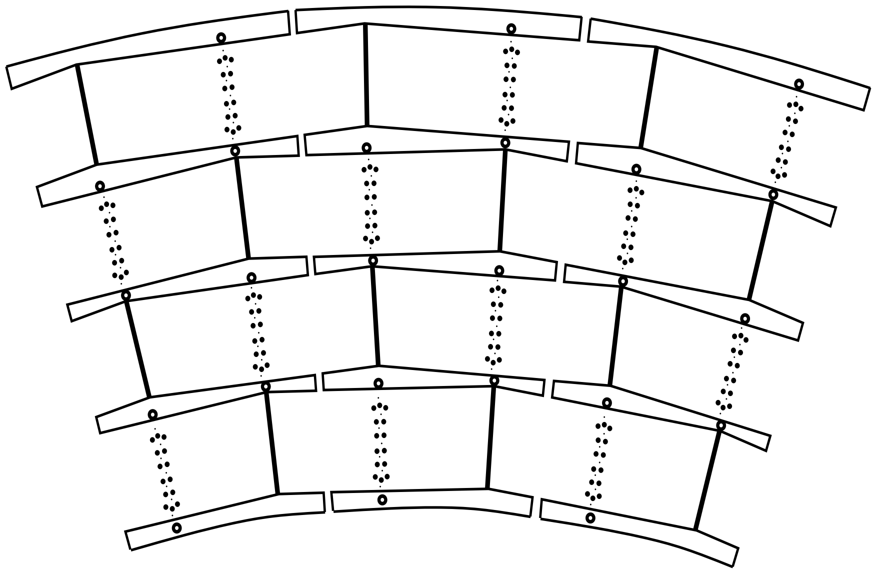

Figure 2.4: Cross section view of three of the 32 sectors of the central drift chamber.

2.2.5 Forward Drift Chambers (FDC)

There are two forward drift chambers (FDC), located north and south of the ends of the CDC, which provide measurements of forward tracks ($1.2 < |\eta| < 2.8$).

Each FDC is made of two θ chambers with a ϕ chamber in between. The θ chambers are rotated relative to each other by $\pi/4$. The θ chambers have a distinctive multirectangular shape. Each is divided into four quadrants, and each quadrant contains six rectangular drift cells. Each drift cell contains eight sense wires and one delay line. The ϕ chamber is divided in ϕ into 36 pie shaped slices, each of which contains 16 sense wires. Figure 2.5 shows a diagram of one of the FDCs.

2.2.6 Calorimeters

The DØ calorimeters are used to measure the energy of the electrons produced in W and Z decays. In conjunction with the tracking detectors they are also used to determine the electron directions. Along with the vertex position (x, y, z) measured with the CDC and VTX chambers they are used to measure $\not{E}_T$ and the hadronic recoil balancing the boson E_T in W and Z events. In other analyses, jets and photons are reconstructed from the calorimeter information, and muons are identified.

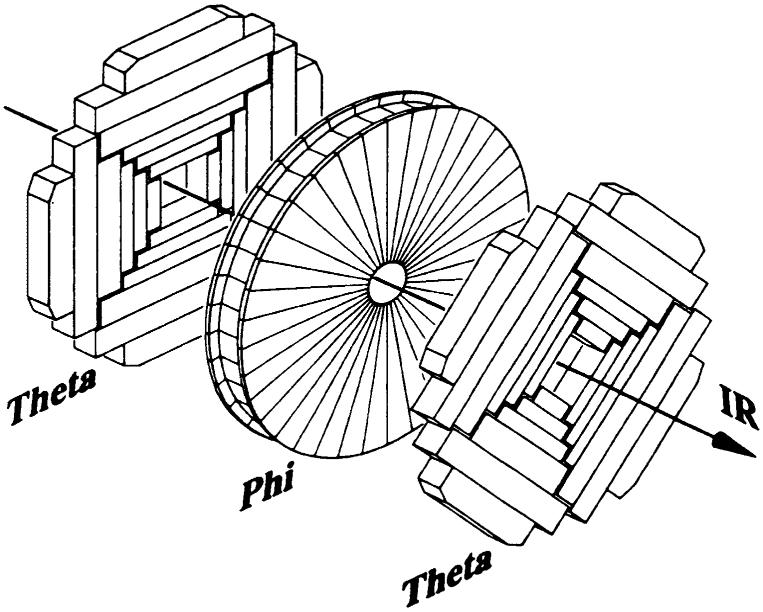

Figure 2.5: Diagram of one of the forward drift chambers.

There are three independent uranium – liquid argon (U–LAr) sampling calorimeters (see figure 2.6.) The uranium absorber was chosen to allow a compact, hermetic design, and to approach e/h compensation. Liquid argon is stable and radiation hard. In practice, compactness, hermeticity and stability were achieved, but the calorimeters are not strictly compensating. The central calorimeter (CC) covers the region $||\eta_{DET}|| < 1.0$. The two endcap calorimeters (EC) cover $-4.0 < |\eta_{DET}| < -1.4$ on the north side (ECN) and $1.4 < |\eta_{DET}| < 4.0$ on the south side (ECS).

The central calorimeter is approximately cylindrical. It is divided in depth into

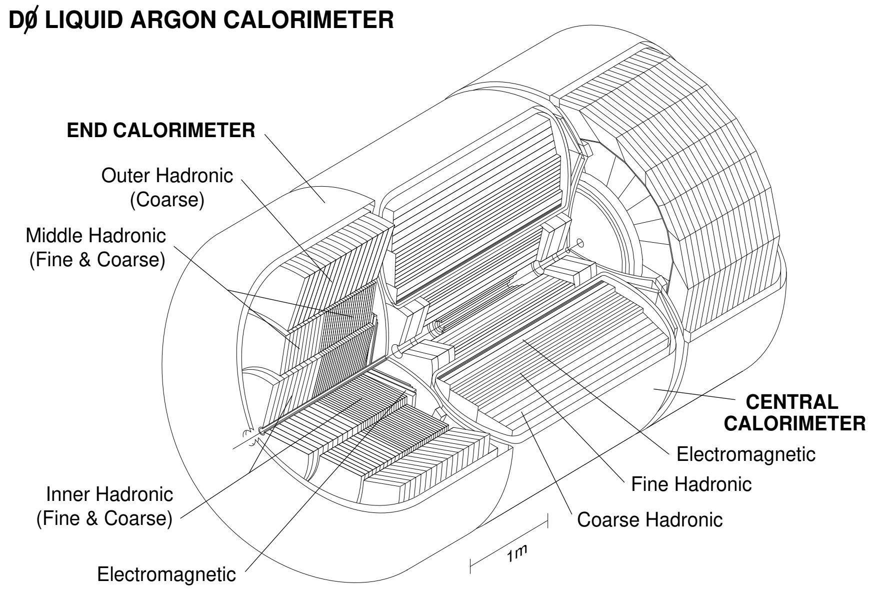

Figure 2.6: Cutaway view of the DØ calorimeters.

three sections, labelled "electromagnetic" (EM), "fine hadronic" (FH) and "coarse hadronic" (CH), according to the primary role of the section. Each section is subdivided in ϕ into modules which are mechanically independent. Each module consists of several plates of absorber material with liquid argon gaps and signal readout boards in between (see figure 2.7). The readout boards are divided into unit cells by cuts on the copper printed circuit pads. Several unit cells are ganged together in depth to make one readout cell. The readout cells are arranged so that the centers of the cells lie on straight lines from the nominal vertex, i.e., in a pseudo-projective geometry. In addition the cell sizes are chosen so that

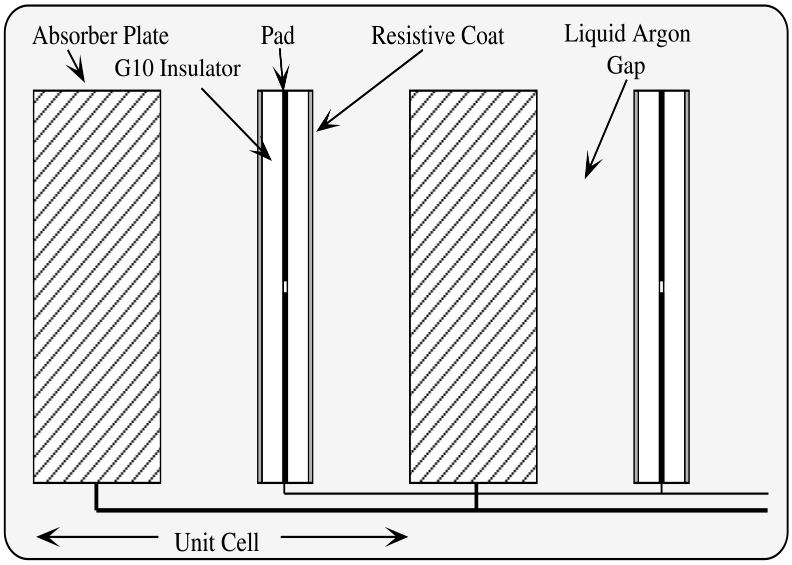

Figure 2.7: Calorimeter unit cell showing the arrangement of absorber plates, argon gaps and readout boards.

the towers are of constant size 0.1 in $|\eta_{DET}|$. This is convenient for triggering and reconstruction. There are 24 such towers in the CC, labelled with an integer index, $i\eta$, which ranges from -12 to $+12$ with 0 missing. The $i\eta$ index of a readout tower is equal to the value of $|\eta_{DET}|$ at the edge of the tower further from the middle of the CC, multiplied by 10.

In the EM section the absorber material is depleted uranium and the plates are 3 mm thick. It is divided into 32 modules, numbered 1 to 32 in increasing ϕ. Module 1 has a ϕ boundary aligned with $\phi = 0$. The primary purpose of

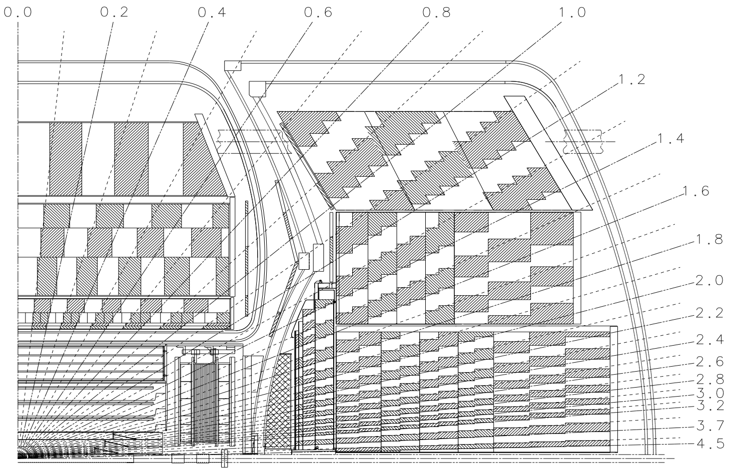

Figure 2.8: Calorimeter side view showing arrangement of cells and towers.

the EM section is to contain and measure electrons and photons, which shower electromagnetically. Typically 20–25 radiation lengths (X_0) are needed to contain an EM shower. The EM section is divided into 4 layers, labelled EM1 to EM4, with depths of 2, 2, 7 and 10 X_0 respectively. In reconstructing electrons and photons the first layer of the FH section is included in the energy measurement so that longitudinal shower leakage effects are negligible. Not all the towers are complete. At $|i\eta| = 12$ there is no EM4 layer; at $|i\eta| = 11$ there is no FH1. As a result the fiducial region of the CC for electrons is the equivalent of $|i\eta| \leq 10$.

The segmentation in $\eta - \phi$ space is 0.1×0.1 as for the rest of the calorimeter, except in EM3 where the cells are further subdivided into 4 so that the segmentation is 0.05×0.05. The shower maximum occurs typically in the EM3 layer, so that the finer segmentation allows better measurement of the shower centroid. The shower shape measurement also benefits, so that background rejection improves.

In the FH section the absorber material is depleted uranium with 1.7% niobium and the plates are 6 mm thick. It is divided into 16 modules. Module 1 has a ϕ boundary aligned with $\phi = \pi/32$, so that the FH intermodule cracks are aligned with the centers of the EM modules. Figure 2.8 shows the arrangement of the cells and towers.

In the CH section the absorber material is copper and the plates are 46.5 mm thick.

2.2.7 Intercryostat detectors

The regions between the central and end calorimeters would compromise the hermeticity of the detector if uninstrumented. To avoid this, scintillator tile detectors were mounted in this region. The tiles are read out with photomultiplier tubes (PMTs) with preamps locally mounted. To correct for time dependent response a laser system was implemented to calibrate the device. Each of the North and South ICD detectors contains 384 tiles, arranged like the calorimeters into units of 0.1×0.1 in $\eta - \phi$ space. Electrons have not been reconstructed in the ICD. However, jets have been successfully found in the ICD and inclusion of the ICD in the $\not{E}_T$ calculation has been demonstrated to improve $\not{E}_T$ resolution.

2.2.8 Level Zero Hodoscopes

The level zero system consists of scintillator detectors close to the beam just inside the north and south end calorimeters. They are used in the trigger to identify inelastic collisions. Each L0 detector consists of two layers of rectangular scintillators, read out with PMTs.

2.2.9 Muon System and Magnet

Outside the calorimeters there is a layer of proportional drift tubes, which are in turn just inside a system of large toroidal magnets. These bend the trajectories of muons, which are expected to be the only charged particles penetrating beyond the calorimeter and toroid. The chambers inside the toroid, called the A layer, provide a measurement of the muon trajectory before it is deflected by the magnet. There are two chambers outside the magnet, the B and C layers, which provide a measurement after deflection. The muon momentum can be computed from the angle of deflection.

The muon system has been used to calibrate the z position measurement of CDC tracks using muons from collider events and cosmic rays. This calibration is an important input to the electron direction measurement.

An elevation view of the muon system is shown in figure 2.9.

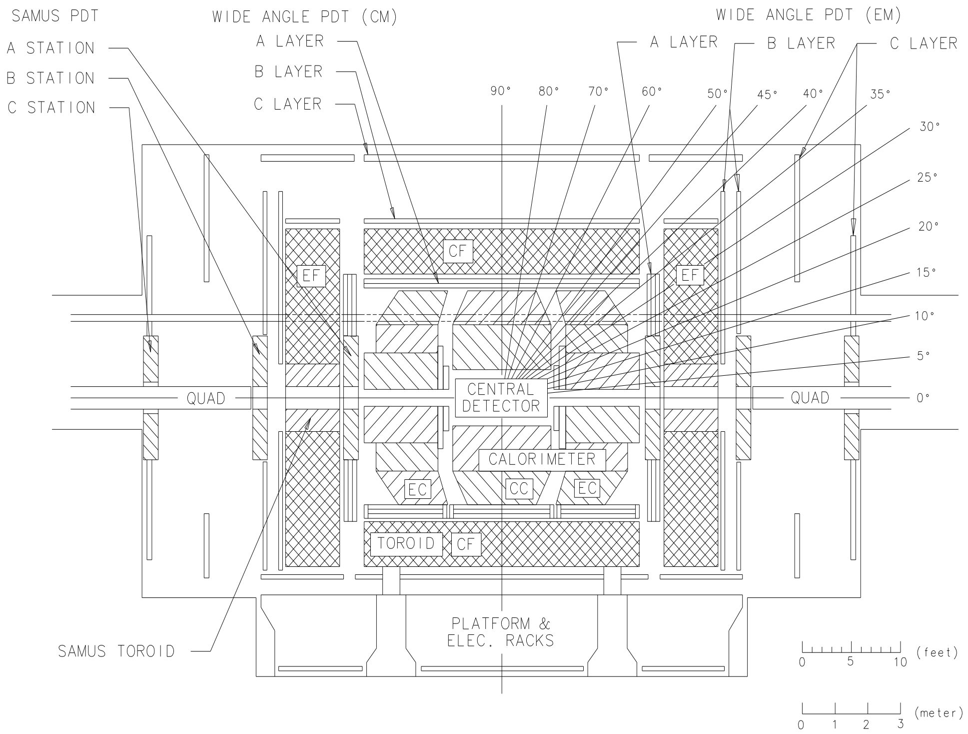

Figure 2.9: Side elevation view showing the muon system.

Chapter 3

Theory

3.1 Overview

To extract the W mass from a sample of W candidate events recorded at DØ, we generate predictions for several kinematic spectra as a function of the W resonance mass. The spectra considered are the electron energy, $E(e)$, electron transverse energy, $E_T(e)$, missing transverse energy, $\not{E}_T$, and transverse mass, M_t. These predictions are compared to the corresponding spectra from the data. The mass is measured by choosing the prediction which best matches the data.

In order to perform the mass fit to any kinematic distribution, we need a mechanism for predicting that distribution, given the W resonance mass. The prediction must correspond to the data actually observed at DØ, and so must include all relevant detector effects. The only satisfactory way to make such a complete prediction is to carry out a Monte Carlo simulation of the W events. A specialized fast Monte Carlo program called CMS was written to perform this simulation at the level of detail necessary for the Run 1b W mass measurement. The acronym CMS stands for Columbia–Michigan State after the institutions of its two primary authors. The first stage of the simulation is the production of $p\bar{p} \to WX \to e\nu X$ or $p\bar{p} \to ZX \to eeX$ events. The basic quantities modelled are the lepton 4–vectors and the recoil transverse momentum vector. No attempt is made to simulate the fragmentation of the recoil partons or underlying event particle production. Instead, these effects are accounted for phenomenologically in the later detector simulation.

This chapter describes the theoretical model upon which CMS 4–vector production algorithm is based. We begin with an overview of $p\bar{p}$ collisions in section 3.1.1 and a discussion of the important transverse mass variable in section 3.1.2. In section 3.2 we discuss W and Z production, and in section 3.3 the relevant characteristics of W and Z decays to electrons, including the important case of radiative decays. Finally in section 3.4 we discuss the modelling of $W \to \tau\nu$ decays which are topologically indistinguishable from $W \to e\nu$ decays and therefore contribute an irreducible background to the $W \to e\nu$ sample.

3.1.1 $p\bar{p}$ collisions

.

In $p\bar{p}$ collisions, high mass states such as W and Z bosons are produced in high Q^2 reactions which are well described by the quark–parton model. Hadrons such as protons and antiprotons are composite objects, made of quarks and gluons. In the crudest approximation the proton may be thought of as three valence quarks, uud, bound together by a cloud of gluons. In practice, this simple picture is inadequate for describing the interactions which produce heavy gauge bosons. A more quantitative procedure specifies the proton as an object consisting of a set of partons, in "flavors" defined as six quarks u, d, c, s, t, b and gluons g. The distribution of the momentum fraction x of the proton carried by flavor i when probed at a momentum scale Q^2 is denoted by the parton distribution function (pdf) $f_i(x, Q^2)$. The set of pdf for all flavors defines a picture of the proton structure. Parton distribution functions are available in the PDFLIB program [25]. The antiproton structure is of course obtained directly from that of the proton by charge conjugation.

In the quark–parton model, a $p\bar{p}$ reaction at high Q^2 can be thought of as a parton–level process in which one parton is supplied by the p and the other by the $\bar{p}$. The cross-section for the process can be computed by computing the "parton–level" cross-section, in which the partons are treated as elementary particles, and convoluting with the pdf. The other partons comprising the proton are not involved in the hard–scattering interaction — this is a physical interpretation of the factorization theorems. For a review of these concepts see, for example, reference [26]. The partons in the proton which do not participate in the hard scatter are called "spectators." The spectators typically cause the collision to contain hadronic debris which does not originate from the hard–scattering process. This debris is usually produced mostly in the forward direction and contains low E_T particles. These particles are collectively referred to as the "underlying event."

In the case where the hard–scattering final state includes colored objects, such as in dijet production, the underlying event fragments are correlated with the hard–scattering products by color coherence. For example, particle production between the jets and the beam is enhanced in dijet events. In W and Z production this complication is not present since the W and Z do not carry color. For recent experimental results on color coherence for events containing both a W and a jet see reference [65].

The underlying event for production of colorless objects qualitatively resembles events recorded in generic inelastic $p\bar{p}$ collisions. These interactions, referred to as "minimum bias" interactions, are believed to be mediated by color singlet objects called pomerons. Like the underlying event, the particles produced in minimum bias events are typically soft and forward.

3.1.2 Transverse Mass

Because the neutrino from the $W \rightarrow e\nu$ decay is not reconstructed, it is impossible to measure the W invariant mass distribution. The quantity which provides maximal information about the mass which is derivable from observed quantities is the "transverse mass" [52]. The transverse mass is computed like an invariant mass except that the 3–momentum is replaced by a 2–momentum in the transverse plane. Explicitly, the formula for the invariant mass is

$$\begin{aligned} M_{inv}^2 &= (p^\mu(e) + p^\mu(\nu) \cdot (p_\mu(e) + p_\mu(\nu)) && (3.1) \\ &= 2\,(E(e)E(\nu) - p_x(e)p_x(\nu) - p_y(e)p_y(\nu) - p_z(e)p_z(\nu)) && (3.2) \\ &= 2\,E(e)E(\nu)(1 - \cos\gamma(e,\nu)) && (3.3) \end{aligned}$$

and that for the transverse mass is

$$\begin{aligned} M_T^2 &= 2\,(E_T(e)E_T(\nu) - p_x(e)p_x(\nu) - p_y(e)p_y(\nu)) && (3.4) \\ &= 2\,E_T(e)E_T(\nu)(1 - \cos\phi(e,\nu)) && (3.5) \end{aligned}$$

where $\gamma(e,\nu)$ is the 3D opening angle between the electron and neutrino momenta and $\phi(e,\nu)$ is the azimuthal opening angle.

The neutrino momentum is not a directly observable quantity. It is inferred from the electron momentum and the recoil momentum. The recoil momentum is equal to the vector sum of the momenta of all particles except the electron and neutrino. By momentum conservation, the recoil momentum balances the W momentum.

$$\vec{P}(rec) = -\vec{P}(W) \tag{3.6}$$

Therefore, if we could measure the recoil we could compute all the components of the neutrino momentum

$$\vec{P}(W) = \vec{P}(e) + \vec{P}(\nu) \tag{3.7}$$

$$\vec{P}(\nu) = -\vec{P}(e) - \vec{P}(rec) \tag{3.8}$$

However, because particles escape down the beampipe the longitudinal component of the recoil momentum is unknown, so only the transverse components of the recoil can be measured. Hence the same is true for the neutrino.

$$\vec{P}_T(rec) = -\vec{P}_T(W) \tag{3.9}$$

$$\vec{P}_T(\nu) = -\vec{P}_T(e) - \vec{P}_T(rec) \tag{3.10}$$

The transverse mass is computed from the transverse momenta of the electron and the recoil. Since the neutrino momentum is not directly observable, we rewrite the transverse mass formula in terms of the electron and recoil transverse momenta as

$$M_T^2 \;=\; 2\left(|\vec{E_T}(e)||\vec{E_T}(e)+\vec{P_T}(rec)| + \vec{E_T}(e)\cdot(\vec{E_T}(e)+\vec{P_T}(rec))\right) \quad (3.11)$$

This expression can be expanded as a Taylor series in $P_T(rec)/E_T(e)$. The expansions to 0th, 1st and 2nd orders are

$$M_T(0) \;=\; 2\,E_T(e) \quad (3.12)$$

$$M_T(1) \;=\; 2\,E_T(e) + u_{||} \quad (3.13)$$

$$M_T(2) \;=\; 2\,E_T(e) + u_{||} + \frac{P_T(rec)^2}{2E_T(e)} - \frac{3u_{||}^2}{16E_T(e)} \quad (3.14)$$

These approximations are very useful for deriving a qualitative understanding of the systematic effects in the W mass fits. However they are approximations true on an event–by–event basis when the P_T^W is small and must be used with caution.

The following distributions are calculated from the unsmeared 4–vectors from the CMS Monte Carlo, where standard DØ acceptance effects have been applied. Figure 3.1 shows the intrinsic resolution of the invariant mass and transverse mass. Figure 3.2 shows the transverse mass and the electron $2E_T(e)$ relative to the invariant mass.

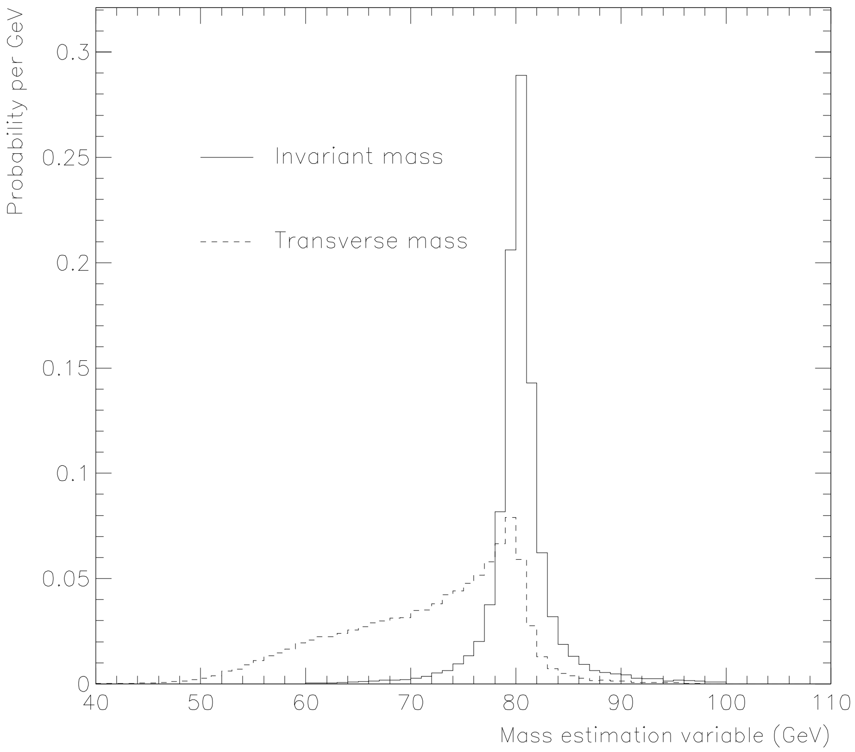

Figure 3.1: Unsmeared invariant and transverse mass distributions from the CMS $W \rightarrow e\nu$ Monte Carlo.

It is clear that the transverse mass has intrinsically the best resolution. If we could build a perfect detector we would clearly optimize the W mass measurement by choosing to fit the M_t spectrum. However, the recoil measurement is a knotty experimental problem. The recoil system is composed mainly of soft hadrons, which are notoriously difficult to measure accurately. For soft hadrons, calorimetry tends to be non–linear and of poor resolution, and it is difficult to calibrate the

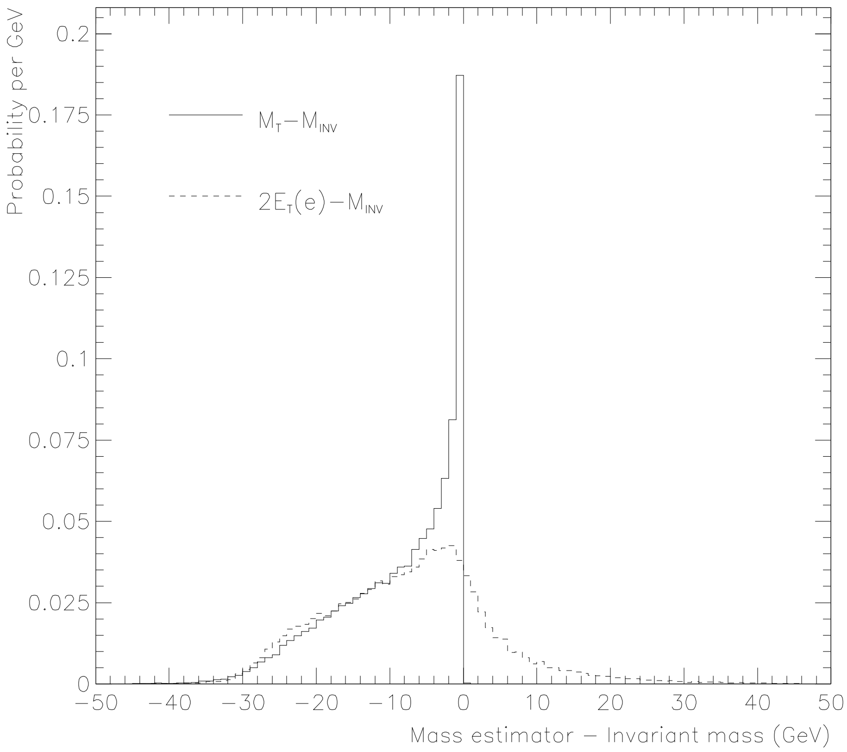

Figure 3.2: Resolutions of the variables M_T and $2E_T(e)$ relative to invariant mass.

absolute hadronic energy scale. The measurement must be summed over the whole acceptance of the detector, so that it is very sensitive to the underlying event, detector noise, multiple interactions and pileup effects from previous beam crossings. Since there is no theoretical model which can accurately predict the composition of the recoil system, the recoil measurement cannot be done with tracking because the relative fractions of charged and neutral hadrons are not known at the required level of accuracy, even if a central magnetic field were available.

From the experimental point of view, therefore, the transverse mass is not necessarily the best quantity to use. While it has optimal statistical power and minimal sensitivity to the theoretical model, it is subject to significant systematic errors from the measurement of the hadronic recoil system. The electron E_T fit provides an attractive alternative, since the detector response and resolution for electrons are easily constrained using $Z\rightarrow ee$ decays. The obstacle to carrying out the electron E_T fit is understanding the production model.

3.2 W and Z production

Ideally the model for W and Z production would begin with the fully differential cross section

$$\frac{\partial^5\sigma}{\partial M\partial p_T\partial y\partial\phi\partial\epsilon} = \mathcal{P}(M, p_T, y, \phi, \epsilon) \tag{3.15}$$

where $M, p_T, y, \phi, \epsilon$ are the IVB mass, transverse momentum, rapidity, azimuthal angle and polarization respectively. $\mathcal{P}(\dots)$ denotes the probability density for producing a boson with state $(\dots)$. We will use this notation rather than the clumsier differential cross section notation. The two are equivalent for shape analyses such as the W mass measurement, and the probability density notation is a reminder that overall normalization factors are irrelevant to this analysis and will be dropped, often without comment.

In the CMS Monte Carlo we assume that the probability density factorizes

$$\mathcal{P}(M, p_T, y, \phi, \epsilon) = \mathcal{P}_M(M)\mathcal{P}_{p_T,y}(p_T, y)\mathcal{P}_\phi(\phi)\mathcal{P}_\epsilon(\epsilon) \tag{3.16}$$

The ϕ distribution is trivial; $\mathcal{P}_\phi$ is taken to be a uniform distribution in $[0, 2\pi)$. Sections 3.2.2 and 3.2.3 describe the distributions of M and (p_T, y). Possible correlations are ignored between M, (p_T, y) and the polarization. In principle this is not strictly valid, since, for example, the events initiated by sea–sea quark pairs could have a different parton luminosity from events which include a valence quark or antiquark, and the polarization distribution for sea–sea events is different from that of valence–initiated events, hence one might expect the mass and polarization to correlate. Also, one expects that high mass bosons should tend to have lower p_T because of parton luminosity effects. However, such correlations have a small effect on the mass.

3.2.1 Lowest order W and Z production

The lowest order W and Z production diagrams are shown in figure 3.3. Though these diagrams are inadequate to describe inclusive gauge boson production at a level of detail sufficient for this analysis, they are nevertheless useful for deriving a qualitative picture of the physics and some approximate results, such as the total cross–section or the relative contributions of the various parton–level production subprocesses. In this analysis, several features of W and Z production are computed at lowest order, namely the fraction of events initiated by sea–sea quark combinations and the consequent boson polarization and angular distribution of the decay products, the ϕ of the W or Z and the parton luminosity weight, which is described in section 3.2.2.

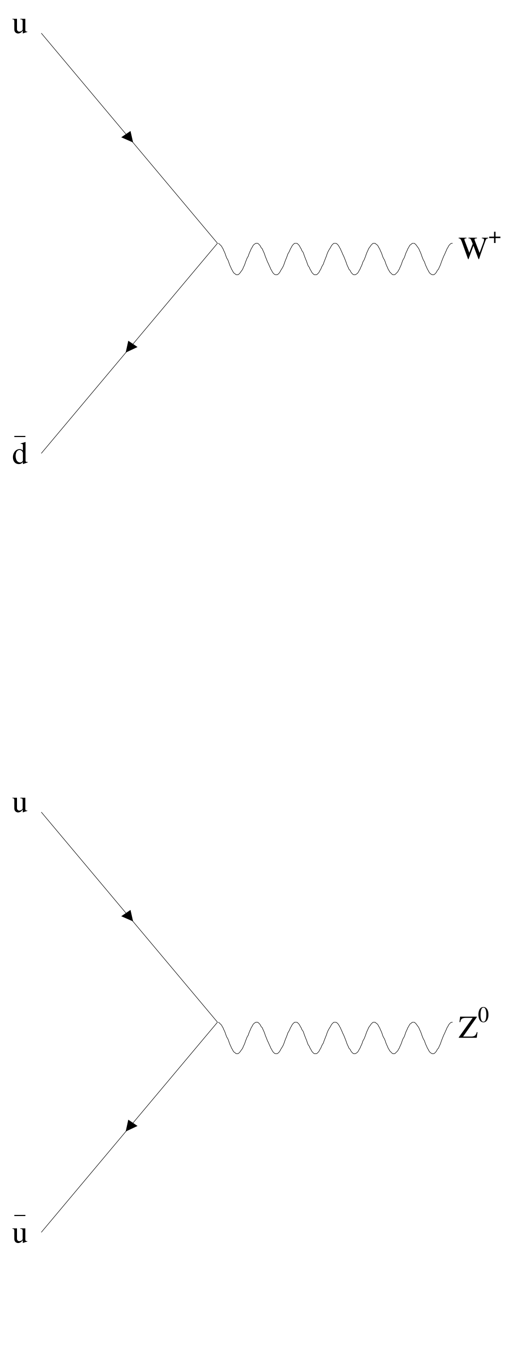

Figure 3.3: Lowest order diagrams for W and Z boson production.

3.2.2 Boson mass distributions

The W and Z bosons are both spin 1 Breit-Wigner resonances produced from two spin 1/2 quarks. The non-relativistic Breit-Wigner cross section is therefore [24]

$$\sigma_{BW} = \frac{3\pi}{s} \frac{B_{IN} B_{OUT} \Gamma^2}{(\sqrt{s} - M_V)^2 + \Gamma^2/4} \tag{3.17}$$

where s is the usual Mandelstam variable, M_V and Γ are the boson mass and width and B_{IN} and B_{OUT} are the branching fractions into the in and out channels. For massless quarks we can write $s = E_{CM}^2$. The branching fractions are independent of momentum and affect only the overall normalization of the cross section. Such factors are irrelevant to the mass analysis and will be dropped.

The non-relativistic form is a reasonable approximation for the narrow width case. It corresponds to the amplitude

$$a_{NR} \quad \propto \quad \frac{-\Gamma}{\sqrt{s} - M_V + i\Gamma/2} \tag{3.18}$$

The relativistic form is obtained by replacing a_{NR} with the relativistic amplitude

$$a_R \quad \propto \quad \frac{-M_V \Gamma}{s - M_V^2 + i M_V \Gamma} \tag{3.19}$$

A further improvement is obtained by replacing $M_V \Gamma$ with $\sqrt{s}\,\Gamma(s)$, where $\Gamma(s) = \sqrt{s}\,\Gamma_0/M_V$. This gives

$$a \quad \propto \quad \frac{-s\Gamma_0/M_V}{s - M_V^2 + is\Gamma_0/M_V} \tag{3.20}$$

which implies that the cross section is

$$\frac{d\sigma_{BW}}{ds} \propto \frac{1}{s} \times |a|^2 \tag{3.21}$$

$$= \frac{1}{s} \times \frac{s^2(\Gamma_0/M_V)^2}{(s-M_V^2)^2 + (s\Gamma_0/M_V)^2} \tag{3.22}$$

To obtain the distribution of the boson mass m, we can set $s = m^2$ and write

$$\sigma_{BW} \propto \frac{m^2\Gamma_0^2/M_V^2}{(m^2-M_V^2)^2 + m^4\Gamma_0^2/M_V^2} \tag{3.23}$$

This formula gives the partonic cross section $\hat{\sigma}$ for the quark–quark reaction used in the CMS Monte Carlo. It is a relativistic Breit–Wigner with $\hat{s}$–dependent width. One of the alternative forms for the amplitude a give the resonance formulae for the relativistic Breit–Wigner with fixed width

$$\sigma_{RBW} \propto \frac{\Gamma_0^2}{(m^2-M_V^2)^2 + M_V^2\Gamma_0^2} \tag{3.24}$$

which is used in HERWIG 5.8 [41], which we will use occasionally for qualitative cross–checks of the model. For the parameter Γ_0, we use the current world average W width, which is measured indirectly from the ratio of the W and Z production cross sections at hadron colliders. For Z production we use the width of the Z measured by the LEP experiments. The finite width of the W and Z bosons arises from loop corrections to the propagators, described in section 3.3.2.

The observed mass spectrum for $p\bar{p}$ interactions is calculated in the usual way

$$\sigma = \sum_{i,j} \int dx_1 dx_2 f_i(x_1, Q^2) f_j(x_2, Q^2) \hat{\sigma}(ij) \tag{3.25}$$

where i and j range over contributing flavors, f_i is the pdf for parton i in the proton and f_j the pdf for parton j in the antiproton and $\hat{\sigma}(ij)$ is the partonic cross section for the process $ij \to V$. We equate the momentum transfer to the mass of the produced boson, $Q^2 = m^2$. We can write as usual

$$x_1 = \sqrt{\tau}\, e^y \tag{3.26}$$

$$x_2 = \sqrt{\tau}\, e^{-y} \tag{3.27}$$

$$\tau = m^2/S \tag{3.28}$$

where y is the rapidity of the IVB.

We can calculate the double differential distribution in mass and rapidity as

$$\frac{d^2\sigma}{dm\, dy} = \sum_{i,j} f_i\left(\frac{m}{\sqrt{S}} e^y, m^2\right) f_j\left(\frac{m}{\sqrt{S}}\, e^{-y}, m^2\right) \frac{m^2\Gamma_0^2/M_V^2}{(m^2 - M_V^2)^2 + m^4\Gamma_0^2/M_V^2} \tag{3.29}$$

We can parametrize the factor which depends on the pdf in a parton luminosity function. For historical reasons we use the exponential form

$$F_{PL} = \frac{e^{-\beta m}}{m} = \sum_{i,j} f_i\left(\frac{m}{\sqrt{S}} e^y, m^2\right) f_j\left(\frac{m}{\sqrt{S}}\, e^{-y}, m^2\right) \tag{3.30}$$

where β is called the parton luminosity slope. Figure 3.5 shows the mass distribution from HERWIG, with a fit to the exponential parametrization for the parton

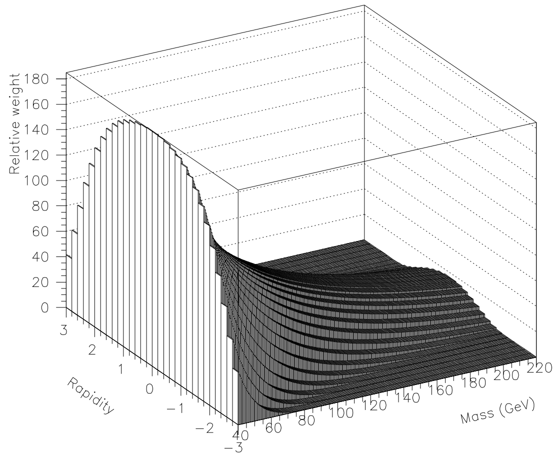

Figure 3.4: Double differential parton luminosity weight $F_{PL}(M, y)$ for Z production

luminosity. The shape is well fit by the parametrization over the entire region of interest. The electron rapidity η_e was required to satisfy $|\eta_e| < 1.0$.

Figure 3.4 shows the parton luminosity weight $F_{PL}(M, y)$ for Z production with MRSA pdf, computed from PDFLIB for inclusive Z production. It shows a correlation between mass and rapidity.

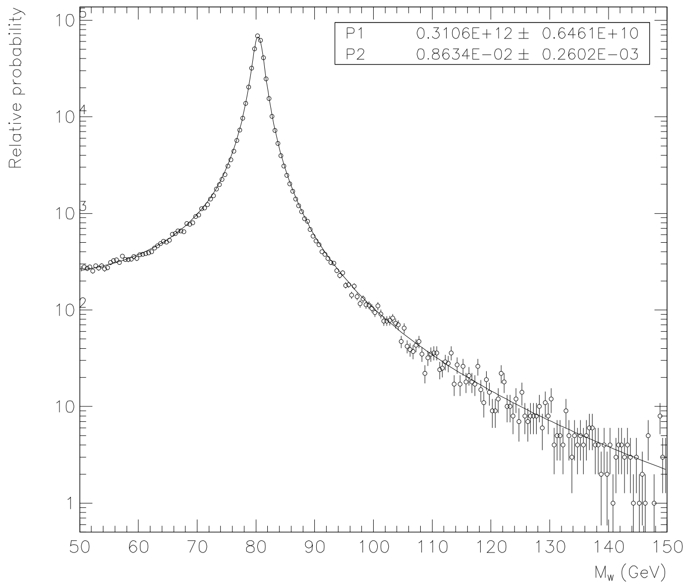

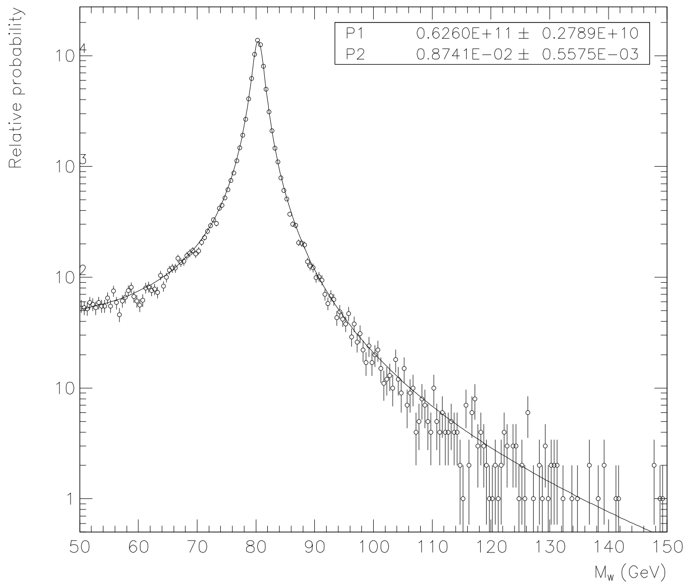

Figure 3.5: Mass distributions from HERWIG showing the parton luminosity effect. (Upper) MRSA$-'$ (Lower) CTEQ3M.

3.2.3 Transverse momentum and rapidity

To lowest order in QCD, W and Z boson production in $p\bar{p}$ collisions occurs via the Drell–Yan diagrams shown in figure 3.3. In the usual parton model formulation the initial state quarks are assumed to have negligible momenta transverse to the p and $\bar{p}$ beam directions. The vector boson then has no p_T since it is the only final state particle in these diagrams. However, higher order processes in QCD allow final states in which hadrons may recoil against the boson. The dominant process is initial state gluon radiation (ISR), though there are others, such as the "Compton" process (figure 3.6.) The "primordial" transverse momentum of the partons in the proton arising from the confinement of the partons to a region of order the proton radius, $R_p \approx 1\,fm$, is of order $\hbar c/R_p \approx 200$ MeV and is negligible compared to the p_T caused by QCD processes.

If one attempts to compute the p_T spectrum using the lowest order $q\bar{q} \rightarrow Vg$ and $qg \rightarrow Vq$ diagrams, where V refers generically to either the W or the Z, the result will be approximately correct at high p_T ($p_T \approx M_V$). However, at low p_T the results diverge. Formally this divergence is cancelled by a negative infinite δ-function at $P_T = 0$ from the virtual diagrams [35]. The calculation will give a reasonable result for the total cross section but cannot be sensibly used to predict the differential cross section.

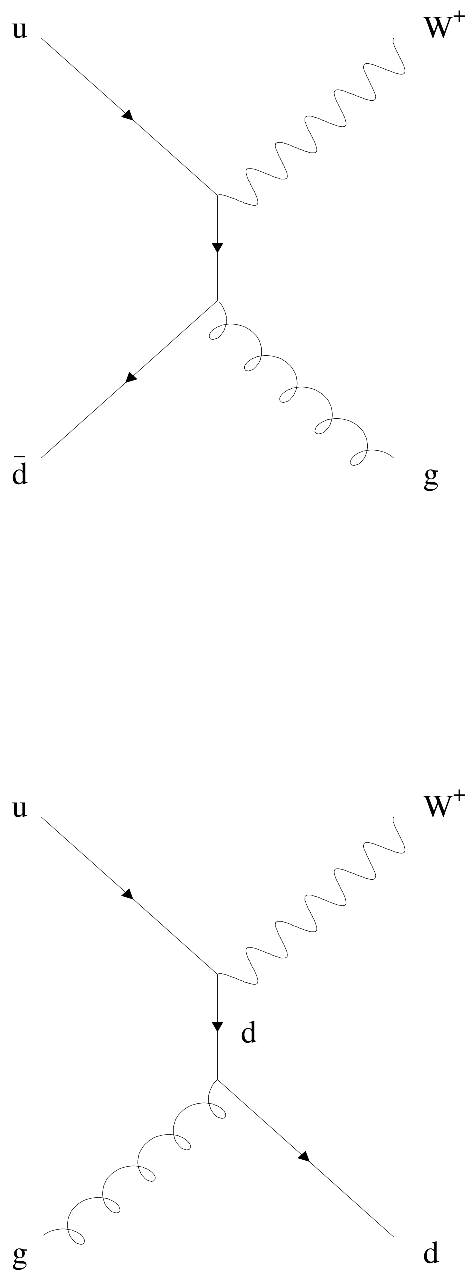

Figure 3.6: (Upper) Initial state radiation and (Lower) Compton diagrams for W boson production.

At low p_T ($p_T \ll M_V$) the problem has two scales, determined by M_V and p_T. This means that terms like $\alpha_S^n (\ln Q^2/q_T^2)^m$ appear in the perturbation series. The large logarithms are the origin of the calculational difficulty. A reliable method of handling these terms has been explored by several theoreticians [35, 27, 31, 33]. This method, resummation, involves rearranging the terms of the perturbation series so that the dominant terms can be summed, generally leading to an exponential factor. The Collins–Soper–Sterman framework [27, 28, 29, 30] provides a consistent way of carrying out such a resummation procedure for IVB production.

The differential cross section for boson production in the parton model is

$$\frac{d^2\sigma_V}{dP_T dy} = \sum_{i,j} \int dx_1 dx_2 f_i(x_1) f_j(x_2) \frac{d^2\sigma(ij \to V)}{dP_T dy} \tag{3.31}$$

where the sum is over contributing parton flavors. In the following the usual folding of partonic cross sections with pdf and summation over flavors will be assumed.

The dominant terms in the perturbation series for the partonic cross sections have the form

$$\frac{d^2\sigma}{dP_T dy} \propto \frac{\alpha_s}{P_T^2} \ln\left(\frac{Q^2}{P_T^2}\right) \left(v_1 + v_2 \alpha_s \ln^2\left(\frac{Q^2}{P_T^2}\right) + v_3 \alpha_s^2 ln^4 \left(\frac{Q^2}{P_T^2}\right) + \ldots\right) \tag{3.32}$$

where the proportionality constant is independent of y and p_T. The resummed formula corresponding to these terms is

$$\left[\frac{d^2\sigma}{dP_T dy}\right]_{RESUM} \propto \int \frac{d^2 b}{(2\pi)^2} e^{i\vec{b}\cdot\vec{P}_T} W(b) \tag{3.33}$$

where b, a variable conjugate to p_T, is interpreted as the impact parameter in the transverse plane. Small values of b correspond to large p_T and large b to low p_T. $W(b)$ is a complicated but well-defined function of b calculated in perturbation theory [31].

The resummed formula includes the dominant terms to all orders in α_s. Two corrections are necessary. First, the resummed formula only accounts for terms as singular as $1/P_T^2$ as $P_T \to 0$. The less singular terms are finite and do not require resummation. These terms are computed by evaluating the (non-resummed) perturbative series $[d^2\sigma_V/dP_T dy]_{PERT}$ (called the "perturbative piece") and the terms in that series as singular as $1/P_T^2$ (called the "asymptotic piece") $[d^2\sigma_V/dP_T dy]_{ASY}$ and subtracting them. Obviously the perturbative and asymptotic cross sections both diverge as $1/P_T^2$ as $P_T \to 0$. However, their difference is well defined and corresponds to the terms left out of the resummation formula. We will refer to this difference as the perturbative correction to the resummed cross section.

Second, since the resummed formula is derived from the perturbation series it breaks down at low p_T (at a scale set by Λ_{QCD}) where non-perturbative physics is important. The standard method of dealing with this problem is to parametrize the low p_T (large b) physics by modifying the function $W(b)$ which appears in the resummed formula,

$$W(b) \quad \rightarrow \quad W(b_*)e^{-S_{NP}(b)} \tag{3.34}$$

where

$$b_* \quad = \quad \frac{b}{\sqrt{1+b^2/b_{max}^2}} \tag{3.35}$$

The replacement $b \rightarrow b_*$ smoothly cuts off the variation of $W(b)$ with b for $b > b_{max}$. The functional form of W is then controlled by $S_{NP}(b)$ at large b, $b \gg b_{max}$, i.e., at low p_T.

The non-perturbative function $S_{NP}(b)$ must obey a few simple rules. At small b, corresponding to high p_T, $b_* = b + \mathcal{O}(b^2)$. Since the non-perturbative physics must vanish in the high p_T limit, $S_{NP}(b) \rightarrow 0$ as $b \rightarrow 0$. Infinitely large impact parameter reactions cannot contribute to the cross section, therefore $e^{-S_{NP}(b)} \rightarrow 0$ as $b \rightarrow 0$, hence as $b \rightarrow \infty$, $S_{NP}(b) \rightarrow \infty$. To all orders in perturbation theory, $S_{NP}(b)$ has the functional form [27]

$$S_{NP}(b) \quad = \quad h_{i/A}(x_A, b) + h_{j/B}(x_B, b) + h_Q(b) \ln\left(\frac{Q}{2Q_0}\right) \tag{3.36}$$

where the subscripts on the first two terms indicate a possible flavor and momentum fraction dependence. There is an arbitrary momentum scale Q_0, and an arbitrary impact parameter length scale b_{max}, which appears in the definition of b_*.

The simplest choice of $S_{NP}(b)$ is that of Davies, Stirling and Webber (DSW) [53], which was also used by Arnold and Kauffman (AK) [31], in which

$$S_{NP}(b) = \tilde{g}_1 b^2 + \tilde{g}_2 b^2 \ln\left(\frac{Q}{2Q_0}\right) \tag{3.37}$$

Davies, Stirling and Webber fit this hypothesis to Drell–Yan data (E288 and R209) using Duke–Owens pdf and obtained

$$\tilde{g}_1 = 0.15\,\mathrm{GeV}^2 \tag{3.38}$$

$$\tilde{g}_2 = 0.40\,\mathrm{GeV}^2 \tag{3.39}$$

where $Q_0 = 2$ GeV and $b_{max} = 0.5$ GeV^{-1} were chosen. These were the parameters employed in the AK calculation. In the more recent work of Ladinsky and Yuan (LY) [33], an updated hypothesis is used which fits the Drell–Yan data somewhat better than the older DSW hypothesis,

$$S_{NP}(b) = g_1 b^2 + g_2 b^2 \ln\left(\frac{Q}{2Q_0}\right) + g_1 g_3 b \ln(100 x_A x_B) \tag{3.40}$$

The first two terms are identical in form to the DSW hypothesis. The extra term allows a $\tau = x_A x_B$ dependence. Ladinsky and Yuan fit their hypothesis to E288, R209 Drell-Yan data and Z production data from CDF using CTEQ2M pdf and obtained

$$g_1 = 0.11^{+0.04}_{-0.03}\,\mathrm{GeV}^2 \tag{3.41}$$

$$g_2 = 0.58^{+0.1}_{-0.2}\,\mathrm{GeV}^2 \tag{3.42}$$

$$g_3 = -1.5^{+0.1}_{-0.1}\,\mathrm{GeV}^{-1} \tag{3.43}$$

where $Q_0 = 1.6$ GeV and $b_{max} = 0.5\,\mathrm{GeV}^{-1}$ were chosen. For both the DSW/AK and LY models the nonperturbative function reduces to a quadratic in b for the production of an object of fixed mass. For W and Z production we can set $Q = M_V$ and $100x_Ax_B = 100M_V^2/s$. The terms which appear in $S_{NP}(b)$ are then

$$S_{NP}^{AK}(b) = 1.4\,b^2 \tag{3.44}$$

$$S_{NP}^{LY}(b) = 2.05\,b^2 + 0.22\,b \tag{3.45}$$

where we have set $M_V = 91.19$ GeV for Z production. We have ignored the Breit-Wigner width of the Z resonance and the modification of the relation $x_Ax_B = M_V^2/s$ due to non–zero p_T of the Z. For either model g_1 and g_2 are not independent for fixed $Q \approx M_V$. Only the combination $g_1 + g_2\ln(Q/2Q_0)$ can be measured from the Z data. However, only the combination $g_1 + g_2\ln(Q/2Q_0)$ is important to the boson p_T calculation, so in either case one degree of freedom in the parameter space drops out of the problem. In the DSW/AK model, the problem is equivalent to constraining the coefficent of b^2 in $S_{NP}(b)$. In the LY model, it is equivalent to constraining the coefficents of b^2 and b.

We will work with the more general LY model. The authors have provided a flexible program, LEGACY [34], which calculates $d^2\sigma_W/dP_Tdy$ and $d^2\sigma_Z/dP_Tdy$ given a choice of pdf and g_1, g_2, g_3. With g_1 held fixed, a determination of the coefficents of b^2 and b is equivalent to a determination of g_2 and g_3. Note also that g_2 appears in the coefficent of b^2 with the factor $\ln(Q/2Q_0) \approx 3.35$, so that if one simply varies g_1 and g_2 in the model one obtains variations in the p_T spectrum which are much bigger for g_2 than for g_1. This is a consequence of the choice of Q_0 for boson production at $Q \gg Q_0$.

Figure 3.7 shows the relative contributions of the terms. Clearly the dominant term is the coefficent of b^2, so that g_2 is the most important parameter [32].

The dominant uncertainties in the shape of the p_T distributions are from the function $S_{NP}(b)$ and the choice of pdf. The perturbative correction is a small contribution compared to the resummed piece. Figure 3.9 shows the p_T distribution for the W from the resummed calculation with and without the perturbative correction. Figure 3.9 shows the variation in the mean p_T of the W and Z vs. Λ_{QCD} for CTEQ3M pdf, illustrating the pdf dependence.

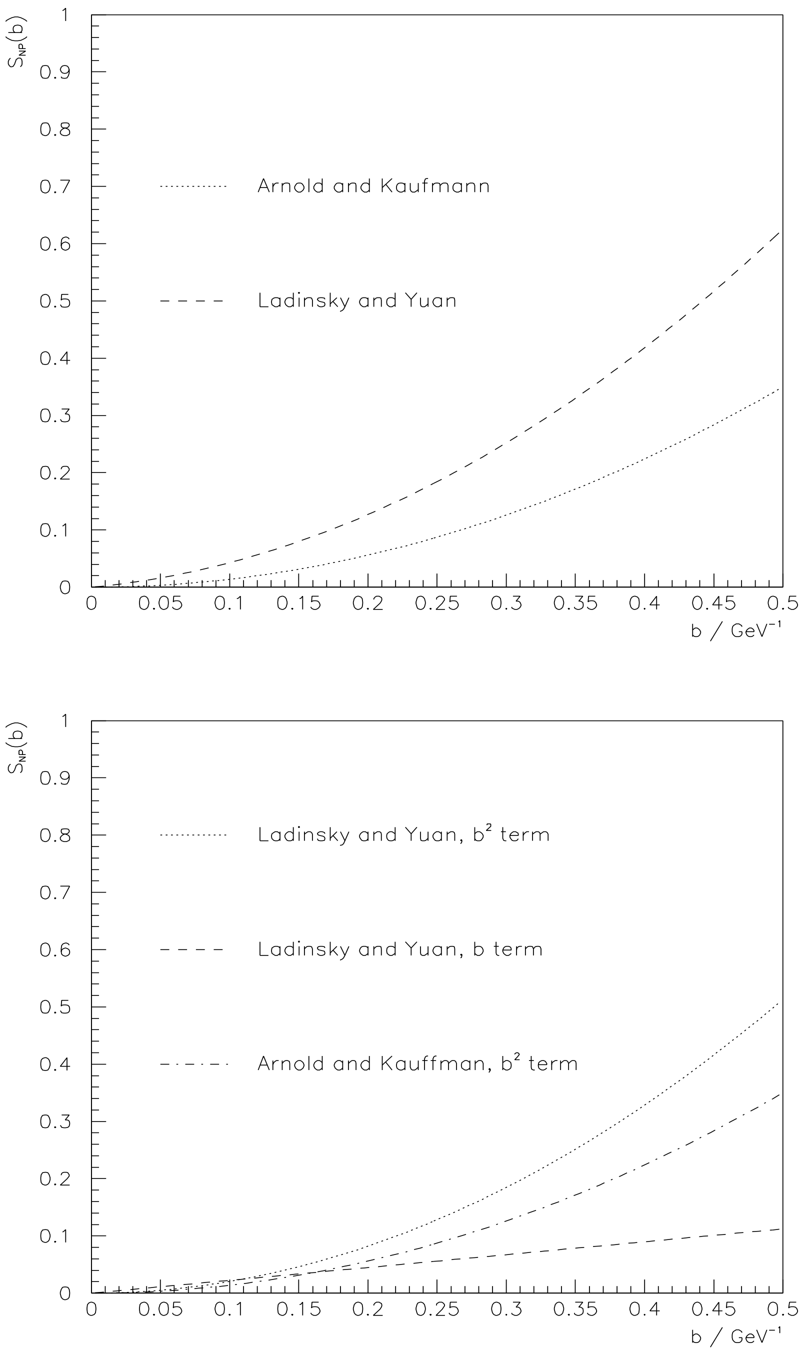

Figure 3.7: Terms in the nonperturbative functions.

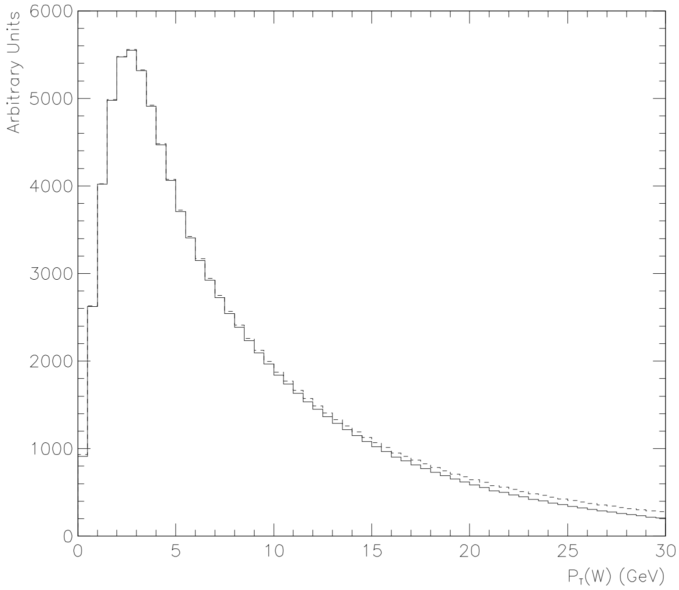

Figure 3.8: Resummed P_T^W calculation with (solid) and without (dashed) the perturbative correction.

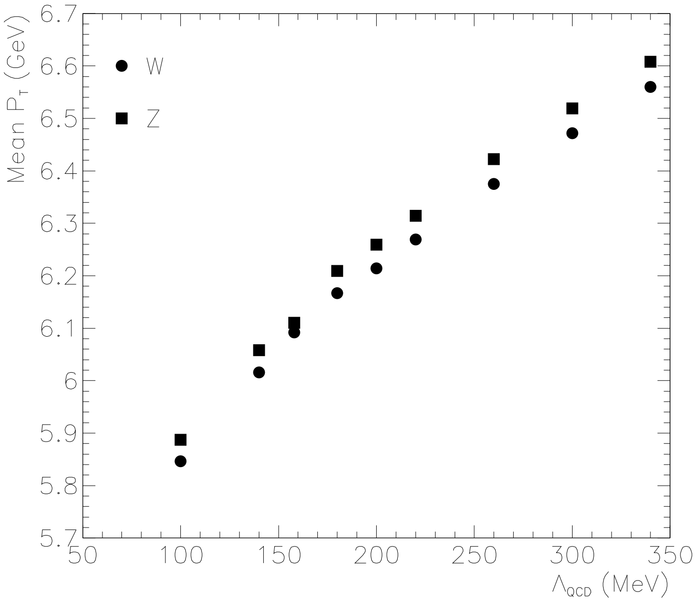

Figure 3.9: Mean P_T^W and P_T^Z vs. Λ_{QCD} for CTEQ3M pdf.

3.2.4 Polarization

The $\bar{u}d \to W^+$ production vertex is proportional to

$$\frac{igV_{ud}}{2\sqrt{2}}\gamma^\mu(1+\gamma^5) \tag{3.46}$$

Similar expressions hold for W^- production and the $\bar{c}s$ vertex, which is suppressed because of the larger masses of the c and s quarks and because of the off–diagonal CKM matrix element. The $V-A$ nature of the interaction is given by the $\gamma^\mu(1+\gamma^5)$ factor. Any massless fermion field such as the quark fields in the interaction Lagrangian can be written as a sum of left and right handed components

$$q = \frac{1+\gamma^5}{2}q + \frac{1-\gamma^5}{2}q = q_R + q_L \tag{3.47}$$

The relations

$$\frac{1+\gamma^5}{2}\frac{1+\gamma^5}{2} = \frac{1+\gamma^5}{2} \tag{3.48}$$

$$\frac{1-\gamma^5}{2}\frac{1-\gamma^5}{2} = \frac{1-\gamma^5}{2} \tag{3.49}$$

$$\frac{1+\gamma^5}{2}\frac{1-\gamma^5}{2} = 0 \tag{3.50}$$

imply that only the left–handed component of the d field and the right–handed component of the $\bar{u}$ field contribute to W^+ production. The d is left–handed if its spin is parallel to its momentum, and the $\bar{u}$ right–handed if its spin is antiparallel to its momentum. The $+z$ direction is defined by the proton beam momentum. If the d comes from the p then the $\bar{u}$ must come from the $\bar{p}$. Since the d must be left–handed and $\bar{u}$ right–handed, the W^+ is produced with spin $+1$, i.e., its spin is along the $+z$ direction. Alternatively, if the d comes from the $\bar{p}$, the $\bar{u}$ must come from the p. The momenta and spins are reversed, so the W^+ is produced with spin along the $-z$ direction. The probability of the interaction coming from a d in the p and a $\bar{u}$ in the $\bar{p}$ is $\propto (V_p^d + S_p^d)(V_{\bar{p}}^{\bar{u}} + S_{\bar{p}}^{\bar{u}})$ and the probability of the reverse case is $\propto (S_p^{\bar{u}})(S_{\bar{p}}^d)$, where V_X^q denotes the probability of obtaining a valence quark of type q in X and S_X^q the corresponding probability of obtaining a sea quark. Using $S_p^{\bar{u}} = S_{\bar{p}}^{\bar{u}}$ and $S_p^d = S_{\bar{p}}^d$, we obtain the W^+ polarization as $+1$ for valence–valence (VV) and valence–sea (VS) interactions, while for sea–sea (SS) events, 50% have polarization $+1$ and 50% have polarization -1. The contribution from sea–sea interactions affects the polarization distribution of the W and is irrelevant for the Z. Table 3.1 shows the fraction of sea–sea W events for various pdf computed from PDFLIB [14] and from HERWIG. Table 3.2 shows the contributions of the possible initial state quark configurations from HERWIG for W^- production.

Parton distribution set	Sea–sea fraction (PDFLIB)	Sea–sea fraction (HERWIG)
MRSA−′	20.7%	$21.0 \pm 0.1\%$
CTEQ3M	20.3%	$20.5 \pm 0.1\%$
MRSD−′	20.1%	$20.3 \pm 0.2\%$
CTEQ2M	20.3%	$20.3 \pm 0.2\%$

Table 3.1: Fraction of W events initiated by sea–sea quark combinations for various pdf.

Proton quark	Antiproton quark	MRSA−′ (%)	CTEQ3M (%)
d	$\bar{u}$	85.13	84.93
d	$\bar{c}$	0.59	0.65
s	$\bar{u}$	1.67	1.78
s	$\bar{c}$	2.08	2.37
$\bar{u}$	d	8.03	7.42
$\bar{c}$	d	0.16	0.17
$\bar{u}$	s	0.26	0.26
$\bar{c}$	s	2.07	2.40

Table 3.2: Relative contributions of possible initial state quark configurations for W^- production.

3.3 W and Z decays

3.3.1 Lowest order decay kinematics

The lowest order decay diagrams for the processes $W \rightarrow e\nu$ and $Z \rightarrow ee$ are shown in figures 3.10 and 3.11. We can take the electron and neutrino to be massless. In the W or Z rest frame the two decay products are back-to-back. In this frame each decay particle has energy equal to 1/2 the boson mass. Given the boson 4–vector, the decay is then completely specified by fixing the azimuthal and polar angles, ϕ and θ, of either decay product in the boson rest frame.

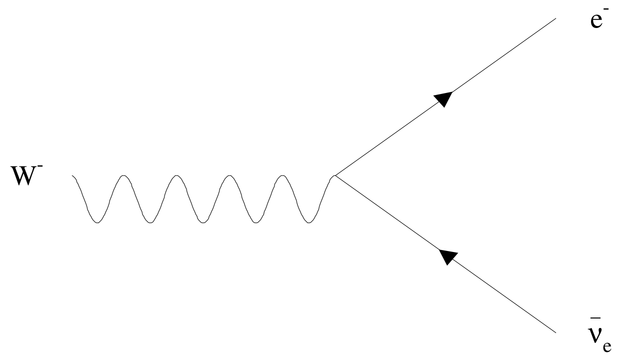

Figure 3.10: Leading order diagram for $W \rightarrow e\nu$ decay.

The distributions of these angles depend on the boson polarization. For W decay, the θ distribution in the W rest frame is given by

$$\mathcal{P}(\theta) \quad \propto \quad (1 - \lambda Q \cos\theta)^2 \tag{3.51}$$

where λ is the W helicity, assumed to be ± 1 and aligned along the $p\bar{p}$ axis, Q

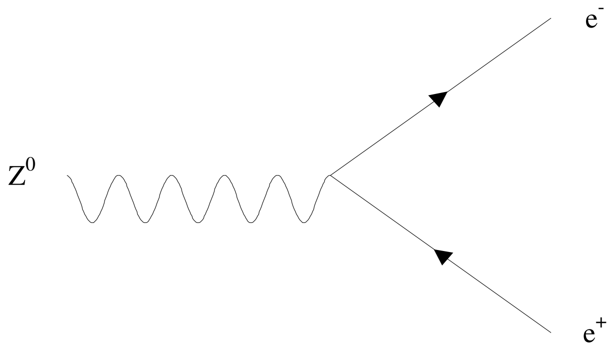

Figure 3.11: Leading order diagram for $Z \rightarrow ee$ decay.

is the W charge, and θ is the angle between the electron and the proton beam axis. Figure 3.12 illustrates the W decay pattern. In the approximation that the boson spin is oriented along the $p\bar{p}$ axis, the ϕ distribution is uniform in $[0, 2\pi)$. The approximation that the $q\bar{q}$ axis coincides with the $p\bar{p}$ axis is, strictly speaking, only true for lowest order production. When the boson is produced with finite p_T the polarization is no longer oriented exactly along the $p\bar{p}$ axis. The corrections due to this effect have been calculated in NLO QCD by E. Mirkes [40] and are found to be relatively small for the low p_T region of interest to this analysis. For the final fit, the P_T^W dependence of the decay angular distribution has been included according to the Mirkes calculation. The polar angle distribution is modified from, for example,

$$(1 + \cos\theta)^2 \rightarrow 1 + \alpha_1 \cos\theta_{CS} + \alpha_2 \cos^2\theta_{CS} \tag{3.52}$$

where the subscript CS means that the angle is defined in the Collins–Soper frame.

In the limit $P_T^W \rightarrow 0$, $\alpha_1 \rightarrow 2$ and $\alpha_2 \rightarrow 1$ so that the modified expression reduces to the original.

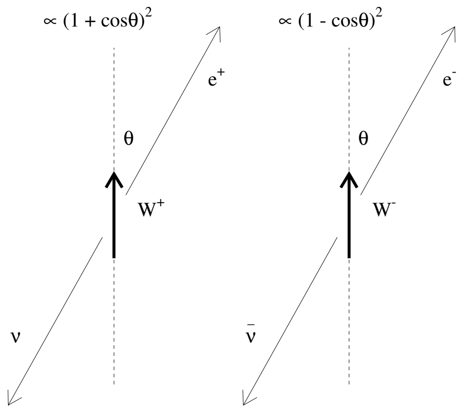

Figure 3.12: W decay pattern for W^+ and W^-.

For Z decay the θ distribution in the Z rest frame is given by

$$\mathcal{P}(\theta) \;\; \propto \;\; 1 + \cos^2\theta \qquad (3.53)$$

where θ is the angle between either electron and the proton beam axis. If the electron charge were observable there would be a term proportional to $\cos\theta$, where θ would denote the polar angle of the positive electron.

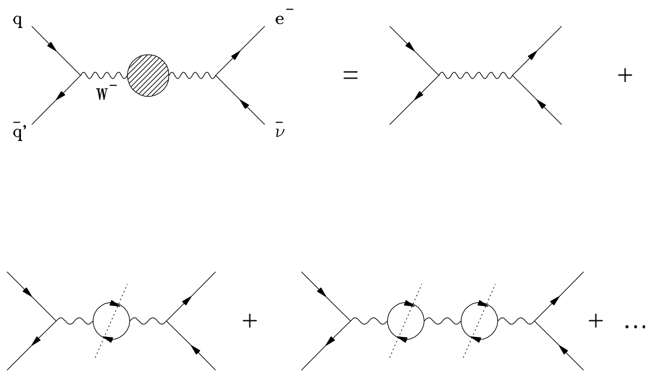

Figure 1

Figure 3.13: Loop contributions to the W propagator, which generate a finite Breit–Wigner width. (Diagram from Ulrich Baur.)

The most important corrections to the lowest order decay processes discussed in the previous section arise from radiation of photons from an electron in the final state or from the W propagator itself. These processes are referred to as "internal bremsstrahlung," to distinguish them from the case of bremsstrahlung caused by the interaction of a final state electron with the material of the detector. Internal bremsstrahlung is a feature of the physics of the $p\bar{p}$ interaction itself. In W and Z events, a photon may be attached to either incoming quark. Such processes are referred to as initial state QED radiation, or ISR. The photon may also be attached

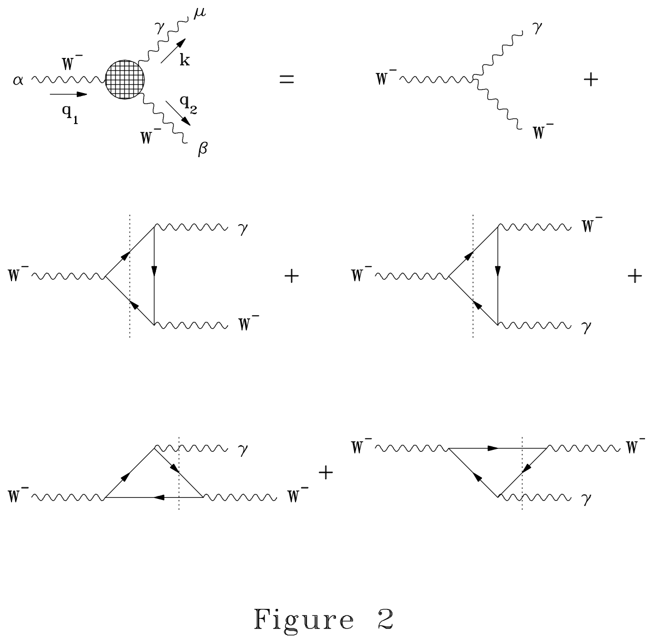

Figure 3.14: Fermion triangle graph contributions to the effective $WW\gamma$ vertex (Diagram from Ulrich Baur.)

to the outgoing electron in W decay, or to either of the outgoing electrons in Z decay. This is called final state QED radiation, or FSR. In the case of W decay, the photon may also be attached to the W propagator, since the W carries electric charge. In this case the diagram contains two W propagators.

The full set of diagrams contributing to lowest order W production has recently been calculated by Baur and Zeppenfeld [36]. The Baur and Zeppenfeld calculation includes initial and final state QED radiation, finite lepton mass effects and finite boson width effects. The calculation is automatically gauge invariant. This is an improvement over the earlier calculation of Berends and Kleiss [38], in which

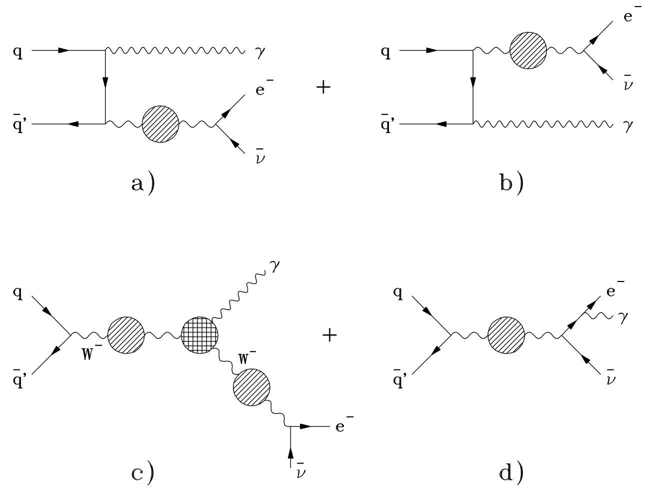

Figure 3.15: Feynman diagrams for the process $q\bar{q} \rightarrow e^{-}\bar{\nu}\gamma$ (Diagram from Ulrich Baur.)

gauge invariance is imposed by splitting the contribution of the graph with a $WW\gamma$ vertex into two pieces, which separately are gauge invariant when combined with the ISR and FSR diagrams. In the Baur and Zeppenfeld calculation, the finite W width is incorporated by resummation of the diagrams shown in figure 3.13. In order to maintain gauge invariance it is then necessary to include the fermion triangle graphs in figure 3.14. In addition the diagrams of figure 3.13 cause violation of unitarity at high energies unless the modifications to the lowest order vertex from the triangle graphs are included. The full amplitude calculated from the graphs shown in figure 3.15 is gauge invariant, has good high energy behavior, and naturally incorporates the effects of finite W width. The complete

Baur and Zeppenfeld calculation has been used to check the approximation used in the Berends and Kleiss program. However, for historical reasons the Berends and Kleiss program is actually used in the W and Z simulations to derive the radiative decay corrections to the mass fits. Thanks are due to Ulrich Baur for allowing me to use figures 1–3 from reference [36].

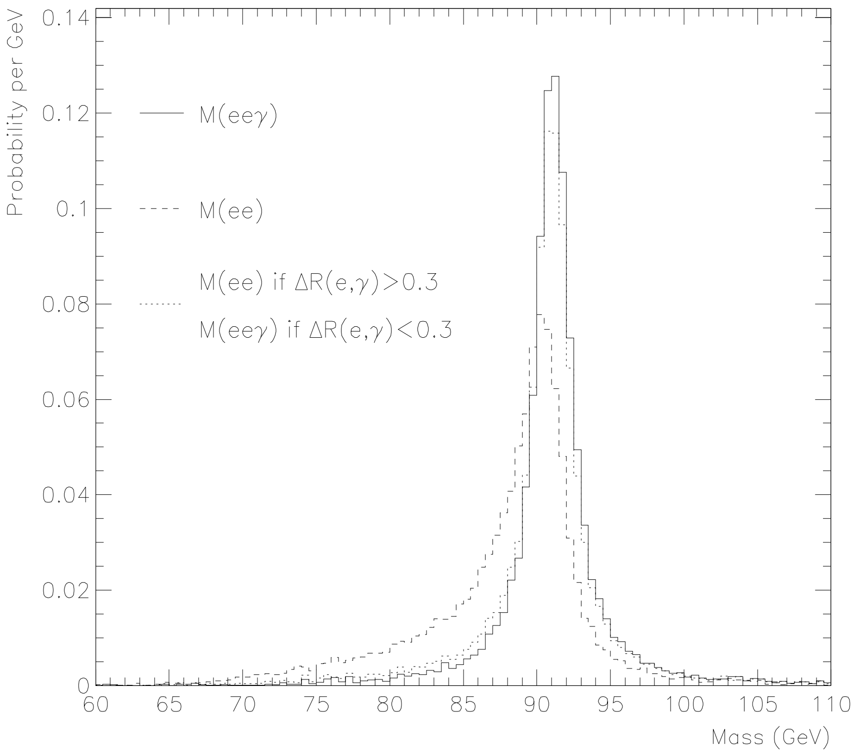

Figure 3.16: Invariant mass distributions for $Z\rightarrow ee\gamma$ radiative decays from the Baur–Zeppenfeld Monte Carlo. (1) The dielectron pair (2) The dielectron plus photon system (3) An approximation to the observed mass in the calorimeter.

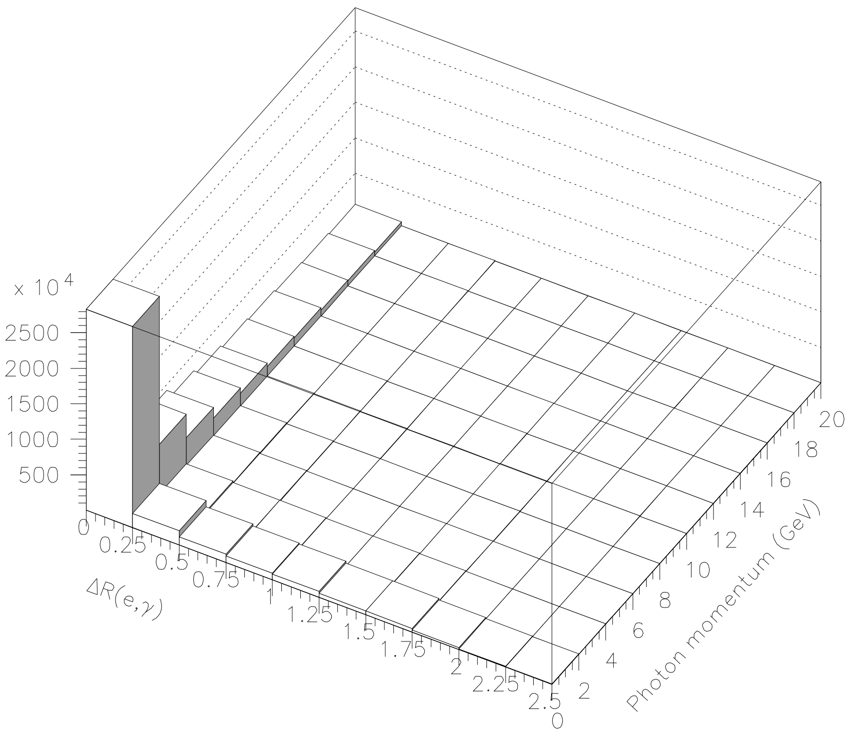

Figure 3.17: Distribution of photon momentum vs. the ΔR between the photon and the nearest electron, linear scale.

The dominant effect relevant to the mass measurement is the case where a final state electron radiates a photon of significant energy (more than about 50 MeV) at a large enough angle from the electron that it is not included in the measurement of the electron shower in the calorimeter [15]. The radiated photons tend to be collinear with the electron. Although the photon can have large (several GeV) momentum, if it is close to the electron its shower in the calorimeter will

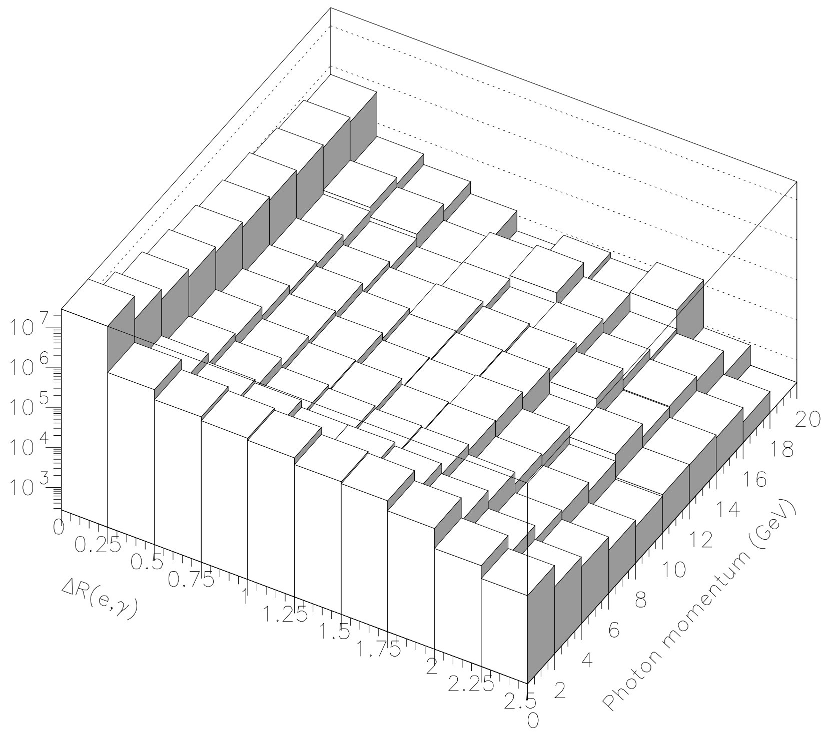

Figure 3.18: Distribution of photon momentum vs. the ΔR between the photon and the nearest electron, log scale.

merge with that of the electron and so its energy will effectively be included in the electron energy measurement. This effect is illustrated in figure 3.16 for the Z. The W case is similar. The invariant mass distribution for the $ee\gamma$ system is a clean Breit–Wigner lineshape. However, the invariant mass distribution of the ee pair is severely skewed towards low mass values because of the energy carried by the photon. If the photon is close enough to one of the electrons that its shower merges with the electron shower then the observed mass of the Z is not as strongly affected. The third distribution shown in figure 3.16 shows that the skewing is greatly reduced, though still observable, if the photon is only lost when it is further from the electron than $\Delta R > 0.3$. This ΔR cut corresponds to the effective merging threshold for the DØ central calorimeter [39]. If one attempted to measure the mass using the momentum measured with the tracking chambers, the result would be much more susceptible to radiative effects, since the photon momentum would never be included in the electron momentum measurement, even for very small ΔR where the photon momentum can be very large. Figures 3.17 and 3.18 show the spectrum of photon momentum vs. the ΔR between the photon and the nearest electron from the Baur–Zeppenfeld Monte Carlo. From the linear plot it is obvious that photons of small angle and low momentum dominate the spectrum, and that the lowest ΔR bin has a hard photon momentum spectrum. The log scale plot shows the shape of the spectrum for finite ΔR and photon momentum, significantly away from the collinear divergence.

Figure 3.19 shows the fraction of events which are radiative as a function of the minimum energy of the photon in the center of mass frame, using the Berends and Kleiss calculation.

3.4 $W \rightarrow \tau\nu$ decays

There is an irreducible background to $W \rightarrow e\nu$ decays from $W \rightarrow \tau\nu$ decays where the τ subsequently decays to an electron. However, the τ is highly boosted and decays to an electron and two neutrinos. The τ mass is $m_\tau = 1.777 \pm 0.0005$ GeV [24] and the p_T of the τ from a $W \rightarrow \tau\nu$ decay is typically of the order of $M_W/2 \approx$ 40 GeV. Since the τ and its decay products are light compared to the τ momentum, the decay products are boosted close to the original direction of the τ. In the lab frame they each have momentum $\approx 1/3$ of the τ momentum. The recoil distributions in a $W \rightarrow \tau\nu$ event are similar to those in a $W \rightarrow e\nu$ event. Since the only decay product observed is the electron, a $W \rightarrow \tau\nu$ decay looks like a $W \rightarrow e\nu$ decay at $\approx 1/3$ of the W mass. In any fit this background therefore affects only the low mass tail.

The fraction of $W \rightarrow \tau\nu$ background in the observed sample can be calculated as

$$f_\tau = \frac{BR(W^+ \rightarrow \tau^+\nu\ ) \times BR(\tau \rightarrow e\nu\bar{\nu})}{BR(W^+ \rightarrow \tau^+\nu\ ) \times BR(\tau \rightarrow e\nu\bar{\nu}) + BR(W^+ \rightarrow e^+\nu\ )} \tag{3.54}$$

The measured branching ratios are [24]

$$BR(\tau \rightarrow e\nu\bar{\nu}) = 0.1801 \pm 0.0018 \tag{3.55}$$

$$BR(W^+ \rightarrow \tau^+\nu\ ) = 0.108 \pm 0.010 \tag{3.56}$$

$$BR(W^+ \rightarrow e^+\nu\ ) \quad = \quad 0.108 \pm 0.004 \tag{3.57}$$

We therefore compute

$$f_\tau \quad = \quad 0.1515 \tag{3.58}$$

The basic kinematics described in the previous section gives a qualitatively correct picture of the effect of $W \rightarrow \tau\nu$ decays. To obtain a quantitative result it is necessary to account for the energy distribution of the electron from the τ decay in the τ rest frame, and the τ polarization. This is done using the ISAJET Monte Carlo program [42]. The $W \rightarrow \tau\nu$ process was simulated and the τ decay products boosted to the τ rest frame. The electron energy in the τ rest frame, $E_\tau(e)$, is kinematically limited to the range $(0, m_\tau/2)$. Figure 3.20 shows the distribution of $E_\tau(e)/(m_\tau/2)$ vs. $\theta(e,\tau)$, where $\theta(e,\tau)$ is the polar angle between the τ momentum and the electron momentum in the τ rest frame in radians [2]. Table 3.3 gives the predicted mass shifts arising from the inclusion of τ decays in the fitting functions for each of the fits.

Quantity fit	$P_T(W)$ cut	Fitting window	Mass shift (MeV)
M_T	15	[60,90]	75 ± 6
$E_T(e)$	15	[30,45]	83 ± 8
$\not{E}_T$	15	[30,45]	118 ± 9
$E(e)$	15	[30,60]	189 ± 13
M_T	30	[60,90]	52 ± 5
$E_T(e)$	30	[30,45]	65 ± 8
$\not{E}_T$	30	[30,45]	99 ± 10
$E(e)$	30	[30,60]	156 ± 13

Table 3.3: Effect of $W \rightarrow \tau\nu$ background on W mass fits. The mass shifts are the differences between fitted mass and input mass for MC experiments generated without $W \rightarrow \tau\nu$ decays, where the fitting functions included $W \rightarrow \tau\nu$ decays. Approximately 4.5 million events were generated for the sample with $P_T(W) < 30$ GeV and 3.9 million events for the sample with $P_T(W) < 15$ GeV.

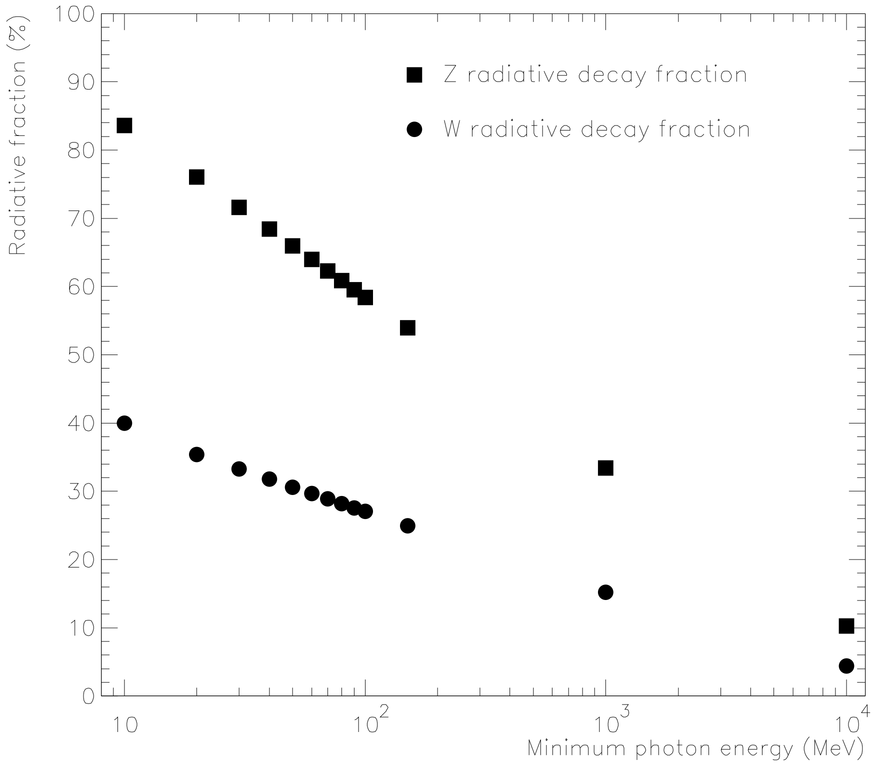

Figure 3.19: Fraction of radiative decays for W and Z events as a function of the minimum photon energy.

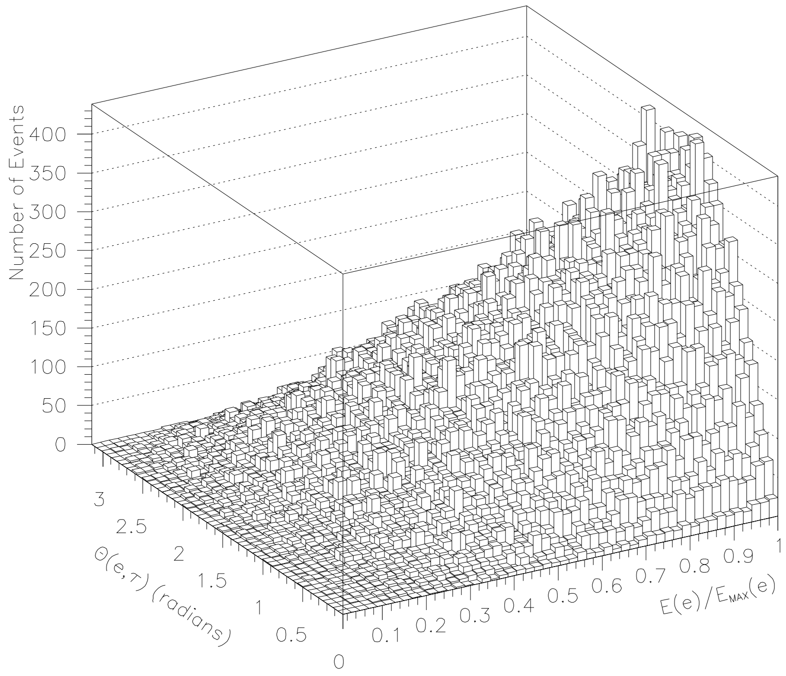

Figure 3.20: Distribution of $E_\tau(e)/(m_\tau/2)$ vs. $\theta(e,\tau)$ from ISAJET in the τ rest frame.

Chapter 4

Data Samples

4.1 Overview

In this chapter the W and Z data selection criteria are discussed. W and Z events are relatively rare, and are characterized by the presence of high p_T leptons. The online criteria for selecting W and Z candidate events are described in section 4.2, the offline criteria in section 4.3, and the resulting data samples in section 4.4. The data sample is the same as that used for the transverse mass analysis [2], except that the P_T^W cut is at 15 GeV rather than 30 GeV.

4.2 Online Criteria

The Tevatron beams cross every $3.5\,\mu$sec, so that $p\bar{p}$ events occur at rates of up to ≈ 286 kHz. The DØ host system was capable of writing events at a rate of about 2–3 Hz with deadtime below 10%. To reduce the very large interaction rate to the output rate several online systems were in place to select interesting events to write out. These trigger systems were implemented in four levels, called L0, L1, L1.5 and L2.

The level zero (L0) trigger required a coincidence in scintillator hodoscopes placed north and south of the interaction region, signalling a $p\bar{p}$ interaction. This requirement rejects empty crossings, single–diffractive, beam halo and beam–gas events. However, at high luminosities most beam crossings contain an interaction, so that the rejection obtainable from the L0 system was not useful for reducing the rate. To allow searches for diffractive W events the L0 requirement was removed from the W trigger in Run 1b, however, the L0 requirement was retained for the Z trigger. To ensure consistency between the W and Z samples the L0 requirement was therefore enforced offline for the W sample.

The level one (L1) calorimeter trigger is based on fast analog pickoff circuits. These circuits essentially differentiate the signals from the preamps to give a fast approximate value for the energy deposited. At level 1, the calorimeter is divided into 0.2×0.2 regions in $\eta - \phi$ space. All electromagnetic cells in any such region together constitute an electromagnetic (EM) trigger tower. Similarly all the hadronic cells are grouped into hadronic (HAD) trigger towers. The energies of the cells in any tower are summed together by analog circuitry.

The W trigger at L1, named EM_1_HIGH, required one EM trigger tower above 10 GeV. The Z trigger, named EM_2_MED, required two EM trigger towers to exceed 7 GeV.

The L1 measurement has the disadvantage that near the tower boundaries there is an efficiency loss because electron showers share energy between two trigger towers, so that neither tower is above threshold. Sometimes energy is shared among several towers. To reduce this loss while maintaining high rejection, a DSP based system called level 1.5 was implemented. The L1.5 algorithm sums two EM towers from level 1 to determine the candidate energy. In addition the L1.5 algorithm computes an electromagnetic fraction based on the L1 EM and HAD tower energies. A loose cut on this fraction allowed for a rejection factor of ≈ 2 for background from jet events while maintaining better than 95% efficiency for isolated electrons. For more details of the L1.5 electron trigger see reference [68].

For the W trigger the L1.5 candidate was required to exceed 15 GeV and have an L1.5 EM fraction greater than 0.85. For the Z trigger, the L1.5 electron candidate corresponding to either L1 candidate was required to exceed 12 GeV and have L1.5 EM fraction greater than 0.85. Not all the W events were collected with the L1.5 condition, since the calorimeter L1.5 hardware was commissioned after Run 1b had already begun.

The level 2 (L2) system is a software trigger at which essentially all the information from the detector is available. The L2 electron candidate is reconstructed from the precision calorimeter readout rather than the fast but less accurate trigger pickoffs. The EM fraction at L2 is calculated using the EM and FH1 layers only. The L2EM candidates were required to have EM fraction exceeding 0.9, and to satisfy very loose shower shape cuts [67]. In addition, an isolation requirement was applied. In principle, a loose tracking requirement should have been applied, based on counting CDC hits in a broad road around the candidate, but because of a benign software bug this cut was never actually applied. The transverse energy of an L2 electron candidate is measured in a 0.5×0.5 window in $\eta - \phi$ space. The W trigger, called EM1_EISTRKCC_MS, required an L2EM candidate with L2 transverse energy above 20 GeV and L2 $\not{E}_T$ greater than 15 GeV. The Z trigger, called EM2_EIS2_HI, required two isolated L2EM candidates with L2 E_T above 20 GeV. For more details of the L2 electron trigger see reference [67].

4.3 Offline Criteria

The offline criteria for the W mass sample were chosen to select well–measured events with low background contamination. The criteria can be divided into kinematic, fiducial, electron quality and detector quality cuts.

4.3.1 Kinematic Cuts

For W events, we require

- an electron candidate with $p_T > 25\,\mathrm{GeV}$
- hadronic recoil $u_T < 15\,\mathrm{GeV}$
- $\not\!\!E_T > 25\,\mathrm{GeV}$

Large $\not\!\!E_T$ indicates the presence of a neutrino. These cuts select events with a high p_T electron and a high p_T neutrino and restrict the P_T^W to low values. The dominant background events come from QCD events in which there is a fake electron and $\not\!\!E_T$ due to the fluctuations in the jet energies deposited. These events have very rapidly falling spectra in $p_T(\mathrm{e})$ and $\not\!\!E_T$, so that the kinematic cuts are very effective in rejecting background events while retaining high efficiency for the signal.

The P_T^W cut was chosen

- to minimize systematic errors in the detector modelling. Since the Z sample has only a few events at high P_T^Z, the detector model is best constrained at low P_T^W.

- to minimize the effect of the $u_{||}$ efficiency

- to optimize the theoretical constraint on the P_T^W model from the P_T^Z measurement

- to reduce background

For Z events we require two electron candidates with with $p_T > 25\,\mathrm{GeV}$. To ensure that the dielectron candidates are from Z decays, the dielectron invariant mass is required to lie in the window 70 GeV$< M_{ee} <$ 110 GeV. To maximize the number of Z events, a loose sample was defined for which the tracking cuts are removed for one central electron candidate.

4.3.2 Fiducial Cuts

The term "fiducial cut" refers to a requirement made on a measured object to constrain it to a well–understood region of the detector. All electron candidates used in this analysis were required to be in good regions of the central calorimeter (CC).

Electrons near to the intermodule cracks were excluded. There are 32 equal modules, so that the cracks are located at $\phi = 2\pi N/32$, where $N = 0 \cdots 31$. The excluded regions were $\mathrm{mod}(\phi, 2\pi/32) < 0.1$ and $\mathrm{mod}(\phi, 2\pi/32) > 0.9$. This region was set by test beam and Monte Carlo studies in which electrons were scanned across the crack region. A 10% cut on either side is sufficient to ensure that the events are not badly mismeasured because of energy loss in the crack region [70].

Electrons near the ends of the central calorimeter were excluded. For the W mass analysis the electron energy is reconstructed using a 0.5×0.5 window in $\eta - \phi$ space. The calorimeter extends to $\eta = 1.2$. To ensure that the electron window is not clipped, the calorimeter cluster centroid z position is required to satisfy $|z_{CAL}| < 107.7\,\mathrm{cm}$. This is approximately equivalent to requiring the electron to satisfy $|\eta| < 1.0$.

To ensure that the electron tracks were well measured in the CDC, the track centroid z position was required to satisfy $|z_{TRK}| < 80\,\mathrm{cm}$. This condition eliminates electron candidates near the ends of the CDC where the delay lines may behave non–linearly.

To mimic the W event topology, the Z sample used to to determine the recoil response and resolution included events in which one of the electrons was allowed to be in either of the end calorimeters. In this case the electron candidate was required to satisfy $1.5 < |\eta| < 2.5$.

4.3.3 Electron Quality Cuts

The electron quality cuts have been tuned to be efficient for high p_T electrons while rejecting background from jets which fluctuate so that much of their energy is electromagnetic.

The first stage in identifying an electron is the requirement of a highly electromagnetic, relatively narrow cluster. This is enforced by accepting only candidates with an electromagnetic fraction of greater than 90%. The electromagnetic fraction, f_{em}, is calculated as the ratio

$$f_{em} = \frac{\sum_{\text{towers}} E_{EM}}{\sum_{\text{towers}}(E_{EM} + E_{HAD})} \tag{4.1}$$

A narrow cluster is enforced by requiring that more than 40% of the cluster energy be in the single most energetic tower. Clusters which pass the preceding criteria are called EM clusters. Additional quality variables are computed for each such cluster, such as the isolation fraction and H–matrix χ^2. The isolation fraction f_{iso} is defined by cones around the candidate in $\eta - \phi$ space

$$f_{iso} = \frac{E_{TOT}(0.4) - E_{EM}(0.2)}{E_{EM}(0.2)} \tag{4.2}$$

where, for example, $E_{TOT}(R)$ refers to the sum of EM and HAD towers in a cone

$\Delta\eta^2 + \Delta\phi^2 \leq R^2$. Electron candidates are required to satisfy $f_{iso} < 0.15$, matching the requirement in the L2 trigger. The H–matrix is a covariance matrix built from plate–level Monte Carlo electron samples. The H–matrix χ^2 is a measure of how closely the shower shape of an electron candidate matches expectations from Monte Carlo simulations, accounting for correlations within the shower. Candidates are required to satisfy $\chi^2 < 100$. For more information about the f_{iso} and χ^2 variables see, for example, reference [69].

For every EM cluster, the centroid of the cluster in the EM3 layer of the calorimeter is computed. This centroid and the event vertex calculated from all the CDC tracks together define a tracking road for the cluster. The road is a window in $\theta - \phi$ space centered on the expected trajectory of the electron. If there is at least one track in the road of a cluster, it is nominally called an electron candidate. The quality of the match between the track and the cluster is defined by the track match significance

$$\sigma_{trk} = \sqrt{\left(\frac{\Delta Z}{\sigma(\Delta Z)}\right)^2 + \left(\frac{\Delta R\phi}{\sigma(\Delta R\phi)}\right)^2} \tag{4.3}$$

where ΔZ is the difference between the cluster z position in the EM3 layer and the CDC track trajectory extrapolated to the EM3 layer, and similarly $\Delta R\phi$ is the difference in the $R\phi$ direction. The errors $\sigma(\Delta Z)$ and $\sigma(\Delta R\phi)$ were determined from the Run 1a $Z \rightarrow ee$ sample. For this analysis, every electron candidate was required to have a well–matched track, satisfying $\sigma_{trk} < 5$ in the central region and $\sigma_{trk} < 10$ in the forward region.

4.3.4 Detector Quality Cuts

Occasionally data was taken with one or more detector subsystems malfunctioning. These runs were noted and a list of bad runs prepared. Events from these runs were excluded if detectors relevant to this analysis were not in order. These detectors include the calorimeters, ICD, CDC, L0. Runs were not excluded if the only non–working detectors were those not directly used in this analysis, such as the small–angle muon system or TRD.

One of the accelerator subsystems, the Main Ring, passes directly through the DØ detector. Two vetoes were used to prevent Main Ring losses from affecting the data. The Main Ring Beam Sync (MRBS) and microblank (μBLANK) veto flags were required for the W sample, and for the Z sample for all studies affecting the hadronic recoil measurement. Since the main ring losses affect only the coarse hadronic calorimeter, the vetos were not required for the Z mass fit used to determine the electromagnetic energy scale.

4.4 Event Samples

The data for this analysis were collected during the Tevatron collider Run 1b. The W signal triggers were exposed to an integrated luminosity of ≈ 76 pb^{-1}. The earliest W and Z candidates were recorded in run 72736 on December 29, 1993 and the last in run 93115 on July 24, 1995. The peak luminosity in Run 1b was $\approx 25 \times 10^{30}\mathrm{cm}^{-2}\mathrm{s}^{-1}$. The highest luminosity at which W candidates were recorded was about $21 \times 10^{30}\mathrm{cm}^{-2}\mathrm{s}^{-1}$. The mean instantaneous luminosity for the W sample was $\approx 7 \times 10^{30}\mathrm{cm}^{-2}\mathrm{s}^{-1}$. For comparison, the peak luminosity for Run 1a was about $9 \times 10^{30}\mathrm{cm}^{-2}\mathrm{s}^{-1}$ and the mean luminosity for the W sample was $\approx 3 \times 10^{30}\mathrm{cm}^{-2}\mathrm{s}^{-1}$. The Run 1a integrated luminosity was ≈ 13 pb^{-1}.

After all cuts, there remain 28323 $W \rightarrow e\nu$ candidate events and 2179 $Z \rightarrow ee$ candidates in the W and Z mass samples. The W mass sample is a data set to which very restrictive cuts have been applied, to ensure that the data is of the highest quality and easily modelled. The actual numbers of reconstructed W and Z events at DØ are of course much higher. Table 4.1 shows the numbers of events surviving as a function of the P_T^W cut. Table 4.2 shows the number of Z events. For comparison the numbers of events used in the W and Z cross section analyses are also provided [43].

Criteria	Number of events
W mass $P_T^W < 15\,\mathrm{GeV}$	28323
W mass $P_T^W < 30\,\mathrm{GeV}$	32361
W cross section cuts	59579

Table 4.1: Numbers of W events surviving different criteria.

Criteria	Number of events
Z mass	2179
Z hadronic constraint	2341
Z cross section cuts	5705

Table 4.2: Numbers of Z events surviving different criteria.

Chapter 5

Electron Measurement

5.1 Overview

In section 5.2 the reconstruction process for electron candidates is outlined. In section 5.3 we discuss the details of the angular measurement, focussing on the calibration of the CDC track centroid z position. In section 5.4 the electromagnetic energy scale calibration is discussed, including the Z mass fit and the reconstruction of the J/ψ and π^0 resonances. Finally the electromagnetic energy resolution is discussed.

5.2 Reconstruction

5.2.1 Calorimeter hitfinding

The first stage in event reconstruction is hitfinding. The signals emerging from the calorimeter are digitized charge measurements from a discrete set of cells in a fixed geometry. For each cell, the distribution of energy read out in the absence of beam is called its "pedestal" distribution. The mean of the pedestal distribution is called the pedestal. The energy deposited in the cell when hit by a particle is proportional to the difference between the energy read out and the pedestal. Therefore, to reconstruct the energy deposited in a cell, it is necessary to first subtract the pedestal, then multiply the result by a conversion factor which relates the energy measurement in ADC counts to the energy measurement in GeV. The pedestal distributions are determined from frequent pedestal calibration runs taken between stores, and the pedestal subtraction was performed online. The ADC count to GeV conversion constant is actually the product of several factors. There is a run–dependent gain factor for each cell determined from gains calibration runs, taken between stores. In these runs the calorimeter preamps are pulsed through precision resistors. These gains factors minimize cell–to–cell variations and time dependence in the electronics response. The cells are assigned sampling weights which are related to the relative amounts of absorber material and liquid argon in each type of cell. Finally for each section there is an overall scale factor.

Not all cells are read out in a given event. Hardware zero–suppression eliminates most cells which were not hit in a given event. The zero–suppression criterion was based on the pedestal distributions. To decide whether or not a cell was hit, the pedestal subtracted energy for that cell was required to be greater in magnitude than 2σ, where σ was the rms of the pedestal distribution for that cell.

The result of the hitfinding for each event is a list of hit cells which contain energy above the zero–suppression threshold. For each cell the deposited energy in GeV is reconstructed by applying the relevant conversion factors to the pedestal–subtracted readout in ADC counts.

5.2.2 Clustering and Position Finder

After calorimeter hitfinding has been performed, the electromagnetic (EM) and hadronic (HAD) tower energies are reconstructed by summing all hit EM (or HAD) layers at a given iη and iϕ. The clustering algorithm runs off this tower list. The clustering begins with a non–empty tower. It looks at all neighbors of that tower and includes the highest energy neighbor in the cluster. The process continues until there are no more towers with a neighbor above threshold. Clusters with transverse energy less than 1.5 GeV are dropped. Electromagnetic candidates are required to have EM fraction exceeding 90%. The EM fraction is defined as the sum of EM towers in the cluster over the sum of EM+HAD towers in the cluster. In addition the hottest tower in the cluster is required to contain at least 40% of the cluster energy.

The calorimeter position finder is applied to electromagnetic clusters, which are electron or photon candidates. The position finder uses as input the cell energies in the EM3 layer of the cluster. A log–energy–weighted center of gravity algorithm is applied to the EM3 shower profile. This algorithm has been extensively studied using test beam data and detailed GEANT Monte Carlo simulations. Based on the simulations, corrections are applied to the shower position to remove a bias which depends on the incident angle of the electron [44, 45]. A further correction is applied based on a calibration using $Z \to ee$ events.

5.3 Angle Measurement

5.3.1 ϕ Measurement

The electron azimuthal angle ϕ can be measured using several subdetectors. Since the (x, y) position of the event vertex moves very little and is determined accurately on a run–by–run basis from the vertex drift chamber (VTX) it is sufficient to measure a single (x, y) point on the electron track in any of the detectors, namely the VTX, central drift chamber (CDC) or the calorimeter. The VTX and CDC also can fit the electron track locally, to determine ϕ independently of the event vertex position. Hence for central electrons ϕ can be determined in five ways — from the VTX (x_{COG}, y_{COG}), the VTX local ϕ, the CDC (x_{COG}, y_{COG}), the CDC local ϕ and the calorimeter (x_{COG}, y_{COG}) in the EM3 layer. In practice best resolution is achieved by using the CDC center of gravity and the beam (x, y) position from the VTX chamber. The VTX track matching efficiency is about 80% for 2D matching (i.e., matching in ϕ only) and less than $\approx 50\%$ for 3D matching (i.e., matching in both ϕ and θ.)

ϕ Calibration

The ϕ measurement in the CDC is self–calibrating because of the offset between successive layers of the CDC. In each layer there are 7 sense wires, which are offset in azimuth by $2\pi/64$ in successive layers. The hits from the 7 sense wires in each layer are used to build a track segment. The four segments are combined into one track. The ϕ measurement could be biased if the drift velocity were incorrect. However, if this were the case the alternate segments would not line up.

ϕ Resolution

Three independent ϕ measurements are used to measure the ϕ resolution of the CDC. The ϕ of an electron candidate can be measured using the fitted ϕ of the CDC track (ϕ_{fit}), and the xy position of the beam spot - accurately determined on a run by run basis using the VTX chamber - in conjunction with the xy position of the calorimeter cluster (ϕ_{cal}) or the xy position of the CDC track center of gravity (ϕ_{cog}). Figure 5.2 shows the distribution of beam spot positions for the $W \rightarrow e\nu$ data.

The CDC track trajectory in the xy view is defined by the track center of gravity (COG), (x_{COG}, y_{COG}), and the fitted ϕ. The xy impact parameter, b, is defined as the distance of closest approach of this trajectory to the beam spot, (x_{beam}, y_{beam}), and is given by

$$b = (x_{COG} - x_{beam}) \sin \phi_{fit} - (y_{COG} - y_{beam}) \cos \phi_{fit} \tag{5.1}$$

To a good approximation we have

$$\sigma^2_{b/R_{CDC}} = \sigma^2_{\phi_{cog}} + \sigma^2_{\phi_{fit}} \tag{5.2}$$

where σ_X refers to the rms of the distribution of a variable X. R_{CDC} is approximately constant. Its distribution is shown in figure 5.2. Ignoring possible relative biases between ϕ_{fit}, ϕ_{cal} and ϕ_{cog} we also have

$$\sigma^2_{\phi_{fit}-\phi_{cal}} = \sigma^2_{\phi_{fit}} + \sigma^2_{\phi_{cal}} \tag{5.3}$$

$$\sigma^2_{\phi_{cog}-\phi_{cal}} = \sigma^2_{\phi_{cog}} + \sigma^2_{\phi_{cal}} \tag{5.4}$$

$$\sigma^2_{\phi_{cog}-\phi_{fit}} = \sigma^2_{\phi_{cog}} + \sigma^2_{\phi_{fit}} \tag{5.5}$$

The last equation and the expression for $\sigma_{b/R_{CDC}}$ cross check each other. Figure 5.3 shows distributions of b/R_{CDC}, $\phi_{fit} - \phi_{cal}$ and $\phi_{cog} - \phi_{cal}$ for electrons from the $W \rightarrow e\nu$ sample. Each distribution is fit to a gaussian plus a flat background. We can extract the ϕ resolutions using

$$\sigma^2_{\phi_{fit}} = \frac{+\sigma^2_{\phi_{fit}-\phi_{cal}} - \sigma^2_{\phi_{cog}-\phi_{cal}} + \sigma^2_b/R^2_{CDC}}{2} \tag{5.6}$$

$$\sigma^2_{\phi_{cog}} = \frac{-\sigma^2_{\phi_{fit}-\phi_{cal}} + \sigma^2_{\phi_{cog}-\phi_{cal}} + \sigma^2_b/R^2_{CDC}}{2} \tag{5.7}$$

$$\sigma^2_{\phi_{cal}} = \frac{+\sigma^2_{\phi_{fit}-\phi_{cal}} + \sigma^2_{\phi_{cog}-\phi_{cal}} - \sigma^2_b/R^2_{CDC}}{2} \tag{5.8}$$

These imply

$$\sigma_{\phi_{fit}} = (2.59 \pm 0.02)\,\mathrm{mrad} \tag{5.9}$$

$$\sigma_{\phi_{cal}} = (2.77 \pm 0.02)\,\mathrm{mrad} \tag{5.10}$$

$$\sigma_{\phi_{cog}} = (0.81 \pm 0.08)\,\mathrm{mrad} \tag{5.11}$$

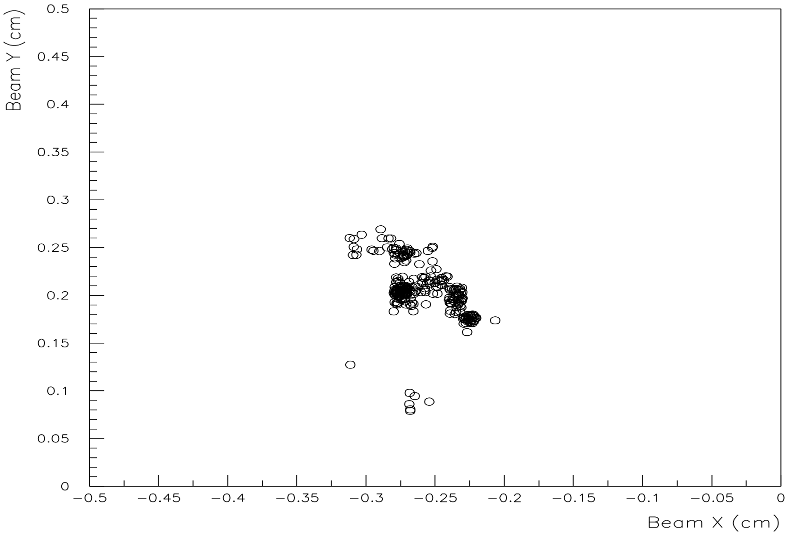

Figure 5.1: The beam spot xy distribution for the $W \to e\nu$ data.

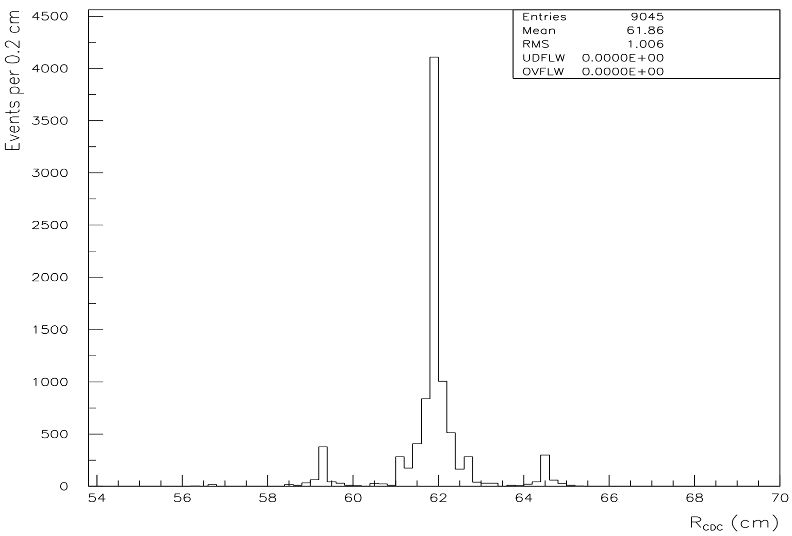

Figure 5.2: The R_{CDC} distribution for the $W \to e\nu$ data.

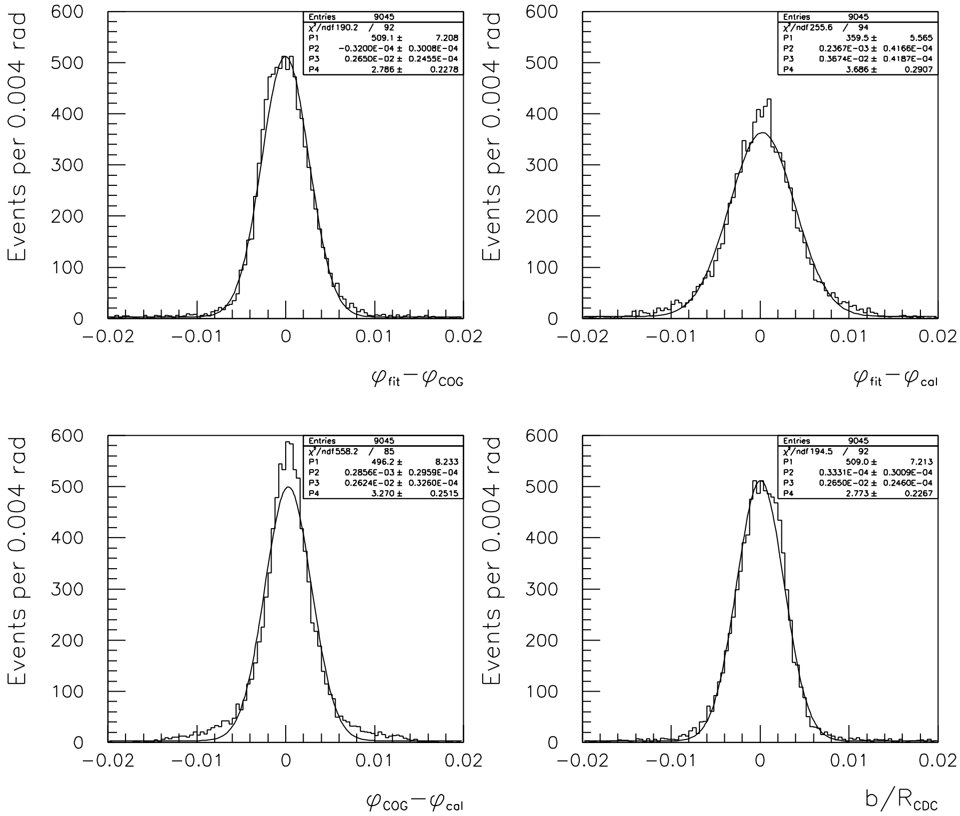

Figure 5.3: ϕ resolutions from Run 1a $W \rightarrow e\nu$ data.

5.3.2 θ Measurement

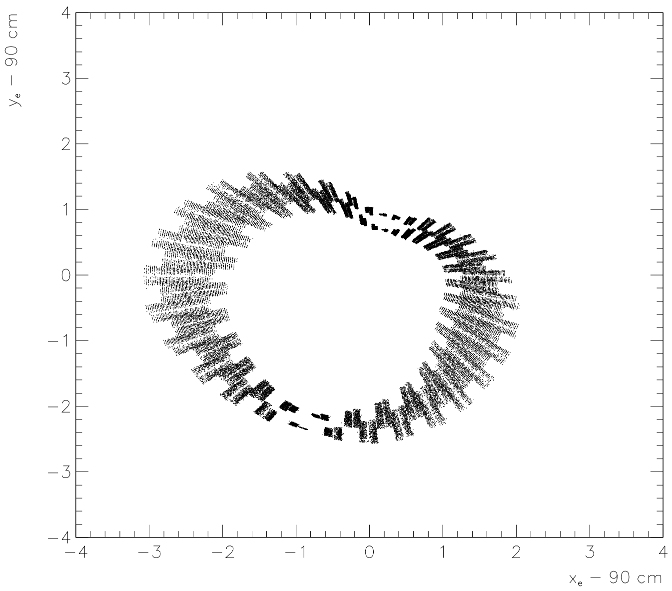

Figure 5.4: Polar plot of the distribution of radial positions for electron clusters. The mean radius is 91.6 cm. The plot shows $(R-90)\sin\phi$ vs. $(R-90)\cos\phi$. The radius is plotted relative to 90 cm to make the structure visible.

The electron polar angle θ is measured using two points on the electron trajectory, the CDC track center of gravity $(X_{TRK}, Y_{TRK}, Z_{TRK})$ and the calorimeter cluster centroid in the EM3 layer $(X_{CAL}, Y_{CAL}, Z_{CAL})$. The polar angle is defined by

$$\theta = \tan^{-1}\frac{R_{CAL}-R_{TRK}}{Z_{CAL}-Z_{TRK}} \tag{5.12}$$

where $R_{CAL} = \sqrt{X_{CAL}^2 + Y_{CAL}^2}$ and $R_{TRK} = \sqrt{X_{TRK}^2 + Y_{TRK}^2}$. The R_{CAL} and R_{TRK} values are constant in the data, to a good approximation. Figure 5.4 is a polar scatterplot of $R_{CAL} - 90$cm vs. ϕ, showing the deformation of the calorimeter under its own weight, and the cell structure of the EM3 layer. The event by event variation in R_{CAL} and R_{TRK} and the calorimeter deformation are accounted for in the reconstruction and the computation of θ for the electron candidates in the data. In the CMS Monte Carlo simulation R_{CAL} and R_{TRK} are fixed to 91.6 cm and 62.0 cm respectively.

The θ measurement is simulated in the Monte Carlo without any biases in the CDC or calorimeter centroid positions. It is therefore necessary that the corresponding measurements in the data be bias–free. The CDC calibration is described in section 5.3.3, and the calorimeter position calibration in section 5.3.4. After correcting the biases, the resolutions are determined.

5.3.3 CDC track centroid position calibration

The CDC track centroid position Z_{CDC} has been calibrated using muons from cosmic ray and collider data. In addition, during Run 1c a specialized detector was installed to assist the CDC calibration effort. This device, called the ZCD detector, can be used to calibrate the CDC using inclusive charged particle tracks.

Cosmic ray muons

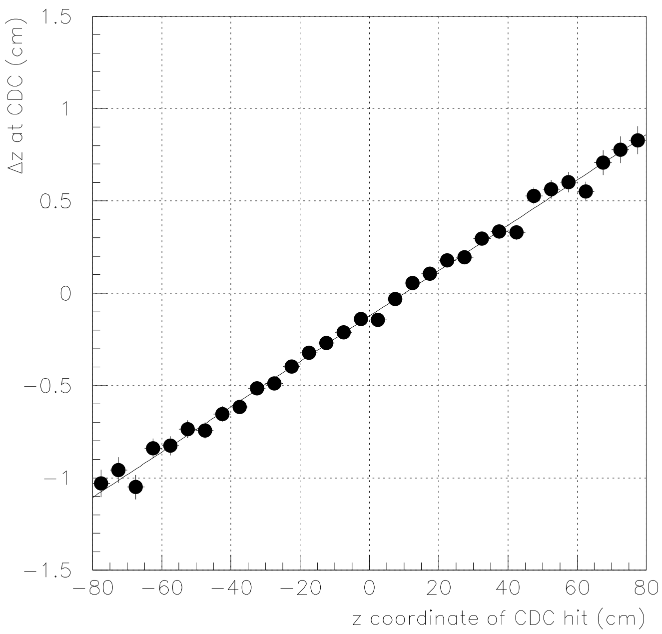

Figure 5.5: CDC calibration using cosmic ray muon events (provided by N. Graf.)

A preliminary measurement of the CDC scale was provided by the analysis of cosmic ray events by N. Graf [57]. In this measurement, cosmic ray muons were required to match back–to–back tracks in the CDC. The true muon trajectory was determined with high accuracy from the back–to–back hits in the A–layers of the muon chambers. The muon trajectory was extrapolated through the CDC and the predicted z position of the centroid of the CDC track was compared to the reconstructed CDC position. Figure 5.5 shows the mean difference between the z predicted from the A–layer hits and the z measured with the CDC. From the observed linear dependence the scale $\alpha_{CDC} = 0.988 \pm 0.002$ was extracted. An updated analysis with more data yields $\alpha_{CDC} = 0.9868 \pm 0.0004(\mathrm{stat})$.

The cosmic muon analysis suffers from some systematic effects. Since the muons come from cosmic rays, they are not synchronized with the detector clock system. This implies that the timing information necessary to reconstruct the muon and CDC tracking hits must be derived on an event–by–event basis. The algorithm for this timing determination is necessarily different from that applied to collider data, where the beam crossing time is precisely known from the accelerator clock. Also, cosmic ray muons have no reason to pass through the beam axis, so the xy impact parameter distribution for cosmics is different for that of collider particles. This implies that the distribution of the incident angle of the muon with respect to the CDC is different for cosmic and collider events. This effect was studied by varying the xy impact parameter cut on the muon tracks. The result was stable for cuts between 2 and 8 cm. For looser cuts the scale increases, indicating that tracks which are very far from the beam axis bias the result.

The cosmic muon sample was used to determine scale factors for each of the 32 sectors. However, the spread in these factors was consistent with the statistical fluctuations expected from the division into subsamples. Applying the sector dependent scales to other samples did not improve the angular resolution. Therefore it was concluded that no strong evidence existed for large sector–to–sector variations in the scale.

The cosmic analysis has the advantage that the environment is very clean and there is a relatively large number of events. The cosmic ray runs were taken over the Run 1a and Run 1b periods so that they roughly coincide in time with the W and Z data.

An analysis has also been performed using cosmic rays collected during collider running [60]. This sample would be a background for any other analysis, but provides a cosmic sample collected under beam conditions and over the same time period as the W and Z data, since the sample was derived from the top dimuon trigger. The method used to derive the CDC scale was $z_1^\mu - z_2^\mu$ minimization, described in section 5.3.3. The result was $\alpha_{CDC} = 0.9880 \pm 0.0009(\text{stat})$.

Collider single muons

An analysis complementary to that of N. Graf was performed by T. Yasuda using an inclusive single muon sample from collider data [58]. In this case there is only one A–layer hit on the trajectory, so the muon trajectory must be anchored using the reconstructed vertex. This introduces a potential source of bias, since the reconstructed vertex is determined using the ensemble of all CDC tracks reconstructed in the event. Thus in this procedure the CDC is to be calibrated using tracks for which the calculated trajectories are not fully independent of the CDC. In spite of this potential bias the collider single muon method is useful because much larger muon samples are available than in the cosmic ray analysis, and the muons are collected throughout the run, so that any time dependence in the CDC would be averaged over correctly. The collider muons originate along the beam axis and at the time of the $p\bar{p}$ collision. Thus systematics associated with the muon being off–axis or out of time are not a factor in the collider analysis. The average CDC scale determined from this analysis was $\alpha_{CDC} = 0.9877 \pm 0.0002$, where the error is statistical only [58].

Collider dimuons

An analysis which has the advantages of both the cosmic rays and the collider single muons is that based on the collider dimuon sample. In this analysis, performed by A. Kotwal [59], events are selected in which a pair of collider muons originate from the same interaction vertex. The trajectories of the two muons are determined from the A–layer hits in the muon chambers and the CDC center of gravity. The difference between the intersections of the two trajectories with the beam axis, $z_1^\mu - z_2^\mu$,is calculated for a range of assumptions of the CDC scale. The measured CDC scale is taken to be that value of α_{CDC} which minimizes the resolution of the $z_1^\mu - z_2^\mu$ distribution.

In this method both muons are from the $p\bar{p}$ interaction and so there are no possible off–axis effects or timing effects as in the cosmic ray analysis. There is no need to make use of the reconstructed vertex as in the case of the analysis of collider single muons. Two samples have been studied, (1) an inclusive dimuon sample dominated by $b\bar{b}$ events and (2) a $Z \to \mu\mu$ sample. The $b\bar{b}$ sample is more powerful statistically, while the $Z \to \mu\mu$ sample has minimal systematic errors, because the muons are well isolated and the background contamination from π/K decays is small.

To determine the statistical error from the dimuon analysis, we note that for an ideal detector $z_1^\mu - z_2^\mu$ is identically zero if the muons come from the same interaction vertex. Therefore we can define a χ^2

$$\chi^2(\alpha_{CDC}) = \sum_{i=1}^{N_{evt}} \frac{(z_1^\mu - z_2^\mu)_i^2}{\sigma(z_1^\mu)^2 + \sigma(z_2^\mu)^2} \tag{5.13}$$

The intrinsic resolution of z^μ is given by $(1/\sqrt{2}) \cdot \sqrt{\sigma_{min}(z_1^\mu - z_2^\mu)^2}$. The χ^2 is automatically equal to the number of degree of freedom at the minimum. The statistical error is given by $\chi^2 = \chi^2_{min} + 1$.

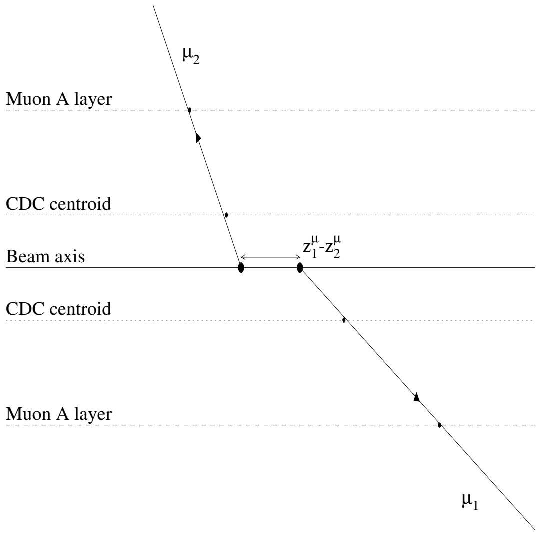

Figure 5.6: Geometry of CDC calibration procedure using collider dimuon events.

From the $Z \rightarrow \mu\mu$ sample the χ^2 minimization gives $\alpha_{CDC} = 0.9878 \pm 0.0014$ and from the $b\bar{b}$ sample $\alpha_{CDC} = 0.9863 \pm 0.0011$.

ZCD Detector

In the period between Run 1b and Run 1c a specialized detector was commissioned to calibrate the CDC delay lines. This ZCD detector covers 10 sectors of the CDC and consists of fibers which run perpendicular to the beam axis mounted on the outer surface of the CDC can. Any charged track which hits one of the ZCD fibers has one point on its trajectory fixed by the location of the fiber. Inclusive tracks from Run 1c which hit any ZCD fiber form the calibration dataset. The analysis is described in detail in reference [61], and yields $\alpha_{CDC} = 0.989 \pm 0.001$ on average.

There are some important systematic effects which affect the ZCD calibration procedure. The ZCD fibers provide only one point with which to anchor the track trajectory. Therefore, the ZCD analyses rely on the local track angle fit in the CDC, which may have systematic effects which have not yet been carefully understood. The ZCD data was taken in Run 1c, therefore any time dependence or any shift in the CDC behaviour which could have occurred during the shutdown between Run 1b and Run 1c would not be correctly accounted for by using the ZCD information. In addition the ZCD covers only 10 sectors of the CDC, and at the time of this thesis the transfer of the ZCD calibration from the 10 sectors covered to the remaining 22 sectors had not been carried out. Therefore, if there were any sector–to–sector variations in the CDC scale they would not be correctly averaged over in the current version of the ZCD analysis. Also, the ZCD fibers were placed approximately 10 cm apart along the length of the CDC can. The responses of the CDC delay lines are therefore sampled by the ZCD only at a few discrete points. While this would not be an issue if the response were known to be perfectly linear, various studies have indicated small non–linearities. It has been shown that small non–linearities do not affect the W mass result, provided that they are averaged over appropriately. Collider muons scan over the length of the CDC and so average over the length of the delay lines, but the particles which hit the ZCD fibers do not.

In spite of these systematic difficulties, the ZCD data provides a useful corroboration of the CDC calibration obtained from the collider dimuons, the cosmic muons and the collider single muons. A complete systematic error analysis has not yet been carried out. Nevertheless, the ZCD promises to be a very useful device which could be used to improve the CDC delay line calibrations dramatically.

Summary

Table5.1 shows the results of the various CDC scale determinations. The different methods agree well (figure 5.1.) The result from single collider muons has a systematic error which is not displayed, from the tendency of the reconstructed vertex to migrate towards $z = 0$ as the luminosity increases. The ZCD result has an undisplayed systematic error from the local track θ measurement. The determinations from muon samples all have a small common systematic error of 0.0003 from the muon chamber alignment [59]. The central value of the CDC scale is

Calibration procedure	CDC scale
Cosmic muons	0.9868 ± 0.0004
Collider muons	0.9877 ± 0.0002
Collider cosmics	0.9880 ± 0.0009
Collider dimuons Z	0.9860 ± 0.0014
Collider dimuons $b\bar{b}$	0.9863 ± 0.0011
ZCD	0.9890 ± 0.0010

Table 5.1: Values of the CDC scale from different methods. The errors are statistical only.

taken to be 0.988, with a total error of 0.001 assigned to cover the spread of values from different methods. This is a conservative error, since the cosmic muon and collider dimuon results which are expected to be bias free at the 0.03% level are consistent.

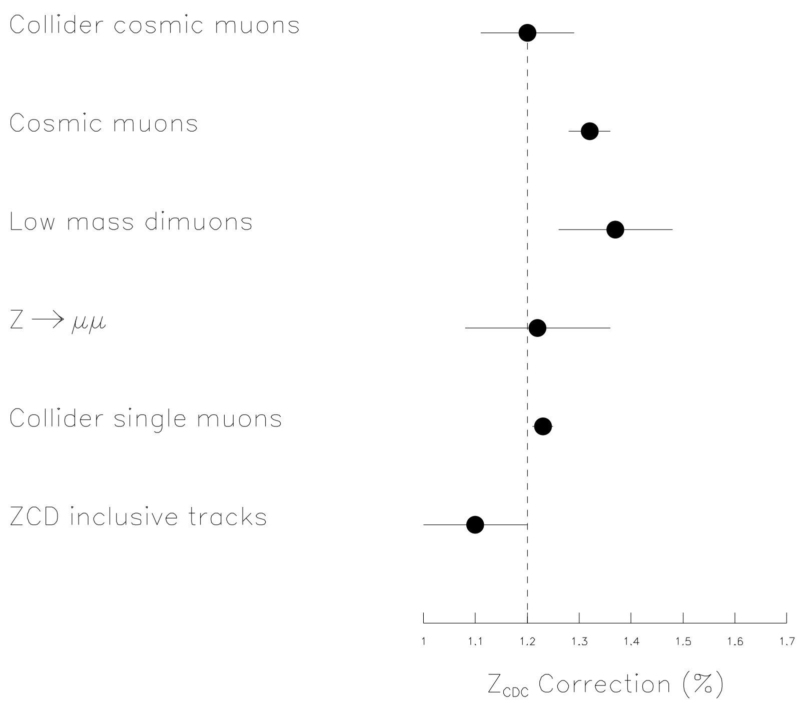

Figure 5.7: Plot of the CDC scale values from different methods, statistical errors only.

5.3.4 Calorimeter Shower Centroid Position Calibration and Resolution

The calorimeter shower centroid position has been calibrated using a sample of fully simulated Monte Carlo electrons [44]. The electrons were generated at a fixed energy of 50 GeV and populated the whole calorimeter. A bias in the cluster Z position was parametrized and corrected, based on a comparison between the intersection of the Monte Carlo trajectory with the EM3 layer of the calorimeter and the reconstructed position.

Given the precise CDC calibration and the Monte Carlo calorimeter position calibration, it is possible to fine tune the calorimeter position using $Z \rightarrow ee$ collider data, with a $z_1 - z_2$ minimization procedure similar to that used in the dimuon CDC calibration (section 5.3.3). This was carried out by E. Flattum [62]. A correction of 0.002 in the calorimeter z scale was derived.

After correcting for the Z bias, the Monte Carlo sample was used to determine the position resolution. The Monte Carlo trajectory was extrapolated to the calorimeter EM3 layer and compared to the reconstructed position. Distributions of the true and reconstructed positions were made in bins of incident angle, θ, and

Parameter	Value (cm)
p_1	0.33183
p_2	5.2281×10^{-3}
p_3	4.1968×10^{-4}
p_4	7.5496×10^{-5}

Table 5.2: Parameters describing calorimeter cluster position resolution.

z position. The resolution was parametrized as

$$\sigma(z) = (p_1 + p_2\vartheta) + (p_3 + p_4\vartheta) \cdot |z| \tag{5.14}$$

where $\vartheta = \pi/2 - \theta$ and the parameters are shown in table 5.2.

5.3.5 Resolution of CDC track centroid position

The CDC track centroid position resolution has been determined directly from the $Z \rightarrow ee$ data. Both electrons from the $Z \rightarrow ee$ decay can be used to determine vertex positions for the event, z_1 and z_2. The best resolution on the event vertex is achieved by taking the vertex to be $(z_1 + z_2)/2$. The difference $z_1 - z_2$ provides a direct measure of the angular resolution. Since both electron must come from the same decay vertex, $z_1 - z_2 = 0$ for perfect angular resolution. Having determined the calorimeter shower centroid position resolution from detailed GEANT simulations, the CDC position resolution can be measured by comparing CMS Monte Carlo predictions of the $z_1 - z_2$ distribution to the measured $z_1 - z_2$ distribution for a range of hypotheses for the CDC z resolution. The simplest hypothesis is that the CDC z resolution is gaussian. However, the $z_1 - z_2$ distribution for the data shows small tails not well modelled by a gaussian CDC resolution. To correct for this, a double gaussian model was used. A fixed "tail" component of width 1.556% was applied for 6% of the tracks. The width of the "core" component was allowed to float, and a maximum likelihood fit was performed to the $z_1 - z_2$ spectrum. The result was $\sigma(z_{CDC}) = (0.27 \pm 0.02)$cm. It turns out that all the W mass fits are insensitive to the values of the CDC or CAL z resolutions. A nice feature of the procedure used to determine the CDC and CAL z resolutions is that any systematic error in the CAL resolution from inadequacy of the GEANT modelling is automatically compensated for by a cancelling error in the CDC resolution, so that the correct overall angular resolution is obtained. The limit on the angular resolution measurement is the statistics of the Z sample.

5.4 Energy Measurement

5.4.1 Response model

The reconstructed electron energy depends on the underlying event leakage into the electron shower and the intrinsic electromagnetic response of the calorimeter. The underlying event correction to the electron energy is described in section 6.4. Based on the test beam analysis we adopt a response model for electromagnetic clusters in which the true and measured energies are linearly related

$$E^{\text{true}} = \alpha E^{\text{meas}} + \beta \tag{5.15}$$

where α is the EM energy scale and β an energy offset. An offset can occur for several reasons, such as underlying event or energy loss in upstream material. The fractional deviation of the test beam data from this response model is illustrated in figure 5.8. The model works very well for $p_T > 10$ GeV or so, which is the region of interest for W and Z events. The lower p_T region is however important for the analysis of the low energy J/ψ and π^0 resonances. The electron clusters from J/ψ decays have a mean energy of about 5 GeV, while the electrons from the π^0 conversions are typically about 2 GeV. Note that the relatively large fractional deviations occur only at very low energies, so that, for example, the fractional deviation of 0.05 at momentum 3 GeV corresponds to a deviation of only 150 MeV.

This uncertainty in the low energy response can be absorbed into an uncertainty in the effective offset, β, relevant to the high p_T electrons from W and Z decays. The low energy response uncertainty dominates the error in determination of the offset.

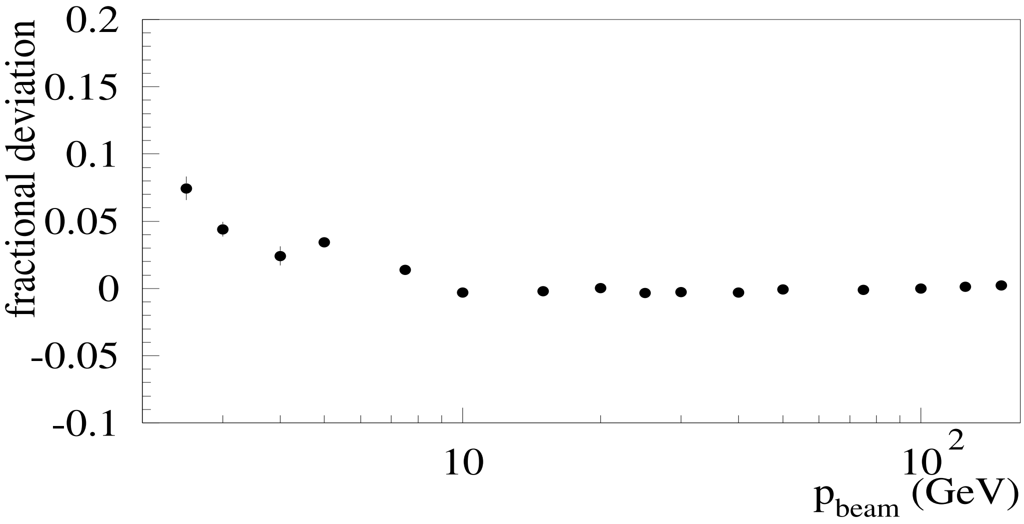

Figure 5.8: Deviation of test beam data from linear response model.

5.4.2 Binned Z method

The electrons from Z decays span a range of energies. The effect of an offset vs. a scale is reflected in the relative effect as a function of energy. If an electron with true energy E is measured as $\tilde{E}$ where

$$\tilde{E} = \alpha E + \beta \tag{5.16}$$

then the true and measured invariant masses of a Z event M and $\tilde{M}$ are related by

$$\tilde{M} = \sqrt{2\tilde{E}_1\tilde{E}_2(1 - \cos\gamma)} \tag{5.17}$$

where γ is the opening angle between the electrons. Substituting and Taylor expanding gives

$$\tilde{M} = \alpha M + f\beta \tag{5.18}$$

where

$$f = \frac{(\tilde{E}_1 + \tilde{E}_2)(1 - \cos\gamma)}{\tilde{M}} \tag{5.19}$$

The factor f can be thought of as the derivative of the measured mass with respect to an offset

$$f = \frac{\partial\tilde{M}}{\partial\beta} \tag{5.20}$$

For dielectron events it is possible to compute f for each event. From the linear relation $\tilde{M} = \alpha M + f\beta$ we can determine both α and β by fitting the Z mass in bins of f. This technique is called the "binned Z method." Figure 5.9 shows the $M(ee)$ vs. f distribution for the Z data.

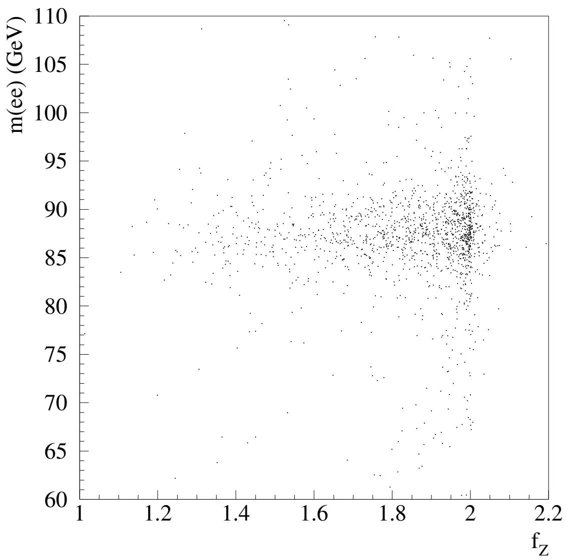

Figure 5.9: The $M(ee)$ vs. f distribution for $Z \rightarrow ee$ candidates.

5.4.3 π^0 decays

The π^0 is one of the lightest hadrons. Its mass has been accurately measured at 134.9743±0.0008 MeV [24]. It is copiously produced in $p\bar{p}$ collisions. The π^0 decays into two photons with a branching fraction of about 99%. At DØ, π^0 candidates are expected to appear as electromagnetic clusters. Since the reconstruction threshold for photon candidates is 1.5 GeV, which is much greater than the π^0 mass, the π^0 must be produced with $p_T > 1.5$ GeV in order to be reconstructed as clusters. At these momenta the separation between the two photons is small, so that they are merged into a single cluster. To reconstruct a mass peak for the π^0 it is necessary to know the opening angle of the $\gamma\gamma$ system. This was accomplished [70, 71] by requiring both decay photons to convert before the CDC, so that the two conversion tracks could be identified in the CDC by their ionization. The conversion tracks provide a measurement of the opening angle. It is not possible to partition the cluster energy into the energies of the two photons, however it is possible to define a mass–like quantity, called "symmetric mass", which is the invariant mass computed as if the two photons had shared the cluster energy equally

$$m_{sym} = \sqrt{\frac{E^2(1 - cos\alpha)}{2}} \tag{5.21}$$

where α is the opening angle between the photons. The symmetric mass lineshape is asymmetric. Without smearing m_{sym} always exceeds the invariant mass.

The π^0 candidate sample consists of electromagnetic clusters with two associated tracks, where the tracks were required to be consistent with photon conversions. When a photon with several GeV of momentum converts, the conversion $\gamma \rightarrow e^+e^-$ consists of two tracks separated by a very small distance. To the tracking reconstruction it looks exactly like a single particle, but the ionization is larger than that of a single MIP. Therefore, each track was required to satisfy $dE/dx > 1.0$ and at least one of which satisfies the $dE/dx > 1.5$, in units where the ionization for a single minimum ionizing particle (MIP) is 1.0. The clusters were also required to satisfy fiducial requirements similar to those imposed on electrons from W and Z decays. The spectrum of m_{sym} observed is shown in figure 5.11.

The background m_{sym} shape was determined using clusters with two associated tracks where both tracks had $dE/dx < 1.0$, with the usual fiducial cuts. The background shape is shown superimposed on figure 5.11. Also shown is the m_{sym} distribution with background subtracted.

To fit the π^0 mass, the m_{sym} lineshape was modelled using a specialized fast Monte Carlo program. The program

- modelled the observed E_T and η distributions
- required the π^0 to be away from the CC cracks
- performed the $\pi^0 \rightarrow \gamma\gamma$ decay isotropically in the π^0 rest frame
- implemented a parametrized reconstruction efficiency as a function of energy
- simulated calorimeter response and offset

- implemented smearing for the track direction and cluster energy

- simulated a $\gamma\gamma$ opening–angle dependent efficiency

To determine the calorimeter response appropriate for W and Z decays, the η distribution of the π^0 sample was reweighted to match that of the Z sample. The fit to the resulting weighted m_{sym} distribution yielded $m_{\pi^0} = 135.4 \pm 3.8$ MeV. The f factor for the π^0 fit was measured to be 0.03.

The contour in the (α, β) plane allowed by the π^0 data is shown as the solid, steep contour in figure 5.14. The slope of the contour is set by the average f for the resonance. For small f the contour is very steep. For comparison, the contour in the (α, β) plane allowed by the J/ψ analysis described in the next section is shown as the dotted, steep curve in figure 5.14. The J/ψ resonance has $f = 0.56$, so that it is somewhat less steep than the π^0 contour.

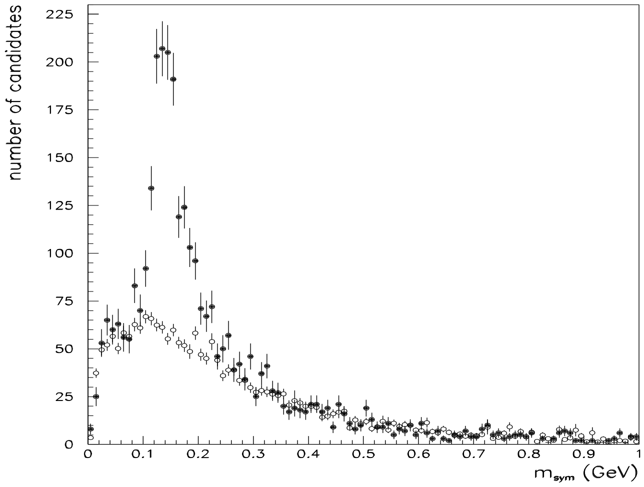

Figure 5.10: Symmetric mass distribution for π^0 signal and background samples

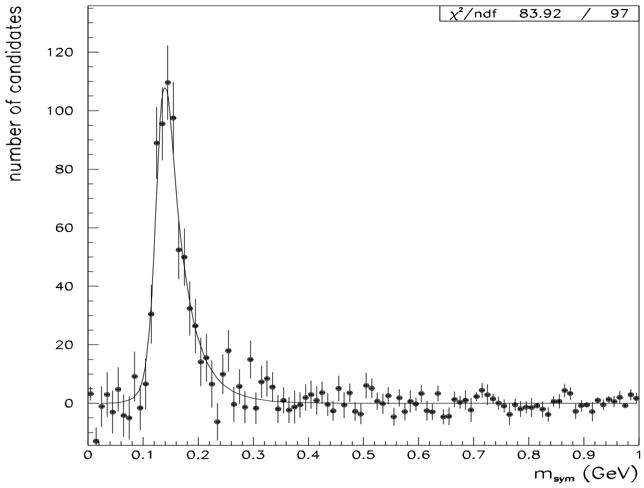

Figure 5.11: Background subtracted π^0 symmetric mass distribution with Monte Carlo fit overlaid.

5.4.4 $J/\psi \to ee$ decays

The J/ψ resonance has been very precisely measured and has a negligible width compared to the resolution at DØ. The PDG values are [24]:

$$M_{J/\psi} = (3.09693 \pm 0.00009)\,\mathrm{GeV} \tag{5.22}$$

$$\Gamma_{J/\psi} = (86 \pm 6)\,\mathrm{keV} \tag{5.23}$$

The J/ψ decays to an e^+e^- pair with a branching fraction of 6.3%. These decays provide an excellent signal for the electromagnetic response calibration. The J/ψ is produced in $p\bar{p}$ collisions via several processes, including B hadron decays, intermediate χ_c states, and fragmentation. In all cases the cross section is largest for low $p_T(J/\psi)$. However, the electrons from a J/ψ with zero transverse momentum have a maximum p_T of 1/2 the J/ψ mass, or about 1.5 GeV. At this very low p_T there is a very large background from QCD processes. Therefore at the trigger level two electromagnetic candidates with transverse energy greater than 3 GeV were required. This significantly reduced the J/ψ cross section, since only events with $p_T(J/\psi)$ above 5 GeV can pass this cut. For $p_T(J/\psi) > 5$GeV the cross section for either the χ_c or B mechanisms is about 200 nb, so that the total cross section times branching ratio for the two processes is 30 nb. At the time of this analysis the contribution from fragmentation processes was controversial. Approximately 100

nb^{-1} were collected with the low trigger thresholds in special runs. Very tight cuts were necessary to extract a signal from the very large QCD background, so that the efficiency was very low. The resulting invariant mass distribution is shown in figure 5.13. The J/ψ resonance is evident, with a statistical significance of about 6 standard deviations. The lower plot shows a two–dimensional fit to the mass and width of the peak. The fitted width is 115 ± 25 MeV, consistent with the width of 140 MeV expected from Monte Carlo studies. The number of events in the peak is about 25. The efficiencies for low energy electrons are difficult to determine, but from Monte Carlo studies the number of events observed was expected to be between 5 and 50, in rough agreement with the observed peak of about 25 events. The background shape was determined from clusters with no tracks, expected to be dominated by π^0 and η decays to photons. The background shape was checked using clusters with doubly ionizing tracks, indicating photon conversions. In both cases no peak was observed in the neighborhood of the J/ψ. The background normalization was determined independently of the mass fit and found to be in good agreement with the result of the fit. The details of this analysis can be found in reference [72].

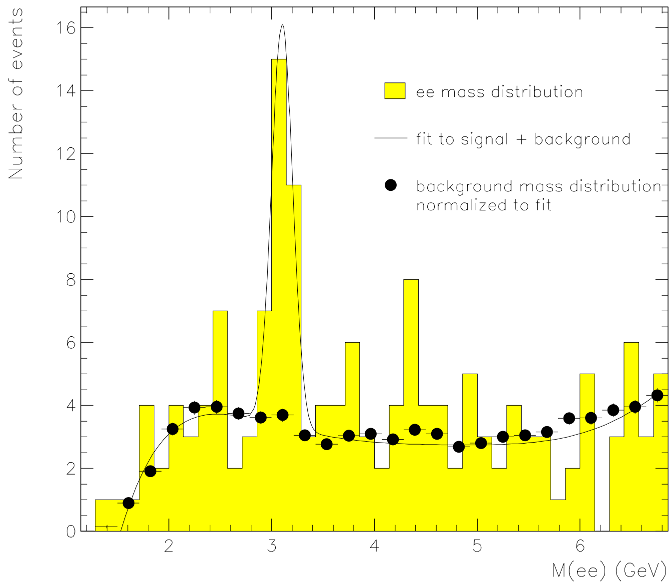

Figure 5.12: Fit to the observed dielectron invariant mass spectrum around the J/ψ resonance.

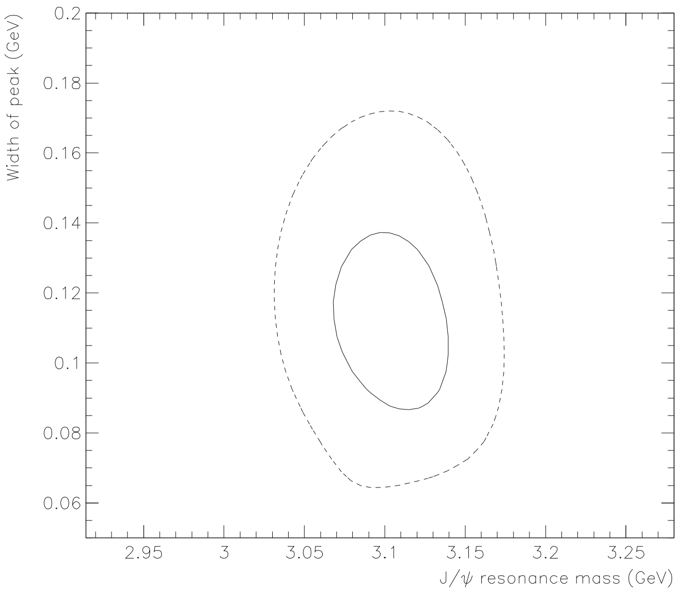

Figure 5.13: Contours for the 68% and 95% confidence level limits for the mass and width of the J/ψ peak. The width is due to detector resolution.

5.4.5 Combined constraint from Z, J/ψ and π^0 data

Figure 5.14 shows the constraints on the electromagnetic response in the (α, β) plane for the binned Z, the π^0 and the J/ψ separately, as described in the previous sections. These constraints from the Z, J/ψ and π^0 data can be combined [73] simply by adding the χ^2 contributions

$$\chi^2_{\mathrm{TOT}}(\alpha, \beta) = \chi^2_{\mathrm{Z}}(\alpha, \beta) + \chi^2_{J/\psi}(\alpha, \beta) + \chi^2_{\pi^0}(\alpha, \beta) \tag{5.24}$$

The small solid contour shows the combined constraint, with all errors except that from the test beam low energy response. The test beam low energy response dominates the systematic error. Including this error, the final result is

$$\beta = -0.16^{+0.03}_{-0.21}\,\mathrm{GeV} \tag{5.25}$$

It is significant that the constraints from the three independent data samples overlap in the (α, β) plane.

After correcting for the offset, the Z mass fit sets the energy scale. Figure 5.15 shows the data and best fit simulation and the likelihood curve. The Kolmogorov–Smirnov probability that the data and simulation are from the same parent distribution is 63%. The fitted energy scale is $\alpha_{CC} = 0.95329$.

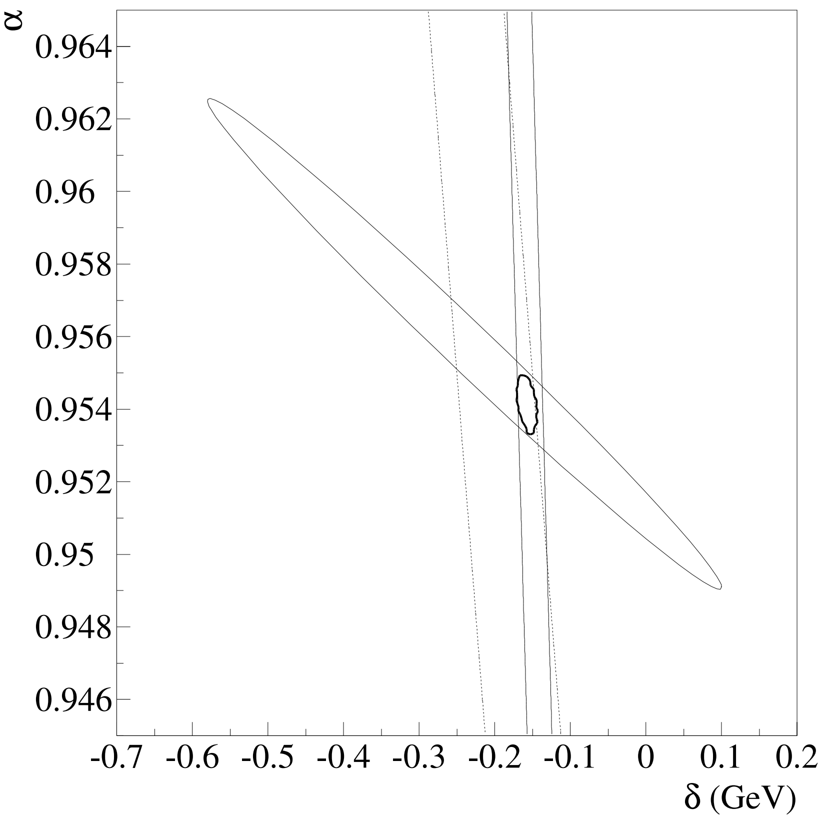

Figure 5.14: Combined energy scale constraint from the Z, J/ψ and π^0 data.

5.5 Electron Energy Resolution

The electron energy resolution is measured from the observed width of the Z. The observed width has contributions from both the Breit–Wigner width and the detector resolution. The Breit–Wigner width is very accurately known from LEP. The detector component is dominated by the energy resolution, though the angular

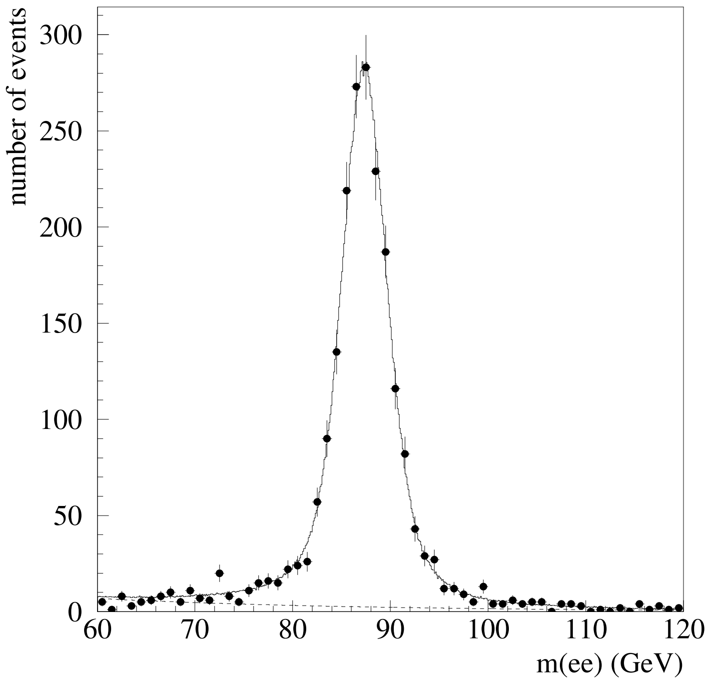

Figure 5.15: Z mass fit after offset correction.

resolutions also contribute. The energy resolution can be written as

$$\sigma(E) \quad = \quad c_{EM}E \oplus s_{EM}\sqrt{\frac{E}{\sin\theta}} \oplus n_{EM} \tag{5.26}$$

The third term is a noise contribution from uranium and electronics noise and underlying event fluctuations. The distribution is taken from the $W\rightarrow e\nu$ data, using a procedure described in detail in section 6.4. The second term is a sampling term, which originates in the partial sampling of the shower. This term is set by the relative depths of absorber and active material, and has been measured in the test beam. The first term is called the constant term. It is due to systematic position or time dependent calibration errors. This term is used to parametrize the electron energy resolution.

To determine the constant term c_{EM}, Monte Carlo Z experiments were generated with c_{EM} between 0% and 1.6%. The predicted invariant mass distribution for each experiment was fit with a simple Breit–Wigner convoluted with a gaussian. The Breit–Wigner width was fixed, but the gaussian width was allowed to float. The fitted gaussian width gives a measure of the average experimental resolution for the invariant mass, $\sigma(M_Z)$. The data was fit in the same way, including an exponential background contribution. The fit is shown in figure 5.16. This simple fit models the spectrum well. Figure 5.16 shows the predicted $\sigma(M_Z)$ vs. c_{EM} for the Monte Carlo experiments. The value of $\sigma(M_Z)$ fitted from the data with its errors is superimposed as the horizontal lines. From this we can read off the constant term

$$c_{EM} = 1.15^{+0.27}_{-0.36}\% \tag{5.27}$$

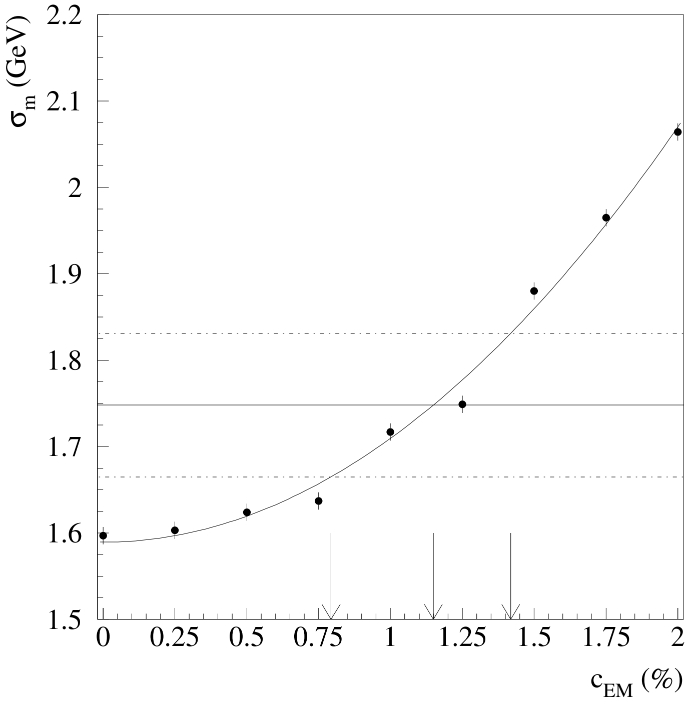

Figure 5.16: Predicted $\sigma(M_Z)$ vs. c_{EM} for data and Monte Carlo. (Plot from E. Flattum.)

Chapter 6

Recoil Measurement

The recoil measurement is of secondary importance to the W mass measurement from the electron E_T fit. The recoil affects the result only because it is necessary to cut on the recoil and on $\not\!\!E_T$ to identify the W events, and through the $u_{||}$ efficiency, which is a topological selection efficiency, which depends on how close the recoil is to the electron and how energetic the recoil. Many of the final details of the tuning of the recoil model have been performed by E. Flattum [2] and U. Heintz. In these cases the methods are described here for completeness and the origin indicated.

6.1 Reconstruction Algorithm

The hadronic recoil vector is reconstructed by simply summing the transverse momentum vectors of all the cells in the calorimeter excluding those cells assigned to the electron. Muons are not included in the p_T sum. The DØ calorimeter is almost hermetic, since successive layers of the calorimeter are staggered such that no particle can entirely escape through a crack. The cracks in the electromagnetic layer point to the module centers of the fine hadronic layer. In the intercryostat regions between the central and end calorimeters there is a scintillator inter–cryostat detector, or ICD. The calorimetry extends to rapidities of $\approx \pm 4.5$, so that even very energetic particles can escape down the beampipe with only a small amount of transverse energy. An absolute upper limit on the E_T lost down the beampipe for an event at the nominal vertex is given by

$$E_T^{max} = E_{CM}/2\cosh\eta \approx E_{CM}e^{-\eta} \approx 20\,\mathrm{GeV} \tag{6.1}$$

In practice this limit does not occur in hard scattering events, since it only occurs for a final state particle with all the energy of either the proton or antiproton. In the present analysis, the reconstructed recoil vector fails to include energy losses from particles lost down the beampipe as well as muons, which are produced occasionally in the hadronization process. These missing particles therefore contribute to the resolution of the recoil vector measurement. These effects are compensated for by the use of collider minimum bias events in the resolution model and the use of the $Z \rightarrow ee$ sample to tune the detector simulation.

6.2 Hadronic Scale

The response of the calorimeter to the hadronic recoil differs from the response to objects which shower electromagnetically. This difference occurs because the hadronic calorimeter modules are physically distinct from the electromagnetic modules, and because the processes by which hadrons interact in material are different from electron and photon interactions.

The response of the calorimeter to single pions was studied in the test beam. In principle, if one knew the particle composition of the recoil it would be possible to simulate the overall response. However, this approach suffers from two defects. Firstly, there is no reliable model to estimate from first principles the particle composition of the recoil system. Secondly, many of the recoil particles are of low momentum, less than the lowest momentum pions studied in the test beam.

However, it is possible to determine the hadronic response directly from $Z \rightarrow ee$ data, by comparing the P_T^Z measured from the electron pair to that measured from the hadronic system. The particle distributions in the W and Z recoil distributions should be very similar, so that by averaging over configurations in the Z sample we expect to derive a picture of the hadronic response which closely approximates that of the W sample.

To perform this comparison it is useful to use a pair of coordinate axes in the transverse plane which depend only on the electron directions, and not the momenta. The η axis, which is unrelated to pseudorapidity, is defined as the inner bisector of the two electron transverse momentum directions. The ξ axis is perpendicular to the η axis. The projections of various transverse momenta $\vec{P}_T$ onto these axes are labelled by subscripts, so that

$$\vec{P}_T = P_\eta \hat{\eta} + P_\xi \hat{\xi} \tag{6.2}$$

The P_T^Z measured from the electron pair is denoted p_T^{ee}, and the same physical P_T^Z measured from the hadronic system is denoted u_T. The projections onto the η and ξ axes are therefore called $p_{T\eta}^{ee}$, $u_{T\eta}$, $p_{T\xi}^{ee}$ and $u_{T\xi}$. These definitions are illustrated in figure 6.1.

The η projections of the recoil are minimally sensitive to the electron energy resolution, so we can best understand the hadronic response by comparing $p_{T\eta}^{ee}$ with $u_{T\eta}$. The true momentum vectors of the dielectron and hadron systems are equal and opposite by momentum conservation. Therefore, if the hadron and electron

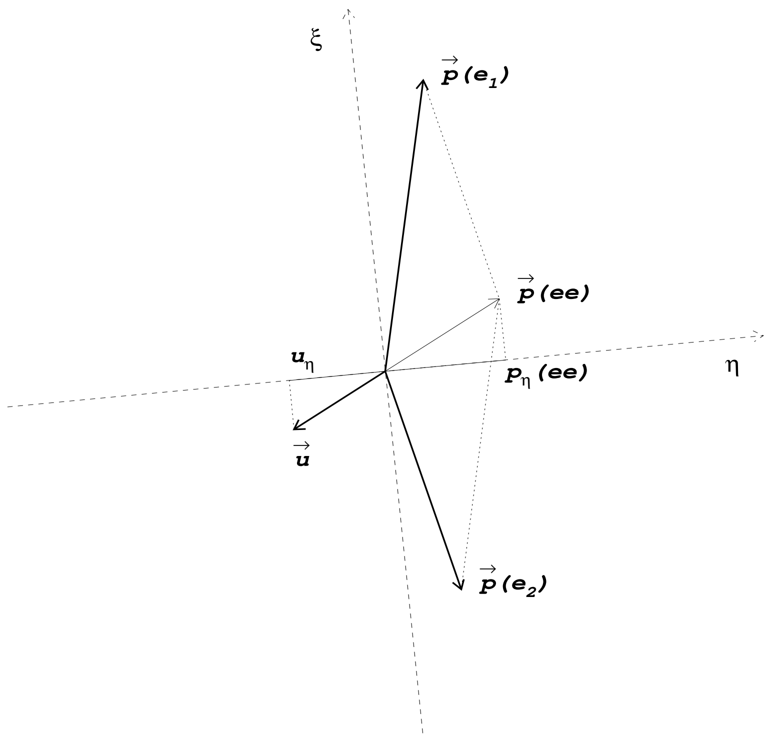

Figure 6.1: Illustration of definitions of the η and ξ axes. (Diagram from U. Heintz.)

responses were equivalent $p_{T\eta}^{ee} + u_{T\eta}$ would be zero on average. A relative scale α_{HAD} would cause a slope of approximately $1 - \alpha_{HAD}$ in the plot of $p_{T\eta}^{ee} + u_{T\eta}$ vs. $p_{T\eta}^{ee}$. This plot is shown in figure 6.2. There is a distinct slope of approximately 0.2, indicating that the average hadronic response for the Z recoil system is is suppressed relative to the electron response by about 20%. No significant deviation from linearity is observed. The intercept is consistent with zero. It is therefore reasonableto assume a model for the hadronic response in which the reconstructed recoil vector is proportional to the true recoil vector

$$p_T^{meas} = \alpha_{CC}\alpha_{HAD}p_T^{true} \tag{6.3}$$

Simply fitting the η balance with a straight line gives a good approximation to the hadronic response relative to the electron response. However, small corrections are necessary due to the underlying event removed from the electron windows. To account for this effect, the mean η balance vs. $p_{T\eta}^{ee}$ for the Z data is compared directly to the Monte Carlo prediction as a function of α_{HAD}. The Monte Carlo simulation includes the electron removal effect. The χ^2 is given by

$$\chi^2(\alpha_{HAD}) = \sum_{i=1}^{N}\left(\frac{\langle p_{T\eta}^{ee}+u_{T\eta}\rangle_i^{data} - \langle p_{T\eta}^{ee}+u_{T\eta}\rangle_i^{MC}(\alpha_{HAD})}{\sigma(p_{T\eta}^{ee}+u_{T\eta})_i}\right)^2 \tag{6.4}$$

where the sum is over bins $i = 1\ldots N$ in $p_{T\eta}^{ee}$. Minimization of the χ^2 with respect to α_{HAD} yields

$$\alpha_{HAD} = 0.78 \pm 0.015 \tag{6.5}$$

For the determination of α_{HAD}, the Z sample used includes those events in which one of the electrons is in an endcap calorimeter. This allows the event topology to more closely mimic that of the W case in which the neutrino rapidity is unrestricted. However, a consistent result is obtained when the Z sample is restricted to the central–central topology. Events which could be affected by main ring losses are removed.

This linear response model has been used as the baseline scheme for most systematic studies quoted in this thesis. However, for the final mass fits a more sophisticated two parameter log–response model has been implemented. In this model the response $\mathcal{R}_{rec}$, defined as the mean ratio of measured to true recoil, is given by

$$\mathcal{R}_{rec} = \alpha_{rec} + \beta_{rec} \log P_T \tag{6.6}$$

This functional form has been motivated by studies of HERWIG Monte Carlo events with GEANT detector simulation, in which the response can be measured directly. Figure 6.5 shows the GEANT response with a fit to the log model. The fit yields $\alpha_{rec} = 0.713 \pm 0.006$ and $\beta_{rec} = 0.046 \pm 0.002$, with a χ^2 of 23/28. The log model also agrees qualitatively with the jet response measured using jet–photon balancing, in which

$$\mathcal{R}_{jet} = \alpha_{jet} + \beta_{jet} \log E + \gamma_{jet} (\log E)^2 \tag{6.7}$$

For 0.7 cone jets the data gives $\alpha_{jet} = 0.6340$, $\beta_{jet} = 0.0642$ and $\gamma_{jet} = -0.0035$. The QCD Monte Carlo gives $\alpha_{jet} = 0.7126$, $\beta_{jet} = 0.055$ and $\gamma_{jet} = -0.0042$. In either case the γ_{jet} term is irrelevant for the low p_T regime appropriate for the W

and Z events used in the mass measurement. In any case, the W and Z recoil systems are not completely equivalent to single jets. Nevertheless, there is some similarity and so it is not unreasonable that the recoil response and jet response should have similar functional forms.

To determine the recoil log response model parameters, a χ^2 minimization simliar to that for the linear model was performed by U. Heintz. The $\eta-$balance plot was generated for the Z data. The same plot was generated using CMS for a range of $(\alpha_{rec}, \beta_{rec})$ pairs and for each pair a χ^2 between data and Monte Carlo was calculated. This analysis yields a correlated $(\alpha_{rec}, \beta_{rec})$ measurement. The one standard deviation contour is shown in figure 6.3. The $\eta-$balance plot for the data and the best fit Monte Carlo is shown in figure 6.4. The best fit is $\alpha_{rec} = 0.693 \pm 0.060$, $\beta_{rec} = 0.040 \pm 0.021$ with a χ^2 of 5/8. A correlated error analysis yields errors of 16 MeV, 20 MeV and 46 MeV for the E_T^e fit, M_T^W fit and $\not{E}_T$ fit respectively.

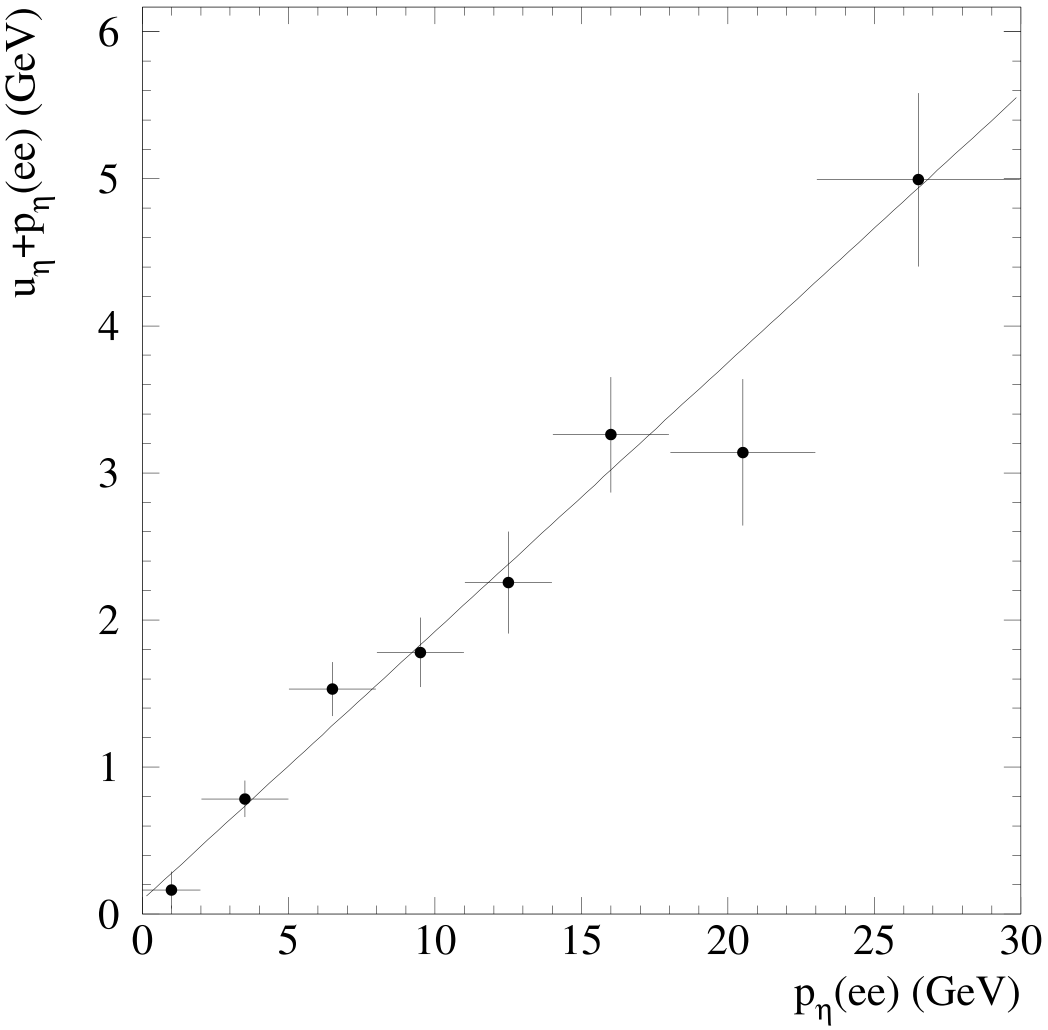

Figure 6.2: Hadron vs. dielectron η balance. (Plot from U. Heintz.)

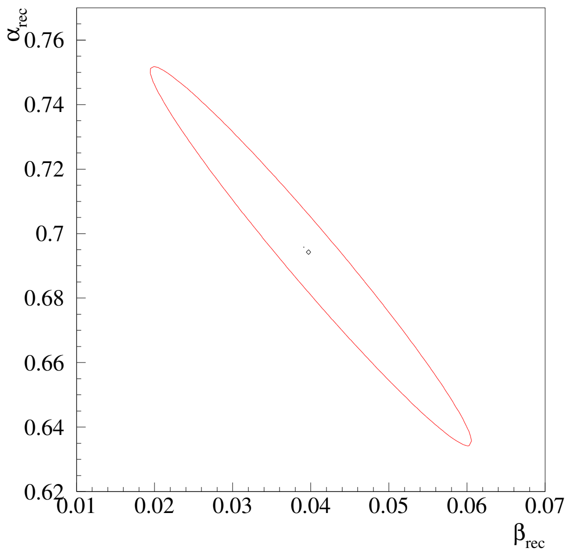

Figure 6.3: Recoil response constraint from $Z \to ee$ data for the log response model.

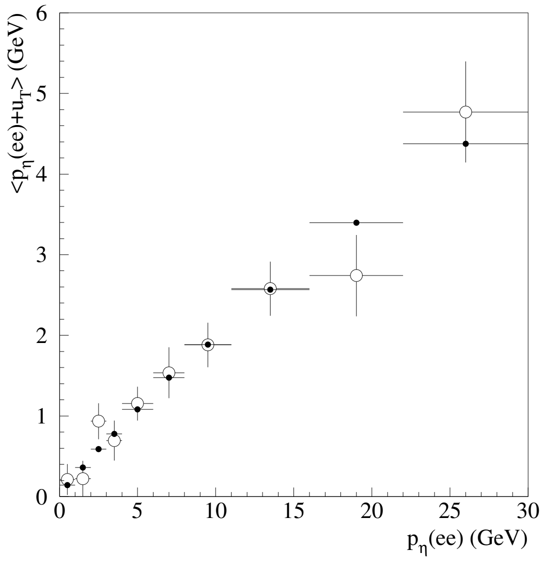

Figure 6.4: Recoil response $\eta-$balance plot for the $Z \to ee$ data and the best fit Monte Carlo

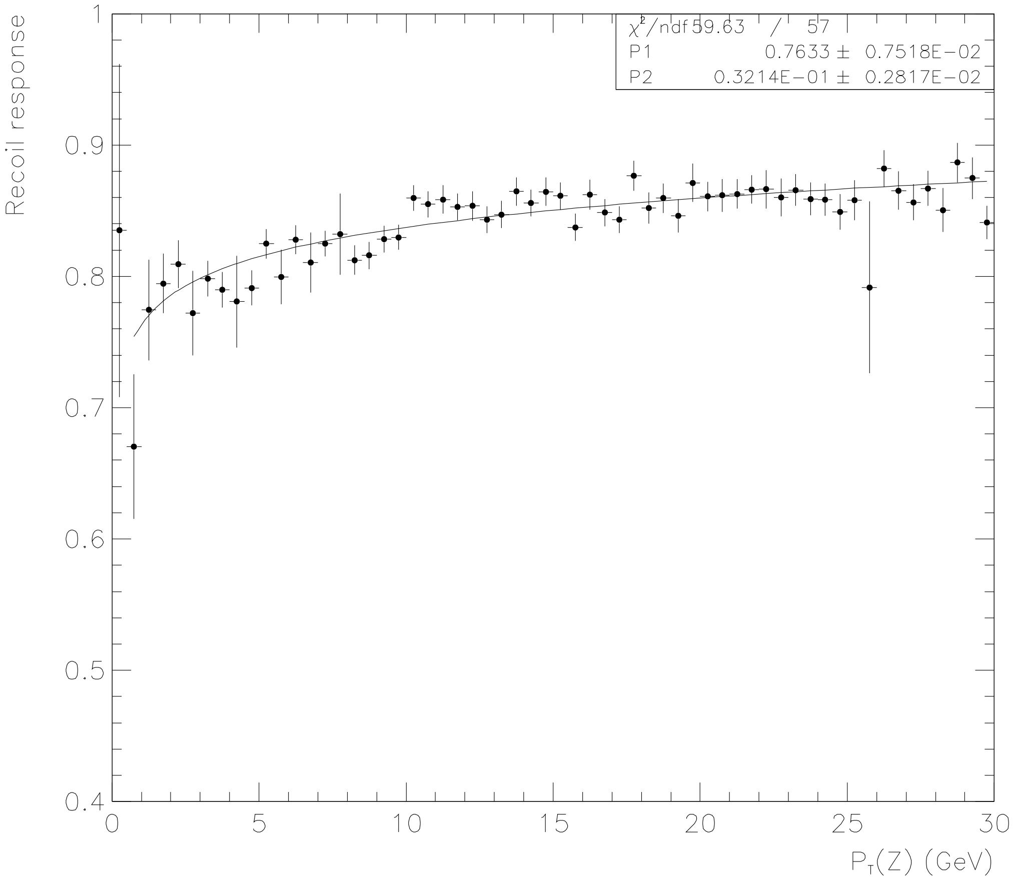

Figure 6.5: Hadronic response from HERWIG with GEANT simulation.

6.3 Hadronic Resolution

Since the recoil is measured using a sum over the entire calorimeter, the hadronic resolution receives contributions from every process which affects the calorimeter. These processes include electronics and uranium noise, pileup, multiple interactions, the W or Z underlying event and the recoil system itself. Clearly the modelling of all these processes from, for example, a GEANT based simulation would be very difficult. However, it is possible to finesse the problem by using collider data directly.

The effects of noise, pileup and multiple interactions are coupled together and are luminosity dependent. In principle it is possible to model these effects using, for example, the NOISY program. However, a better model can be easily obtained using collider minimum bias events. Zero bias events are recorded using a trigger in which the detector is read out based only on the accelerator clock. Minimum bias events are a subset of the zero bias sample for which some minimal requirement is applied to select events in which there is an inelastic interaction, i.e., to reject empty beam crossings. At DØ a convenient definition for a minimum bias event is the requirement of coincident hits in the North and South level zero scintillators. Minimum bias events were recorded throughout both Run 1a and Run 1b to provide luminosity monitoring and a diagnostic event sample. Using minimum bias events over a range of luminosities allows a direct modelling of noise, pileup and luminosity dependent effects.

We adopt a model for the hadronic resolution in which there are two components. The "asymmetric" component smears the recoil p_T with a vector which is oriented parallel to the true recoil p_T, with a magnitude given by

$$\Delta u_T \quad = \quad (S_{HAD}\sqrt{u_T} \oplus C_{HAD}u_T) \cdot n(0,1) \tag{6.8}$$

where $n(0,1)$ is a Gaussian variable of zero mean and unit rms. The u_T vector has been scaled to reflect the hadronic response before the resolution is computed. A "symmetric" component adds a smearing vector to the recoil p_T which is randomly oriented in azimuth. Intuitively this component corresponds to the effects of noise, underlying event, pileup and multiple interactions, while the asymmetric component corresponds to the recoil jet. It should be kept in mind that the recoil system most frequently consists of a soft energy flow which is not readily identifiable as a jet. It may also be composed of more than one jet. In intermediate cases the recoil looks like a single jet. The model adopted here does not rely fundamentally on the assumption that the recoil consists of a single jet. It is always possible to split the resolution into symmetric and asymmetric components, since there is only one preferred direction, namely that of the recoil. The detailed modelling of the two components is based on a physical picture in which the recoil is analogous to a jet system, so that when averaged over the jet multiplicity and rapidity distributions its resolution can be modelled with the usual terms employed to model jet resolutions, possibly with parameters different from those appropriate for single jets. For single jets, the constant term determined from jet balancing studies was 4%, and the sampling term was 80%. For the case of the W recoil it is not necessarily true that the recoil parameters are equal to those appropriate for jets. Nevertheless we expect the parameters to be roughly similar. In the present analysis the W mass fit is performed with on a sample with $P_T^W < 15$ GeV. For a single jet, the contributions of the constant and sampling terms to the hadronic resolution at 15 GeV would be 0.6 GeV and 3.1 GeV respectively. From this we expect the sampling term to dominate over the range of interest. We therefore choose to fix the constant term to zero and measure the sampling term from Z data. The value of the constant term is largely irrelevant, since a mistake in the constant term is compensated for by the tuning of the sampling term with the Z.

6.3.1 Minimum Bias Library

The symmetric component of the resolution is modelled using minimum bias events. Since these events should not contain high p_T neutrinos, the $\not{E}_T$ vector distribution of minimum bias events is indicative of the resolution due to noise, pileup, fluctuations in the momentum measurements of the soft hadrons, energy losses down the beampipe, soft muons and neutrinos from pion and kaon decays in the underlying event.

In zero bias events at luminosity $\mathcal{L}$, the mean number of interactions $\bar{n}(\mathcal{L})$ is given by

$$\bar{n}_{zb}(\mathcal{L}) \quad = \quad \sigma t \mathcal{L} \tag{6.9}$$

where σ is the total inelastic cross section and t is the beam crossing time, which is 3.5μ s for the Tevatron. The product of the DØ acceptance and the inelastic cross section from the average of the CDF and E710 experiments is 48.2 mb.

The number of interactions in zero bias events follows a Poisson distribution, with the probability $\mathcal{P}$ of n interactions given by

$$\mathcal{P}(n) = \frac{n^{\bar{n}} e^{-n}}{\bar{n}!} \tag{6.10}$$

This obeys the requirements $\sum_{n=1}^{\infty} \mathcal{P}(n) = 1$ and $\sum_{n=1}^{\infty} n\mathcal{P}(n) = \bar{n}$. For minimum bias events the distribution is similar except that the $n = 0$ case does not occur, since at least one interaction is required. Therefore the distribution is

$$\mathcal{P}(n) = \begin{cases} \frac{n^{\bar{n}} e^{-n}}{\bar{n}!} \times \frac{1}{1-e^{-\bar{n}}} & n > 0 \\ 0 & n = 0 \end{cases} \tag{6.11}$$

The minimum bias distribution looks like the zero bias distribution with the zero bin removed and the other bins scaled up so that the overall normalization is kept at unity. The mean number of interactions at luminosity $\mathcal{L}$ is given by

$$\bar{n}_{mb}(\mathcal{L}) = \frac{\sigma t \mathcal{L}}{1 - e^{-\sigma t \mathcal{L}}} \tag{6.12}$$

For events for which the cross section is very small compared to the inelastic cross section, such as W events, there is at least one interaction from the W, while the distribution of additional interactions follows the zero bias distribution. The distribution for W events therefore looks like the zero bias distribution translated by one bin.

$$\mathcal{P}(n) = \begin{cases} \frac{(n-1)^{\bar{n}} e^{-(n-1)}}{\bar{n}!} & n > 0 \\ 0 & n = 0 \end{cases} \tag{6.13}$$

The mean number of interactions in a W event at luminosity $\mathcal{L}$ is given by

$$\bar{n}_W(\mathcal{L}) = 1 + \sigma t \mathcal{L} \tag{6.14}$$

These distributions are illustrated in figure 6.6

The W sample and the minimum bias sample have different event multiplicity distributions, though both are modified Poisson distributions with no zero interaction events. It is necessary to apply some procedure to account for this in using the minimum bias events to model the resolution. One method which has been used is luminosity matching. The luminosity distribution of the W sample is an input to the simulation. With each simulated event is associated an instantaneous luminosity $\mathcal{L}_W$. In the luminosity matching technique, a W event at luminosity $\mathcal{L}_W$ is smeared using the $\not{E}_T$ vector from a minimum bias event at a corresponding luminosity $\mathcal{L}_{mb}$ such that the mean number of interactions is the same, $\bar{n}_W(\mathcal{L}_W) = \bar{n}_{mb}(\mathcal{L}_{mb})$. This corresponds to picking a minimum bias event at a higher luminosity than the W, given by the solution to the implicit equation

$$\frac{\bar{n}(\mathcal{L}_{mb})}{1 - e^{-\bar{n}(\mathcal{L}_{mb})}} \quad = \quad 1 + \bar{n}(\mathcal{L}_W) \tag{6.15}$$

where $\bar{n}$ refers to the zero bias mean number of interactions. Figure 6.7 shows the result of solving this equation over the luminosity range of the W sample. In practice, it is most efficient to parametrize the solution with a polynomial

$$\mathcal{L}_{mb} \quad = \quad A_0 + A_1\mathcal{L}_W + A_2\mathcal{L}_W^2 + A_3\mathcal{L}_W^3 + A_4\mathcal{L}_W^4 \tag{6.16}$$

The coefficients A_i can be read off from figure 6.7. The luminosity matching procedure suffers from certain defects. The most important is that the event multiplicity distributions of the W sample and the luminosity matched minimum bias sample are simply different, though the mean multiplicity is the same. This implies that the shape of the resolution is not well modelled by the luminosity matched minimum bias events. Secondly, the matching procedure assumes that the efficiency of the W selection is independent of the number of additional interactions in the W event. The W selection can depend on the number of multiple interactions via the electron identification cuts or the efficiency of reconstructing the vertex correctly. In this case the mean number of interactions in the W events is modified to

$$\bar{n}(\mathcal{L}_W) = 1 + \sum_{i=0}^{\infty} \mathcal{P}(i) \cdot \varepsilon(i) \tag{6.17}$$

where $\varepsilon(i)$ is the efficiency for a W event with i additional interactions to survive selection criteria. Since no corresponding selection criteria are imposed on minimum bias events, there is no such modification to $\bar{n}(\mathcal{L}_{mb})$. Thirdly, by using minimum bias events at a different luminosity than the W, the effects of noise and pileup are distorted. Pileup widens the pedestal distributions of the calorimeter cells as the luminosity increases. This effect is not correctly modelled in the luminosity matching procedure since the minimum bias events are from a different luminosity distribution than the W events. A fourth problem is that the W events were taken at luminosities up to $20 \times 10^{30}\mathrm{cm}^{-2}\mathrm{s}^{-1}$. At this luminosity the equivalent minimum bias luminosity is about $25 \times 10^{30}\mathrm{cm}^{-2}\mathrm{s}^{-1}$, which is higher than the peak luminosity recorded. Hence the matching procedure is incapable of modelling high luminosity W events.

To overcome these problems an alternate method was devised. If there were a reconstructed variable f with the property that its spectrum depended on the event multiplicity, then the minimum bias sample could be reweighted such that its f distribution agreed with that of the W sample. One such variable available at DØ is the "multiple interaction flag," or MIFLAG, an integer variable with values 1,2,3 or 4, which refer to increasing probability of a multiple interaction. The primary information used to concoct the MIFLAG are the level zero timing and the number of reconstructed vertices. The MIFLAG distribution should be skewed towards low values (1 or 2) for low luminosity data and towards high values (3 or 4) for high luminosity data. This trend is observed. We choose therefore to reweight the MIFLAG distribution of the minimum bias events in luminosity bins to agree with the MIFLAG distributions for W events in the same bins. As expected, the minimum bias events with higher MIFLAG values are weighted higher than those with low values when this procedure is applied. This provides an alternative way of matching the event multiplicity distributions in the W and minimum bias samples. Any efficiency vs. event multiplicity for the W events is automatically taken into account. The W events at a given luminosity are modelled using minimum bias events at the same luminosity so that the noise and pileup contributions are correct. Minimum bias events are available in every luminosity bin, so it is possible to model the high luminosity W events consistently. This second technique is called the miflag–reweighted minbias library method.

In either case, having chosen a procedure for handling the luminosity dependence of the resolution, the model is tuned to the η balance width in the Z sample. To allow this tuning we scale the $\not{E}_T$ vector chosen from the minimum bias sample by a scale factor, α_{MB}, and choose α_{MB} so that the simulated η balance width for the Z events agrees with the observed Z data. Any mismodelling should therefore show up only as a luminosity dependence in the W mass fit, but should not cause an overall bias, since the Z sample was collected under the same conditions as the W sample. By tuning the resolution to the η balance width the analysis should be insensitive to the details of the modelling.

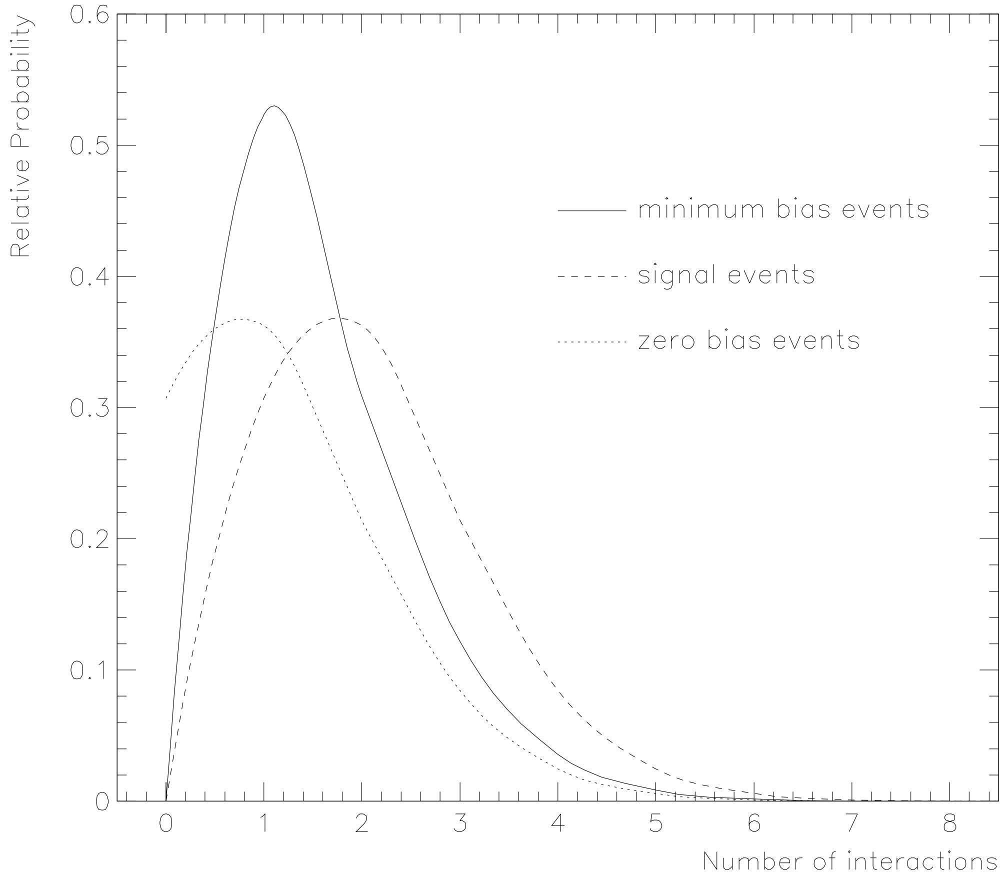

Figure 6.6: The distribution of number of interactions for zero bias, minimum bias and W events at an instantaneous luminosity $\mathcal{L}$ such that $\bar{n}_{zb}(\mathcal{L}) = 2$.

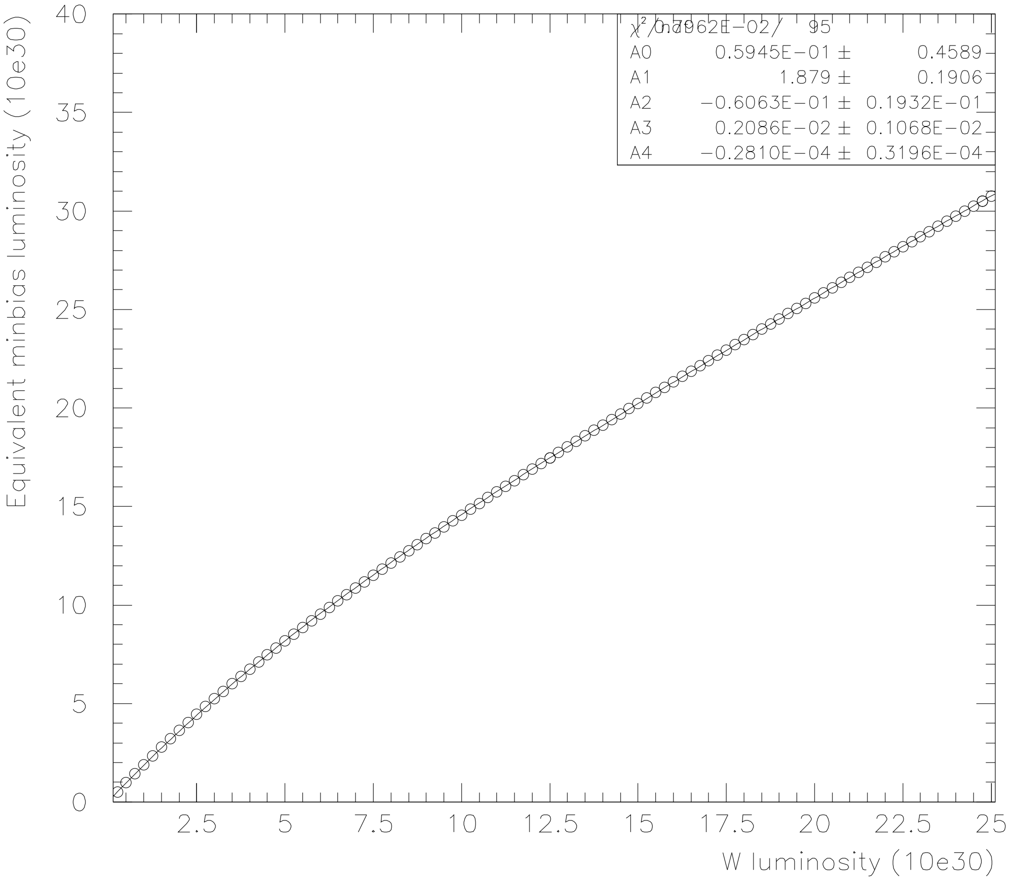

Figure 6.7: Mapping between equivalent luminosities for W events and minimum bias events.

6.3.2 Evaluation of α_{MB} and S_{HAD}

The minimum bias scale factor, α_{MB}, and the hadronic sampling term, S_{HAD}, are determined using the width of the distribution of $u_{T\eta}/\alpha_{HAD} - p^{ee}_{T\eta}$. The resolution of this quantity, called the η balance width, depends mainly on the hadronic resolution. The electron resolution is known from the Z invariant mass distribution and is a small contribution to the η balance width, partly because the electron resolution is intrinsically better than the hadron resolution and partly because of the choice of the η axis which minimizes the effect of the electron resolution.

It is possible to extract both α_{MB} and S_{HAD} from the η balance width using the fact that the resolution from α_{MB} is independent of p_T while the contribution from S_{HAD} increases with p_T. A simultaneous fit to the dependence of the η balance width on $p^{ee}_{T\eta}$ therefore can be used to obtain α_{MB} and S_{HAD}. For more details of this method see references [2, 1]. Figure 6.8 shows the components of the resolution, and the constraint on α_{MB} and S_{HAD}.

The optimal values measured from the $Z \rightarrow ee$ sample are

$$\alpha_{MB} = 1.032 \pm 0.028 \tag{6.18}$$

$$S_{HAD} = 0.49 \pm 0.14 \tag{6.19}$$

To determine the resolutions appropriate for the W events a further correction is necessary. Studies of the $\not\!\!E_T$ resolution from minimum bias events indicate that the resolution degrades with increasing scalar E_T, where the scalar E_T is simply the sum over all calorimeter cells of the cell E_T values. Figure 6.9 shows this relationship. In the W and Z events the corresponding quantity $\mathcal{S}_W$ or $\mathcal{S}_Z$ is the scalar E_T after removal of one or both electrons. The measured values are

$$\mathcal{S}_W = 98.8 \pm 0.3\,\mathrm{GeV} \tag{6.20}$$

$$\mathcal{S}_Z = 93.7 \pm 0.9\,\mathrm{GeV} \tag{6.21}$$

To correct for this difference, the α_{MB} value for the W events is set to 1.064 and for the Z events to 1.032, where the correction factor of 1.03 is based on the resolution vs. $\mathcal{S}$ function from the minimum bias events.

Samples of about 100,000 HERWIG W and Z events with GEANT detector simulation were checked. For these events we find no difference between $\mathcal{S}_W$ and $\mathcal{S}_Z$. It is reasonable to hypothesize that the difference between $\mathcal{S}_W$ and $\mathcal{S}_Z$ is due to the identification cuts imposed upon the second electron in the case of the Z. This has been checked explicitly by relaxing the identification cuts for one electron in the Z sample. For this sample, $\mathcal{S}_Z$ is consistent with $\mathcal{S}_W$. The effect of increased background in the loose sample was checked.

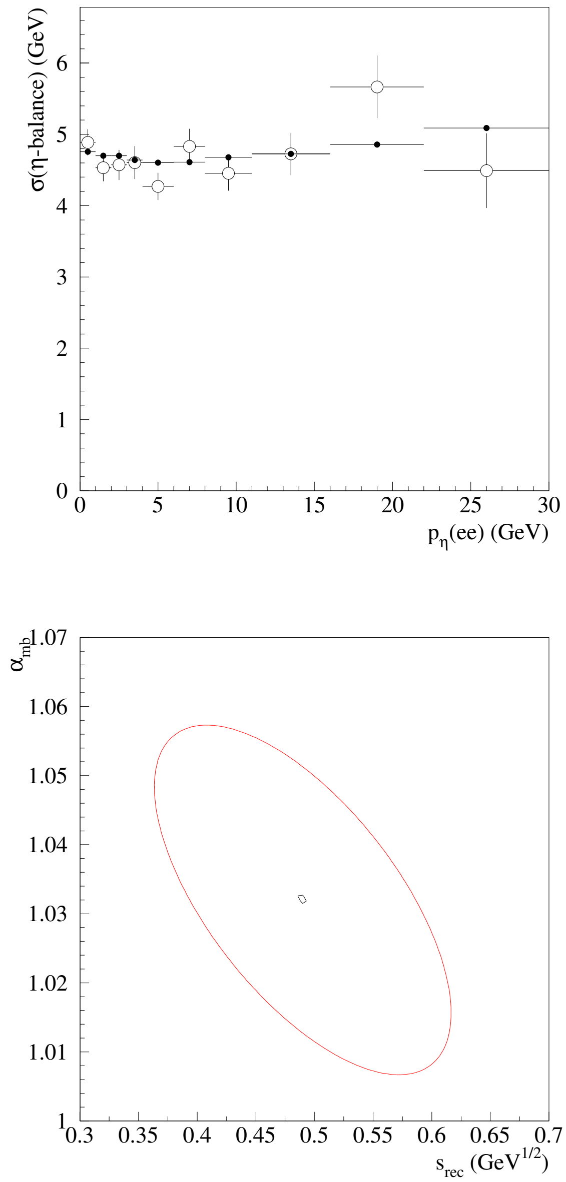

Figure 6.8: Constraint on α_{MB} and S_{HAD}. (Plots from U. Heintz.)

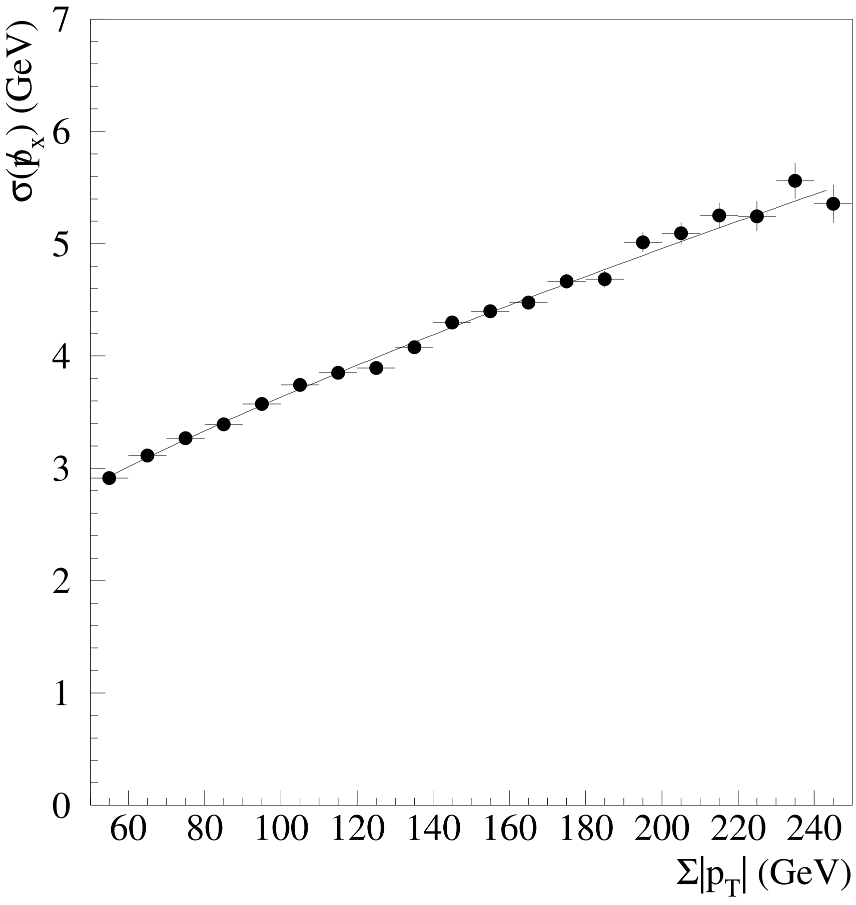

Figure 6.9: $\not{E}_T$ resolution from minimum bias events as a function of scalar E_T. (Plot from U. Heintz.)

6.4 Underlying Event Correction

The underlying event contributes energy to the electron since particles from the underlying event may overlap with the electron window. This tends to increase the electron energy. Also, since the electron window is excluded from the recoil sum, the underlying event energy in the electron window also biases the recoil measurement. Only the component of the recoil parallel to the electron direction is biased. We refer to this recoil component as $u_{||}$, and the bias is called the $u_{||}$ correction.

The $u_{||}$ correction has been determined using the W and Z data. The window in $\eta - \phi$ space used to measure the electron shower is rotated in azimuth away from the actual position. The energy flow into the rotated positions is due to noise and underlying event energy. For each rotated position an isolation variable is computed. Rotated positions for which the electron would have failed the isolation requirement if it had been there are rejected. This cut is necessary in order to remove rotated positions in which there is jet activity. Inclusion of these would bias the correction high since electrons close to jets are removed from the sample by the isolation requirement. The distribution of the energy flow into the rotated positions is shown in figure 6.10.

The $u_{||}$ correction has two important dependencies. Firstly, the energy flow into the electron window increases with luminosity because the mean number of interactions increases. Based on equation 6.14 we expect this dependence to be linear, with a slope proportional to the energy flow due to a single minimum bias interaction, and an intercept at $\mathcal{L} = 0$ representing the energy due to the W underlying event as well as fake energy due to uranium noise in the calorimeter. Figure 6.11 shows the observed luminosity dependence. The slope is 11.2 MeV per $10^{30}\mathrm{cm}^{-2}\mathrm{s}^{-1}$.

The second dependence is that the $u_{||}$ correction increases with $u_{||}$ itself. This occurs because the when the recoil gets close to the electron, more of the energy flow from the recoil is included in the electron window. This dependence is shown in figure 6.11. For negative $u_{||}$ the recoil is in the hemisphere opposite to the electron and there is no $u_{||}$ dependence. For positive $u_{||}$ the recoil is in the same hemisphere as the electron. As the recoil approaches the electron, $u_{||}$ becomes more positive and the correction increases. For large $u_{||}$, the correction does not increase further because of the isolation cut. This function has been parametrized with a polynomial.

The two dependencies are incorporated in the formula

$$\Delta u_{||} \quad = \quad \Delta + \langle \Delta u_{||} \rangle + \langle \Delta u_{||}(u_{||}, \mathcal{L} = 0) \rangle + 11.2 \frac{\mathrm{MeV}}{10^{30}\mathrm{cm}^{-2}\mathrm{s}^{-1}} \mathcal{L} \qquad (6.22)$$

where Δ is a random variable chosen from the distribution in figure 6.10.

The same distribution and dependences are used to model the underlying event contribution to the electron. For the electron it is necessary to account for zero–suppression effects. These are incorporated with a single overall correction Δ_{zs} so that the correction applied to the electron is

$$\Delta E_T(e) \quad = \quad \Delta u_{||} - \Delta_{zs} \tag{6.23}$$

The parameter Δ_{zs} has been determined by overlaying Monte Carlo electrons onto non–zero–suppressed minimum bias collider events to be $\Delta_{zs} = 212 \pm 25$ MeV.

The largest error in the $u_{||}$ correction is the isolation cut, because the denominator in the isolation fraction is the electron energy which is undefined at the rotated positions. To solve this problem an alternative analysis was carried out by U. Heintz [1]. In this analysis, the energy flow in a 1×5 slice in $\eta - \phi$ tower space was measured as a function of the azimuthal separation from the electron cluster centroid. The energy flow into the 1×5 slice falls rapidly as the slice center moves away from the electron center, and approaches a flat noise level. Scaling to a 5×5 window yields

$$\Delta u_{||}(W) \quad = \quad 479 \pm 2(stat) \pm 6(sys) \text{ MeV} \tag{6.24}$$

$$\Delta u_{||}(Z) \quad = \quad 468 \pm 7(stat) \pm 6(sys) \text{ MeV} \tag{6.25}$$

The systematic error is derived by comparing the noise level in the region $0.2 < |\Delta\phi| < 0.4$ with that in $0.4 < |\Delta\phi| < 0.6$. The first region is maximally biased by the isolation requirement while second lies outside the isolation cone. There is a small difference between the W and Z $u_{||}$ corrections, which is not in itself statistically significant. However, energy flow studies indicate that the total energy flow is somewhat higher in W events than Z events, because of the electron identification conditions on the second electron in the Z selection. Therefore we choose to use corrections derived from the W and Z events separately. The difference of 11 ± 7 MeV does not cancel out in the W/Z mass ratio, and dominates the error due to the underlying event correction.

6.5 $u_{||}$ Efficiency

As discussed in the previous section, the energy flow close to the electron increases as the recoil approaches the electron, and as the recoil becomes more energetic. This implies that the electron identification efficiency should depend on $u_{||}$, with decreasing efficiency as $u_{||}$ increases. This efficiency has been measured by superimposing GEANT simulations of single electron showers onto the W data. This procedure is described more fully in reference [74]. The transverse shape of the showers in the overlapped Monte Carlo electrons sample agrees very well with the electrons in the data. Figure 6.12 shows the measured $u_{||}$ efficiency. The efficiency vs. $u_{||}$ has been parametrized with a function of the form

$$\varepsilon(u_{||}) \propto \begin{cases} 1 & u_{||} < u_0 \\ 1 - s(u_{||} - u_0) & u_{||} > u_0 \end{cases} \tag{6.26}$$

For the fit we obtain $s = -0.013 \pm 0.010$ GeV^{-1} and $u_0 = 3.85 \pm 0.55$ GeV.

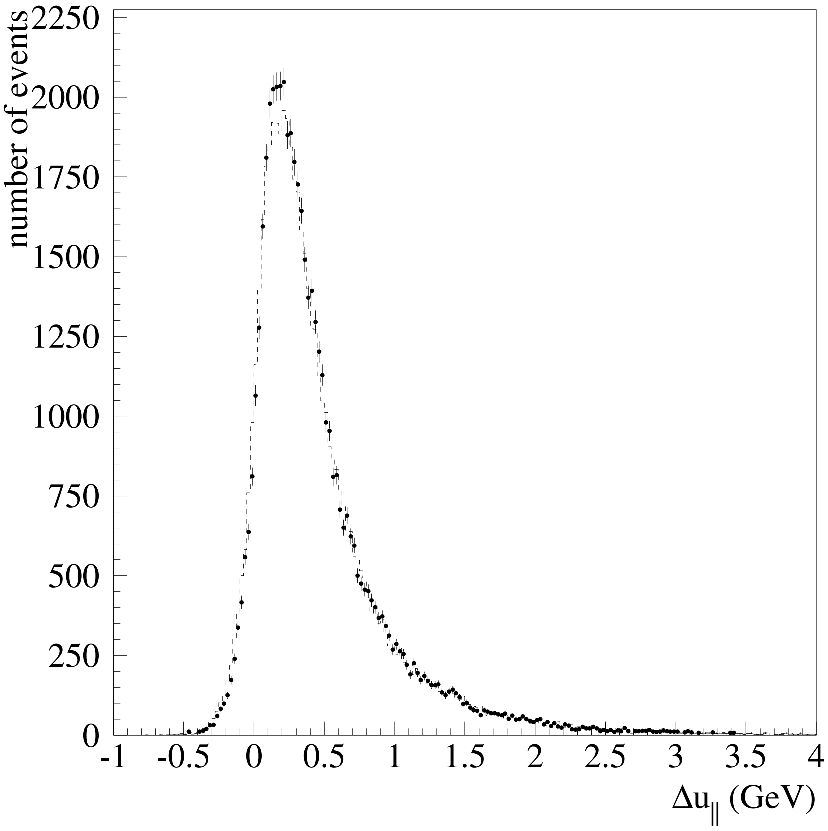

Figure 6.10: Distribution of energy in rotated windows in $W \to e\nu$ events. The points are the data and the dotted line the CMS simulation. (Plot from U. Heintz.)

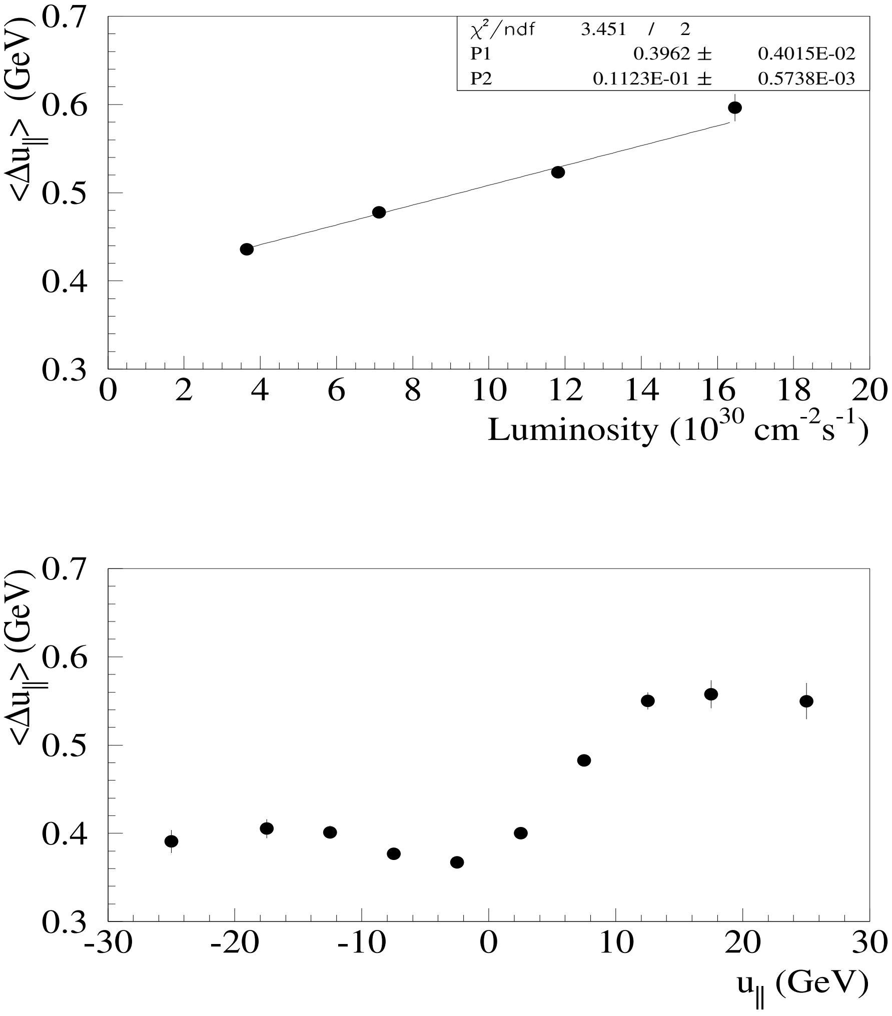

Figure 6.11: (Upper) Luminosity dependence of the energy in rotated windows in $W \rightarrow e\nu$ events. (Lower) $u_{||}$ dependence. (Plots from E. Flattum.)

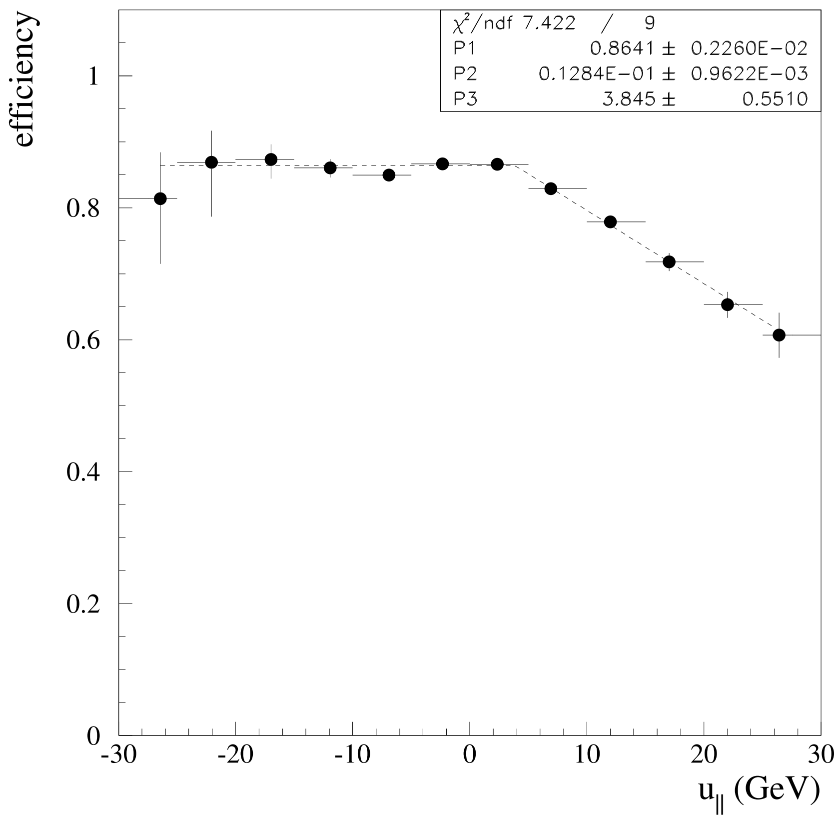

Figure 6.12: $u_{||}$ efficiency function measured with Monte Carlo electrons overlaid on W data events. (Plot from U. Heintz.)

Chapter 7

Production model constraint from Z data

7.1 Overview

The W mass measurement requires a detailed model of the p_T distribution of the W. In the DØ Run 1a analysis, the model used is the theoretical calculation of Ladinsky and Yuan (LY) [33]. The validity of the calculation has been checked by comparing the predicted and measured p_T spectra of the W and Z, where the prediction includes all the relevant detector effects. The calculation contains three free parameters which have been obtained from a global fit to the world's Drell–

Yan data. These fit parameters are used to determine the nominal p_T spectra input to the W and Z simulations used for the W mass fit. The uncertainty in the p_T spectra are determined from the errors on the global fit. The theory predicts a correlation between the boson p_T and rapidity, y. This is shown qualitatively in figures 7.1 and 7.2 which show the mean p_T vs. y for Z and W^- production.

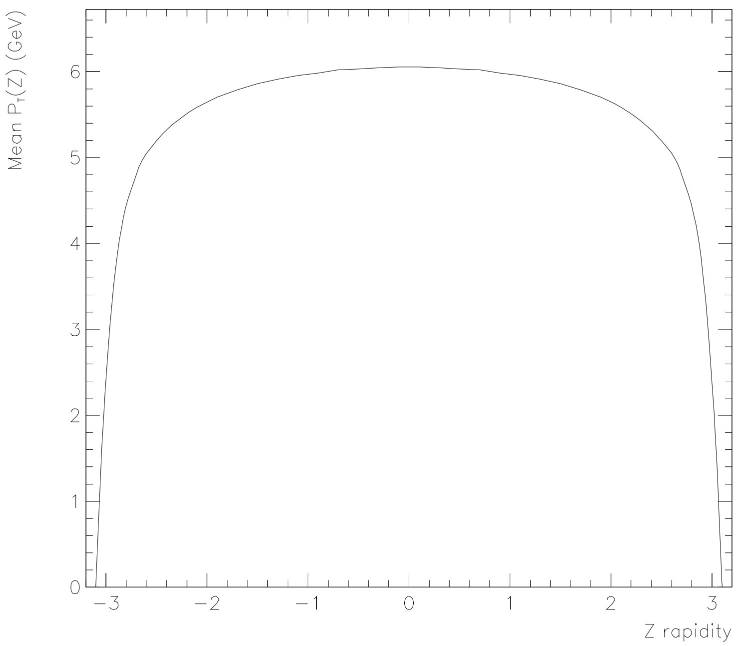

Figure 7.1: Mean p_T vs rapidity y for Z production, using the Ladinsky and Yuan calculation with MRSA pdf.

The published CDF Run 1a W mass measurement [46] uses a procedure in

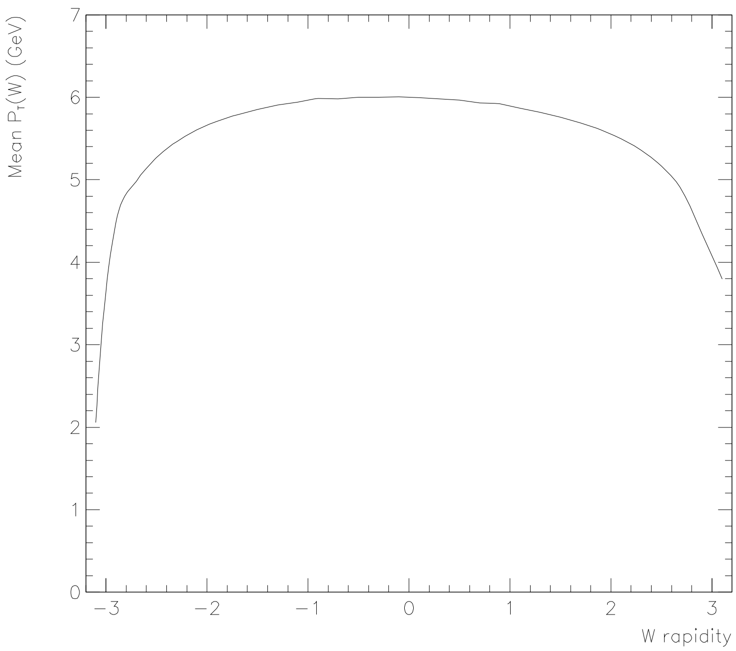

Figure 7.2: Mean p_T vs rapidity y for W^- production, using the Ladinsky and Yuan calculation with MRSA pdf.

which the p_T spectrum of the W is assumed to be p_T spectrum of the Z, corrected for resolution effects and scaled by a multiplicative factor. This factor is chosen so that the $u_\perp$ distribution of the W simulation agrees with that of the W data. Its numerical value is approximately 1.12, which is surprisingly different from one [47]. Note also that the correlation between the boson rapidity and p_T is not implemented in the CDF W mass fit. CDF estimated the effect of this correlation to be small. [46]

In the present approach, we use DØ $Z \rightarrow ee$ data to constrain the inputs to the Ladinsky–Yuan model. This approach has several advantages.

- DØ data is used to constrain the model directly, so that the sensitivity of the measurement to external inputs is reduced.

- Unlike the CDF analysis, the correlation between the boson rapidity and p_T is modelled, and there is no ad hoc scale factor which relates the p_T distributions of the W and Z. Note that we do not require p_T distributions of the W and Z to be identical. For a given choice of parameters the differential cross sections $d^2\sigma_W/dP_T dy$ and $d^2\sigma_Z/dP_T dy$ are calculated independently and are in fact somewhat different, because of the mass difference between the bosons and the different initial state partons which participate in W production *vs.* Z production.

- The p_T modelling constraint error decreases as the number of events increases, so that for high statistics experiments such as those of Run II or TeV33 the error from the p_T model can be made small.

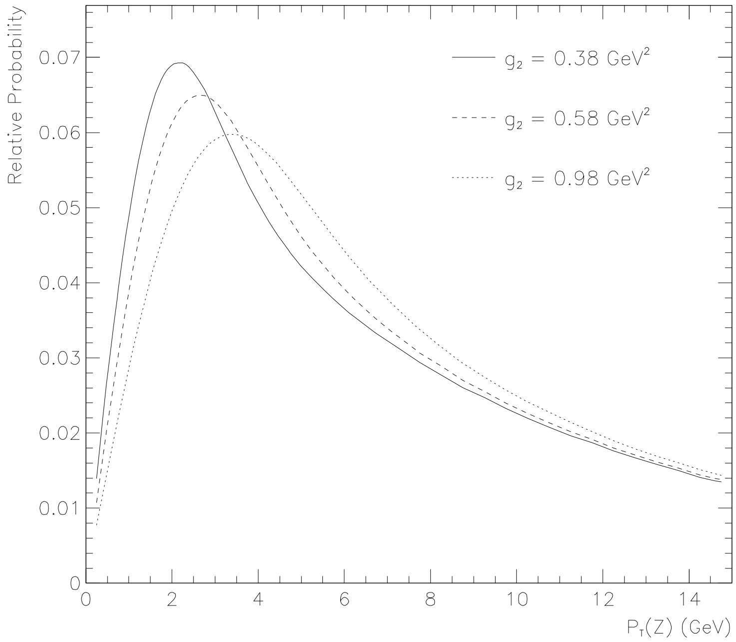

Figure 7.3: P_T^Z spectra vs. g_2 from the Ladinsky–Yuan calculation using MRSA pdf.

7.2 Fitting for g_2

As described earlier, the inputs to the LY model which dominate the p_T spectra for W and Z production are the choice of pdf and the choice of the non–perturbative cutoff function $S_{NP}(b)$. In turn the dominant error from $S_{NP}(b)$ is due to the coefficient g_2. Figures 7.3 and 7.4 shows the variation in the P_T^Z and P_T^W spectra for a range of g_2 values, for MRSA pdf. Similar variations are obtained with other pdf choices. Figure 7.5 shows the variation in the mean P_T^Z vs. g_2 for several pdf

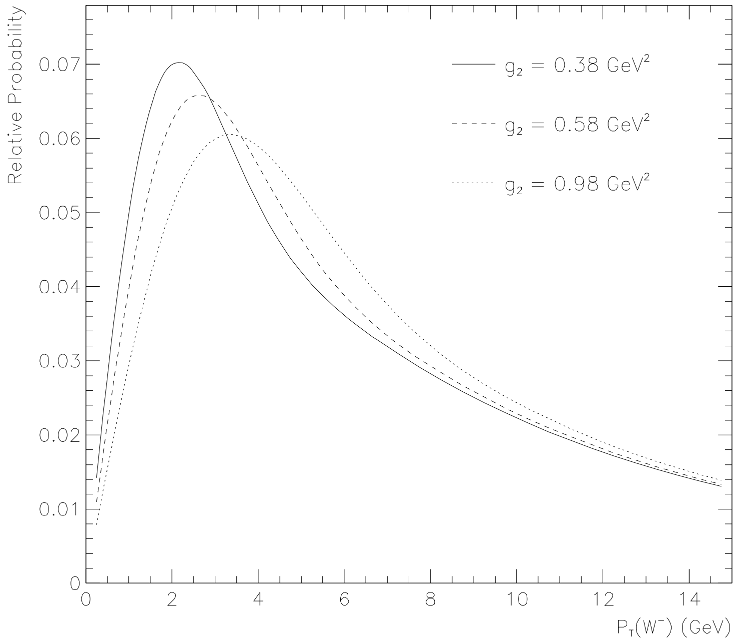

Figure 7.4: P_T^W spectra vs. g_2 from the Ladinsky–Yuan calculation using MRSA pdf.

choices, and 7.6 the corresponding variation for the mean P_T^W. In both cases the mean p_T is computed over the range [0,15] GeV, integrated over all rapidity. For a given value of g_2, the mean p_T of the W or Z boson depends on the pdf choice.

Since the P_T^Z spectrum is sensitive to g_2, it is possible to use the Z data to measure g_2 within the framework of the LY model. Since the P_T^Z distribution is also dependent upon g_1 and g_3 and the pdf, a measurement of g_2 from the P_T^Z data makes sense only for a given choice of these other inputs. For the purposes of the

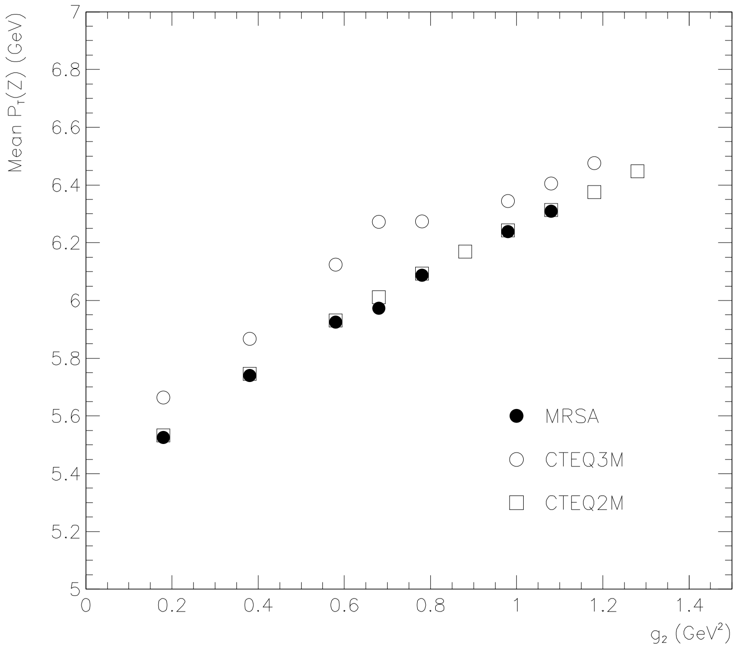

Figure 7.5: Mean P_T^Z vs. g_2, prior to detector simulation.

W mass measurement, it is reasonable to simply fix g_1 and g_3 and determine g_2 with that fixed choice. We choose to set g_1 and g_3 to the values fit by Ladinsky and Yuan [33], see table 7.1. We will then measure g_2 for several pdf choices, namely MRSA, MRSD$-'$, CTEQ3M and CTEQ2M. The fits done by Ladinsky and Yuan were performed using CTEQ2M pdf, so the g_2 value determined from DØ data using CTEQ2M can be compared directly to the published Ladinsky and Yuan value.

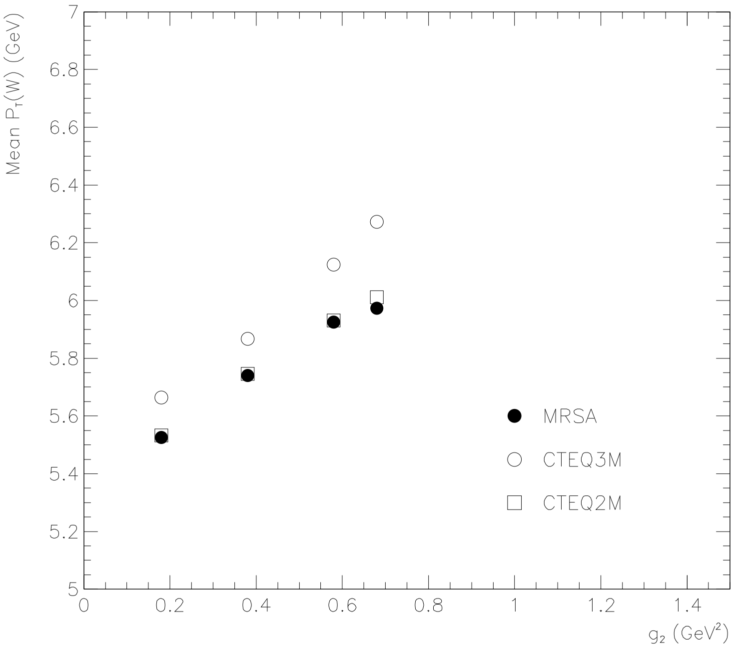

Figure 7.6: Mean P_T^W vs. g_2 prior to detector simulation.

There are several possible approaches to measuring g_2 given a $Z \rightarrow ee$ data sample.

One option is to "unfold" instrumental effects in the data and so correct the measured, smeared P_T^Z spectrum to calculate the "true" unsmeared P_T^Z spectrum. This unfolded spectrum could then be compared directly to the theoretical calculation, and the theoretical parameters chosen to optimize agreement with the data. An analysis based on this type of procedure can be found in reference [64]. This

Parameter	Value
g_1	$0.11^{+0.04}_{-0.03}$ GeV^2
g_2	$0.58^{+0.1}_{-0.2}$ GeV^2
g_3	$-1.5^{+0.1}_{-0.1}$ GeV^{-1}

Table 7.1: Parameters of S_{NP} in the Ladinsky and Yuan model from a global fit to Drell–Yan data using CTEQ2M pdf.

method has the advantage that new theoretical models can be directly compared to the unfolded experimental result without intermediate simulation steps.

A second option is to use a detector simulation to generate a prediction for several theoretical calculations. These predictions can then be compared directly to the observed data. The advantage of this procedure is that the errors are easily propagated, while the unfolding procedure requires a complicated correlated error analysis. This type of analysis is described here.

A third option is to use the spectrum of the ϕ difference between the two electrons from the Z decay, denoted $\Delta\phi(ee)$. If the Z mass and decay kinematics are well understood then the set of possible P_T^Z distributions is in 1–1 correspondence with the set of $\Delta\phi(ee)$ distributions. This is illustrated in figure 7.17, which shows the predicted $\Delta\phi(ee)$ distributions for MRSA pdf and a range of choices of g_2. A P_T^Z distribution with higher average mean p_T corresponds to a wider $\Delta\phi(ee)$ distribution. The $\Delta\phi(ee)$ distribution has the advantage that it is extremely insensitive to reconstruction biases – the ϕ_e measurement is the simplest and most precise experimental observable available. However, the $\Delta\phi(ee)$ distribution carries less information about the true P_T^Z spectrum then the $p_T(ee)$ distribution, so that for a given number of events the statistical error from a $\Delta\phi(ee)$ fit is about 1.4 times that from the corresponding $p_T(ee)$ fit. In the limit of very high statistics it may prove that the statistical power of the $p_T(ee)$ fit may be outweighed by the higher systematic errors incurred compared to the $\Delta\phi(ee)$ fit. In the present analysis the $\Delta\phi(ee)$ fit is used as a cross check only.

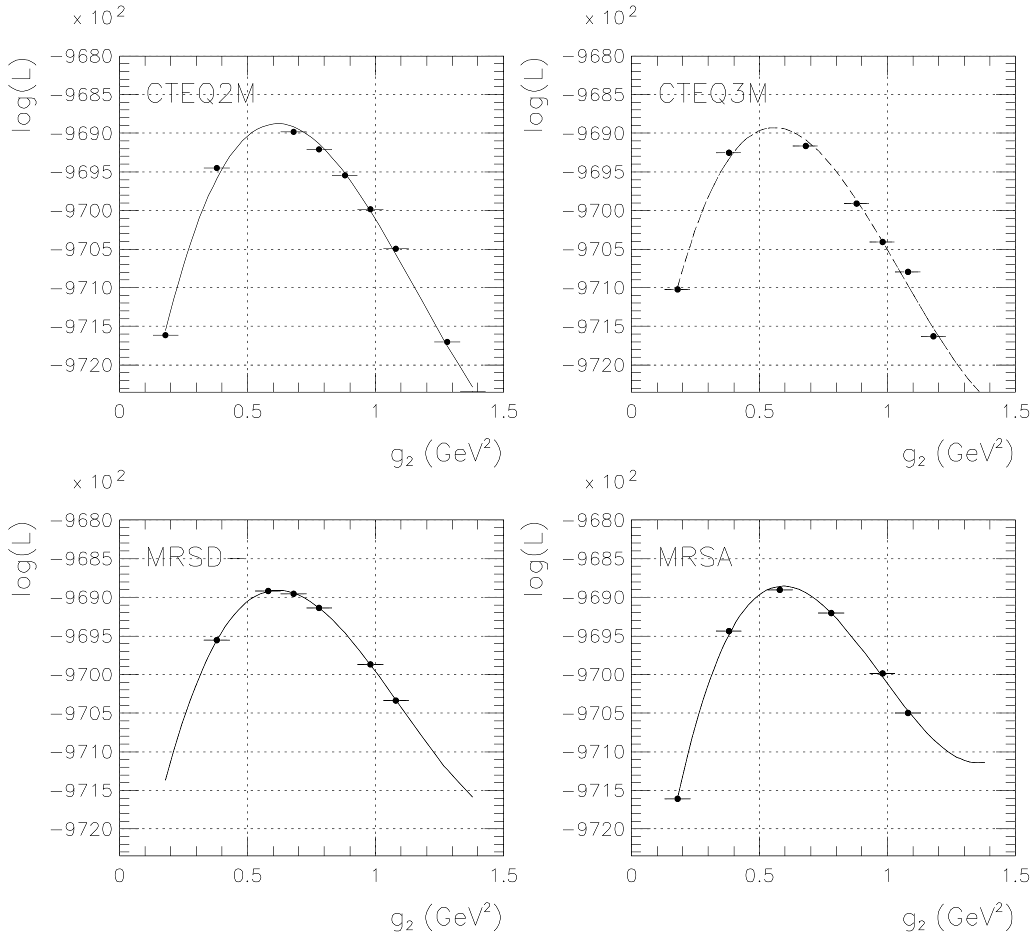

Figure 7.7: $\log \mathcal{L}$ curves vs. g_2 for four pdf choices, for a fit to a MC experiment generated with MRSA pdf and $g_2 = 0.58$ GeV^2.

7.3 Fit to the $p_T(ee)$ spectrum

7.3.1 Fitting Procedure

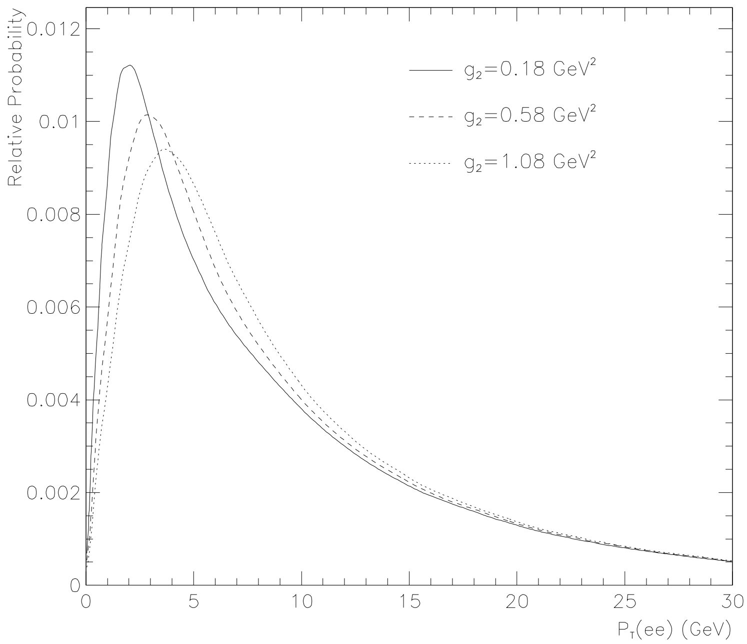

Figure 7.8: Predicted $p_T(ee)$ spectra after detector simulation using MRSA pdf. Larger g_2 values correspond to harder $p_T(ee)$ distributions.

Figure 7.8 shows the predicted $p_T(ee)$ spectra for a range of g_2 values. These distributions can be used as likelihood functions to fit for g_2. To test the fitting procedure, large Monte Carlo experiments were generated at fixed values of g_2

pdf choice	g_2 input (GeV^2)	g_2 fit	$\frac{g_2^{fit} - g_2^{true}}{\delta g_2}$
CTEQ2M	0.68	0.6887 ± 0.0070	$+1.24\,\sigma$
MRSA	0.58	0.5797 ± 0.0063	$-0.05\,\sigma$

Table 7.2: g_2 fits to MC experiments

and fitted. The random number seeds were changed so that these Monte Carlo experiments were statistically independent of the likelihood functions. The results of the fits are shown in table 7.2. The likelihood curves are displayed in figure 7.7 for the MRSA experiment.

These Monte Carlo ensemble tests show that over the large range of g_2 considered, the likelihood curve is asymmetric. In the limit of infinite statistics, the likelihood curve must be quadratic in a neighborhood of the maximum. However, it need not be quadratic over a large region. In the case of the P_T^Z fit, the model is not valid unless g_2 is positive. Therefore, from first principles the likelihood is zero for $g_2 \leq 0$. It follows that the log(likelihood) goes to $-\infty$ at $g_2 = 0$. This constraint forces the likelihood curve away from a quadratic shape. This does not pose a fundamental problem for the fit, it is simply necessary to account for the non–quadratic shape. Alternatively, one can restrict the fit to a small region around the maximum where the curve is better approximated by a quadratic, but this requires generating many more calculations in a small region around the maximum. Such a process would require a large amount of CPU time. In this analysis I account for the asymmetry by fitting the likelihood curve with a cubic polynomial. For a quadratic, $\log\mathcal{L} = ax^2 + bx + c$, the fitted value and error are given by

$$g_2^{fit} = \frac{-b}{2a} \pm \frac{1}{\sqrt{-2a}} \tag{7.1}$$

for a cubic, $\log\mathcal{L} = Dx^3 + Cx^2 + Bx + A$, the corresponding formula is

$$g_2^{fit} = \frac{-C - \sqrt{C^2 - 3BD}}{3D} \pm \frac{1}{\sqrt{2(C^2 - 3BD)}} \tag{7.2}$$

The maximum is just the point at which $\mathcal{L}' = 0$ and $\mathcal{L}'' < 0$. The error is given by $1/\sqrt{-\mathcal{L}''}$, evaluated at the maximum. The justification for using a cubic polynomial is that it returns the correct values for the Monte Carlo ensemble fits. This implies that a cubic function adequately accounts for the asymmetry in the $\log\mathcal{L}$ curve. A fitting error is assigned to the procedure which is equal to the deviation of the CTEQ2M fit value from the nominal. Although this deviation is not statistically significant, the error is quoted for the sake of conservatism as well as to highlight the need for care in the fitting procedure.

7.3.2 Background

To model the experimentally observed spectrum one must include a background contribution. The background $p_T(ee)$ spectrum has been determined by Dylan Casey [64] from a sample of fake dielectron events with kinematics similar to that of the Z sample. The fakes were selected by requiring the electron candidates to fail quality cuts. The $p_T(ee)$ spectrum for the fake sample is parametrized with a function of the form

$$\frac{d\sigma}{dp_T(ee)} \propto e^{-Ap_T(ee)}(p_T(ee) + B)^N \tag{7.3}$$

As a cross check, the same procedure was carried out for a sample of events with two jets, each of which was required to have an EM fraction exceeding 70%. The results of the two background parametrizations are shown in table 7.3. The difference between the two parametrizations are used to set the systematic error from the background shape. The two shapes are shown in figure 7.9

The mean $p_T(ee)$ for either background method is somewhat higher than the corresponding values for the Z simulation, which are 5.82 GeV for the range [0,15] GeV and 8.40 GeV for the range [0,30] GeV. This implies that background contamination tends to raise the fitted value of g_2. The background shapes from bad electrons and dijets differ at high $p_T(ee)$ values, so that the sensitivity to the

Background method	Bad electrons	Dijets
A	0.1308	0.4191
B	0.3993	1.5922
N	1	3
χ^2	22.2/16	11.8/12
$\langle p_T(ee)\rangle$ in [0,15] GeV range	7.99	7.02
$\langle p_T(ee)\rangle$ in [0,30] GeV range	12.41	7.97

Table 7.3: Background parameters for the $p_T(ee)$ spectrum. The χ^2 values quoted characterize the quality of the two parametrizations of the background $p_T(ee)$ spectra.

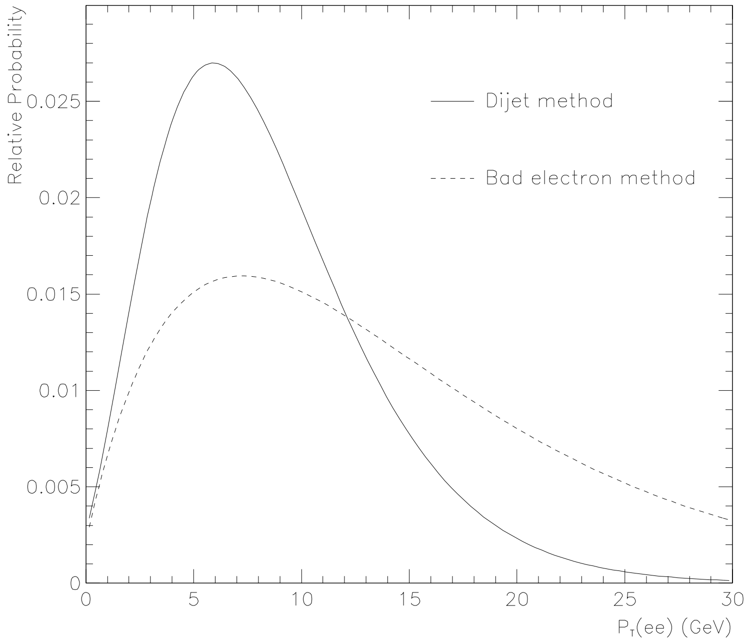

Figure 7.9: Background parametrizations for the $p_T(ee)$ spectrum.

background can be reduced by restricting the fitting range to $p_T(ee) \leq 15$ GeV.

To further reduce the sensitivity to background, the invariant mass of Z candidates used for the g_2 fit is required to be in the region [78,97] GeV. Recall that the Z peak is at ≈ 87 GeV rather than 91.1884 GeV because all energies are quoted using the test beam energy scale. This tight mass window requirement has a very small effect on the statistical error of the g_2 fit and reduces the background fraction by a factor of about 2 relative to the usual mass window of [70,110] GeV. It is also appropriate since the LEGACY calculations were performed in the zero–width approximation. There is a slight correlation between the mass and the p_T, the effects of which are minimized by the tight mass window cut.

7.3.3 Fit Results

Having verified the fitting procedure and determined the background shape, we proceed to fit the Run 1b P_T^Z data. Figures 7.11 and 7.12 show the likelihood curves obtained for each pdf for fits to the regions $p_T(ee) < 15$ GeV and $p_T(ee) < 30$ GeV respectively.

The g_2 values for the fits in the $p_T(ee) < 30$ GeV range and $p_T(ee) < 15$ GeV range are very close. This is expected because the shape of the P_T^Z spectrum becomes insensitive to g_2 at P_T^Z values above 15 GeV or so. Theoretically this kind of behaviour makes sense since the formalism is designed to handle the low P_T^Z region, and the terms included in the resummation are the dominant terms in the limit $P_T^Z \to 0$.

The absolute value of $\log \mathcal{L}$ has no significance. However, the differences between $\log \mathcal{L}$ values between the various fits are significant. For the fits in the $p_T(ee) < 30$ GeV range the different pdf, the maximum $\log \mathcal{L}$ values are different. Higher $\log \mathcal{L}$ values correspond to models which fit the data better. The CTEQ2M model fits the data best, followed by MRSD$-'$, MRSA and lastly CTEQ3M. Relative to the CTEQ2M value the other $\log \mathcal{L}$ values are -4, -6 and -8 respectively, corresponding to 2.8σ, 3.5σ and 4.0σ deviations. In the $p_T(ee) < 15$ GeV range all the pdf maximize at the same $\log \mathcal{L}$ to within 0.2 units, indicating that all the pdf model the data equally well in this $p_T(ee)$ range. Therefore the variation in the likelihood values for the $p_T(ee) < 30$ GeV range is due to a normalization difference in the ranges [0,15] GeV and [15,30] GeV. The relative normalization between these regions depends not only on the pdf choice but also on detector effects such as the $u_{||}$ efficiency. To minimize the pdf error, detector effects and the background contamination, we choose to use the g_2 fit in the range $p_T(ee) < 15$ GeV. The fits in the $p_T(ee) < 30$ GeV range do not give significantly different g_2 values and so provide a cross check. The g_2 fit results for the different pdf choices are shown in table 7.4. Table 7.5 shows the results for the [0,30] GeV region.

Figure 7.10 shows the $p_T(ee)$ spectrum observed in the data and the Monte Carlo prediction for the best fit g_2 value using MRSA pdf. The Kolmogorov–Smirnov probability that the two distributions are from the same parent distribution is 77.7% and the χ^2 statistic is 25.5 for 29 degrees of freedom. Both of these tests indicate that the fit quality is good.

The result of the CTEQ2M fit is 0.608 GeV^2, in good agreement with the

pdf choice	g_2 (GeV^2)	δg_2 (stat) (GeV^2)
MRSA	0.587	0.095
MRSD$-'$	0.613	0.104
CTEQ3M	0.544	0.096
CTEQ2M	0.608	0.098

Table 7.4: Values of g_2 fit to the Run 1b P_T^Z data for the range $p_T(ee) < 15$ GeV

pdf choice	g_2 (GeV^2)	δg_2 (stat) (GeV^2)
MRSA	0.568	0.092
MRSD$-'$	0.586	0.102
CTEQ3M	0.515	0.094
CTEQ2M	0.581	0.097

Table 7.5: Values of g_2 fit to the Run 1b P_T^Z data for the range $p_T(ee) < 30$ GeV

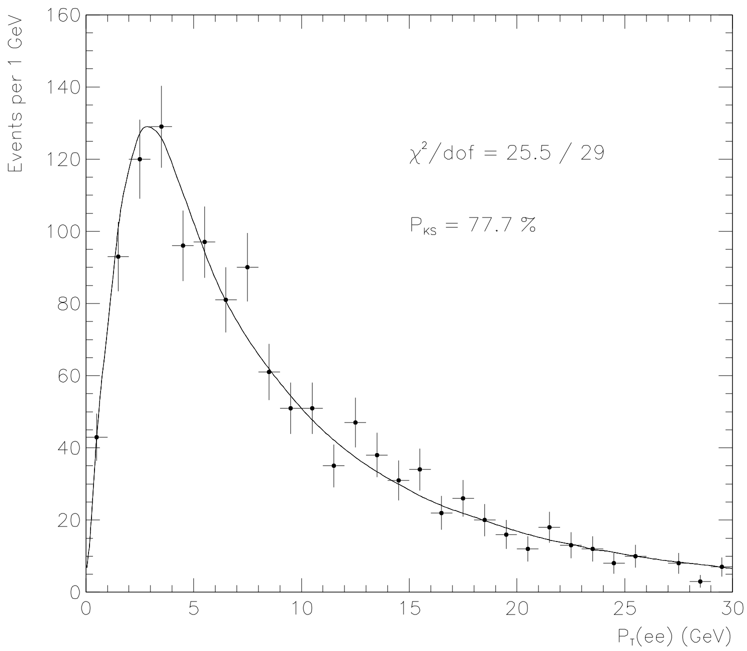

Figure 7.10: Comparison on $p_T(ee)$ data and simulation for the best fit g_2 using MRSA pdf.

value of $0.58^{+0.1}_{-0.2}$ GeV^2 obtained by Ladinsky and Yuan. Taking into account the independent statistical errors the difference is 0.2 standard deviations.

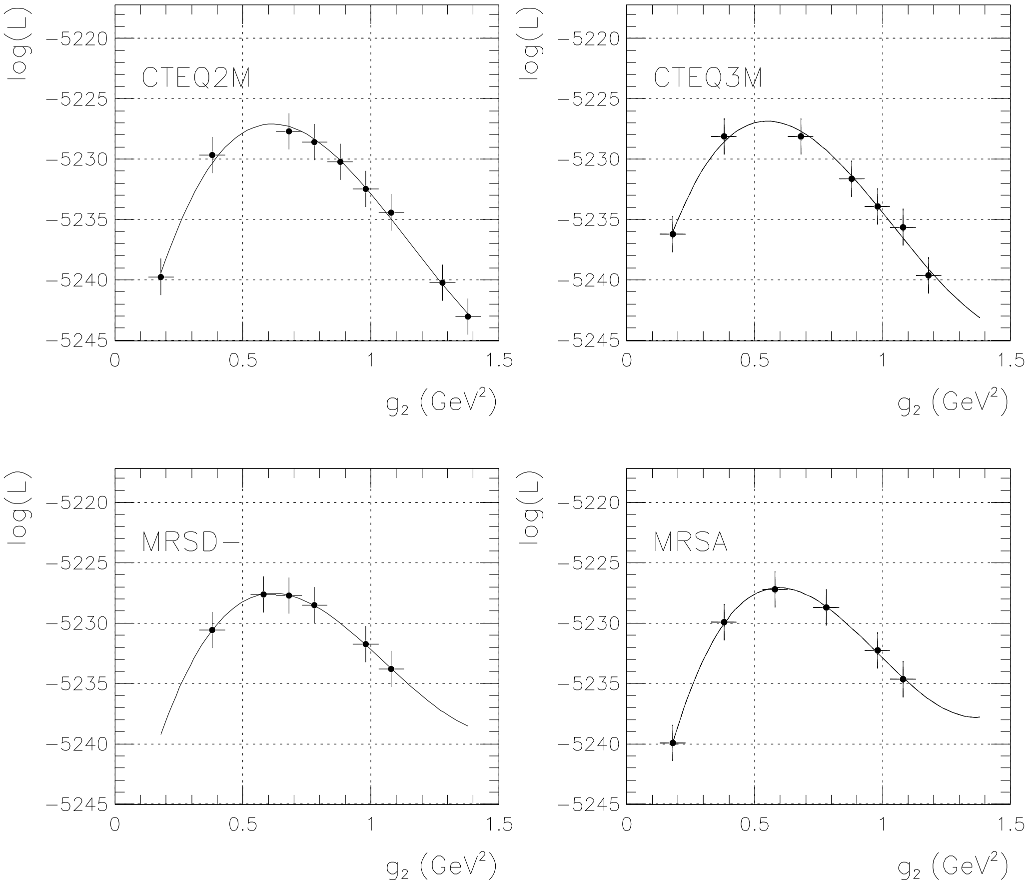

Figure 7.11: $\log \mathcal{L}$ curves vs. g_2 for four pdf choices. The fit range is [0,15] GeV.

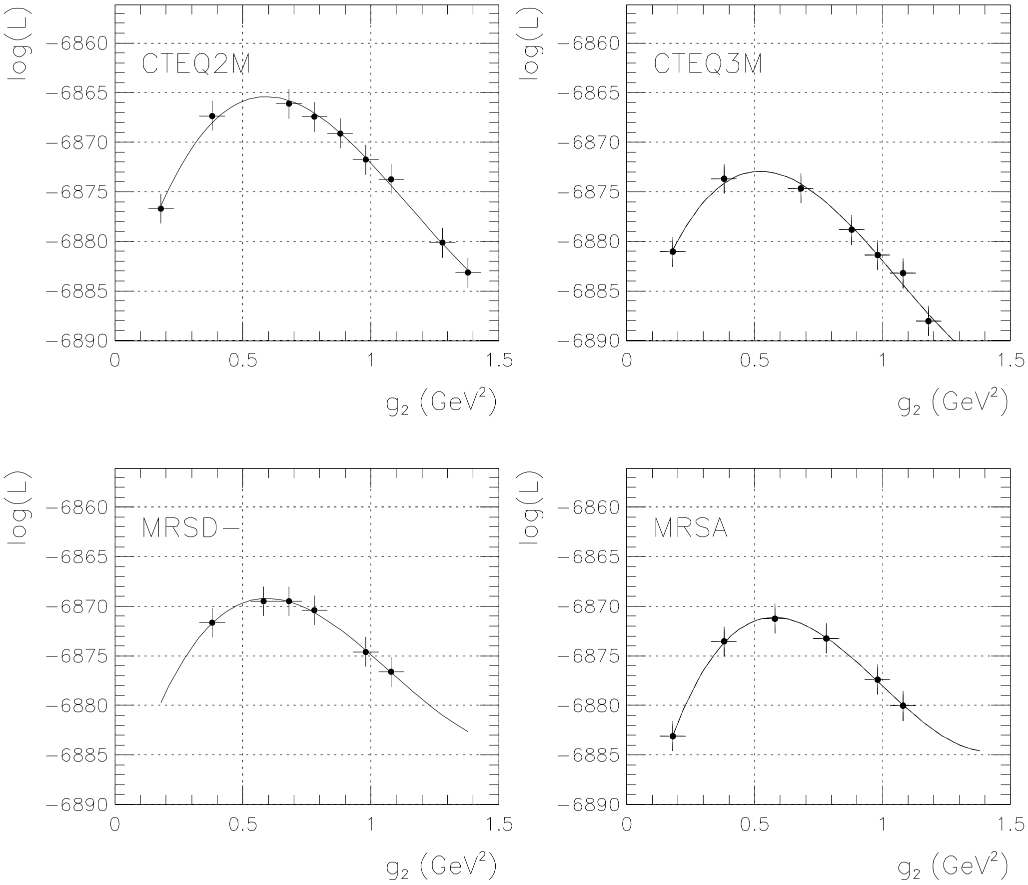

Figure 7.12: $\log \mathcal{L}$ curves vs. g_2 for four pdf choices. The fit range is [0,30] GeV.

7.4 Systematic Errors

The systematic errors for both the $p_T(ee)$ and $\Delta\phi(ee)$ fits are much smaller than the statistical errors given the present number of $Z \rightarrow ee$ events. It is therefore possible to make extremely conservative error estimates without affecting the result. In the following, in most cases the systematic error determined is an upper limit rather than an actual estimate of the error. To determine the errors better would require a great deal of CPU time and would not significantly improve the result.

The systematic errors in the g_2 fit using the $Z \rightarrow ee$ data have been estimated using either of two methods. To estimate the error due to the electron energy resolution, u efficiency parametrization, CC crack cut and the radiative decay model, simulated Monte Carlo experiments have been constructed with different assumptions, and fit using the standard likelihood functions excluding the background estimates. To estimate the error due to the electron energy scale, background fraction and background shape, the data were corrected for a range of assumptions and fit using the standard likelihood functions.

7.4.1 Background

We consider two sources of error for the background, the shape and the normalization. The normalization is computed from the Z invariant mass lineshape, which

Background fraction, $f_b(\%)$	g_2 (GeV^2)
0.0	0.6039
1.0	0.5972
2.0	0.5904
2.5	0.5875
3.0	0.5842
4.0	0.5777
5.0	0.5710

Table 7.6: Values of g_2 fit to the P_T^Z data for varying background fraction, using MRSA pdf.

is fit to a sum of the predicted lineshape from CMS and an exponential background. From this fit the normalization of the background is determined. The Drell–Yan contribution is treated as a background in the invariant mass fit, but since the dielectron p_T spectrum is the same for Z production and for Drell–Yan production at the Z mass scale, it should not be treated as a background for the g_2 fit.

We assume for the g_2 fit that the background fraction is $f_b = (2.5 \pm 2.5)\%$. This range of f_b is large enough to account for the Drell–Yan correction, the variation in

f_b with the $p_T(ee)$ range and the statistical error on the invariant mass fit. Table 7.6 shows the value of g_2 fit to the data for f_b between 0% and 5%, for MRSA pdf. Since the same sample is used the points are completely correlated. The results of these fits can be parametrized as

$$g_2^{fit} = 0.6038 - 0.006549 f_b \tag{7.4}$$

where f_b is a percentage. The results of these fits are displayed in figure 7.13. With the very conservative range $f_b = (2.5 \pm 2.5)\%$ the error from the background normalization is $\delta g_2 = \pm 0.017$ GeV^2.

Using $f_b = 2.5\%$ and using MRSA pdf, we fit using two background parametrizations described earlier. For the bad electron parametrization the fit is $g_2 = 0.587$ GeV^2 and for the dijet parametrization it is $g_2 = 0.581$ GeV^2. The systematic error from the background shape is equal to the difference, $\delta g_2 = \pm 0.006$ GeV^2.

7.4.2 Electron Energy Resolution

To determine the error due to the energy resolution, Monte Carlo Z experiments were generated with the constant term varied. The MC experiments were then fit using the standard likelihood templates. The results are shown in table 7.7 and plotted in figure 7.14. We take the CC constant term to be $0.9^{+0.3}_{-0.5}\%$. The corresponding error on g_2 is $\delta g_2 = \pm 0.02$ GeV^2.

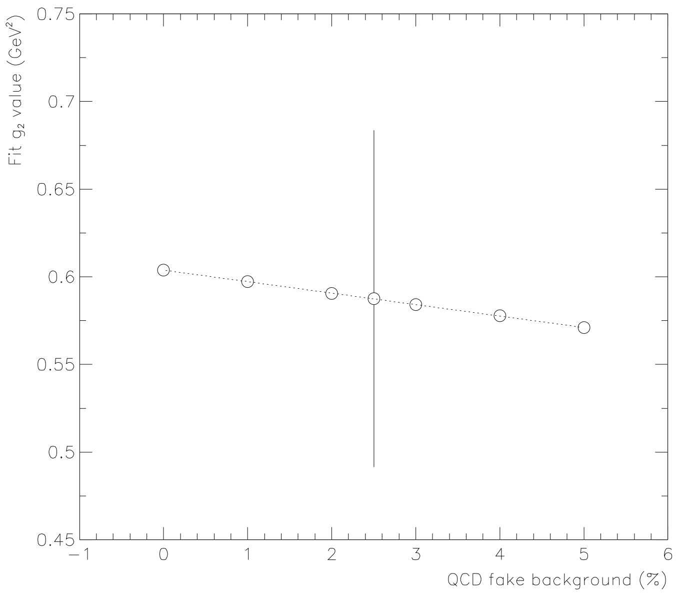

Figure 7.13: Fitted value of g_2 assuming different background fractions. The statistical errors on the points are completely correlated, so the error bar is shown only for the central value.

7.4.3 Electron Energy Scale

The electron energy scale has been determined to an accuracy of better than 0.1% using the Z invariant mass peak. To estimate the derivative of the g_2 fit with respect to the energy scale, the energies of the electrons in the data were scaled by a factor varying between 0.95 and 1.05 relative to the nominal scale and the data refitted. The results are in table 7.8 and displayed in figure 7.15. Since the same data are used, the fits are fully correlated.

Though the electron energy scale is precisely known, a large range was chosen

CC constant term	g_2 (GeV^2)
0.000	0.5528 ± 0.0062
0.007	0.5747 ± 0.0063
0.015	0.6004 ± 0.0066
0.020	0.6329 ± 0.0067

Table 7.7: Values of g_2 fit to the P_T^Z MC experiments for varying electron energy resolution. The errors are the MC statistical uncertainties.

to indicate the sensitivity of the corresponding fit to the P_T^W spectrum to the hadronic energy scale, which is not as well constrained as the EM scale.

The electron energy scale α_{EM} is assigned a very conservative error of 0.5% to account for variations due to the CDC length scale and other factors. The result can be parametrized as

$$g_2^{fit} = 0.587 + 1.7135(\alpha_{EM} - 1) \tag{7.5}$$

For $\delta\alpha_{EM} = \pm 0.005$ the error on g_2 is $\delta g_2 = \pm 0.02$ GeV^2.

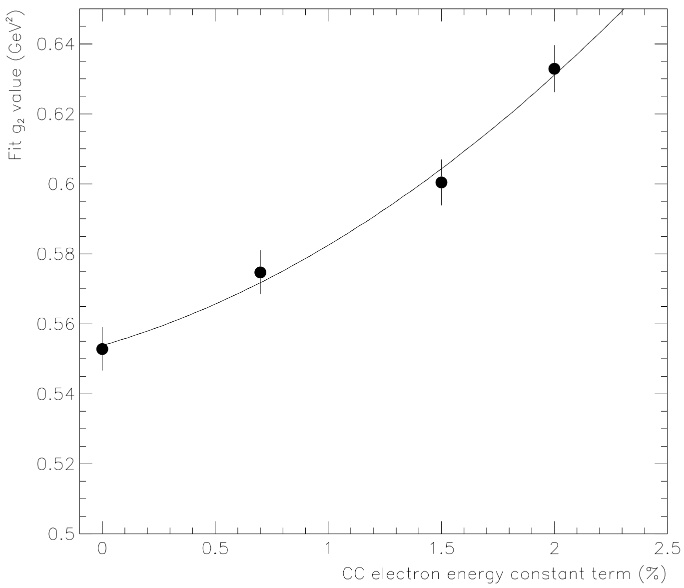

Figure 7.14: Fitted value of g_2 for MC experiments with varying electron energy resolution. The error bars are from Monte Carlo statistics.

7.4.4 Crack Cut

The crack cut excludes 10% of each CC module on either side. As discussed in section 7.5.1 the ϕ dependent acceptance has a small impact on the $\Delta\phi(ee)$spectrum and therefore also on the $p_T(ee)$ spectrum. To assign an error, a Monte Carlo experiment was generated with MRSA pdf and $g_2 = 0.58$ GeV^2, with the crack cut turned off in the simulation. The g_2 value fit for the experiment was $g_2 = 0.5905 \pm 0.0056$ GeV^2. This is 1.9 standard deviations higher than the input value. This difference is consistent with a statistical fluctuation, however we treat the

Relative energy scale	g_2 (GeV^2)
0.950	0.5021
0.975	0.5397
1.000	0.5875
1.025	0.6231
1.050	0.6746

Table 7.8: Values of g_2 fit to the scaled $p_T(ee)$ data for varying electron energy scale, using MRSA pdf.

difference as a contribution to the systematic error, $\delta g_2 = \pm 0.01$ GeV^2. This is an overestimate, because the uncertainty in the crack cut modelling is very small. Completely turning off the crack acceptance loss is a much more drastic change than is actually necessary to estimate this error.

7.4.5 Radiative Decays

In radiative decays of the Z, if the final state photon is separate from the electron clusters in the calorimeter, then the p_T of the dielectron pair is not equal to the p_T of the Z. The radiated photons are typically low energy objects. Also, because they

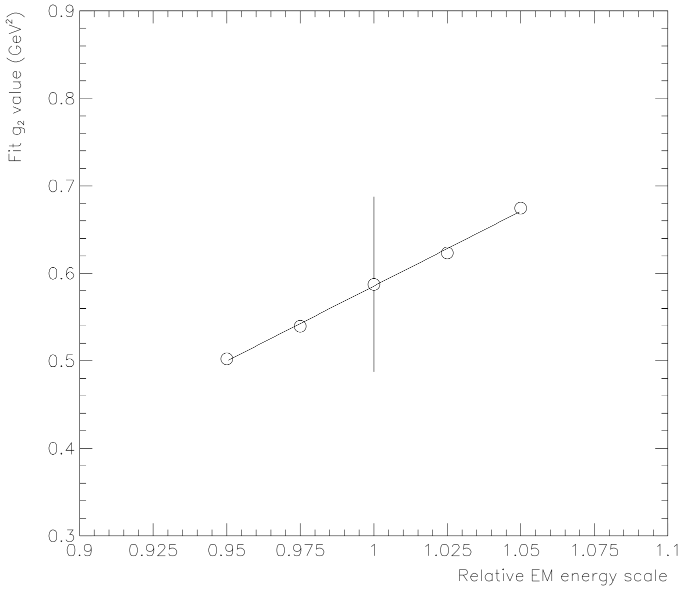

Figure 7.15: Fitted value of g_2 assuming different EM energy scale corrections to the data. The error on the EM energy scale is less than 0.1%. The statistical errors on the points are completely correlated, so the error bar is shown only for the central value.

tend to be radiated collinear to the electron direction, they have a low probability of separating from the electron cluster in the calorimeter. Therefore radiative decays are not expected to cause a large bias in the g_2 fit. This would not be true if the P_T^Z were reconstructed using momentum measurements from tracking.

The likelihood functions include radiative Z decays. To estimate the importance of radiative effects, a Monte Carlo experiment was generated with radiation turned off at $g_2 = 0.58$ GeV^2. The fit to this experiment was $g_2 = 0.5511 \pm 0.0058$ GeV^2, which is 5 standard deviations lower than the input value. This demonstrates that it is necessary to include radiative effects in the model. We treat the difference as a contribution to the systematic error, $\delta g_2 = \pm 0.03$ GeV^2. This is clearly an overestimate of the error.

7.4.6 $u_{||}$ efficiency

The $u_{||}$ efficiency translates into a P_T^Z–dependent efficiency, which directly affects the g_2 fit. The $u_{||}$ efficiency can be parametrized as

$$\varepsilon(u_{||}) \propto \begin{cases} 1 & u_{||} < u_0 \\ 1 - s(u_{||} - u_0) & u_{||} > u_0 \end{cases} \tag{7.6}$$

where the nominal values of these parameters are $s = -0.013 \pm 0.001$ GeV^{-1} and $u_0 = 3.85 \pm 0.55$ GeV. To study this effect, Monte Carlo experiments with $g_2 = 0.58$ GeV^2 were generated with a range of $u_{||}$ efficiency parameters and fit with the nominal likelihood functions. Table 7.9 shows the results of these fits. The maximum deviation from the nominal is taken to be the systematic error, $\delta g_2 = \pm 0.02$ GeV^2.

7.5 Consistency Checks

Consistency checks have been performed to verify the stability of the g_2 fit using the $Z \rightarrow ee$ data.

u_0 (GeV)	s (GeV^{-1})	g_2 (GeV^2)
3.85	-0.0030	0.5798 ± 0.0063
3.85	-0.0230	0.5508 ± 0.0062
3.85	0.0	0.5905 ± 0.0064
0.00	-0.0130	0.5591 ± 0.0063

Table 7.9: Values of g_2 fit to MC experiments for various $u_{||}$ efficiency parameters.

Figure 7.16 shows the variation in the g_2 fit obtained from the data as a function of the upper edge of the fitting window in P_T^Z. It would not make sense to vary the lower edge of the window as the data are primarily low p_T and the validity of the calculation is optimized in the low p_T region.

Table 7.10 gives the variation in the g_2 fit to the data for two different invariant mass windows. Part of the difference may be due to the zero–width approximation made in calculating the p_T spectrum. In any case the variation is much smaller than the statistical error and is therefore irrelevant.

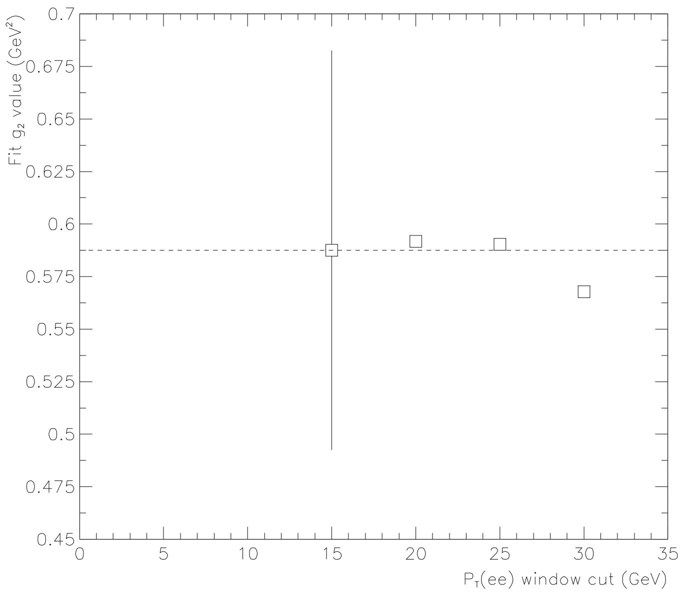

Figure 7.16: Fitted value of g_2 for varying $p_T(ee)$ fitting window.

7.5.1 Fit to the $\Delta\phi(ee)$ spectrum

Figure 7.17 shows the predicted $\Delta\phi(ee)$ spectra for a range of g_2 values. No background contribution has been included. Models with larger average values of $p_T(ee)$ predict wider $\Delta\phi(ee)$ spectra. The bumps in the $\Delta\phi(ee)$ spectra are due to the fiducial cut requiring the electrons to be away from the intermodule cracks in the central calorimeter. The cracks are narrow in ϕ and are spaced periodically, at $\phi = N \cdot (2\pi/32)$ where $N = 0 \ldots 31$. For a configuration with fixed $\Delta\phi(ee)$, the crack cut is more efficient for the case $\Delta\phi(ee) = M \cdot (2\pi/32)$ where M is any integer. For such a configuration, whenever one electron is lost in a crack, the

$M(ee)$ window	Background fraction	g_2 fit (GeV^2)
[78,97]	2.5%	0.587 ± 0.095
[70,110]	5.0%	0.595 ± 0.094

Table 7.10: Variation of the g_2 fit with the $M(ee)$ window, using the $p_T(ee)$ spectrum with MRSA pdf.

other is lost also. Therefore the acceptance is given by

$$\mathcal{A} = 1 - 32\frac{w}{2\pi} \tag{7.7}$$

where w is the width of the crack in radians. For the case $\Delta_\phi(ee) \neq M \cdot (2\pi/32)$, either electron may be lost so that the acceptance is

$$\mathcal{A} = 1 - 2 \times 32\frac{w}{2\pi} \tag{7.8}$$

Therefore one expects the crack cut to cause bumps in the $\Delta\phi(ee)$ spectrum at multiples of $\pi/16$ of height $\approx w/16\pi$ and width w.

Table 7.11 shows the fits to the $\Delta\phi(ee)$ data. Figure 7.18 shows the likelihood curves. The statistical errors are about a factor of 1.4 larger than for the $p_T(ee)$ fits, as expected. The fit g_2 values are about 0.5 standard deviation higher than for the $p_T(ee)$ fits, and are therefore statistically consistent. However, no background was included in the $\Delta\phi(ee)$ fit so the fit is expected to be slightly higher.

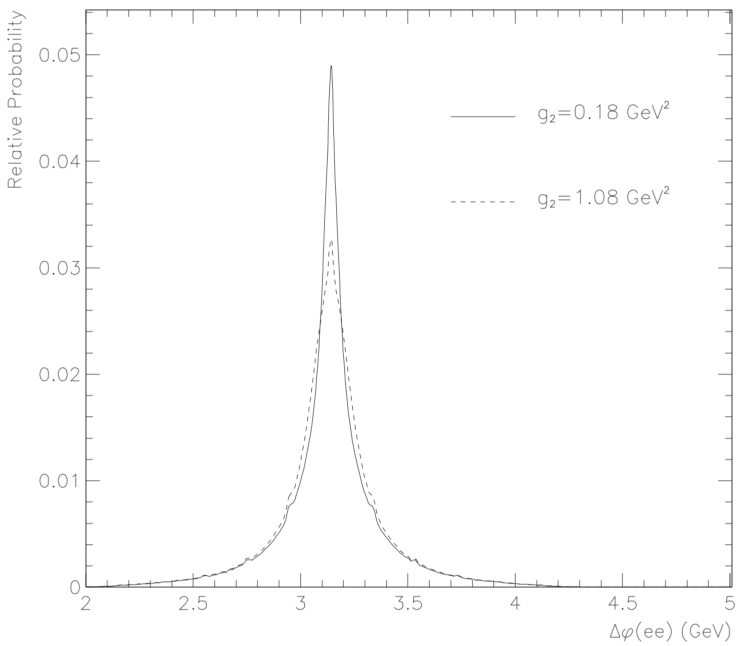

Figure 7.17: Predicted $\Delta\phi(ee)$ spectra after detector simulation. Larger g_2 values correspond to wider $\Delta\phi(ee)$ distributions.

The error in the g_2 measurement is dominated by the statistical error, therefore the $p_T(ee)$ fit does better than the $\Delta\phi(ee)$ fit since it is intrinsically more powerful statistically. However, the $\Delta\phi(ee)$ fit has smaller systematic errors. For example, the electron energy scale and resolution have negligible effect the $\Delta\phi(ee)$ fit. Therefore it is possible that in a future very high statistics regime such as TeV33 the $\Delta\phi(ee)$ fit might be superior to the $p_T(ee)$ fit.

pdf choice	g_2 (GeV^2)	δg_2 (stat) (GeV^2)
MRSA	0.640	0.136
MRSD$-'$	0.697	0.150
CTEQ3M	0.567	0.134
CTEQ2M	0.669	0.141

Table 7.11: Values of g_2 fit to the Run 1b $\Delta\phi(ee)$ data. The cut $p_T(ee) < 15$ GeV has been applied. No background has been included in the fitting functions.

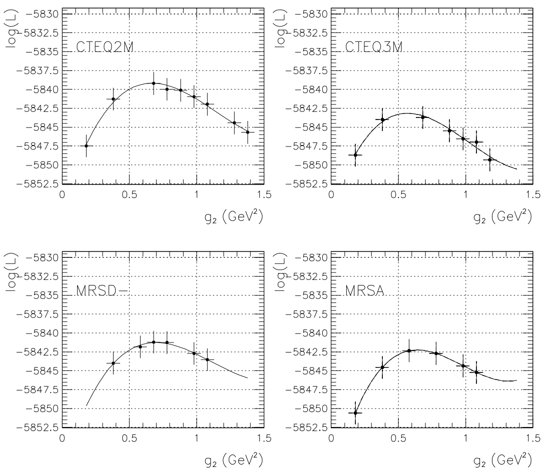

Figure 7.18: Likelihood curves for the $\Delta\phi(ee)$ fit for g_2.

7.6 Conclusion

Table 7.12 summarizes the errors in the g_2 measurement, for a given pdf. One can also quote a pdf error. The maximum difference from the nominal MRSA pdf is for the CTEQ3M set, which gives a g_2 value which is 0.043 GeV^2 low. The result is therefore

$$g_2 = 0.587 \pm 0.095(\mathrm{stat}) \pm 0.052(\mathrm{sys}) \pm 0.043(\mathrm{pdf})\ \mathrm{GeV}^2 \tag{7.9}$$

Adding the errors in quadrature and rounding gives

$$g_2 = 0.59 \pm 0.12\ \mathrm{GeV}^2 \tag{7.10}$$

The value is consistent with that obtained by Ladinsky and Yuan.

Source of Error	Error (GeV^2)
Statistical	0.095
Systematic	0.052
Background normalization	< 0.017
Background shape	< 0.007
Energy scale	< 0.02
Energy resolution	0.02
$u_{\|\|}$ efficiency	< 0.02
ϕ acceptance	< 0.01
Radiative decays	< 0.03
Fitting procedure	< 0.009
Total error	0.108

Table 7.12: Errors on the g_2 fit using the $p_T(ee)$ spectrum for MRSA pdf. A $<$ symbol indicates that the error has been overestimated.

Chapter 8

Systematic Errors: Theoretical Model

In this chapter I describe the uncertainties associated with the W mass measurement due to the theoretical model. In section 8.1 I discuss the errors due to the production model and in 8.2 the uncertainties due to the decay model, including radiative decays and $W \rightarrow \tau\nu \rightarrow e\nu\nu\nu$ decays.

8.1 Production Model

The distribution of the 4–vectors of the W or Z can be conveniently described by specifying the distributions of mass, rapidity, transverse momentum and azimuthal angle, ϕ. The ϕ distribution is of course simply uniform in $[0, 2\pi]$.

8.1.1 Mass distribution

The W or Z boson mass distribution depends upon the resonance mass, the Breit–Wigner width and the skewing of the mass spectrum arising form the parton luminosity function. The resonance mass is the quantity to be measured. The form of the mass distribution around the resonance has been discussed in detail earlier.

To determine the systematic error due to the W width, Monte Carlo experiments were generated with a range of widths and fit to a template generated with the nominal width. The results are shown in table 8.1. The derivatives of the four mass fits are calculated by fitting the variation from the Monte Carlo experiments vs. the W width. Using the most recent world average [63], $\Gamma_W = 2.062 \pm 0.059$ GeV, and setting $\Delta M_W = (\partial M_W / \partial \Gamma_W) \cdot \Delta \Gamma_W$ leads to the errors shown in table 8.2. The Z mass fit from the invariant mass spectrum is insensitive to the assumed width Γ_Z. In the simulation the current world average is used [63], $\Gamma_Z = 2.4963 \pm 0.0032$ GeV.

W width (GeV)	E_T^e fit	M_T^W fit	$\not{E}_T$ fit	E^e fit
1.7	-47 ± 19	-45 ± 14	-48 ± 23	-37 ± 35
1.9	-15 ± 8	-22 ± 6	-11 ± 10	-12 ± 35
2.3	$+31 \pm 8$	$+37 \pm 6$	$+23 \pm 10$	-28 ± 35
2.5	$+45 \pm 18$	$+75 \pm 13$	$+45 \pm 23$	$+4 \pm 35$

Table 8.1: Fits to Monte Carlo experiments with varying Γ_W.

Fit quantity	Γ_W derivative (MeV per GeV)	Error due to Γ_W (MeV)
E_T^e fit	149 ± 12	6.7 ± 0.8
M_T^W fit	114 ± 14	8.8 ± 0.7
$\not{E}_T$ fit	95 ± 14	5.6 ± 0.8
E^e fit	43 ± 36	2.5 ± 2.1

Table 8.2: Errors on W mass fits due to Γ_W. The uncertainties quoted for the derivative and the error are due to Monte Carlo statistics.

To assign an error to the parton luminosity function, we compute the parton luminosity slope for several pdf choices. The parton luminosity calculation must be performed consistently for the W and Z, since the W and Z parton luminosity slopes are correlated. This is shown in figure 8.1 which shows the W parton luminosity slope β_W vs. the Z parton luminosity slope β_Z for an ensemble of pdf choices, where no rapidity cuts have been made [14].

For each choice of pdf Monte Carlo experiments were generated for both the W and Z and fit to a nominal template. The results are shown in tables 8.4 and 8.5. Figure 8.1 shows the dependence of the mass fits on the parton luminosity slope for the CDF Run 1a analysis. Because of the correlation of the W and Z parton luminosity slopes, shown in figure 8.1, there is a significant cancellation in the W/Z mass ratio uncertainty. Figure 8.2 shows the dependence of the W mass fits on the parton luminosity slope for DØ.

The parton luminosity slopes for different pdf should be calculated with the appropriate rapidity distribution of the W or Z after the electron pseudorapidity cuts. Since the boson rapidity y is correlated with the rapidity of the decay products, the electron η cut affects the y distribution of the boson. The easiest way to apply this cut is to use a parton–model generator such as HERWIG or RESBOS [55] to generate the W or Z events and perform the decay, then to apply the lepton

pdf	β_W (GeV^{-1})	β_Z (GeV^{-1})
MRSA	0.00863 ± 0.0007	0.0036
CTEQ3M	0.00874 ± 0.0007	0.0033
CTEQ2M	0.00876 ± 0.0007	–
MRSD$-'$	0.00964 ± 0.0007	0.0038

Table 8.3: Parton luminosity slopes from HERWIG for W events and RESBOS for Z events after electron rapidity cuts.

fiducial cut. Using this method, the W parton luminosity slopes have been calculated using HERWIG and the Z slopes using RESBOS [1]. The results are in table 8.3. The errors quoted for the W include a statistical error of 0.0003 from the size of the HERWIG samples, in quadrature with a 0.0006 contribution from varying the electron η cut between 1.0 and 1.2.

Table 8.6 shows the derivatives of the W and Z mass fits with respect to the W and Z slopes. It is evident that among the modern pdf there is very little variation of the slopes and that the W derivatives are small even without the Z cancellation taken into account. We assign an error of 10 MeV for each fit to cover a slope deviation of 0.001 GeV^{-1} and ignore the W/Z cancellation.

β_W	E_T^e fit	M_T^W fit	$\not{E}_T$ fit	E^e fit
0.004	$+37 \pm 8$	$+20 \pm 8$	$+8 \pm 10$	$+17 \pm 15$
0.008	-3 ± 8	-11 ± 8	-21 ± 10	-33 ± 15
0.010	-28 ± 8	-37 ± 8	-57 ± 10	-66 ± 15
0.012	-55 ± 8	-48 ± 8	-61 ± 10	-69 ± 15

Table 8.4: Fits to W Monte Carlo experiments with varying parton luminosity slope. The slope used in the fitting template was $\beta_W = 0.00636$ GeV^{-1}

In the CDF run 1a analysis, the pdf error is set by performing mass fits to the $W \rightarrow e\nu$ data with templates generated with 17 different pdf choices. In the CDF simulation the pdf are not used in computing the P_T^W distribution so that the pdf choice affects only the mass and rapidity distributions. CDF attributes the variation in the fit masses to the W rapidity distribution. This interpretation is based on the observed correlation between the mean charge asymmetry predicted with a given pdf and the mass fit using that pdf. This correlation is shown in figure 8.3. CDF defines a quantity ζ for each pdf which is the difference between the predicted mean charge asymmetry for $0.2 < |\eta| < 0.7$ and the measured value,

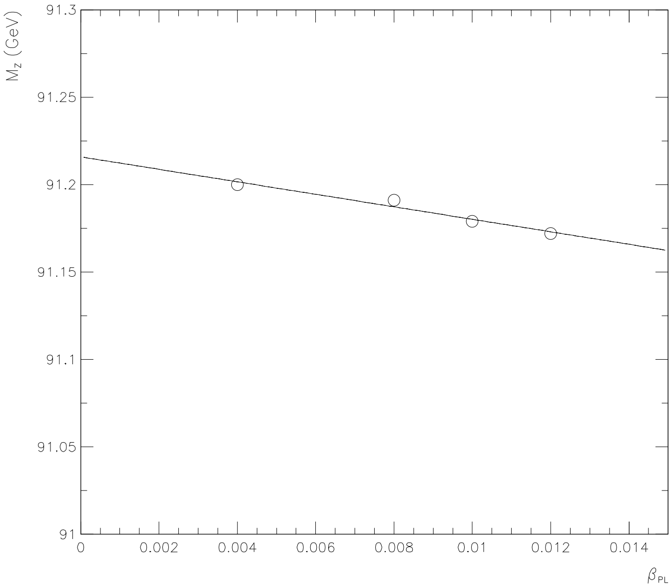

β_{PL}	M_Z fit
0.001	91.200
0.003	91.191
0.005	91.179
0.007	91.172

Table 8.5: Fits to Z Monte Carlo experiments with varying parton luminosity slope.

Fit type	β_{PL} derivative (MeV per 0.001 GeV^{-1})
M_T^W fit	-8.8 ± 1.0
E_T^e fit	-11.4 ± 1.3
$\not{E}_T$ fit	-9.3 ± 1.7
E^e fit	-11.4 ± 12.5
$M(ee)$ fit	-3.6 ± 0.1

Table 8.6: Derivatives of the W and Z mass fits with the parton luminosity slope.

normalized to the error on the measurement

$$\zeta = \frac{A_{PDF} - A_{DATA}}{\delta A_{DATA}} \tag{8.1}$$

The W mass from the transverse mass fit for any pdf is characterized by its difference ΔM_W with the fit obtained using MRSD$-'$ pdf, which was the nominal pdf choice.

For each pdf choice used by CDF we consider the parton luminosity slopes for W and Z production, β_W and β_Z. For easy comparison we calculate these slopes without any rapidity cuts. In figure 8.3 the slope β_W is plotted against the CDF ζ. There is a clear correlation between parton luminosity slope and the asymmetry. Figure 8.1 shows ΔM_W vs. β_W. Since the slope β_W directly biases the mass distribution, it is not surprising that the mass fit correlates with β_W. However, the interesting point is that β_W correlates with ζ. This implies that some of the pdf dependence observed by CDF is due to parton luminosity effects, rather than the W rapidity distribution.

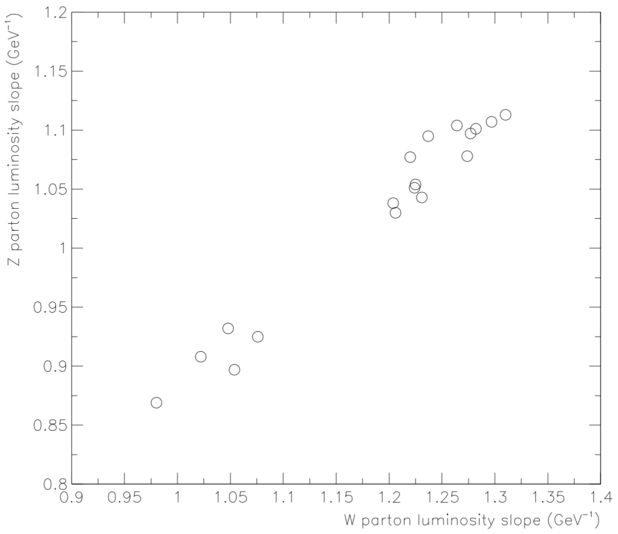

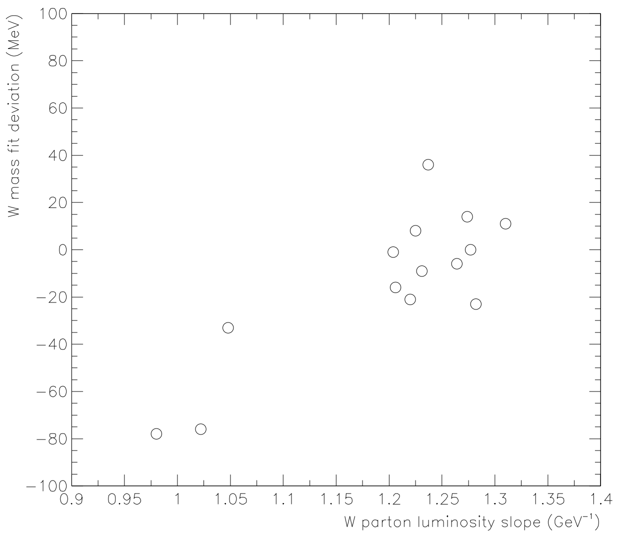

Figure 8.1: (Upper) Correlation between the fitted mass for a pdf choice (ΔM_W) and the W parton luminosity slope for that choice from the CDF Run 1a analysis. (Lower) Correlation between the W and Z parton luminosity slopes.

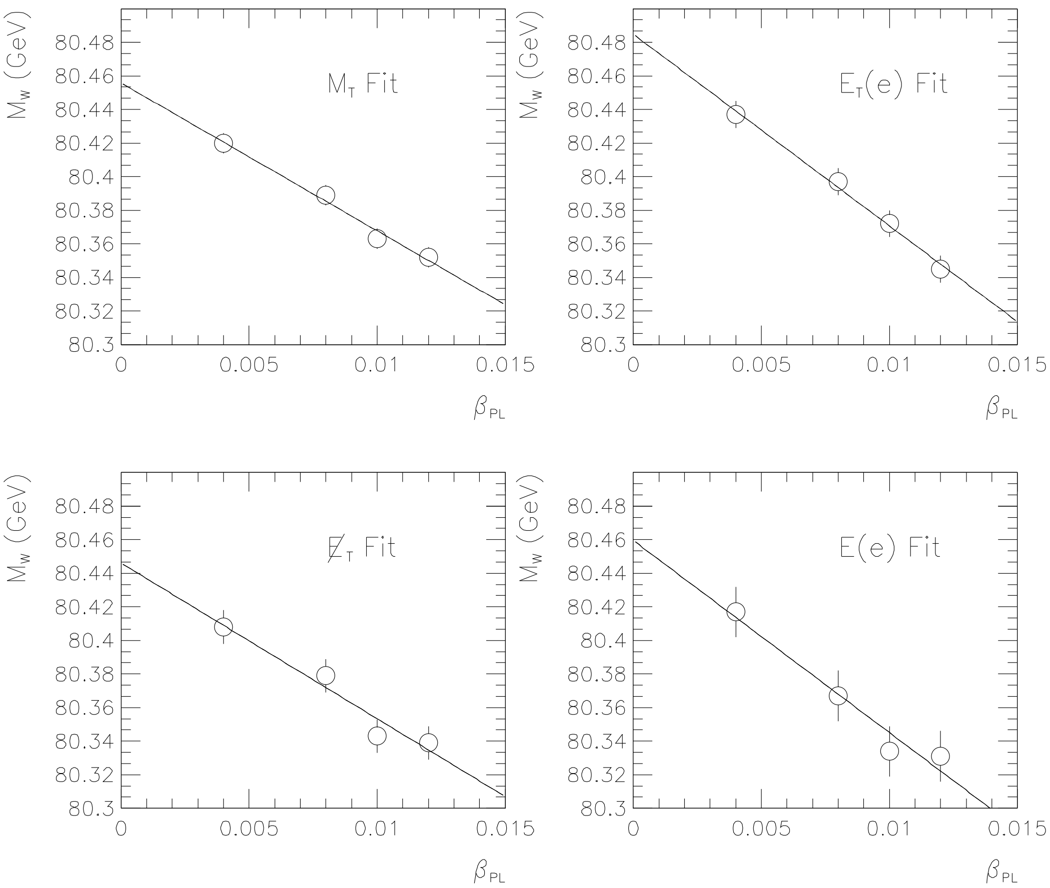

Figure 8.2: Dependence of the W mass fits on the parton luminosity slope β_{PL}.

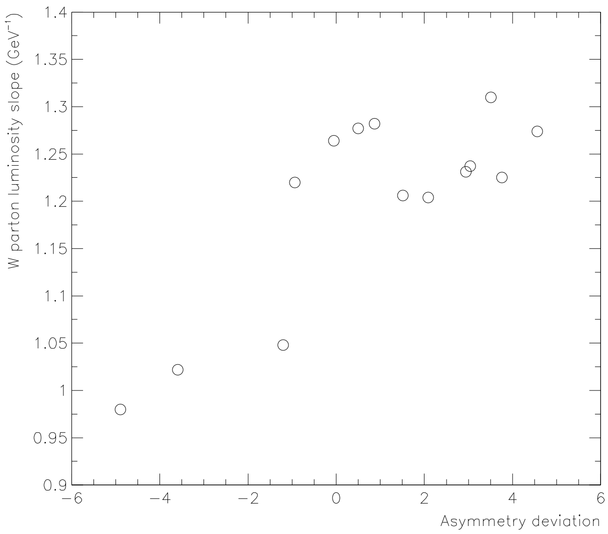

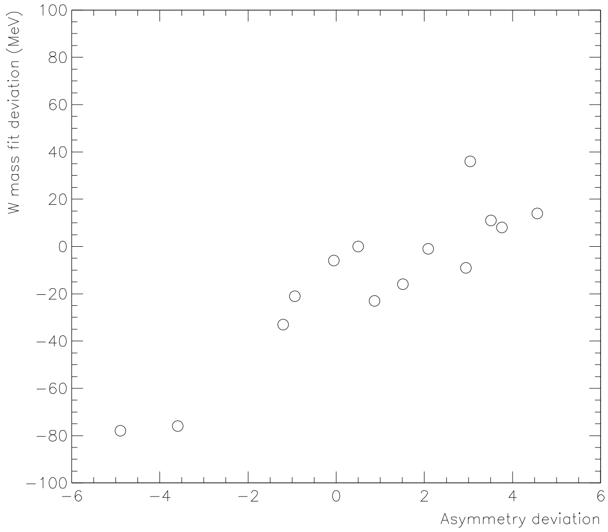

Figure 8.3: W parton luminosity slope (upper) and fitted mass deviation, ΔM_W (lower) vs. CDF charge asymmetry, ζ. ζ is the deviation of the predicted W charge asymmetry from CDF data from the nominal, which is MRSD$-'$. Each point represents a pdf choice.

8.1.2 Rapidity distribution

The effect of the W rapidity distribution was studied by generating Monte Carlo experiments in which only the rapidity distribution was varied. The experiments produced in this way do not correspond to any actual pdf choice, since the pdf affect not only the rapidity spectrum but also the P_T^W spectrum and the parton luminosity slope. Nevertheless it is useful to vary the rapidity distribution independently of other factors so as to understand how it affects the W mass fits.

The Ladinsky–Yuan program LEGACY computes the double–differential distribution $d^2\sigma_W/dP_T dy$, including the correlation between P_T^W and the rapidity, y. Fake y spectra were generated by projecting the double–differential distributions onto the rapidity axis. Fake $d^2\sigma_W/dP_T dy$ grids were generated by multiplying the y spectra with a fixed P_T^W spectrum, namely that computed for MRSA pdf at $y = 0.1$. The resulting grids do not implement the correlation between P_T^W and y. The same P_T^W distribution is used for every y value, for every choice of y distribution.

To check the Ladinsky–Yuan y calculation, HERWIG was used to generate y distributions, integrated over P_T^W and mass. Figure 8.4 shows the rapidity distributions for MRSA and CTEQ3M pdf. The discrepancy between the HERWIG and Ladinsky–Yuan y spectra at large $|y|$ values is due to the mass distributions. In

y calculation	M_T^W fit (± 6 MeV)	E_T^e fit (± 8 MeV)
LEGACY MRSA	0	0
HERWIG MRSA	+5	−4
LEGACY CTEQ3M	+11	+11
HERWIG CTEQ3M	+10	+13
LEGACY CTEQ2M	−20	−33

Table 8.7: Fits to Monte Carlo experiments with different rapidity spectra. Deviations are quoted relative to the value for the LEGACY MRSA experiment.

HERWIG the mass is generated according to a Breit–Wigner, and events which are generated at lower mass may go to higher $|y|$, since the rapidity limit for an object of mass M is $|y| < \log(\sqrt{s}/M)$. In LEGACY, the zero–width approximation is used, so the mass for every event is equal to the resonance mass. Because of the fiducial cut on the electron rapidity, no W events from the high rapidity region enter the sample. The mass fits are therefore insensitive to this mismodelling at high $|y|$.

Table 8.7 shows the mass fits obtained by fitting experiments generated with various rapidity calculations. We chose to consider MRSA and CTEQ3M since these were the most recent pdf from the two major pdf groups at the time of this thesis, and both included the Run 1a W asymmetry data from CDF [49] in their initial data. For both of these pdf choices we calculated the y spectrum using both HERWIG and LEGACY. The HERWIG and Ladinsky–Yuan calculations give the same result within Monte Carlo statistical errors for both MRSA and CTEQ3M. The MRSA and CTEQ3M fits were also consistent with each other within errors. As an excursion from the nominal y distribution we used that calculated from CTEQ2M pdf, using LEGACY. Among those pdf checked, the CTEQ2M pdf showed the largest discrepancy with the CDF asymmetry data. Figure 8.5 shows the folded charge asymmetry measurement from Run 1a, compared to the predictions from several pdf. Since the asymmetry is an experimental observable closely correlated to the W rapidity, this choice corresponds to a large change in the W rapidity spectrum. In fact the CTEQ2M experiment in table 8.7 shows the largest deviation from the others. However, we note that the deviation of the CTEQ2M value of the mean asymmetry from that measured by CDF is 4.56 σ while that of MRSA is 0.87 σ [46]. Therefore the mass shift from CTEQ2M must be interpreted as a several ($\approx$ 3-4) standard deviation effect. Scaling the observed 25 MeV shift down by 3 yields a 1 standard deviation error on M_W of less than 10 MeV. Note that this takes into account only the published CDF Run 1a asymmetry data. Including the preliminary analysis from Run 1b [50] puts an even tighter constraint on the y distribution, as shown in figure 8.5, which is the preliminary combined measurement from Runs 1a and 1b. We conclude that the W mass is insensitive to the y distribution, within the constraints of the present asymmetry measurements.

However, the rapidity distribution will be an important issue for future mass analyses based on forward electrons or muons, such as the DØ Run 1b measurement using electrons from the end calorimeters. For this kinematic regime the rapidity distribution is correlated with the mass distribution, because the events are close to the boundary of the available phase space.

8.1.3 Transverse Momentum distribution

The transverse momentum distribution of the W, P_T^W, is the dominant production model uncertainty in each of the mass fits. In the resummation calculation of the P_T^W distribution, the largest uncertainties arise from the choice of the non–perturbative cutoff function, S_{NP}, and from the choice of pdf. In turn S_{NP} is mostly affected by the parameter g_2 at the Q^2 scales of W and Z production.

In this analysis the choice of g_2 has been set by measuring the P_T^Z distribution, with g_1 and g_3 fixed at the values measured by Ladinsky and Yuan. At a fixed Q^2, the parameter g_1 is 100% correlated with g_2 if the P_T^Z constraint is applied, since g_1 and g_2 appear in S_{NP} only in the combination $g_1 + g_2 \log(Q/Q_0)$ where Q_0 is a

pdf	g_2	E_T^e fit	M_T^W fit	$\not{E}_T$ fit	E^e fit
MRSA	0.38	-55	-3	-29	-47
MRSA	0.78	+59	+8	+17	+18
MRSA	0.98	+97	+14	+18	+34
CTEQ3M	0.38	+31	+17	+15	-26
CTEQ3M	0.58	+72	+22	+32	+11
CTEQ3M	0.78	+129	+30	+53	+21
CTEQ3M	0.98	+169	+16	+66	+53
CTEQ2M	0.38	-75	-32	-68	-81
CTEQ2M	0.58	-20	-18	-35	-58
CTEQ2M	0.78	+15	-23	-10	-31
CTEQ2M	0.98	+72	-20	+3	+4

Table 8.8: Fits to Monte Carlo experiments with different $d^2\sigma_W/dP_T dy$ spectra.

pdf	g_2	M_T^W fit	E_T^e fit	$\not{E}_T$ fit	E^e fit
CTEQ3M	0.544	+5	+48	+22	−21
CTEQ2M	0.608	−21	−17	−30	−39
MRSD−′	0.613	+20	+19	+20	+32

Table 8.9: Fits to Monte Carlo experiments with $d^2\sigma_W/dP_T dy$ spectra computed for different pdf choices with the corresponding values of g_2 from the P_T^Z fits for each pdf. The fitting spectra were generated with nominal MRSA. The values quoted are deviations in MeV from the input value of 80.4 GeV.

constant. Similarly the parameter g_3 is highly correlated with g_2 because we chose to constrain g_2 with the P_T^Z distribution. If a different value of g_3 were chosen, then the value of g_2 from the P_T^Z fit would have to change in such a way that the P_T^Z prediction matched the data. Since varying g_2 provides the largest variations in the P_T^Z and P_T^W spectra, and because of the strong correlations between g_2 and the other parameters from the P_T^Z fit, we choose to vary only g_2 to evaluate the error from the choice of S_{NP}, within the error determined from the P_T^Z fit.

The uncertainty in the P_T^W spectrum due to pdf is also reduced by the P_T^Z fit. For each pdf choice, it is necessary to evaluate a corresponding value of g_2 from the

P_T^Z fit. Choosing a pdf which has a higher average p_T for the Z than the nominal causes the fitted value of g_2 to move down to accommodate the P_T^Z data. The p_T of the W correlates with that of the Z. The net effect is that the p_T distribution of the W changes very little when the choices of pdf and g_2 are simultaneously changed in such a way that the P_T^W modelling is consistent with the Z data.

Table 8.8 shows the variation in the mass fits when Monte Carlo experiments with varying g_2 values are fit with a nominal template for MRSA, CTEQ3M and CTEQ2M pdf. Table 8.9 shows similar fits where for each pdf choice we fix g_2 to the value fit from the P_T^Z data using that pdf choice. The fits were performed with the nominal MRSA template. The variation shown in this table is used to set the pdf error from the $d^2\sigma_W/dP_T dy$ distribution.

The parameter g_2 is constrained to finite precision from the Z sample, where the error is mainly statistical. Figures 8.6, 8.7 and 8.8 show the variations in the mass fits with g_2 for different pdf choices. The derivatives are approximately independent of the pdf choice. Table 8.10 shows the derivatives for MRSA, CTEQ3M and CTEQ2M pdf.

Fit type	MRSA derivative	CTEQ3M derivative	CTEQ2M derivative
E_T^e fit	258 ± 18	236 ± 18	238 ± 18
M_T^W fit	30 ± 13	3 ± 13	16 ± 13
$\not\!\!E_T$ fit	79 ± 22	87 ± 22	119 ± 22
E^e fit	131 ± 34	124 ± 34	141 ± 34

Table 8.10: Derivatives of the mass fits with respect to g_2 for different pdf choices.

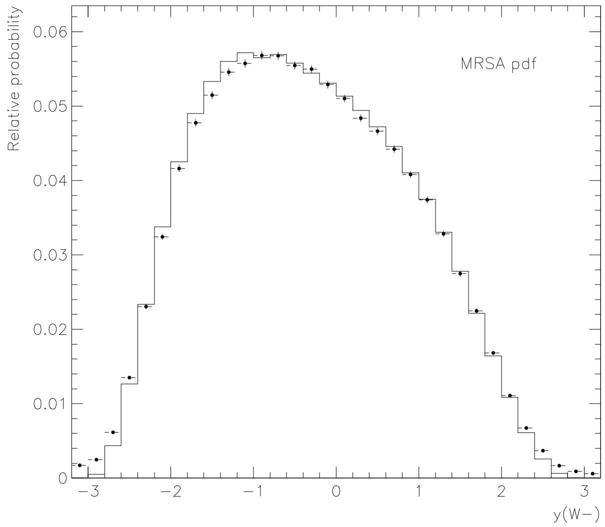

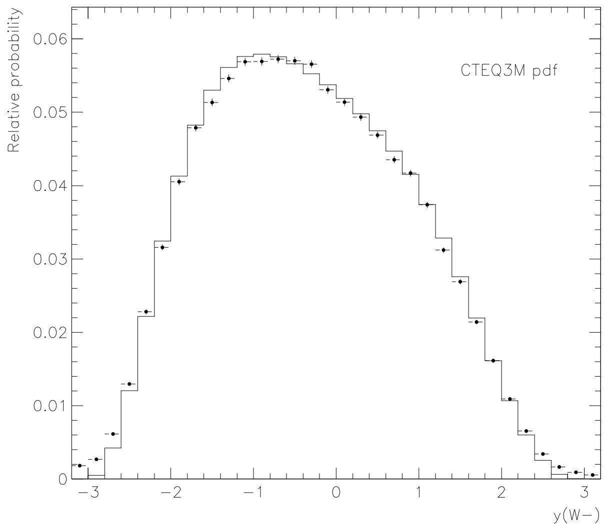

Figure 8.4: Rapidity distributions for W^- production from HERWIG (solid circles) and LEGACY (line) for MRSA pdf (upper) and CTEQ3M pdf (lower).

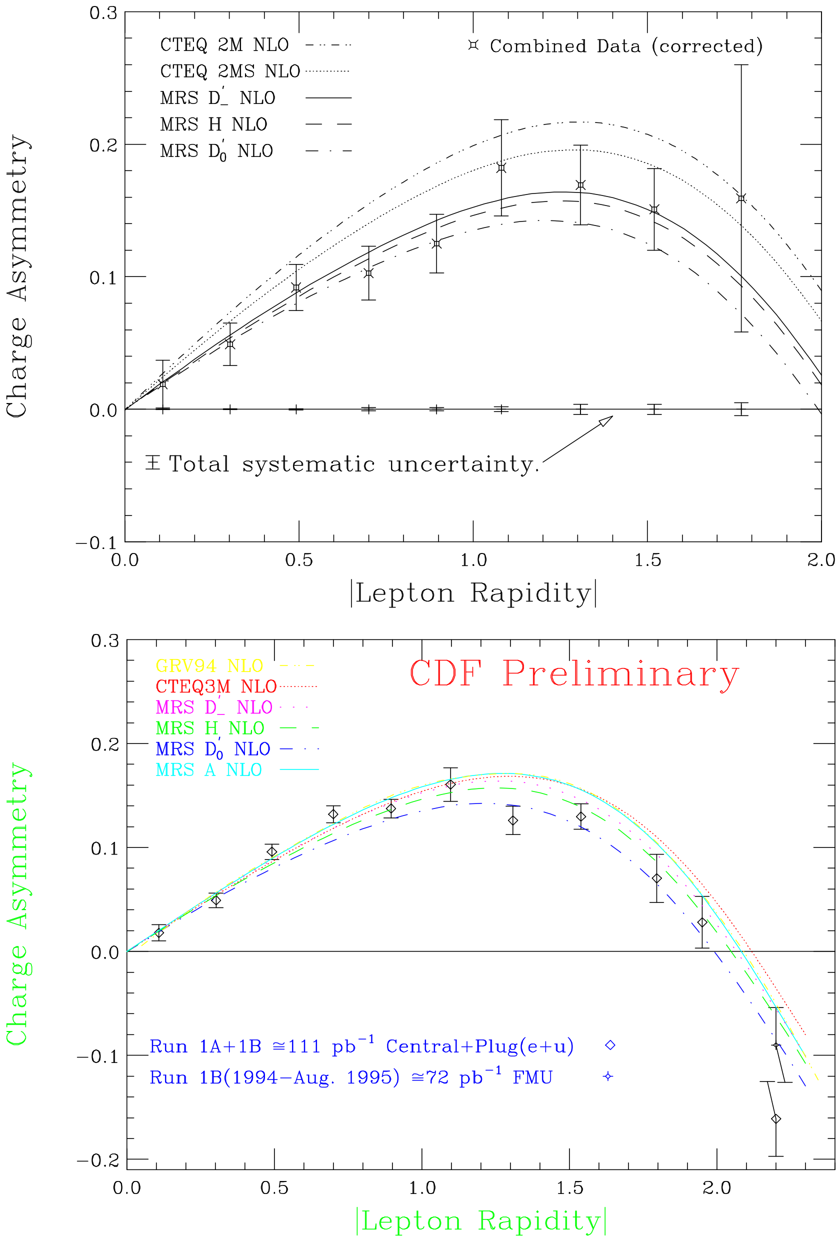

Figure 8.5: (Upper) The published CDF charge asymmetry measurement from Run 1a (Lower) The preliminary measurement from Run 1b and 1a combined, including forward lepton data.

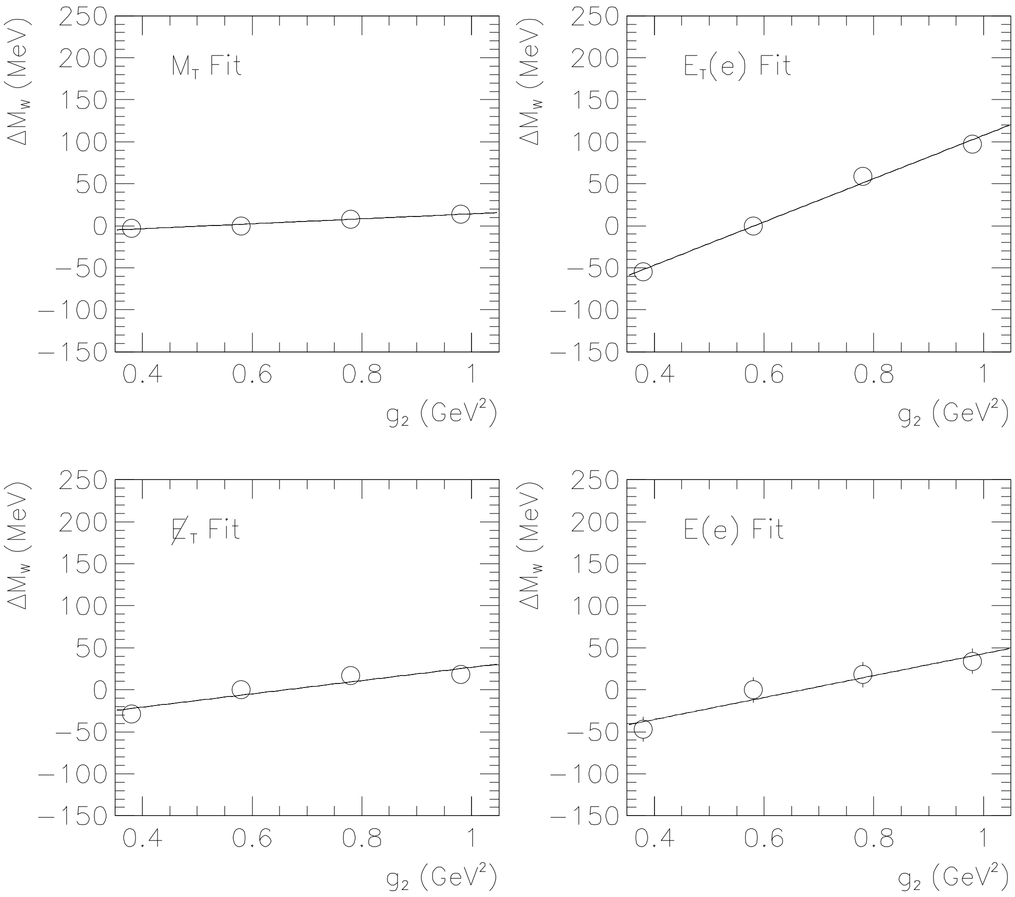

Figure 8.6: Variation in the W mass fit with respect to g_2 for MRSA pdf.

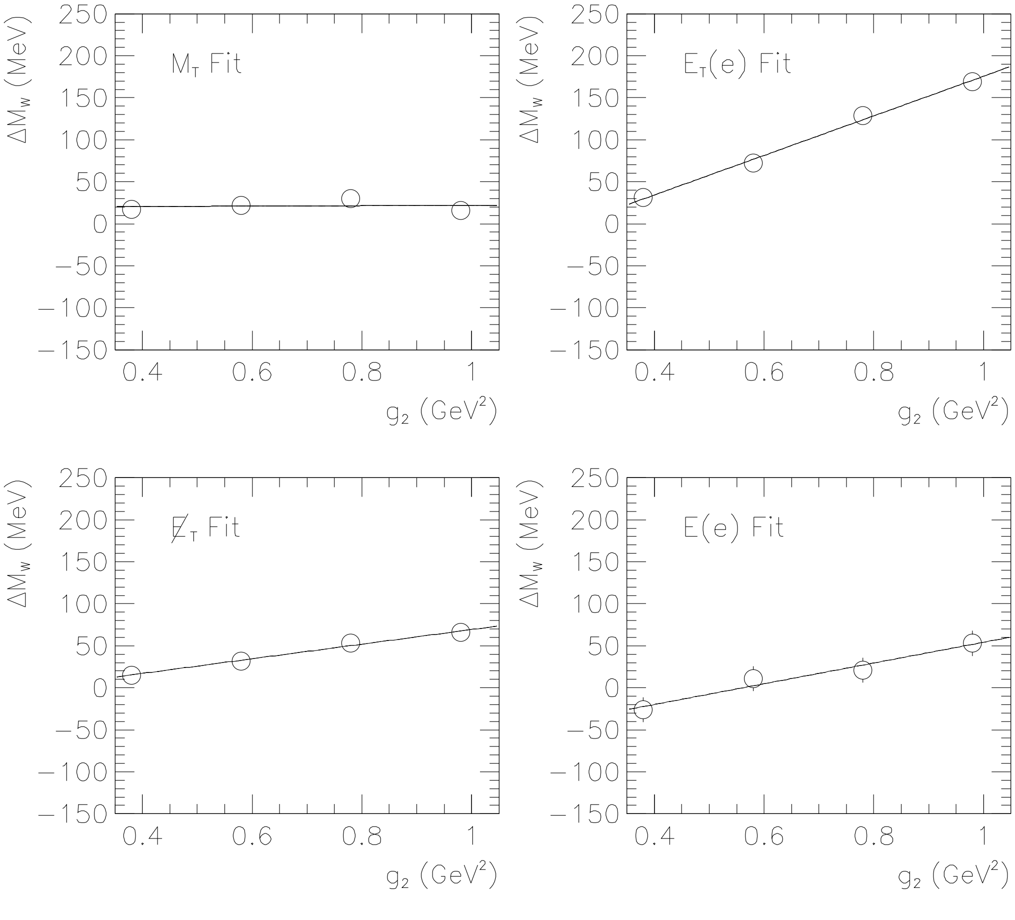

Figure 8.7: Variation in the W mass fit with respect to g_2 for CTEQ3M pdf.

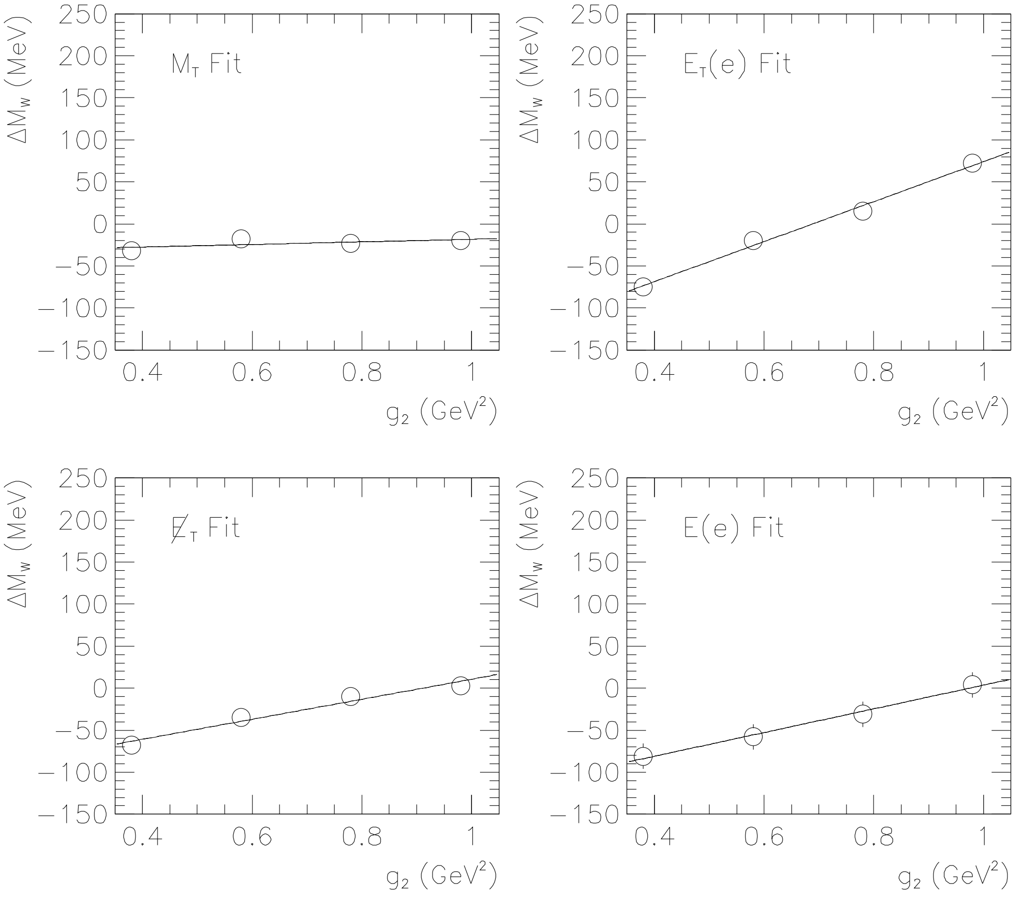

Figure 8.8: Variation in the W mass fit with respect to g_2 for CTEQ2M pdf.

8.2 Decay Model

8.2.1 Radiative decays

We assign an error to the modelling of radiative decays based on the varying the detector parameters E_γ^{min} and $\Delta_R^{coalesce}$. E_γ^{min} defines the minimum photon energy generated and corresponds to a cutoff below which the photon does not reach the calorimeter. $\Delta_R^{coalesce}$ defines the maximum separation between the photon and electron directions above which the photon energy is not included in the electron shower. In general radiation shifts the fitted mass down for the transverse mass and electron fits, because for a fraction of the events the photon energy is subtracted from the electron. Hence increasing $\Delta_R^{coalesce}$ decreases the radiative shift. Similarly, decreasing E_γ^{min} decreases the radiative shift. Therefore the fitted W mass depends on the assumed values of E_γ^{min} and $\Delta_R^{coalesce}$. However, the fitted Z mass depends on these parameters in a similar manner and so there is a partial cancellation in the W/Z mass ratio. To estimate the systematic error, Monte Carlo experiments were generated with varying E_γ^{min} and $\Delta_R^{coalesce}$ and fit with a nominal template using $E_\gamma^{min} = 50\,\mathrm{MeV}$ and $\Delta_R^{coalesce} = 0.3$. The results for the W are shown in tables 8.11 and 8.12 and for the Z in tables 8.13 and 8.14.

There are also theoretical errors in the radiative decay calculation. The radia-

E_γ^{min} (MeV)	E_T^e fit	M_T^W fit	$\not{E}_T$ fit	E^e fit
25	-2	$+3$	-4	$+19$
75	$+6$	$+15$	$+9$	$+12$
100	$+4$	$+2$	$+28$	$+1$
125	$+10$	$+16$	$+16$	$+45$
150	-2	-3	$+2$	-6

Table 8.11: Fits to W Monte Carlo experiments with varying E_γ^{min}. The fitting template was generated with $E_\gamma^{min} = 50\,\text{MeV}$.

$\Delta_R^{coalesce}$	E_T^e fit	M_T^W fit	$\not{E}_T$ fit	E^e fit
0.1	$+3$	-10	$+23$	-12
0.2	$+11$	-2	$+19$	$+1$
0.4	$+16$	$+6$	$+24$	$+62$
0.5	$+13$	$+7$	$+20$	$+37$

Table 8.12: Fits to W Monte Carlo experiments with varying $\Delta_R^{coalesce}$. The fitting template was generated with $\Delta_R^{coalesce} = 0.3$.

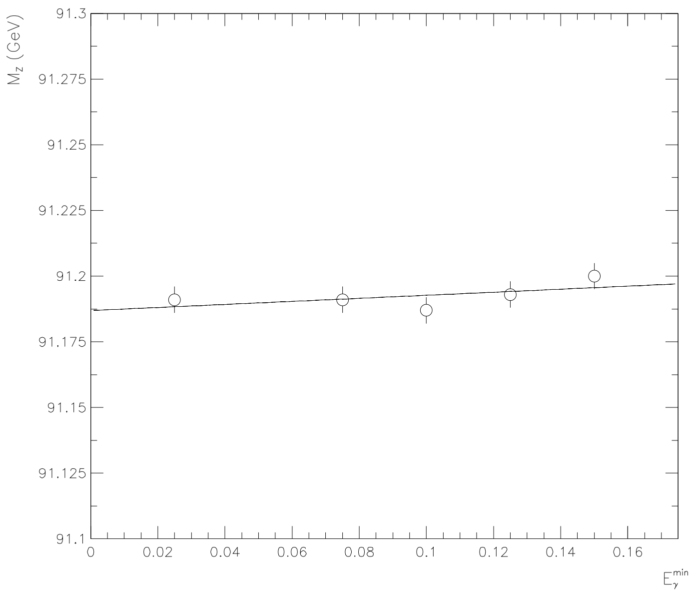

E_γ^{min} (MeV)	$M(ee)$ fit
25	91.191
75	91.191
100	91.187
125	91.193
150	91.200

Table 8.13: Fits to Z Monte Carlo experiments with varying E_γ^{min}. The fitting template was generated with $E_\gamma^{min} = 50\,\text{MeV}$.

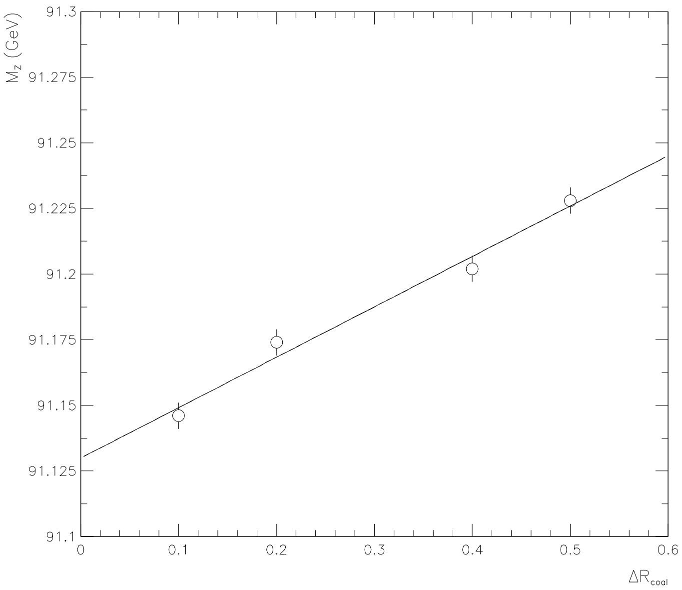

$\Delta_R^{coalesce}$	$M(ee)$ fit
0.1	91.146
0.2	91.174
0.4	91.202
0.5	91.228

Table 8.14: Fits to Z Monte Carlo experiments with varying $\Delta_R^{coalesce}$. The fitting template was generated with $\Delta_R^{coalesce} = 0.3$.

Fit type	$\Delta_R^{coalesce}$ derivative (MeV per 0.1)
M_T^W fit	2.5 ± 0.6
E_T^e fit	4.2 ± 0.6
$\not\!\!E_T$ fit	-0.1 ± 2.8
E^e fit	15.9 ± 5.3
$M(ee)$ fit	19.2 ± 0.6

Fit type	$\Delta_R^{coalesce}$ derivative (MeV per 0.1)	Error (MeV)
M_T^W fit	-14.4	15
E_T^e fit	-12.7	13
$\not\!\!E_T$ fit	-17.0	17
E^e fit	-1.1	2

Table 8.15: (Upper) Derivatives of the W and Z mass fits with respect to $\Delta_R^{coalesce}$. (Lower) W mass fit derivatives after the Z mass is rescaled to the LEP value.

Fit type	E_{γ}^{min} derivative (MeV per 0.1)
M_T^W fit	0.025 ± 0.037
E_T^e fit	-0.020 ± 0.093
$\not{E}_T$ fit	0.091 ± 0.061
E^e fit	-0.058 ± 0.135
$M(ee)$ fit	0.058 ± 0.032

Fit type	E_{γ}^{min} derivative (MeV per 0.1)
M_T^W fit	-0.03 ± 0.07
E_T^e fit	-0.07 ± 0.05
$\not{E}_T$ fit	0.04 ± 0.08
E^e fit	-0.11 ± 0.18

Table 8.16: Derivatives for radiative decay parameter E_{γ}^{min}. All derivatives are consistent with zero, so no error has been assigned.

tive cross section depends on the electron mass and the fine structure constant. However, these are very precisely known [66] and do not contribute significantly to the error. Initial state QED radiation is not included in the Berends and Kleiss calculation, however, initial state radiation does not affect the final state kinematic distributions used to fit the mass. Finally, the calculation only includes processes in which a single photon is radiated. The two–photon calculation is involved and is not expected to be completed for some time, though substantial progress has been made, with calculations available for the muon case [37]. Naively one might expect two–photon effects to be large, since the fraction of radiative events is large, approximately 31% for W events and 66% for Z events for a photon threshold of 50 MeV. However, the mass shift from radiative events is caused by those events in which the photon does not merge with the electron shower. Therefore the relevant fraction of events is not the total radiative fraction, but the fraction of radiative events with $\Delta_R(e,\gamma) > \Delta_R^{coalesce}$. Ignoring quantum mechanical interference effects, the mass shift from two–photon events can be roughly estimated as this fraction multiplied by the shift caused by single photon events. For the W this fraction is about 3.5%. The radiative shifts are about 50 MeV for the transverse mass fit and electron E_T fit. We therefore expect that the two–photon events will affect the fits at the 5 MeV level. Following reference [15] we increase the radiative decay error to 20 MeV for each mass fit to cover two–photon effects. This is a fairly conservative estimate since the total radiative shift in the W/Z mass ratio is only $60 - 100$ MeV depending on the fit type. Table 8.17 shows the radiative shifts for each fit, where the shift is calculated as the mass fit using spectra generated with radiation to a Monte Carlo experiment generated with radiation turned off.

Fit type	Mass shift (MeV)
M_T^W fit	$+50 \pm 7$
E_T^e fit	$+43 \pm 9$
$\not\!\!E_T$ fit	$+30 \pm 11$
E^e fit	$+63 \pm 16$
$M(ee)$ fit	$+143 \pm 4$

Fit type	Mass shift (MeV)
M_T^W fit	-76 ± 8
E_T^e fit	-80 ± 10
$\not\!\!E_T$ fit	-96 ± 12
E^e fit	-63 ± 16

Table 8.17: (Upper) Radiative shifts in W and Z mass fits. (Lower) Radiative shifts in W mass fits after rescaling the Z mass to the LEP value.

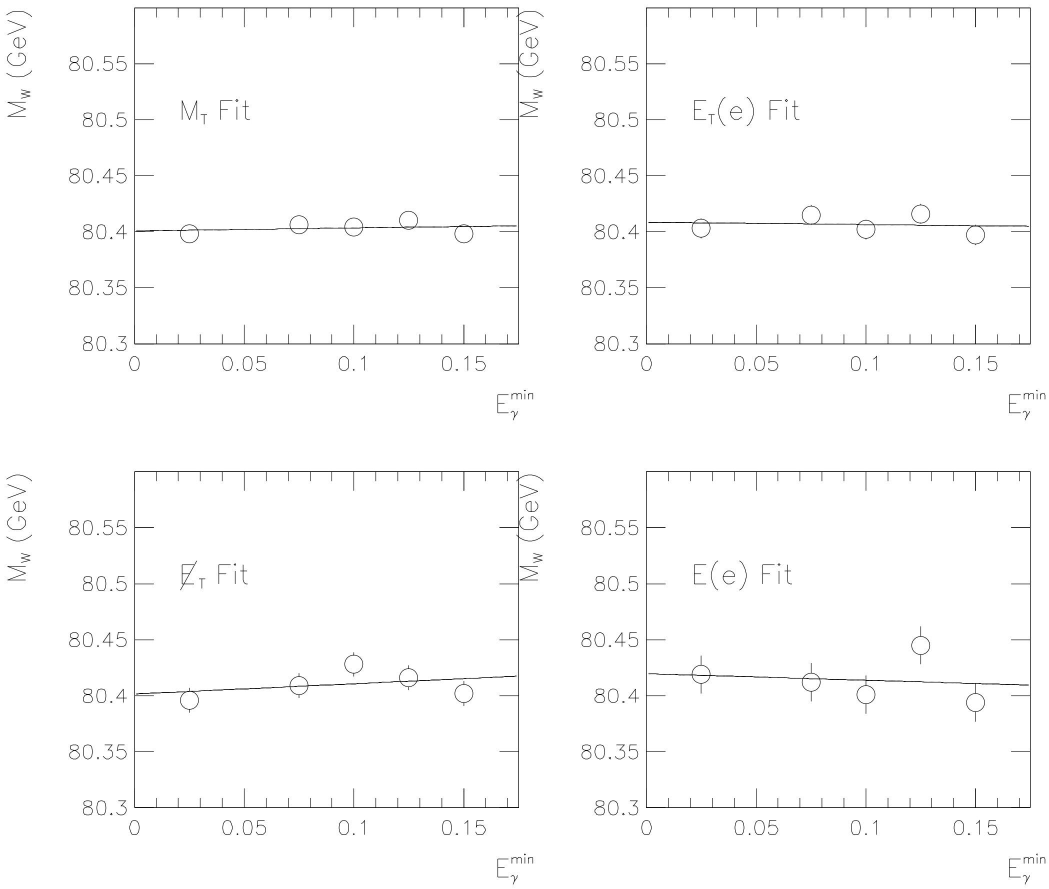

Figure 8.9: W fits vs. E_γ^{min}, without rescaling the Z mass to the LEP value.

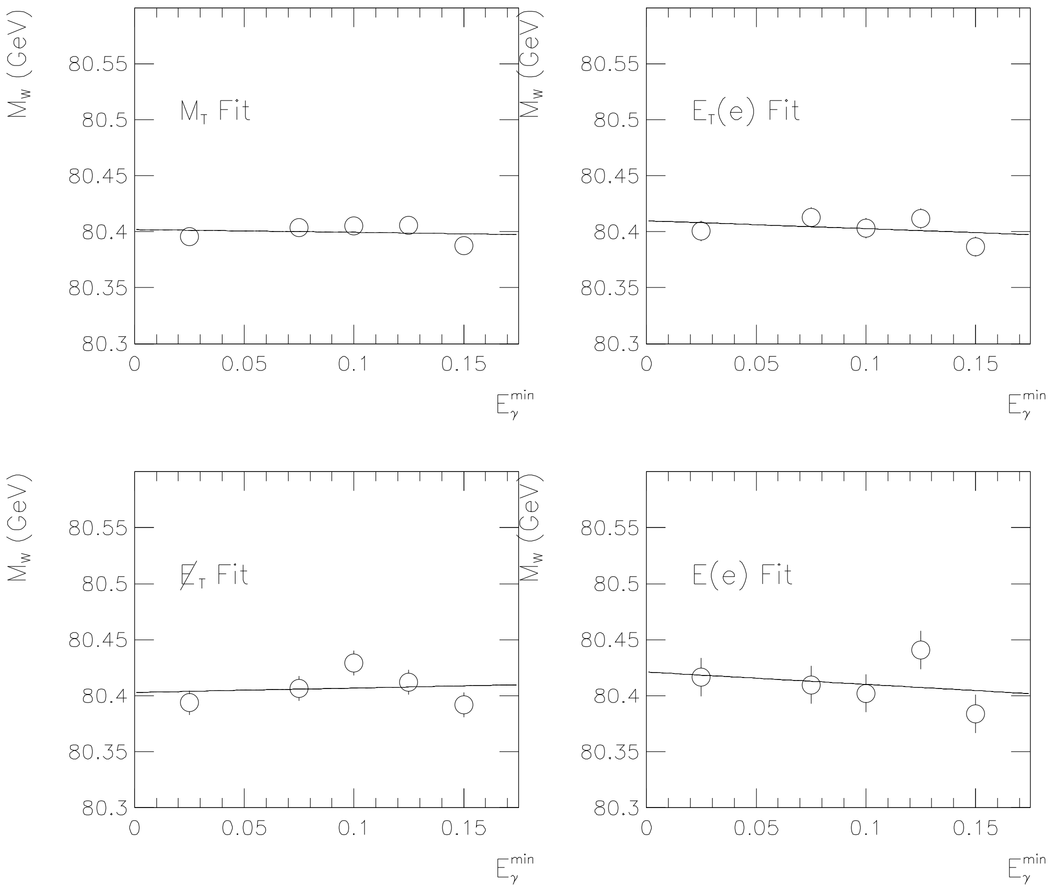

Figure 8.10: W fits vs. E_γ^{min}, after rescaling the Z mass to the LEP value.

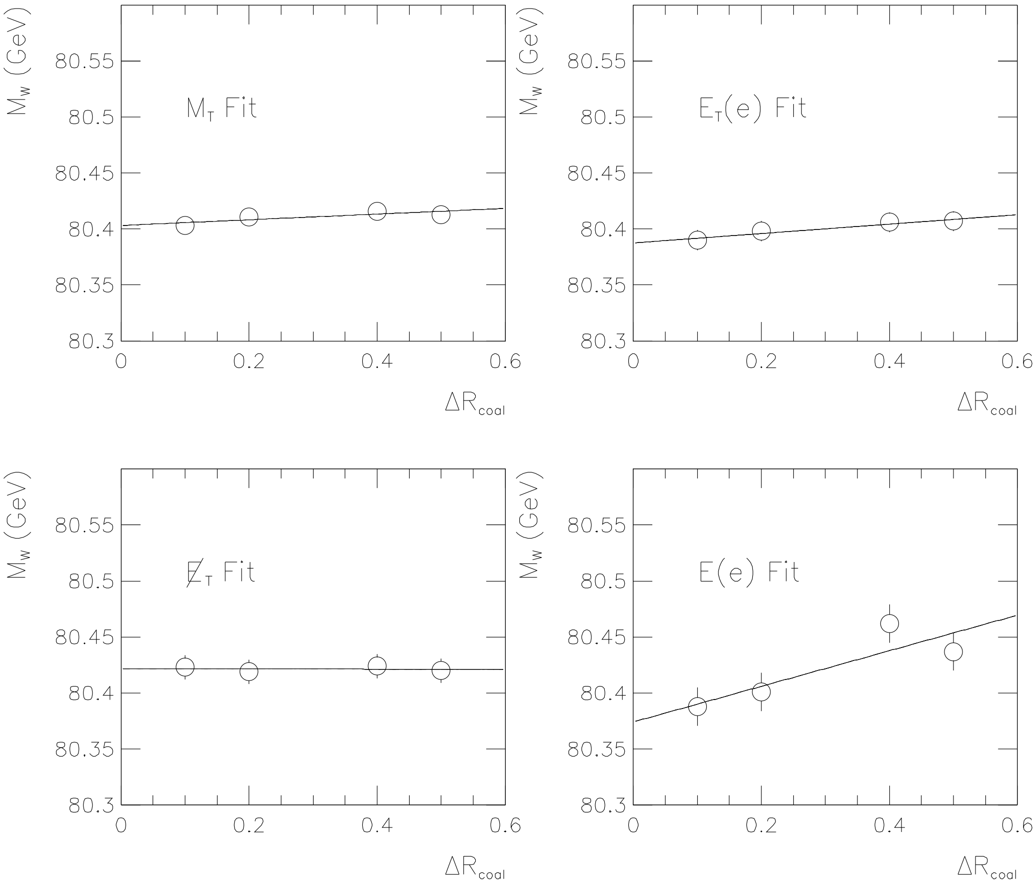

Figure 8.11: W fits vs. $\Delta_R^{coalesce}$, without rescaling the Z mass to the LEP value.

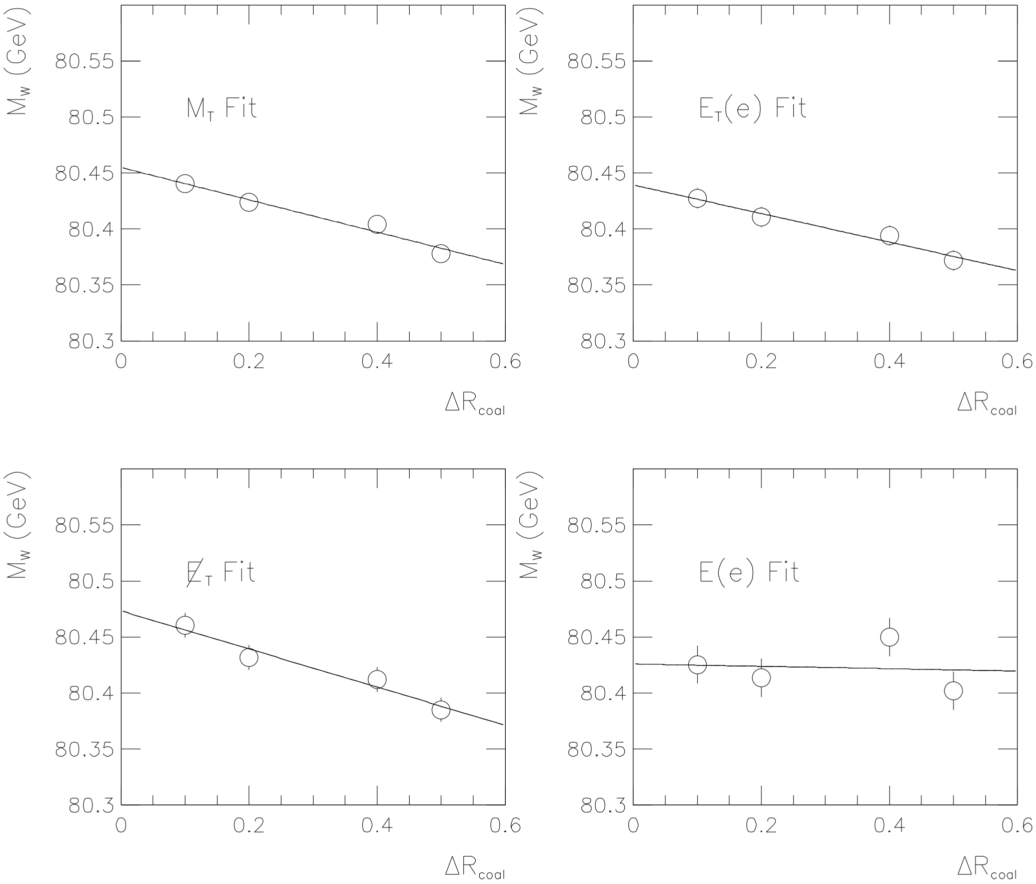

Figure 8.12: W fits vs. $\Delta_R^{coalesce}$, after rescaling the Z mass to the LEP value.

8.2.2 $W \to \tau\nu \to e\nu\nu\nu$ decays

The irreducible $W \to \tau\nu \to e\nu\nu\nu$ background is included in the CMS simulations. The W kinematics are done the same way as the $W \to e\nu$ decays. The dominant uncertainty from τ events arises from the τ fraction, since the τ mass and decay kinematics are precisely known.

The fraction of events in the W sample originating from $W \to \tau\nu \to e\nu\nu\nu$ decays, f_τ, is given by

$$f_\tau = \frac{BR(W^+ \to \tau^+\nu) \times BR(\tau \to e\nu\bar{\nu})}{BR(W^+ \to \tau^+\nu) \times BR(\tau \to e\nu\bar{\nu}) + BR(W^+ \to e^+\nu)} \tag{8.2}$$

The error on f_τ can be minimized by writing

$$f_\tau = \frac{Rg}{Rg+1} \tag{8.3}$$

where $R = BR(W^+ \to \tau^+\nu)/BR(W^+ \to e^+\nu)$ and $g = BR(\tau \to e\nu\bar{\nu})$. The particle data group values for R and g are

$$R = 1.00 \pm 0.08 \tag{8.4}$$

$$g = 0.1801 \pm 0.0018 \tag{8.5}$$

The derivatives of f_τ with respect to R and g are

$$\frac{\partial f_\tau}{\partial R} = \frac{g}{(Rg+1)^2} \approx 0.1293 \tag{8.6}$$

$$\frac{\partial f_\tau}{\partial g} = \frac{R}{(Rg+1)^2} \approx 0.7181 \tag{8.7}$$

The errors on f_τ from R and g are therefore

$$\frac{\partial f_\tau}{\partial R} \cdot \Delta R = (0.1293)(0.08) = 0.0103 \tag{8.8}$$

$$\frac{\partial f_\tau}{\partial g} \cdot \Delta g = (0.7181)(0.0018) = 0.0013 \tag{8.9}$$

Therefore the error on f_τ is dominated by the R measurement

$$\Delta f_\tau = 0.0104 \tag{8.10}$$

The calculated value of f_τ is 0.1525. Setting the τ fraction to zero produces mass shifts in the fits shown in table 3.3. Scaling these shifts by the ratio 0.01/0.1525 gives the systematic errors in table 8.18.

Note that if we assume lepton universality then the error due to f_τ becomes negligible. Lepton universality implies that the branching ratio of W to τ and electron final states is the same up to a small correction due to the τ mass, so that $R = 1$. Currently the f_τ error contributes very little in any case to the overall error, so that the decision to assume lepton universality or not is really a matter of taste.

Fit quantity	f_τ error	
	$P_T^W < 30$ GeV	$P_T^W < 15$ GeV
E_T^e fit	5	6
M_T^W fit	4	5
$\not{E}_T$ fit	7	8
E^e fit	11	13

Table 8.18: Systematic errors from the τ fraction.

8.3 Summary

The theoretical errors in the W mass fits are shown in table 8.19. Cancellations in the W/Z mass ratio have been taken into account.

Source of error	E_T^e fit	M_T^W fit	$\not{E}_T$ fit	E^e fit
Production model				
Parton luminosity	10	10	10	10
W width	7	9	6	3
$d^2\sigma_W/dP_Tdy$: pdf	48	21	30	39
$d^2\sigma_W/dP_Tdy$: g_2	28	5	9	14
Decay model				
$W\to\tau\nu\to e\nu\nu\nu$ fraction	6	5	8	13
radiative decays	20	20	20	20
Total	61	33	40	49

Table 8.19: Summary of theoretical errors in the W mass fits.

Chapter 9

Systematic Errors: Experimental Effects

9.1 Overview

An accurate W mass measurement requires careful modelling of detector effects. Smearing effects which would have little or no consequence for an invariant mass fit may affect the W mass fits because the W appears as a Jacobian edge rather than a peak. The elements of the detector model are in most cases constrained by the $Z \rightarrow ee$ data. Since there is only a finite Z sample, there is an error associated with each part of the detector model. Although these errors are considered as systematic errors for the W mass fit, they are really statistical errors which depend on the number of Z events. In other cases, some aspect of the detector model is determined by an external analysis which carries its own statistical and systematic error.

In this chapter I discuss the uncertainties from the electron reconstruction, recoil reconstruction, efficiencies which bias the event kinematics and backgrounds.

9.2 Electron Reconstruction

9.2.1 Electron Energy Response and resolution

As discussed previously, the electron response in the central calorimeter can be described with a scale, α_{CC}, and an offset, β_{CC}. The scale factor cancels exactly in the W/Z mass ratio. To estimate the effect of an offset, W and Z Monte Carlo experiments were generated with a varying offset introduced. Because the energies of electrons from W and Z events are very similar, the effect of the offset largely cancels in the ratio. Table 9.1 shows the results of fits to Monte Carlo experiments with varying energy offsets for W events, and table 9.2 the corresponding numbers for Z events. Table 9.3 shows the derivatives of the fit results, including the W fits after rescaling to the Z mass from LEP for each β_{CC}, showing the cancellation

MC experiment β_{CC} (MeV)	M_T^W fit	E_T^e fit	$\not{E}_T$ fit	E^e fit
-100	-160	-161	-156	-166
-50	-67	-89	-80	-100
50	$+120$	$+110$	$+111$	$+117$
100	$+220$	$+189$	-215	-209

Table 9.1: Fits to MC experiments with different β_{CC}.

which occurs in the W/Z mass ratio.

To determine the error from the energy resolution, Monte Carlo experiments were generated changing the constant term c_{EM} in the energy resolution. The fits to these experiments are shown in table 9.4. Table 9.5 shows the errors associated with the fits. The error is computed to be 1/2 the spread between the fit values for 0% and 1% constant terms. No cancellation occurs in the W/Z ratio because the Z mass is insensitive to the resolutions.

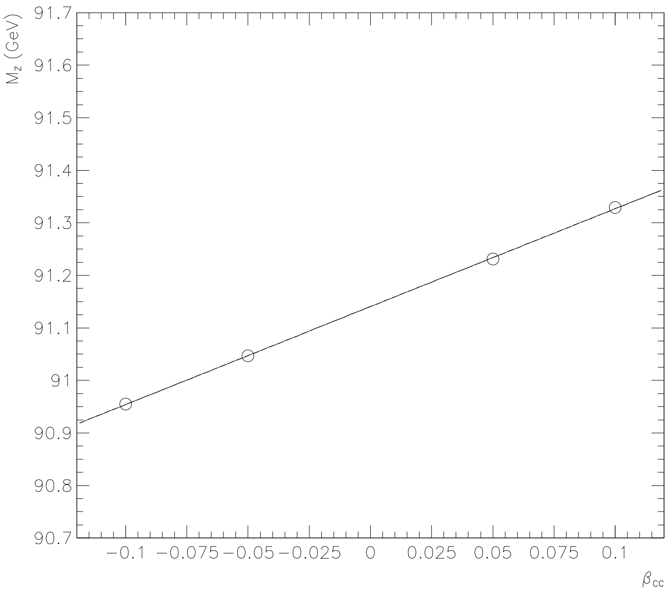

MC experiment β_{CC} (MeV)	$M(ee)$ fit
-100	-233
-50	-141
50	$+43$
100	$+141$

Table 9.2: Fits to $Z\rightarrow ee$ MC experiments with different β_{CC}.

Fit type	β_{CC} derivative (MeV per MeV)
M_T^W fit	1.890 ± 0.045
E_T^e fit	1.798 ± 0.053
$\not\!\!E_T$ fit	1.864 ± 0.079
E^e fit	1.934 ± 0.107
$M(ee)$ fit	1.864 ± 0.019

Fit type	β_{CC} derivative (MeV per MeV)	M_W Error
M_T^W fit	0.245 ± 0.044	51
E_T^e fit	0.153 ± 0.057	32
$\not\!\!E_T$ fit	0.219 ± 0.078	46
E^e fit	0.289 ± 0.109	61

Table 9.3: (Upper) Derivatives of W and Z mass fits with respect to β_{CC}. (Lower) Derivatives of W mass fits after rescaling the Z to the LEP value.

MC experiment c_{EM}	M_T^W fit	E_T^e fit	$\not{E}_T$ fit	E^e fit
0.000	80.381	80.390	80.397	80.415
0.005	80.386	80.391	80.400	80.366
0.010	80.409	80.403	80.405	80.394
0.015	80.452	80.426	80.428	80.418
0.020	80.507	80.461	80.509	80.395

Table 9.4: Fits to MC experiments with different c_{EM}. The fitting functions were generated with $c_{EM} = 0.009$.

Fit	M_W error (MeV)
M_T^W fit	14
E_T^e fit	7
$\not{E}_T$ fit	4
E^e fit	0

Table 9.5: Systematic errors for the electron energy resolution.

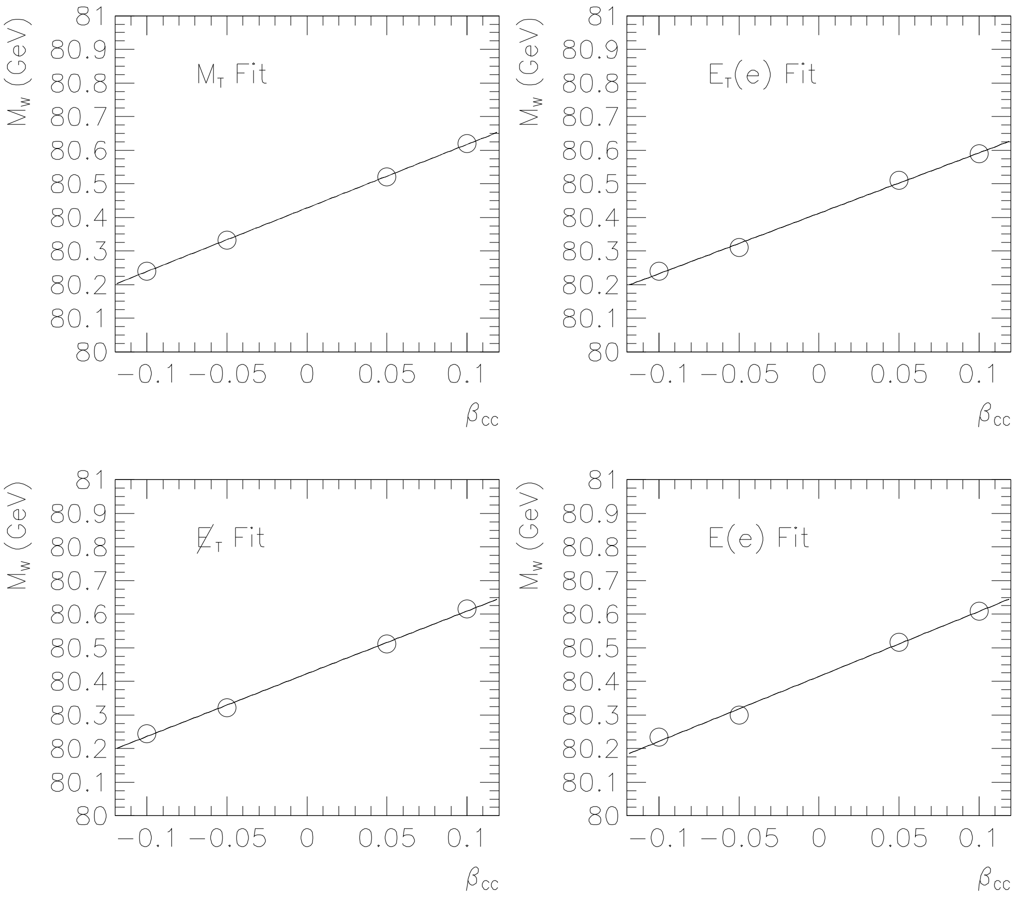

Figure 9.1: W mass fits without rescaling the Z mass to the LEP value.

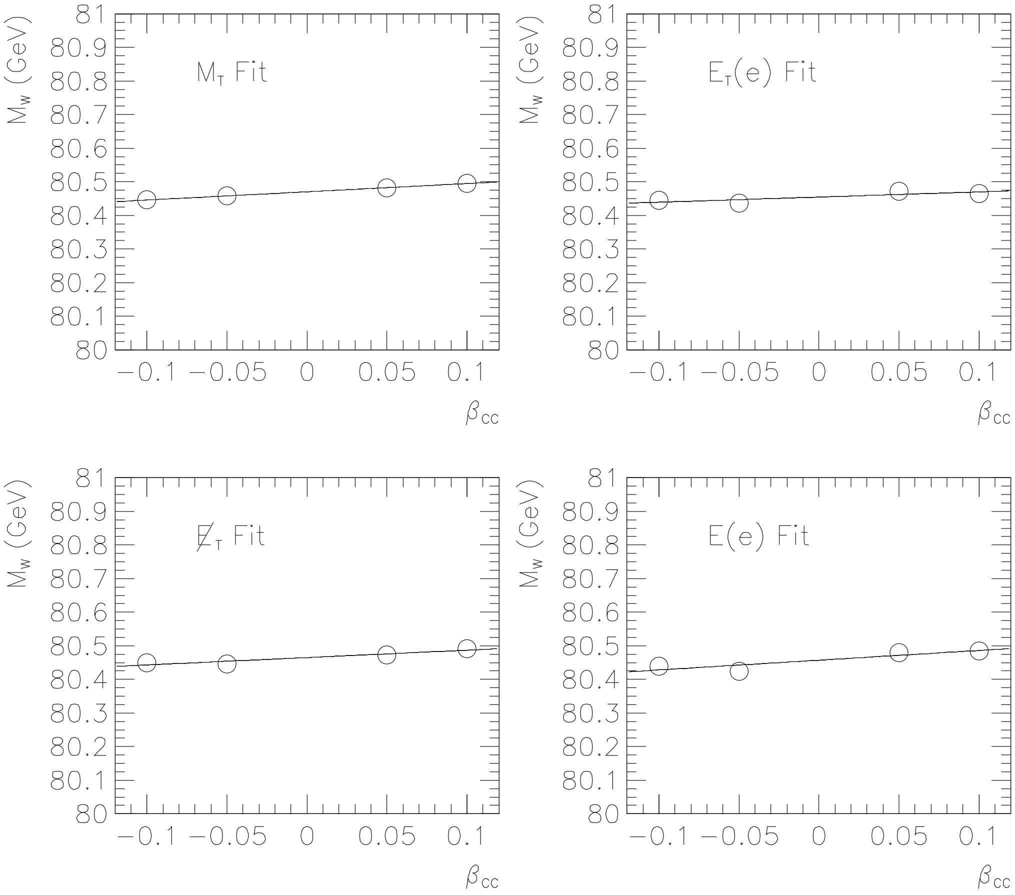

Figure 9.2: W mass fits after rescaling the Z mass to the LEP value.

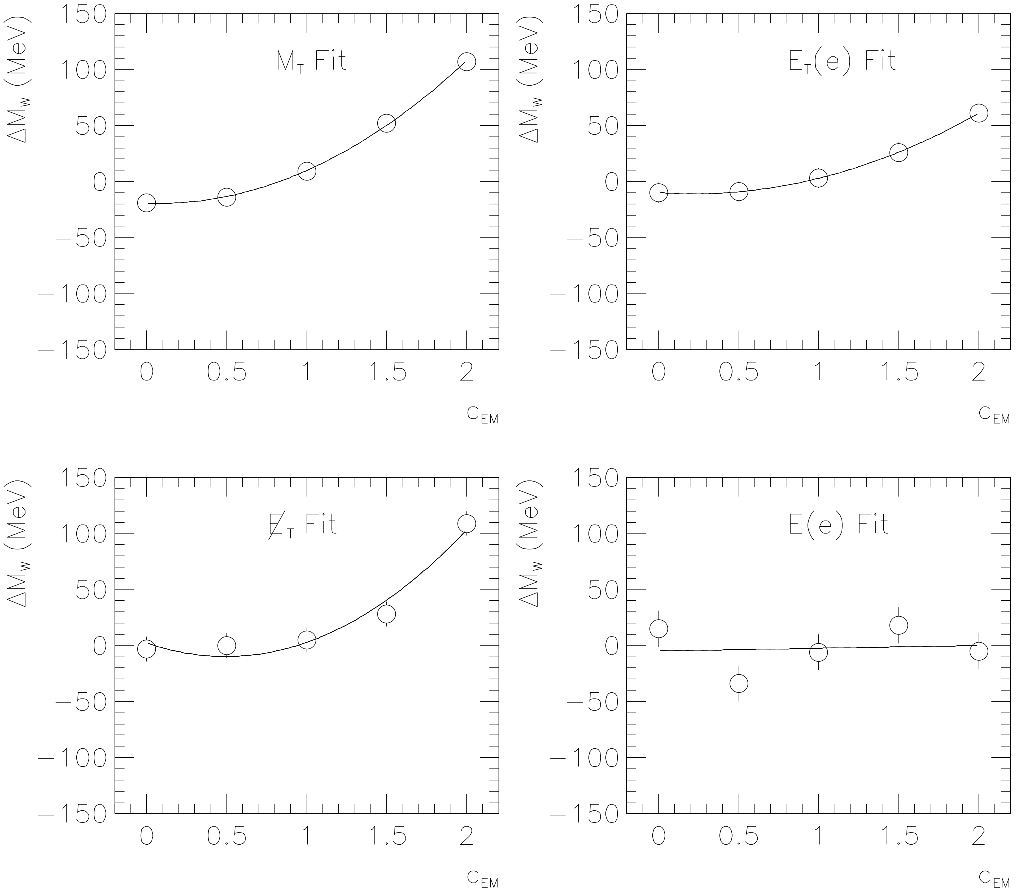

Figure 9.3: Variations in mass fits with respect to the electron energy resolution

9.2.2 Electron Angle

The dominant error from the electron angle is from the error on the CDC track z position scale calibration. The z_{TRK} measurement has been calibrated using muons, and the scale factor for the CDC averaged over all CDC sectors is $\alpha_{CDC} = 0.988 \pm 0.001$. To estimate the error one must account for a partial cancellation which occurs in the W/Z mass ratio. Monte Carlo experiments were generated with a range of CDC scale values for W and Z events. The results of the W fits are in table 9.6 and the Z mass fits in table 9.7. The variation of the W fits and rescaled W fits are shown in figures 9.4 and 9.5.

A similar variation is necessary for the calorimeter position. However, since the calorimeter position cailbration is performed by $z_1 - z_2$ minimization in $Z \rightarrow ee$ events, the calorimeter and CDC z scales are correlated. An error analysis which accounts for this correlation has been performed by E. Flattum [62]. The correlated error is shown in table 9.19, and corresponds approximately to an error of 0.0015 in the CDC scale alone.

MC CDC scale	M_T^W fit	E_T^e fit	$\not{E}_T$ fit	E^e fit
0.950	78.770	78.702	78.781	80.773
0.990	80.089	80.058	80.087	80.509
0.995	80.257	80.231	80.246	80.452
1.005	80.598	80.581	80.589	80.412
1.010	80.769	80.758	80.759	80.337
1.050	82.195	82.133	82.098	80.015

Table 9.6: Fits to $W \rightarrow e\nu$ MC experiments with different CDC scale factors. The fitting functions were generated with a CDC scale of 1.0. The errors are 7,9,11 and 16 MeV for the M_T^W fit, E_T^e fit, $\not{E}_T$ fit and E^e fit respectively.

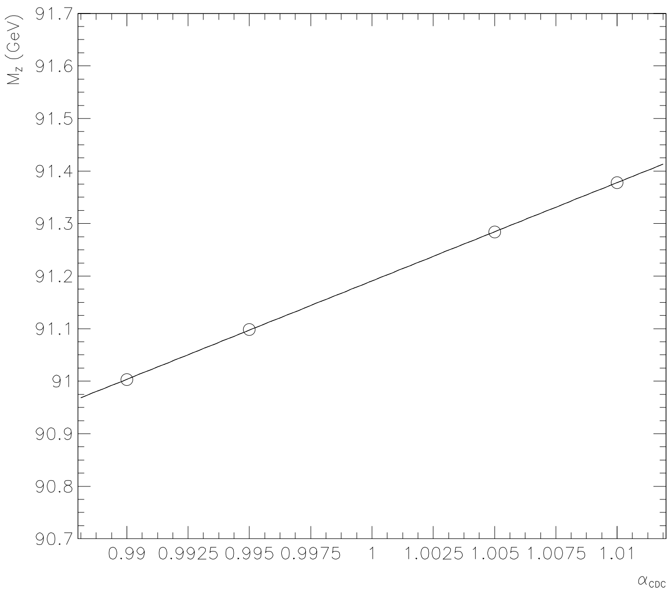

MC experiment CDC scale α_{CDC}	$M(ee)$ fit (± 3 MeV)
0.990	91.003
0.995	91.098
1.005	91.284
1.010	91.378

Table 9.7: (Lower) Fits to $Z \rightarrow ee$ MC experiments with different CDC scale factors. The fitting functions were generated with a CDC scale of 1.0. (Upper) Z mass fit vs. α_{CDC}.

Fit	α_{CDC} derivative (MeV/0.001)
M_T^W fit	34.02 ± 0.17
E_T^e fit	35.00 ± 0.07
$\not{E}_T$ fit	33.74 ± 0.09
E^e fit	-7.67 ± 0.13
$M(ee)$ fit	18.72 ± 0.02

Fit	α_{CDC} derivative (MeV/0.001)	M_W error (MeV)
M_T^W fit	17.51 ± 0.06	18
E_T^e fit	18.49 ± 0.07	19
$\not{E}_T$ fit	17.21 ± 0.09	18
E^e fit	-24.19 ± 0.13	25

Table 9.8: Derivatives of the mass fits with respect to the CDC length scale.

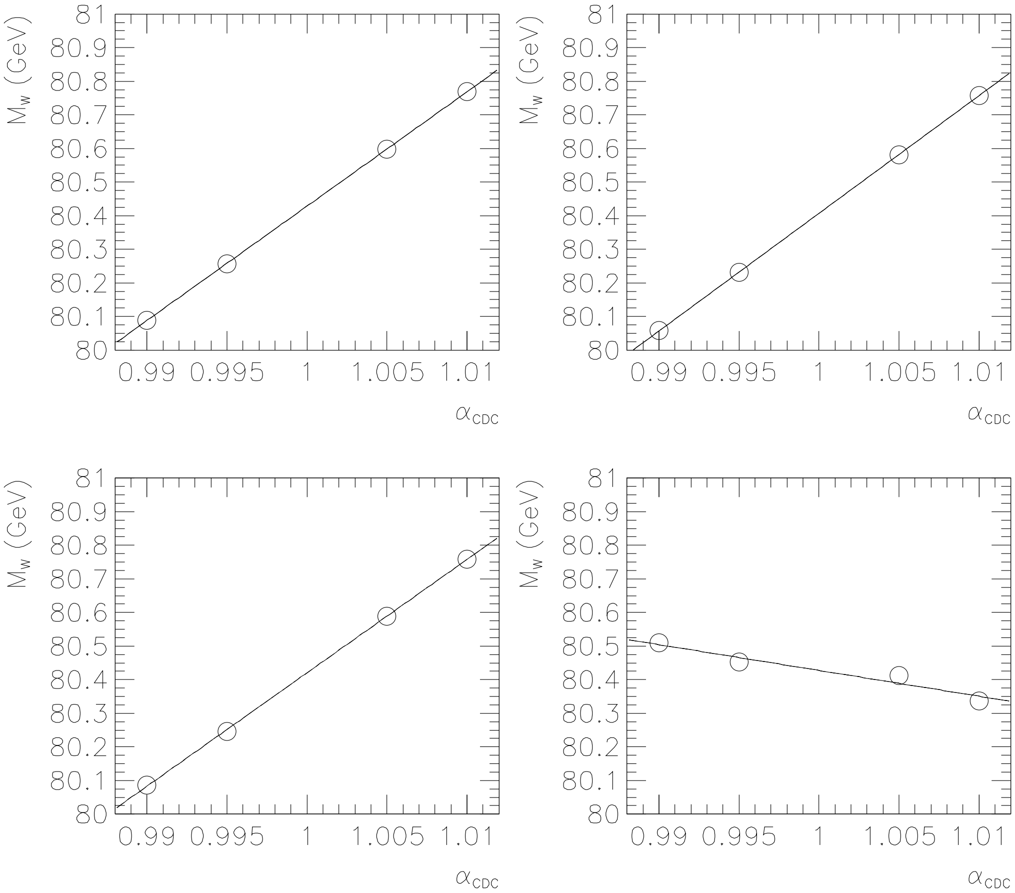

Figure 9.4: Variation of W mass fits with respect to the CDC scale, without rescaling the Z mass.

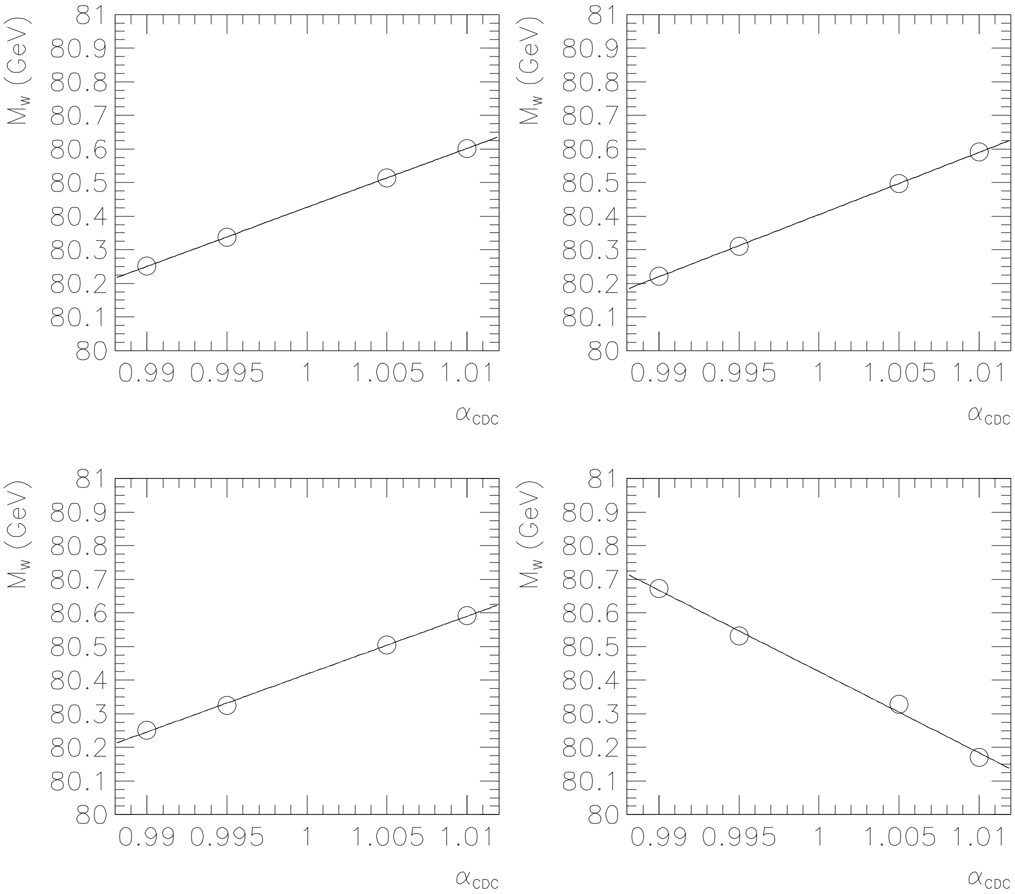

Figure 9.5: Variation of W mass fits with respect to the CDC scale, after rescaling to the Z mass from LEP.

9.3 Recoil Reconstruction

9.3.1 Hadronic Response

The hadronic recoil scale has been measured relative to the electromagnetic scale by comparing the p_T of the Z measured from the recoil to that measured from the electron pair. This approach makes the measurement insensitive to the details of the hadronic reconstruction, such as jet energy corrections. For any hadronic reconstruction algorithm the W and Z recoil systems should behave in the same way, since the p_T distributions, jet multiplicity and energy distributions should all be essentially the same for W and Z events. Therefore systematic effects largely cancel if the effective hadronic response is measured from the Z sample. In this analysis, the recoil is simply the vector sum of calorimeter E_T over all cells except those in the electron window. No jet corrections are applied. In principle one could improve the recoil resolution by applying jet corrections. However, in the present analysis this is not done because the recoil distributions of W and Z events are soft, typically a few GeV. The events with hard recoil are removed by requiring the recoil to be less than 15 GeV. Since the jet corrections are not well measured for low p_T jets, it is not clear that they would improve the recoil measurement. In addition, at DØ jets are not reconstructed below 8 GeV, so that the analysis would suffer from threshold effects.

To determine the systematic error from the hadronic recoil scale, Monte Carlo experiments were generated at scales from 0.75 to 0.83. The results are shown in table 9.9 and displayed in figure 9.6. The derivatives computed from these linear fits are shown in table 9.10.

A more sophisticated model using a two parameter non–linear response has also been investigated. The response assumed is

$$\mathcal{R}_{rec} = \alpha_{rec} + \beta_{rec} \log P_T \tag{9.1}$$

where $\mathcal{R}_{rec}$ is the ratio of the measured to true recoil on average. The parameters α_{rec} and β_{rec} are fit from $Z \rightarrow ee$ data and are therefore correlated. The resulting correlated error in the mass fits is shown in table 9.19.

These numbers have the interesting feature that variations in α_{HAD} move the M_t and $\not{E}_T$ fits in opposite directions. The electron fits vary because the cut on P_T^W becomes more severe as α_{HAD} is increased. Therefore the samples which survive the P_T^W cut have on average smaller P_T^W, and the mass fits from the electron decrease. However, the electron fits are affected much less than the M_t or $\not{E}_T$ fits. The transverse mass can be approximated as $M_t = 2p_T(e) + u_{||}$. The mean value of $u_{||}$ is negative. Increasing the hadronic scale therefore increases the magnitude of $u_{||}$ on the average, which decreases the M_t on average since $u_{||} < 0$. On the

α_{HAD}	M_T^W fit	E_T^e fit	$\not{E}_T$ fit	E^e fit
0.75	$+40$	$+27$	-50	$+26$
0.77	$+25$	$+14$	-19	$+13$
0.79	-2	$+1$	$+40$	0
0.81	-55	-41	$+46$	-17
0.83	-63	-34	$+101$	-13

Table 9.9: Results of fits to MC experiments with varying α_{HAD}. The result quoted is the shift in MeV from the input mass of 80.4 GeV.

other hand the magnitude of the $\vec{\not{E}_T}$ vector can be written $\not{E}_T = |\vec{p_T}(e) + \vec{u}|$. The $\not{E}_T$ can be thought of as the $\vec{p_T}(e)$ vector, with a two–dimensional smearing from the $\vec{p_T}^W$ vector. Smearing a vector in two dimensions increases its magnitude on average. Therefore increasing the hadronic response increases the mean $\not{E}_T$.

Fit	Derivative (MeV per %)	M_W error (MeV)
M_T^W fit	14.3 ± 1.1	43
E_T^e fit	8.9 ± 1.4	27
$\not{E}_T$ fit	-18.4 ± 1.7	55
E^e fit	5.4 ± 2.5	16

Table 9.10: Derivatives of the mass fits with respect to α_{HAD} and corresponding errors in M_W.

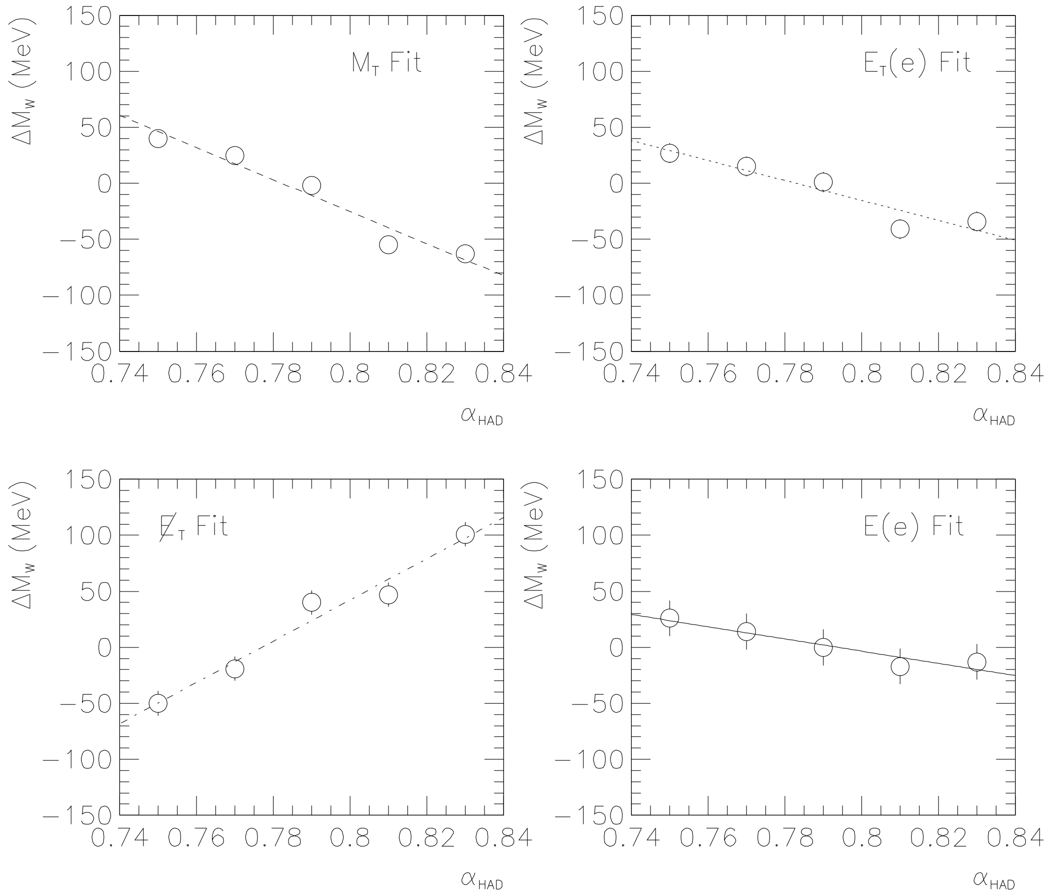

Figure 9.6: Results of fits to MC experiments with varying α_{HAD}.

9.3.2 Hadronic Recoil Resolution

Since the hadronic recoil is measured using the entire calorimeter excluding the electron, it includes resolution contributions from both the recoil hadrons and the underlying event, as well as noise, pileup and multiple interactions. The resolution due to the recoil hadrons should be oriented parallel to the recoil direction, while that from all other effects should be uncorrelated in azimuth with the recoil direction. The first resolution component is called the "asymmetric" piece and the second the "symmetric" piece.

The asymmetric hadronic recoil resolution is oriented along the recoil direction and is parametrized using a sampling term

$$\sigma(P_T^W) = S_{HAD}\sqrt{P_T^W} \tag{9.2}$$

The sampling term S_{HAD} is left as a parameter to be constrained from the Z. The symmetric hadronic recoil resolution (uniform in azimuth) is modelled using the $\not{E}_T$ distributions of minimum bias events. For each event a $\not{E}_T$ value is picked from the reweighted minimum bias library in luminosity bins described previously, scaled by a parameter α_{MB}, and added to the simulated W event. The values of α_{MB} and S_{HAD} are correlated since they are both obtained by fitting the same Z data. If one makes S_{HAD} larger then one is forced to a lower α_{MB} to be consistent

α_{MB}	M_T^W fit	E_T^e fit	$\not{E}_T$ fit	E^e fit
0.90	-138	-2	-383	-57
0.95	-80	0	-222	-14
1.00	-30	$+14$	-74	-10
1.05	$+51$	$+18$	$+98$	$+4$
1.10	$+103$	$+25$	$+262$	$+28$

Table 9.11: Variation in the W mass fits with α_{MB}.

with the observed hadronic resolution in the Z events, and vice–versa.

Table 9.11 shows the results of fits to Monte Carlo experiments with varying α_{MB}, and table 9.13 similar results for varying S_{HAD}. The results are plotted in figures 9.7 and 9.8. The derivatives of the mass fits are tabulated in tables 9.12 and 9.14. The tables show the uncertainties in the mass fits due to the errors on α_{MB} and S_{HAD} separately. A correlated error analysis performed by E. Flattum and U. Heintz yields the errors shown in the summary table 9.19.

Fit type	α_{MB} derivative (MeV per unit)	M_W error (MeV)
E_T^e fit	144 ± 57	4
M_T^W fit	1226 ± 44	37
$\not{E}_T$ fit	3220 ± 70	97
E^e fit	378 ± 101	11

Table 9.12: Derivatives of the W mass fits with respect to α_{MB}.

S_{HAD}	M_T^W fit	E_T^e fit	$\not{E}_T$ fit	E^e fit
10%	-39	$+8$	-27	$+27$
30%	-29	$+15$	-21	$+24$
70%	$+52$	-12	$+53$	-12
90%	$+112$	$+8$	$+135$	$+35$

Table 9.13: Variation in the W mass fits with S_{HAD}.

Fit type	S_{HAD} derivative (MeV per 100%)	M_W error (MeV)
E_T^e fit	-14 ± 12	2
M_T^W fit	192 ± 11	29
$\not\!\!E_T$ fit	199 ± 17	30
E^e fit	-10 ± 25	2

Table 9.14: Derivatives of the W mass fits with respect to S_{HAD}.

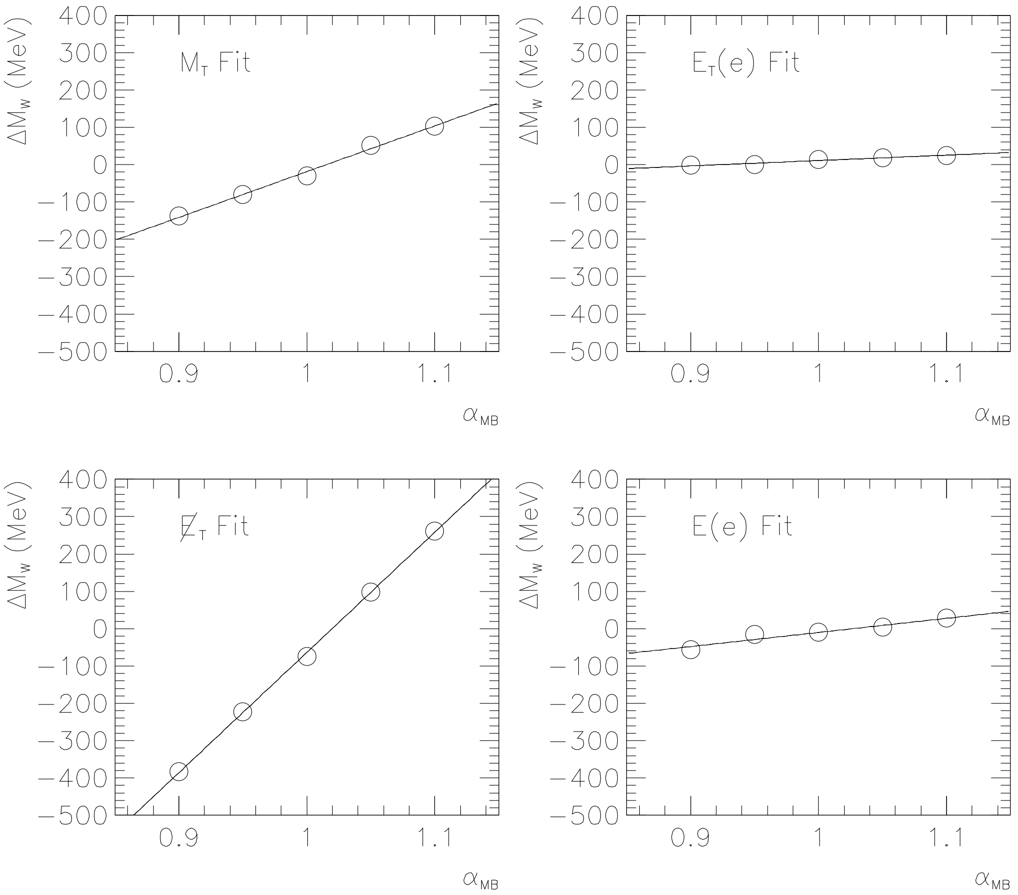

Figure 9.7: Results of fits to MC experiments with varying α_{MB}.

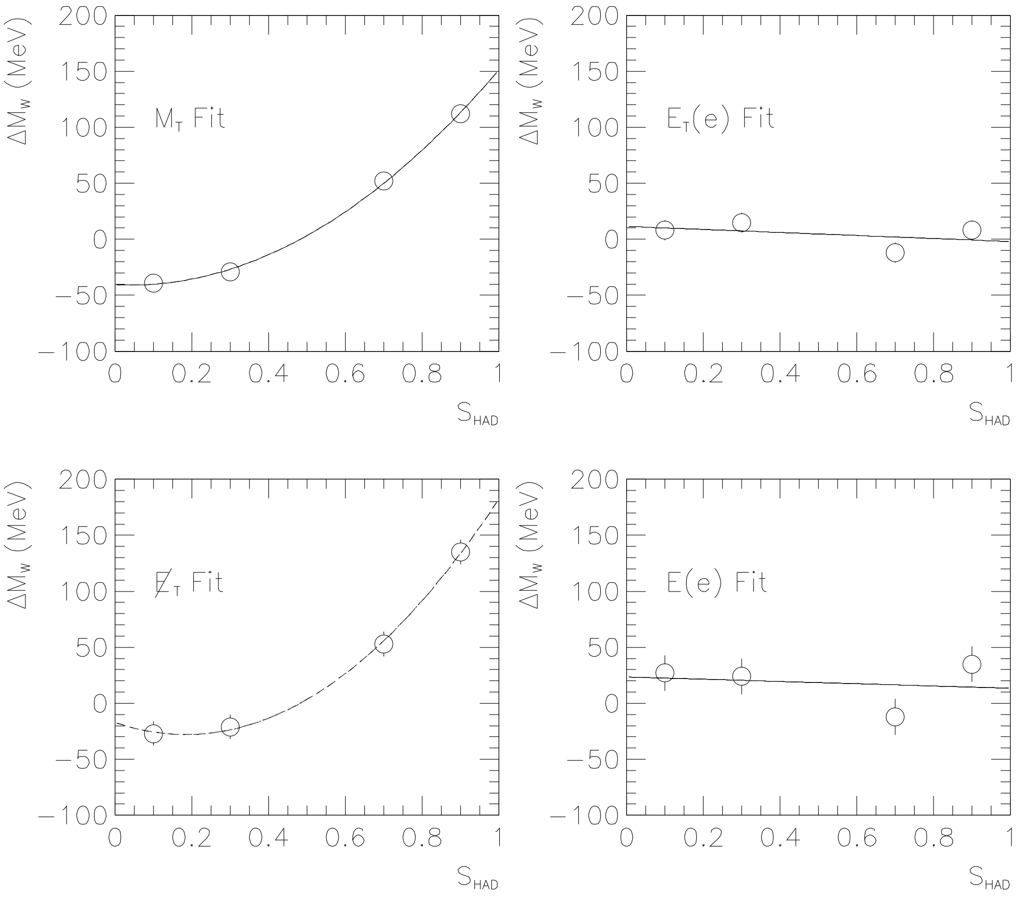

Figure 9.8: Results of fits to MC experiments with varying S_{HAD}.

MC experiment	M_T^W fit	E_T^e fit	$\not\!\!E_T$ fit	E^e fit
No $p_T(e)$ trigger efficiency	$+3 \pm 6$	$+11 \pm 8$	-21 ± 10	-26 ± 15
No $\not\!\!E_T$ trigger efficiency	$+13 \pm 6$	$+2 \pm 6$	$+15 \pm 10$	-1 ± 15

Table 9.15: Results of MC experiments with trigger efficiency curves turned off. The results quoted are the differences in MeV between the fit to the MC experiment and the input mass of 80.4 GeV.

9.4 Efficiencies

9.4.1 Trigger Efficiencies

Monte Carlo experiments were generated with the electron trigger efficiency turned off, and with the $\not\!\!E_T$ trigger efficiency turned off. The results are in table 9.15. In all cases there are no statistically significant shifts when the trigger efficiencies are removed. This expected since the trigger inefficiency only affect those events close to the kinematic boundaries, which have a very small effect on the mass fits. For the M_t and E_T fits such events are excluded because of the fitting windows. An error of 10 MeV is assigned to each fit for the trigger efficiencies.

$u_{\|\|}$ slope	u_0	M_T^W fit (± 6 MeV)	E_T^e fit (± 8 MeV)	$\not\!E_T$ fit (± 10 MeV)
-0.0100	3.85	80.402	80.396	80.415
-0.0160	3.85	80.404	80.426	80.371
-0.0130	3.35	80.400	80.424	80.364
-0.0130	4.35	80.408	80.402	80.429
-0.0100	3.35	80.402	80.399	80.404
-0.0160	3.35	80.407	80.435	80.371
-0.0100	4.35	80.421	80.413	80.465
-0.0160	4.35	80.404	80.414	80.389

Table 9.16: Results of fits to Monte Carlo experiments with different $u_{||}$ efficiency parameters.

9.4.2 $u_{||}$ Efficiency

Monte Carlo experiments were generated with a range of $u_{||}$ efficiency parameters which spanned the uncertainty in the $u_{||}$ efficiency model. The results are shown in table 9.16. For each fit the error assigned is half of the total spread in the MC experiments.

Fit type	Maximum	Minimum	1/2 Spread
E_T^e fit	80.435	80.396	20
M_T^W fit	80.421	80.400	10
$\not\!\!E_T$ fit	80.465	80.371	47
E^e fit	80.449	80.371	39

Table 9.17: Spread in the W mass fits for varying $u_{||}$ efficiency parameters.

9.5 Backgrounds

The main backgrounds in the $W \rightarrow e\nu$ sample are due to τ decays, QCD fakes and $Z \rightarrow ee$ events in which one electron is missed. The τ decays are included in the simulation. QCD fakes enter the sample because there is a small probability ($\approx 10^{-4}$) that a jet fakes an electron by fluctuating electromagnetically. Such events may have enough $\not\!\!E_T$ to pass the 25 GeV cut because of the jet energy resolution. This background has been determined [2, 1] using a sample of fakes from a prescaled monitor trigger in which no $\not\!\!E_T$ cut was applied online. This sample consists mostly of QCD fakes. It would also contain the W sample except that the W content is reduced by the prescale factor of 10. This sample is divided into low and high $\not\!\!E_T$ regions. The low $\not\!\!E_T$ region is essentially entirely composed of fakes.

The high $\not{E}_T$ region contains a large fraction of W events. By applying anti–quality cuts to the electron candidates we extract the $\not{E}_T$ distribution of the fakes, which is determined by the jet resolution. This distribution is normalized to the inclusive sample in the low $\not{E}_T$, fake–dominated region. The shape of the $\not{E}_T$ distribution is then extrapolated into the high $\not{E}_T$ region. From this method the QCD background has been determined to be $1.4 \pm 0.2\%$. From the sample of fake events satisfying the kinematic cuts and the anti–quality cuts, the distributions of the relevant kinematic quantities are extracted for the background. These distributions are shown in figure 9.9. The systematic error due to the QCD background has been determined by refitting the data with varying background fraction f_{QCD}. The derivatives of the mass fits with respect to f_{QCD} are shown in table 9.18.

To estimate the fraction of $Z \rightarrow ee$ events which satisfy the W selection, we use a Monte Carlo sample of approximately 100,000 $Z \rightarrow ee$ events generated with HERWIG and simulated with the showerlibrary version of GEANT. The boson p_T spectrum from HERWIG agrees reasonably well with the Ladinsky and Yuan calculation [75]. $Z \rightarrow ee$ events typically enter the W sample when one electron satisfies the W cuts while the second electron is lost or mismeasured, causing the event to have large $\not{E}_T$.

Approximately 1.1% of the $Z \rightarrow ee$ events have an electron with rapidity $|\eta| >$

4.2, which is the acceptance limit of the end calorimeters. Most of these are events with low $\hat{s}$, for which both electrons are relatively soft. The fraction of $Z \rightarrow ee$ events which contain one electron with $|\eta| > 4.2$, another with $|\eta| > 1.0$, and $P_T(e) > 25$ GeV is approximately 0.04%. The contribution from the case of an electron lost down the beampipe is therefore relatively small.

An electron is most frequently mismeasured when it hits the ICD. In this case it is not reconstructed, but its shower is included in the recoil sum. Large $\not\!\!E_T$ is more likely for these events than for the case where both electrons hit one of the calorimeters. The mismeasured electron contributes to the recoil when the event is treated as a W, since the ICD cells are included in the recoil vector sum. The fraction of Z events in the W sample therefore depends on the $P_T(W)$ cut.

The Monte Carlo Z sample was modified to match the $Z \rightarrow ee$ data. The electron energies were scaled down by 0.95, and the recoil by 0.88 (0.87) for a recoil p_T cut of 30 (15) GeV. The $\not\!\!E_T$ vector from a minimum bias event was added to the recoil vector. We find that 10987 events pass the CC-CC $Z \rightarrow ee$ selection, and 1318 (758) pass the W selection with a recoil cut of 30 (15) GeV. After taking into account the electron identification efficiency for the seciond electron in the Z sample of approximately 79%, the fraction of Z events in the W sample is

$$f_Z \quad = \quad 0.62 \pm 0.01(\mathrm{stat})\% \;\; P_T(W) < 30\mathrm{GeV} \tag{9.3}$$

Fit	f_Z derivative (MeV per %)	f_{QCD} derivative (MeV per %)
E_T^e fit	-148	-8
M_T^W fit	48	-13
$\not{E}_T$ fit	38	4

Table 9.18: Derivatives of the mass fits with respect to f_{QCD} and f_Z.

$$f_Z = 0.42 \pm 0.01(\text{stat})\% \; P_T(W) < 15\text{GeV} \tag{9.4}$$

The results based on the showerlibrary sample agree with those based on a sample of approximately 10,000 events generated with ISAJET and simulated with full showering mixture level GEANT. Figure 9.10 shows the kinematic distributions for the Z events which enter the W sample. These shapes are included in the fitting spectra.

9.6 Summary

The errors in the W mass fits due to experimental effects are summarized in table 9.19. The errors for the recoil lepton removal, electron response η dependence and QCD background are taken from reference [1].

Source of error	M_T^W fit	E_T^e fit	$\not{E}_T$ fit
Electron energy offset	51	32	46
Electron energy resolution	14	7	4
Electron response η dependence	10	10	10
CDC and CAL z scale	28	28	28
Recoil response: α_{rec} and β_{rec}	23	21	40
Recoil resolution: α_{MB} and S_{HAD}	33	9	126
Recoil lepton removal	16	16	20
Trigger efficiencies	10	10	10
$u_{\|\|}$ efficiency	10	20	47
QCD background	11	16	22
Z background	3	8	2
Total	77	60	154

Table 9.19: Summary of experimental errors in the W mass fits.

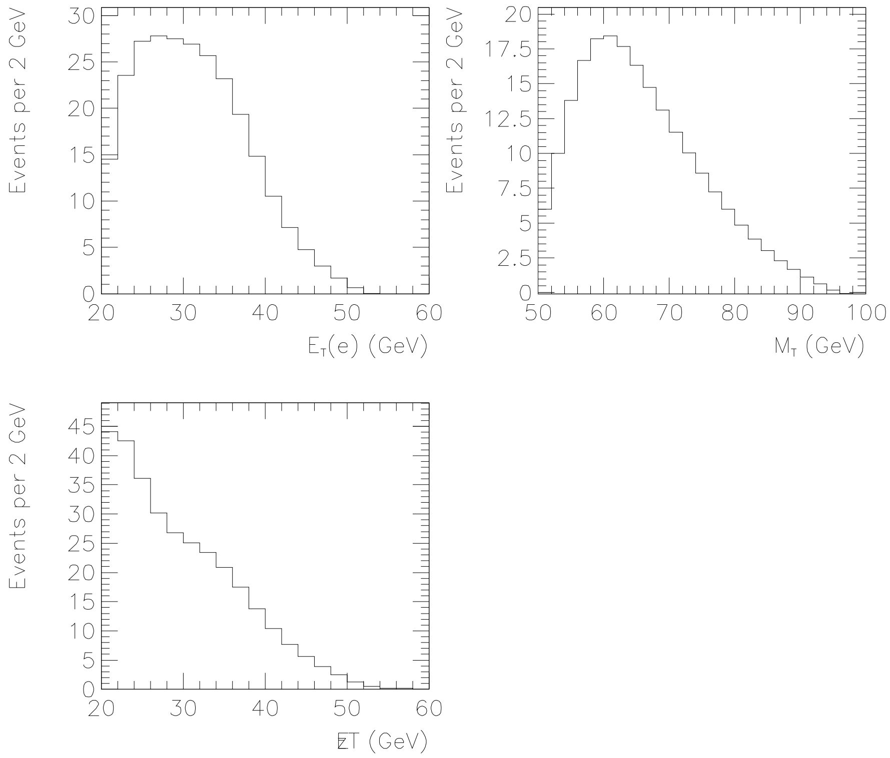

Figure 9.9: Distributions of kinematic quantities for QCD background events.

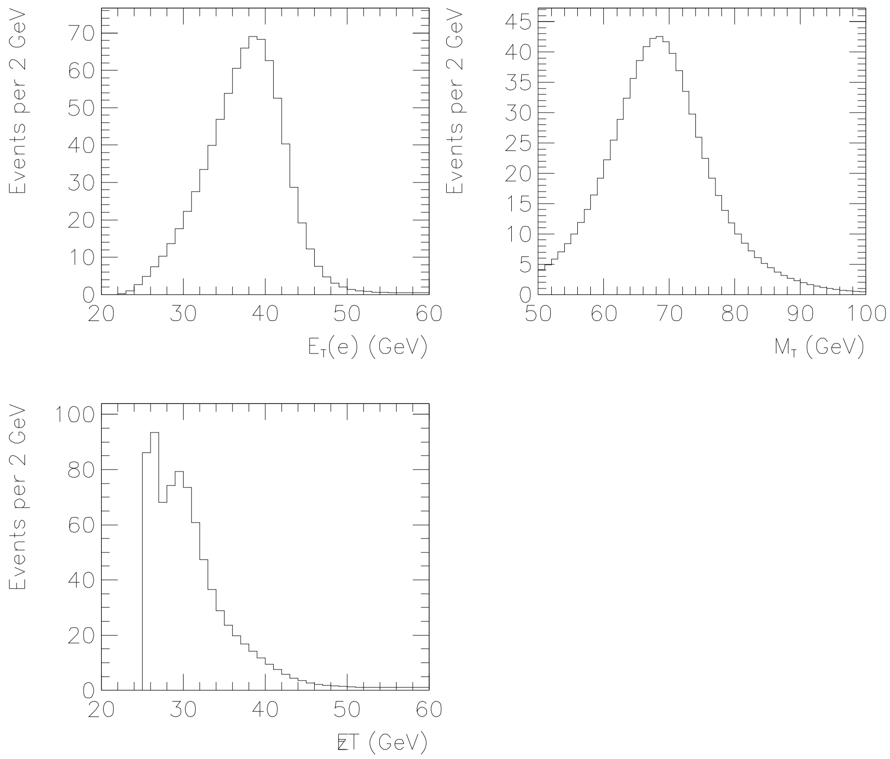

Figure 9.10: Distributions of kinematic quantities for Z background events, in which one electron is missed and fake $\not{E}_T$ arises from resolution effects.

Chapter 10

Results and Conclusion

10.1 Fitting Procedure

There are several ways to determine the "best match" between predicted and measured spectra, such as the χ^2 test, Kolmogorov–Smirnov (KS) test, and the maximum likelihood (ML) test. We chose to use the maximum likelihood method because it is relatively insensitive to tails in distributions and can be performed in an effectively unbinned manner. We use the χ^2 and KS tests to check the quality of the fits.

The CMS Monte Carlo program is used to determine the likelihood functions for the Z invariant mass and the W transverse mass and electron E_T. Given a

W pole mass M_W, the program calculates the probability distribution $P(q|M_W)$ of observing an event with mass estimator q, where q is used generically to refer to transverse mass, electron E_T, $\not{E}_T$ or electron energy. For a dataset of N events, the probability of the dataset given a W mass M_W is then

$$\mathcal{P}(M_W) = \prod_{i=1}^{N} P(q_i|M_W) \tag{10.1}$$

The maximum likelihood fit value for M_W is the value which maximizes the probability $\mathcal{P}(M_W)$. Numerically it is easier to use the logarithm of the probability rather than the probability itself, and one can minimize $-\log \mathcal{P}(M_W)$ or maximize $\log \mathcal{P}(M_W)$ interchangeably. The statistical error interval is given by the points at which the $-\log \mathcal{P}(M_W)$ increases by $1/2$ from its minimum value.

10.2 Fits to the Kinematic Spectra

Figures 10.1, 10.2 and 10.3 show the fits to the electron E_T, M_T and $\not{E}_T$ spectra. Also shown are the corresponding likelihood curves and plots of the bin–by–bin deviations of the data from the fit normalized to the expected error. Table 10.1 gives the Kolmogorov–Smirnov probability and χ^2 statistic for each fit.

The variations of the fitted values with the lower and upper edges of the fitting window are shown in figures 10.4 and 10.5. In each case the variations in the lower

Fit type	Fitting Window	KS probability	χ^2
E_T^e fit	[30,50]	61.0%	38.8/39
M_T^W fit	[60,90]	78.7%	79.9/59
$\not{E}_T$ fit	[30,50]	79.6%	33.2/39

Table 10.1: Goodness of fit measures for W mass fits.

edge are consistent with fluctuations and with effects of approaching the kinematic cuts.

For the electron E_T method the fit is stable with respect to the upper window edge, excepting the dip between 40 and 45 GeV which appears to be statistical fluctuation, since no systematic slope is apparent. This fluctuation is visible in the electron E_T distribution at around 82–83 GeV. However, the variation with the upper edge of the window is large for the $\not{E}_T$ fit, and smaller but still significant for the M_T fit. In the present analysis the M_T and $\not{E}_T$ fits are used as qualitative cross checks only. The variation in the KS probability as a function of the edge was used to select the fitting window. To each fit a systematic error has been included to span reasonable variations in the window upper edge, from 46 GeV to 54 GeV for the electron E_T and $\not{E}_T$ fits and from 92 GeV to 108 GeV for the M_T

Source of error in fit	E_T^e fit (MeV)	M_T^W fit (MeV)	$\not{E}_T$ fit (MeV)
Statistical	87	69	107
Scale	65	65	65
Systematic	86	84	159
Theoretical model	61	33	40
Detector effects	60	77	154
Fitting window	8	12	51
Total	139	127	209

Table 10.2: Summary of errors in the W mass fits.

fit. The large variation with the upper edge in the $\not{E}_T$ fit indicates mismodelling of the recoil. The extent to which this affects the fit results are quantified by the fitting error. The electron fit is insensitive to such mismodelling.

10.3 Summary of Results

For the electron E_T fit we obtain

$$M_W = 80.472 \pm 0.087(\mathrm{stat}) \pm 0.065(\mathrm{scale}) \pm 0.086(\mathrm{sys})\ \mathrm{GeV} \qquad (10.2)$$

$$= \quad 80.472 \pm 0.139\,\mathrm{GeV} \tag{10.3}$$

For the transverse mass fit we obtain

$$M_W \quad = \quad 80.437 \pm 0.069(\mathrm{stat}) \pm 0.065(\mathrm{scale}) \pm 0.084(\mathrm{sys})\,\mathrm{GeV} \tag{10.4}$$

$$= \quad 80.437 \pm 0.127\,\mathrm{GeV} \tag{10.5}$$

For the $\not{E}_T$ fit we obtain

$$M_W \quad = \quad 80.357 \pm 0.107(\mathrm{stat}) \pm 0.065(\mathrm{scale}) \pm 0.159(\mathrm{sys})\,\mathrm{GeV} \tag{10.6}$$

$$= \quad 80.357 \pm 0.203\,\mathrm{GeV} \tag{10.7}$$

These total errors due not include the uncertainty due to the fitting window choice. Monte Carlo ensembles of 30000 events were generated, and for each experiment the three fits were performed. The rms over these ensembles of the differences between the mass fits are given in table 10.3. The fits are consistent with each other. The $\not{E}_T$ fit provides only a very weak cross check because the systematic error and fitting window variation are large. Table 10.2 summarizes the errors the each fit.

Fit type difference	MC ensemble rms	Observed Difference
M_T^W fit $-$ E_T^e fit	105	35
M_T^W fit $-$ $\not{E}_T$ fit	112	80
E_T^e fit $-$ $\not{E}_T$ fit	165	115

Table 10.3: Expected variations between fits for a 30000 event sample.

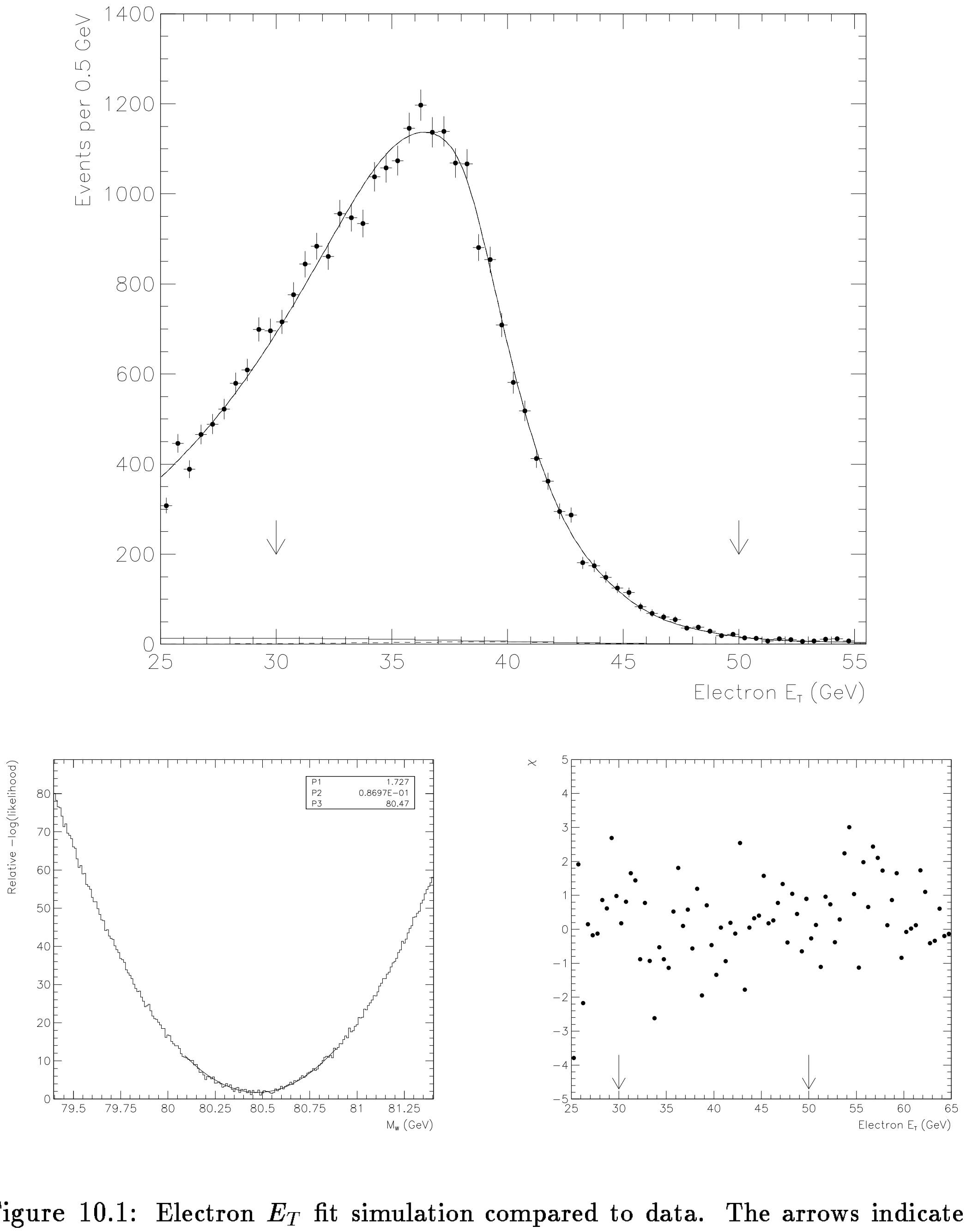

Figure 10.1: Electron E_T fit simulation compared to data. The arrows indicate the fit region. The background contributions are also shown. The lower figures are the likelihood curve and χ vs. bin plot.

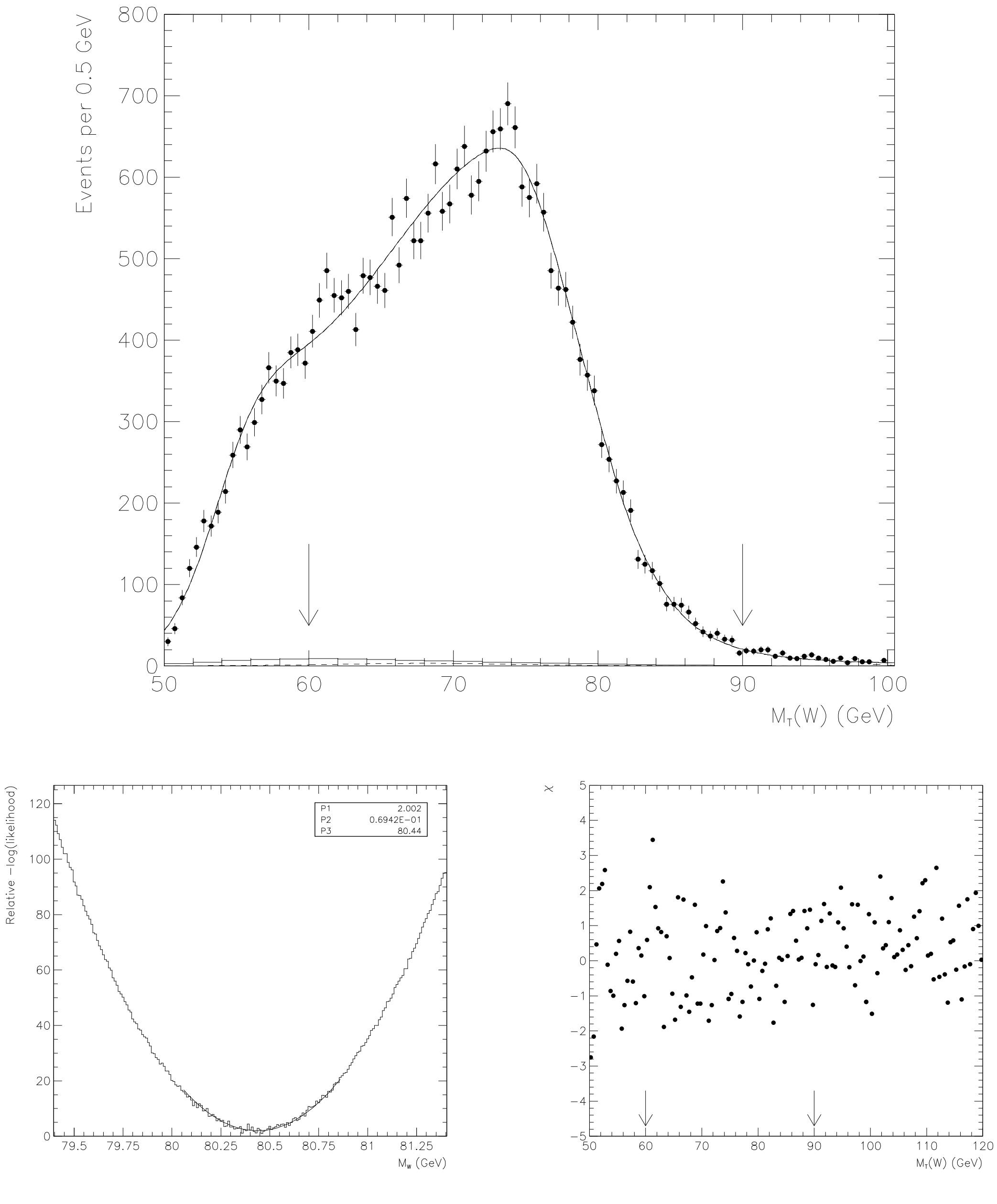

Figure 10.2: M_T fit simulation compared to data. The arrows indicate the fit region. The background contributions are also shown. The lower figures are the likelihood curve and χ vs. bin plot.

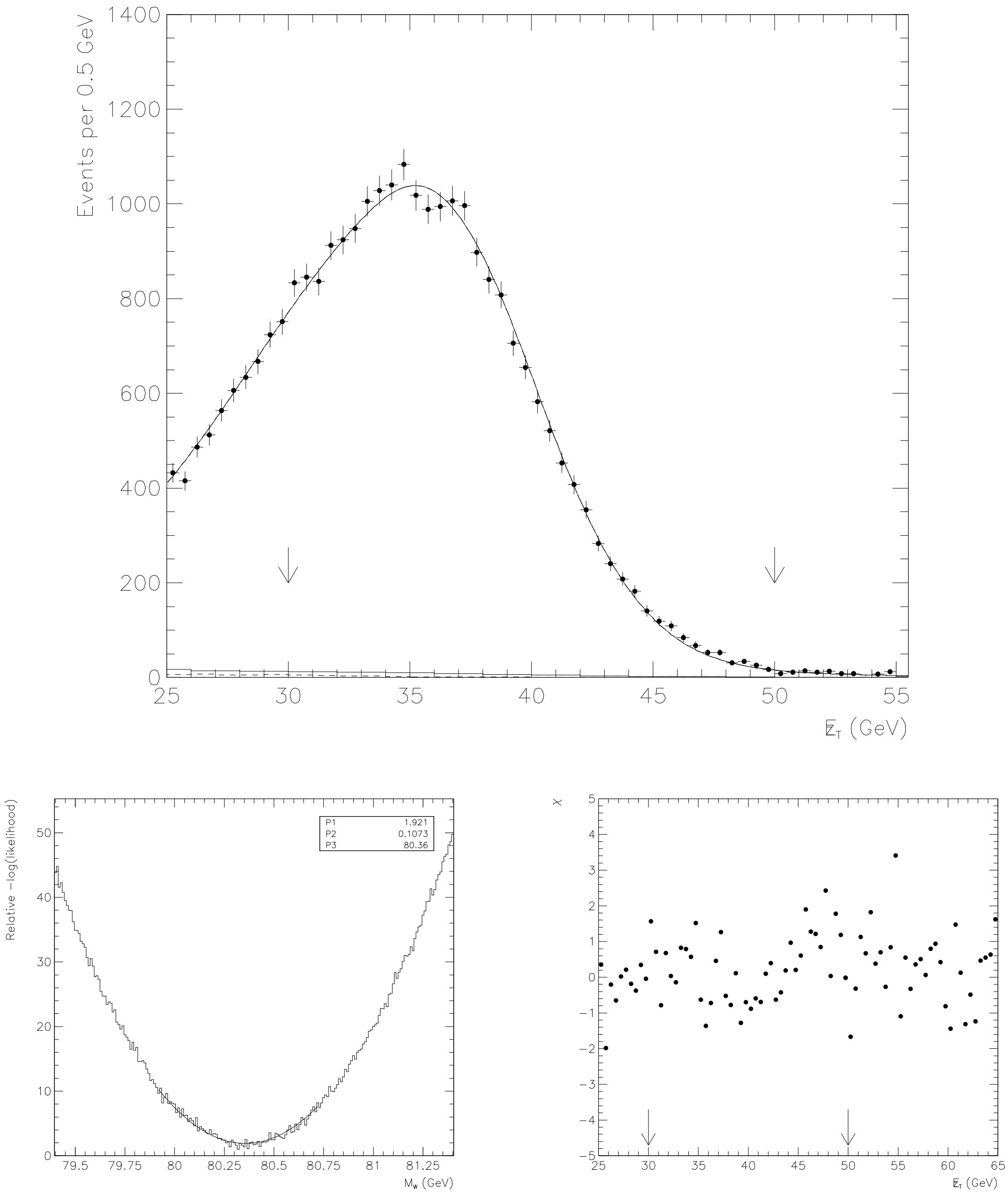

Figure 10.3: Missing E_T fit simulation compared to data. The arrows indicate the fit region. The background contributions are also shown. The lower figures are the likelihood curve and χ vs. bin plot.

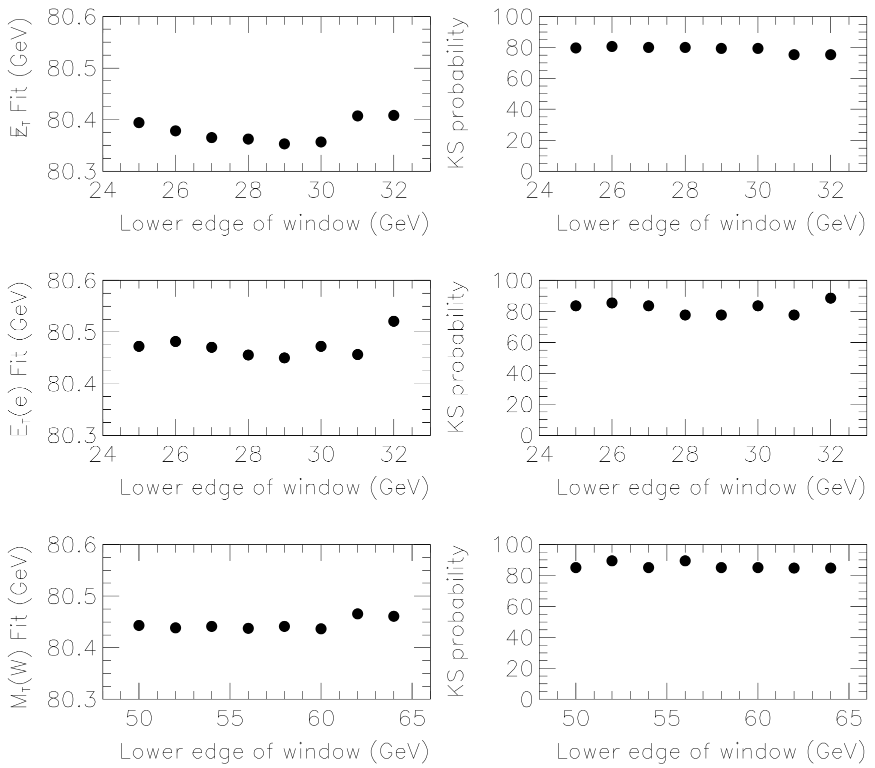

Figure 10.4: Variations in the mass fits with respect to the lower edge of the fitting window, and the corresponding values of the KS probabilities.

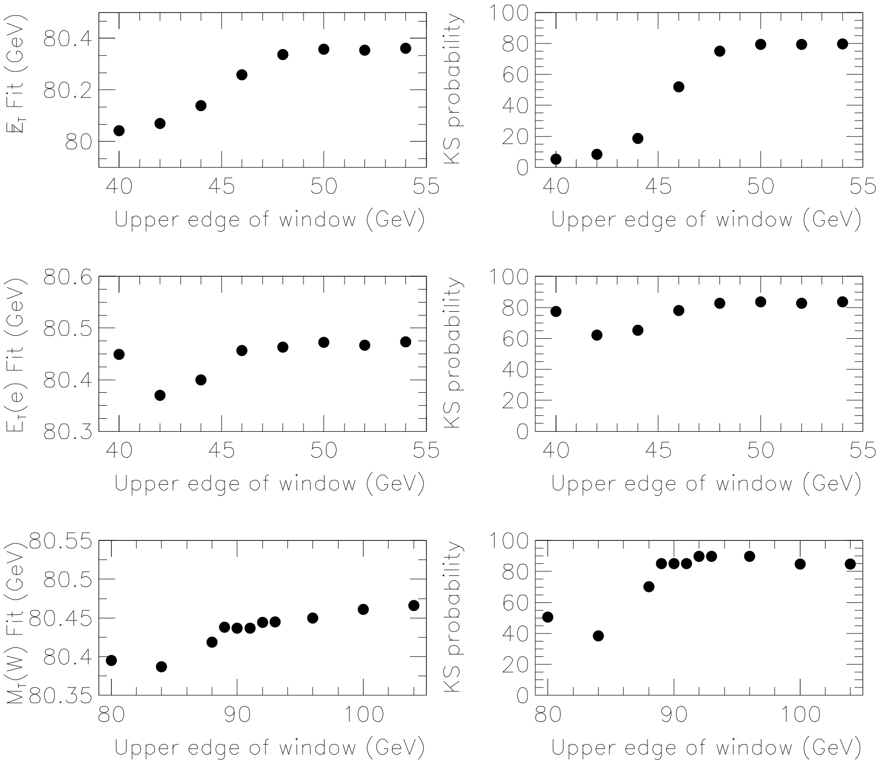

Figure 10.5: Variations in the mass fits with respect to the upper edge of the fitting window, and the corresponding values of the KS probabilities.

10.4 Conclusion and Future Prospects

DØ has presented a preliminary W mass using the transverse mass fit at the Summer 1996 conferences of

$$M_W = 80.38 \pm 0.17\,\text{GeV} \tag{10.8}$$

This measurement has since been improved. New features include a better model for the hadronic response and resolution, a more precise calibration of the central drift chamber, and a lower uncertainty due to the production model. With these updates the total error will decrease to about 120 MeV. In the longer term the inclusion of electrons in the endcap calorimeters have the potential to increase the sample size by about 50%. With this larger sample the anticipated error is about 100 MeV.

Using the electron E_T spectrum, the W mass has been measured using the DØ Run 1b data to be

$$M_W = 80.47 \pm 0.14\,\text{GeV} \tag{10.9}$$

The total error is 0.17%. This result is more precise than any previously published direct measurement, and is comparable to the standard M_T fit to the same data set. Figure 10.6 shows the present result compared to a recent calculation based on the Standard Model [12], with the top quark mass set to 175 GeV. With the present experimental uncertainty it is not yet possible to rule out the Standard Model.

This method is viable because although the theoretical error in the p_T distribution of either the W or Z is large, the error in their difference is small. Therefore it is possible to constrain the P_T^W model using Z events. This method would not have been useful with earlier data because of the limited number of Z decays available.

The W mass measurement from the electron spectrum is interesting for several reasons. For the present data it provides a measurement technique competitive with the standard transverse mass method. Though it is more sensitive to the P_T^W model and has less statistical power than the M_T method, it has the advantage of being much less sensitive to hadronic systematic effects which are experimentally difficult to handle.

As a spinoff of the electron E_T measurement, the production model error in the standard M_T measurement has been reduced significantly. Since this is the primary common error between hadron collider measurements, reducing it can in principle enhance the power of combining all the $p\bar{p}$ measurements.

The electron E_T method will become even more interesting in the next generation of Tevatron experiments. In Run II the high luminosity environment will degrade the $\not{E}_T$ resolution and render the hadronic recoil even more difficult to model, while the electron resolution will not get much worse. There will also be a large increase in the number of Z events, with corresponding improvements in the P_T^W model constraint. These considerations apply *a fortiori* to the proposed Tevatron Run III with accelerator upgrades capable of delivering luminosities in excess of $10^{33}\mathrm{cm}^{-2}\mathrm{s}^{-1}$.

With the combined results from the next generation of Tevatron data and the complementary measurements from LEP II it should be possible within the next decade to zero in on this fundamental parameter of electroweak physics.

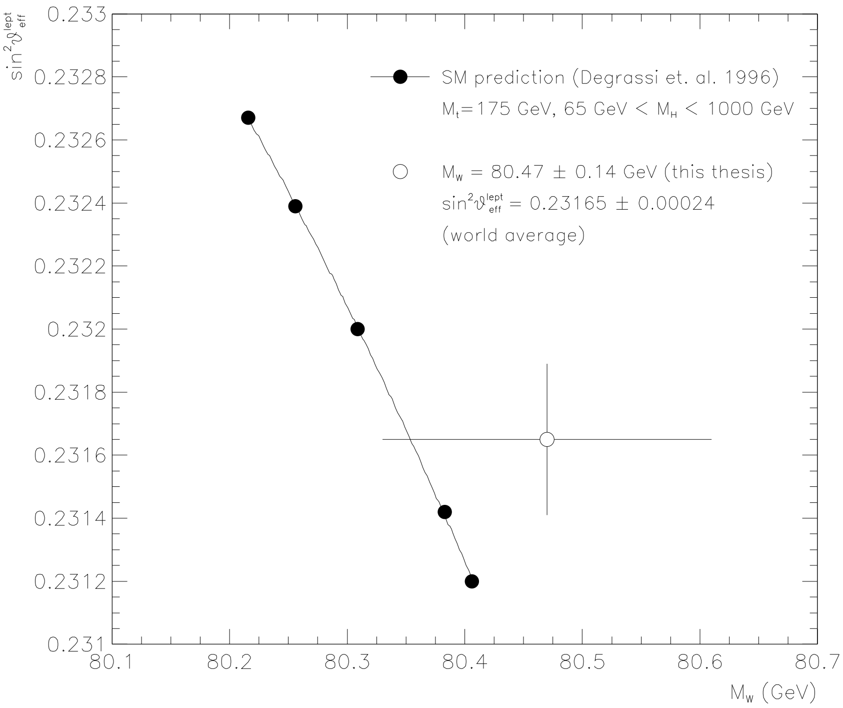

Figure 10.6: A recent Standard Model calculation of M_W vs. $\sin^2\theta_{eff}^{lept}$ for a range of Higgs masses. The top quark mass has been fixed to 175 GeV.

Appendix A

Conventions

This appendix describes various conventions and jargon.

A.1 Units

We use units in which $\hbar = c = 1$. In these units energies and momenta are measured in GeV, distances and times in GeV^{-1}. A useful conversion factor is $\hbar c \approx 200\mathrm{MeV} \cdot \mathrm{fm}$ for converting GeV^{-1} to distances in fermi (fm), where 1 fm = 10^{-15} meter.

A.2 Coordinate Systems

DØ uses a right–handed coordinate system. The beam axis runs approximately north–south at the DØ interaction region. The $+z$ axis is along the proton direction, which is south. The x axis is horizontal with the $+x$ orientation pointing towards the center of the ring. The y axis is vertical with the $+y$ orientation pointing upwards.

Azimuthal angles, ϕ, are measured with respect to the $+x$ axis so that $\phi = 0$ coincides with the $+x$ axis and $\phi = \pi$ with the $-x$ axis. The range of ϕ is $[0, 2\pi)$. Polar angles, θ, take values in $[0, \pi]$ and are measured from the $+z$ axis.

Other specialized local coordinate systems are used by the various subdetectors.

A.3 Rapidity and pseudorapidity

The rapidity y of a particle with 4–momentum p^μ is given by

$$y = \log \frac{E - p_z}{E + p_z} \tag{A.1}$$

The pseudorapidity η of a particle is defined by

$$\eta = -\log \tan \frac{\theta}{2} \tag{A.2}$$

For a massless particle the two definitions are equivalent and $y = \eta$. Pseudorapidity is useful in this case because it is easily calculated from the polar angle alone. For massive particles such as W and Z bosons pseudorapidity is not a useful quantity.

For many final state particles of interest, such as leptons and photons, it is usually a good approximation to assume them to be massless. Rapidity is a useful quantity because rapidity distributions are invariant under longitudinal Lorentz boosts. Also, many processes have differential distributions which are approximately constant in rapidity. For example, the particle production cross section in minimum bias events $dN/d\eta$ obeys $dN/d\eta \approx$ constant. For this reason the detectors and trigger systems are segmented longitudinally in units of pseudorapidity.

A.4 Assorted Jargon

Experimental physicists often compare two distributions by saying that one is "harder" than the other, meaning that it is skewed towards higher values. Similarly a "softer" distribution is skewed towards lower values.

A differential distribution of a quantity x is called "flat" if dN/dx is constant.

W and Z bosons are often called intermediate vector bosons (IVB) for historical reasons.

Bibliography

[1] I. Adam, E. Flattum, U. Heintz, "W Boson Mass Measurement using Run 1b Data," DØ note 3198.

[2] E. Flattum, PhD Thesis, Michigan State University, 1996 (unpublished.)

[3] Q. Zhu, PhD Thesis, New York University, 1993 (unpublished.)

[4] D. Griffiths, "Introduction to Elementary Particles," Wiley, New York 1987.

[5] R. Cahn and G. Goldhaber, "The Experimental Foundations of Particle Physics," Cambridge University Press, New York 1989.

[6] L. Ryder, "Quantum Field Theory," Cambridge University Press, New York 1988.

[7] C. Itzykson and J. Zuber, "Quantum Field Theory," McGraw Hill, New York 1980.

[8] DØ collaboration, “Observation of the top quark,” Phys. Rev. Lett. 74 (1995) 2632-2637

[9] CDF collaboration, “Observation of top quark production in $p\bar{p}$ collisions,” Phys. Rev. Lett. 74 (1995) 2626-2631.

[10] A. Sirlin, Phys. Rev. D 22 (1980) 971.

[11] P. Gambino and A. Sirlin, “Relation between $\sin^2\hat{\theta}_W(m_Z)$ and $\sin^2\theta_{eff}^{lept}$,” Preprint NYU-TH-93/09/07

[12] G. Degrassi, P. Gambino and A. Sirlin, “Precise calculation of M_W, $\sin^2\hat{\theta}_W(m_Z)$ and $\sin^2\theta_{eff}^{lept}$,” Preprint NYU-TH-96/11/02

[13] D. Pierce et. al., “Precision corrections in the minimal supersymmetric standard model,” Preprint SLAC-PUB-7180, June 1996.

[14] M. Demarteau, J. Sculli and K. Streets, “Measurement of the W Mass,” DØ note 2929 (1996)

[15] M. Demarteau, J. Sculli and K. Streets, DØ note 2470.

[16] J. Thompson, “Introduction to Colliding Beams at Fermilab,” DØ note 2367, FERMILAB-TM-1909.

[17] HTTP://FNNEWS.FNAL.GOV/ACCEL_TOUR.HTML

[18] DØ Collaboration, "The DØ Detector", Nucl. Instr. Meth. A 338 (1994) 185.

[19] S. Snyder, PhD Thesis, SUNY Stony Brook, May 1995 (unpublished) http://d0hs19.fnal.gov/newthesis/ps/ch3.ps

[20] C. Brown et al., "DØ muon system with proportional drift tube chambers", Nucl. Instr. Meth. A 279 (1989) 331.

[21] J. Detoeuf et al., "Status of the Transition Radiation Detector for the DØ experiment", Nucl. Instr. Meth. A 279 (1989) 310.

[22] A. Clark et al., "The central tracking detectors for DØ", Nucl. Instr. Meth. A 279 (1989) 243.

[23] A. Clark et al., "DØ vertex drift chamber construction and test results", Nucl. Instr. Meth. A 315 (1992) 193.

[24] Particle Data Group, L. Montanet et.al., Phys. Rev. D50 (1994)

[25] H. Plothow–Besch, Comp. Phys. Comm.75 (1993) 396–416.

[26] CTEQ Collaboration, "Handbook of Perturbative QCD," Rev. Mod. Phys. bf 67 1, January 1995. HTTP://WWW.PHYS.PSU.EDU/ CTEQ/HANDBOOK

[27] J. Collins, D. Soper and G. Sterman, Nucl. Phys. B250 (1985) 199.

[28] J. Collins and D. Soper, Nucl. Phys. B193 (1981) 381.

[29] J. Collins and D. Soper, Nucl. Phys. B194 (1982) 445.

[30] J. Collins and D. Soper, Nucl. Phys. B197 (1982) 446.

[31] P. B. Arnold and R. P. Kauffman, Nucl. Phys. B349, 381 (1991)

[32] M. Reno, "Relative distributions of W's and Z's at low transverse momenta", Phys. Rev. D49, (1994) 4326-4330.

[33] G. A. Ladinsky and C.-P. Yuan, "The Nonperturbative Regime in QCD Resummation for Gauge Boson Production at Hadron Colliders," Phys. Rev. D50 (1994) 4239.

[34] G. A. Ladinsky and C.-P. Yuan, "Documentation on LEGACY: Routines for Gauge Boson Production at Hadron Colliders", 31 August 1994.

[35] G. Altarelli, R. K. Ellis, M. Greco and G. Martinelli, " Vector Boson Production at Colliders: A Theoretical Reappraisal", Nucl. Phys. B246 (1984) 12-44.

[36] U. Baur and D. Zeppenfeld, "Finite Width Effects and Gauge Invariance in Radiative W Production and Decay", Phys. Rev. Lett. 75 6 (1995) 1002

[37] U. Baur et al., "Implications of $\mu\nu\gamma\gamma$ production on precision measurements of the W mass," UB-HET-96-03, October 1996.

[38] F. A. Berends and R. Kleiss, Z. Phys. C27 (1985) 365

[39] E. Flattum, DØ note 2396.

[40] E. Mirkes and J. Ohnemus, "W and Z polarization effects in hadronic collisions", Phys. Rev. D 50 9 (1994) 5692-5703.

[41] G. Marchesini et. al., Computer Physics Communications 67 (1992) 465.

[42] F. Paige and S. Protopopescu, "ISAJET: A Monte Carlo Event generator for pp and $p\bar{p}$ reactions"

[43] DØ W and Z cross section results presented at ICHEP96, Warsaw, 1996.

[44] A. Goldschmidt and S. Glenn, DØ note 2419.

[45] M. Narain, CM3POS_PV implementation.

[46] CDF Collaboration, FERMILAB-PUB-95/033-E. Section 7.3.1

[47] D. Saltzberg, PhD thesis, University of Chicago, 1995 (unpublished.)

[48] CDF Collaboration, FERMILAB-PUB-90/162-E.

[49] CDF Collaboration, Phys. Rev. Lett. 74 (1995) 850–854

[50] HTTP://CDFSGA.FNAL.GOV/PHYSICS/EWK/WASYM.HTML

[51] UA2 Collaboration, "An improved determination of the ratio of W and Z masses at the CERN $p\bar{p}$ collider," Phys. Lett. B 276 (1992)

[52] J. Smith, W. L. Van Neerven, J. A. Vermaseren, "Transverse Mass and Width of the W boson," Phys. Rev. Lett. 50 22 (1983) 1738-1740.

[53] C. Davies, B. Webber and W. Stirling, Nucl. Phys. B256 (1985) 413.

[54] C. Balazs, J. Qiu, C.-P. Yuan, "Effects of QCD resummation on Distributions of Leptons from the decay of Electroweak Vector Bosons", MSUHEP-50319, April 1995.

[55] C. Balazs, J. Qiu, C.-P. Yuan, Phys. Lett. B355 548 (1995).

[56] The TeV2000 Study Group, "Future Electroweak Physics at the Tevatron: Report of the TeV 2000 Study Group," FERMILAB-PUB-96/082, April 1996.

[57] N. Graf, private communication.

[58] T. Yasuda, DØ Note 2782.

[59] A. Kotwal, "Calibration of the CDC z scale using Dimuon Events in Run 1b," DØ Note 3134.

[60] A. Kotwal, "Calibration of the CDC z scale using Cosmic Rays in Run 1b Collider Data," DØ Note 3187.

[61] H. Mao et. al., "ZCD Data Analysis and CDC z Bias Correction," DØ Note 3140.

[62] E. Flattum, DØ Note 3179.

[63] P. Renton, "Review of Experimental Results on Precision tests of Electroweak Theories," Preprint OUNP-95-20, October 1995.

[64] D. Casey, PhD thesis, University of Rochester, in preparation.

[65] J. Jaques, PhD thesis, University of Notre Dame, unpublished (1996).

[66] T. Kinoshita, "The Fine Structure Constant," Cornell Preprint CLNS 96-1406, April 10, 1996.

[67] J. McKinley, PhD thesis, Michigan State University, unpublished (1996).

[68] R.J. Genik, PhD thesis, Michigan State University, in preparation.

[69] S. Fahey, PhD thesis, Michigan State University, unpublished (1995).

[70] U. Heintz, DØ note 2209.

[71] U. Heintz, DØ note 2268.

[72] I. Adam et al., DØ note 2298.

[73] U. Heintz and I. Adam, DØ note 2739.

[74] U. Heintz, DØ note in preparation.

[75] A. Gupta and A. Kotwal, DØ note 3195